

Bank erosion in regulated navigable rivers

Duro, G.

10.4233/uuid:805eaec5-3b87-4bd6-bbe3-fa896da3b1c5

Publication date 2020

Document Version Final published version

Citation (APA)

Duro, G. (2020). Bank erosion in regulated navigable rivers. [Dissertation (TU Delft), Delft University of Technology]. https://doi.org/10.4233/uuid:805eaec5-3b87-4bd6-bbe3-fa896da3b1c5

Important note

To cite this publication, please use the final published version (if applicable). Please check the document version above.

Copyright

Other than for strictly personal use, it is not permitted to download, forward or distribute the text or part of it, without the consent of the author(s) and/or copyright holder(s), unless the work is under an open content license such as Creative Commons.

Please contact us and provide details if you believe this document breaches copyrights. We will remove access to the work immediately and investigate your claim.

This work is downloaded from Delft University of Technology. For technical reasons the number of authors shown on this cover page is limited to a maximum of 10.

Bank Erosion in Regulated Navigable Rivers

Gonzalo Duró

Bank Erosion in Regulated Navigable Rivers

Gonzalo DURÓ

Bank Erosion in Regulated Navigable Rivers

Dissertation

for the purpose of obtaining the degree of doctor
at Delft University of Technology
by the authority of the Rector Magnificus Prof. dr. ir. T. H. J. J. van der Hagen,
chair of the Board for Doctorates
to be defended publicly on
Friday 22 January 2021 at 10:00 o'clock

By

Gonzalo DURÓ

Master of Science in Hydraulic Engineering, IHE-Delft, the Netherlands born in La Plata, Argentina

This dissertation has been approved by

Prof. dr. ir. W. S. J. Uijttewaal, promotor

Dr. ir. A. Crosato, copromotor

Composition of the doctoral committee:

Rector Magnificus Chairperson

Prof. dr. ir. W. S. J. Uijttewaal Delft University of Technology, promotor

Dr. ir. A. Crosato IHE-Delft, copromotor

Prof. dr. M. G. Kleinhans Utrecht University

Independent members:

Prof. dr. S. E. Darby University of Southampton, United Kingdom

Prof. dr. ir. A. J. F. Hoitink Wageningen University & Research

Dr. ir. A. W. D. Sieben Rijkswaterstaat, the Netherlands

Prof. dr. ir. R. F. Hanssen Delft University of Technology





Keywords: river morphodynamics, bank erosion, navigation, retreat modelling, river restoration

Copyright © 2020 by Gonzalo Duró

ISBN: 978-94-6366-352-6

Cover design: Adriana P. Magni

Layout and design: Eduard Boxem | www.persoonlijkproefschrift.nl

Printing: Ridderprint | www.ridderprint.nl

An electronic copy of this dissertation is available at http://repository.tudelft.nl/

To my family and to Sofía, in particular

CONTENTS

<u>Summary</u>	11
Samenvatting	15
CHAPTER 1 Introduction	
1.1. Context and relevance	22
1.2. Riverbank erosion	25
1.2.1. Primary causes and scale of analysis	25
1.2.2. Bank erosion cycle	26
<u>Entrainment</u>	26
<u>Failure</u>	28
Slump blocks	29
1.2.3. Drivers of bank erosion	30
<u>Flow</u>	30
Ship waves	32
Bank hydrology: rainfall, water level changes and seepage	33
<u>Subaerial erosion</u>	33
1.2.4. Bank vegetation	34
Hydraulics and entrainment	34
Resistance against failure	35
Slump block degradation	35
Bank height, root depth and vegetation position on the bank	36
1.2.5. Navigable rivers and technical-biological bank protections	38
1.2.6. Bank erosion prediction for navigable rivers	41
1.3. Research objective	43
1.4. Approach and research components	43
1.5. Thesis outline	45
CHAPTER 2 Reach-scale bank erosion processes measured with UAV-SfM	
2.1. Introduction	48
2.2. Framework of analysis	49
2.3. Techniques to measure bank erosion at different scales	49
2.3.1. Structure from motion photogrammetry	51
2.4. Methodology	53
2.4.1. UAV flights for image acquisition	55

2.4.2. SfM workflow	56
2.5. Results	59
2.5.1. DSM precision: identifying necessary photographs	59
2.5.2. DSM precision over the reach: comparison with ALS	61
2.5.3. DSM accuracy: rotation around GCP axis	64
2.5.4. Bank erosion features and process identification	65
2.6. Discussion	68
2.6.1. UAV flight and SfM precision	68
2.6.2. Comparison of two reach-scale techniques: SfM and ALS	71
2.6.3. UAV-SfM challenges to measure bank erosion processes	72
<u>Vertical surfaces</u>	72
<u>Linear domain</u>	73
Recommendations	73
2.6.4. Surveying bank erosion with UAV-SfM and other techniques	75
2.7. Conclusion	77
CHAPTER 3 Distinct patterns of bank erosion in a navigable regulated rive 3.1. Introduction	er 82
	_
3.2. Study sites and erosion patterns	83
3.3. Methods	85
3.3.1. Mechanisms for erosion	86 88
3.3.2. Factors affecting bank resistance	
3.4.1 Currents	89 89
3.4.1. Currents	
3.4.2. Ship waves 3.4.3. Lithological succession and stratification	91 91
3.4.4. Upper-bank erosion	91 95
3.5. Interpretation of results	95 96
3.5.1. Currents	96
3.5.2. Ship waves	97
3.5.3. Trees	98
3.5.4. Lithological succession and stratification	99
3.5.5. Other factors	103
3.6. Discussion	104
3.6.1. Ship-induced waves and terrace formation	104

3.6.2. Effects of tree roots on bank erosion	104
3.6.3. Floodplain heterogeneity on bank erosion and river migration	105
3.7. Conclusions	106
CHAPTER 4 Bank erosion processes in a regulated navigable river	
4.1. Introduction	110
4.2. Methods	111
4.2.1. Wave measurements	112
4.2.2. Upper bank	114
4.2.3. Terrace and lower bank	114
4.3. Results and interpretation	115
4.3.1. Ship-wave characteristics	115
4.3.2. Upper-bank erosion processes	118
4.3.3. Differences in bank retreat	121
4.3.4. Terrace and lower-bank evolution	123
4.4. Discussion	125
4.4.1. Ship-wave and flood contributions to bank erosion	125
4.4.2. Vegetation and biofilm effects on bank erosion	127
4.4.3. Conceptualization	130
4.4.4. Long-term erosion prediction	132
Primary wave drawdown	133
Primary wave surge	134
Wave run-up	136
Secondary waves	136
Morphological update	137
Modelled conditions	138
Model results	138
<u>Discussion of model results</u>	139
4.5. Conclusions	14:
CHAPTER 5 Discussion	
5.1. Erosion of re-naturalized banks in other settings	140
5.1.1. Gravel layer and toe protection: case at Sint Agatha, Meuse River	140
5.1.2. Composite banks: case at Neerloon, Meuse River, the Netherlands	149
5.1.3. Currents and river planform: case at Thurnhaufen, Danube River	154

5.1.4. Unregulated water levels: cases at Worms (Rhine River), Steinmauern, (Rhine River), Fortmond (IJssel River), and Tiel (Waal River)	157
Worms, Rhine River	158
Steinmauern, Rhine River	159
Fortmond, IJssel River	159
<u>Tiel, Waal River</u>	160
Interpretation of observations	161
5.2. How to combine navigation, reduced erosion and more natural banks?	163
5.3. Modelling ship-induced bank erosion	166
5.3.1. Bank erosion rates in regulated rivers	167
5.3.2. Bank erosion in unregulated rivers	169
CHAPTER 6 Conclusions and recommendations	
6.1. Conclusions	174
6.2. Recommendations for further research	177
<u>Bibliography</u>	180
<u>Acknowledgements</u>	204
<u>Curriculum Vitae</u>	207
<u>Publications</u>	209

SUMMARY

Banks constitute important areas for the river ecology since they provide a multitude of favourable conditions for flora and fauna. The hydromorphological diversity typical of these transitional zones between water and land, and the associated processes of erosion and accretion, make riverbanks vital for many aquatic and riparian plants and animals. In recent decades, the increasing awareness of the ecological significance of rivers and water bodies resulted in the gradual implementation of extensive stream, river and floodplain restoration. In the EU, these practices are regulated by the Water Framework Directive. An important and largely applied re-naturalization measure in highly trained watercourses is the removal of bank protections to reactivate erosion processes and promote habitat diversity.

In rivers used as waterways, ship waves can be an important cause of bank erosion and ecological disturbance. The sediment yield from bank erosion may alter navigable depths, the water quality, and flood conveyance, for which enhancing the hydromorphology is a challenge in multifunctional rivers. Due to pressing needs to improve riverine habitats, large-scale restoration works have been implemented based on conceptual schemes without a comprehensive knowledge of wave erosion processes or a precise estimate of long-term bank retreat. The Meuse River in the Netherlands constitutes a remarkable example of systematic rehabilitation, where bank protections have been removed along 100 km between 2008 and 2020.

Given that ship-induced erosion is still poorly understood, the management of navigable rivers and the planning of restoration measures would benefit from a solid and deeper understanding of natural bank dynamics induced by ship waves, for both economic and ecological reasons. Moreover, more precise estimates of long-term bank retreat would help to optimize different functions and reduce conflicts of interest within the river system. Therefore, the main objective of this investigation is to understand and predict erosion processes and the morphological evolution of natural banks in regulated navigable rivers.

The research goal is pursued through the thorough investigation of a river reach that presents a wide range of erosion rates after the removal of bank protections. This main case study consists of a 1.2-km straight reach in the Meuse River, near Oeffelt in the Netherlands, the left bank of which was re-naturalized in 2010 by extracting the riprap. The Meuse is a midsize river with a pluvial regime, which has been canalized and is regulated with a series of weirs to enable navigation. Here, field techniques and complementary laboratory tests are utilized including topographic surveys with UAV, wave measurements with ADV, soil coring, geotechnical tests, and RTK GPS profiling. Processing and analysis of data are carried out with MATLAB.

Four research steps are conducted. First, a methodology to quickly survey the 3D bank topography along a midsize river reach is determined to measure bank erosion processes. Second, distinct patterns of bank erosion that appeared along the Meuse River after protection removal are investigated. The aim is to disentangle the causes of the size, location and asymmetry of large embayments before analysing erosion processes at single river sections. Third, bank erosion processes in regulated navigable rivers are characterized and conceptualized. Fourth, a tool to estimate long-term or final retreat of re-naturalized banks in regulated navigable rivers is developed.

The results of the first research component show that structure from motion photogrammetry applied to photos taken from an UAV is a practical and accurate method to measure riverbank erosion. By distributing ground-control points sufficiently spaced from the bank into the floodplain, digital surface models are georeferenced with sufficient accuracy to compare bank profiles between successive surveys. The identification of ground-control points in photographs is facilitated by placing oblique plaques on the floodplain, reducing the need for another perspective along banks. A single UAV flight with an oblique perspective of the bank becomes then sufficient to capture its three-dimensional complexity. Eight overlaps among consecutive images is the minimum number not to reduce the precision potential of a single UAV flight. The proposed methodology is fast to deploy in the field and surveys reach-scale riverbanks in sufficient resolution and accuracy to quantify bank retreat and identify morphological features of the complete erosion cycle, which enables the characterization of bank erosion at the process scale.

Second, the oblique orientation of heterogeneous sedimentary strata with respect to the canalized Meuse River alignment explains the formation and asymmetry of large embayments. Depositional layers of varying compositions, structured by scroll-bar formation during former river meandering, led to wide-ranging erosion rates within a relatively short reach, which formed distinct bankline patterns across diverse lithologies and above the controlled water level of the river. The frequent occurrence of this water

level and the persistent ship wave attack shaped bank profiles of varying strengths with a mild sloping terrace. The presence of isolated trees on the floodplain only locally delay erosion rates. Bank retreat rates at single cross sections primarily depend on the lithology near the minimum regulated water stage.

Third, the evolution of bank profiles revealed the active role of ship waves in erosion progression, even at well-developed terraces. Currents initially contribute to all phases of the erosion cycle, but they gradually exert less shear stresses on the upper bank as the terrace elongates. Their later role at intermediate stages of development is reduced to the destabilization of steep high banks through water level fluctuations, without capacity to transport slump blocks. The resistance to erosion of the bank lithology defines the terrace geometrical proportions and the pace of morphological evolution of bank profiles. For instance, at a given time after protection removal, less cohesive banks can be present at intermediate stages of development while more cohesive banks remain at early stages. The latter present shorter and shallower terraces whereas the opposite holds for the former. Vegetation temporarily protects the upper bank from failure and toe erosion, but its permanence is subject to terrace stability and effectiveness to dissipate waves. Biofilms are able to partially cover well-developed terraces, changing entrainment thresholds.

Fourth, based on the above conceptual framework of bank profile evolution, a model was developed which captures the observed non-linear morphodynamics driven by ship waves in regulated settings. This new tool estimates long-term retreat by accounting for the main erosion drivers and essential mechanisms. Equilibrium bank profiles are reached once wave-induced shear stresses fall below the threshold for entrainment of cohesive soils. Unlike previous models of ship-induced erosion, the process-based approach enables to distinguish the contribution of each factor to erosion. Primary waves are found to exert the highest loads on the terrace, shaping long-term profiles and defining ultimate retreat. To apply the model, it is necessary to measure or estimate the largest primary wave and the soil cohesion at the controlled level, preferably in the range -1.00 m to +0.50 m with respect to it.

The above findings are based on cohesive banks in a straight reach of a regulated river. The presence of gravel layers in the bank changes the morphological response to ship waves due to the armouring of lower strata. In such cases, the bank terrace can reach a transverse slope in dynamic equilibrium defined by grain size, as long as longitudinal currents do not transport the gravel to the lower bank. The lower non-cohesive layer of composite banks responds in a similar way, eventually reaching a dynamic equilibrium, after which a final retreat of the upper cohesive layer is possible. The position of banks in the river planform affects the magnitude and duration of the contribution of currents

to upper bank erosion. Their direct impact, especially during high floods, can dominate bank retreat during long periods if the flow is persistently steered against the upper bank, as at outer bends. Unregulated rivers present higher shear stresses than those with controlled stages. Their sandy strata of composite banks are normally exposed to currents and waves, creating larger morphodynamics and more challenging conditions for vegetation growth.

The new model to estimate final retreat of cohesive banks may be used to prepare a reach scale strategy that defines the most convenient approach for stretches with similar morphological behaviour and available space to develop. In this way, the eventual need to reduce or stop erosion at sections with future excess retreat is determined in advance. In order to make the most of re-naturalized banks in terms of their benefits for ecological processes and habitat diversity in navigable rivers, the advantages of shallow areas with less perturbated zones should be sought where possible. Two phases of interventions are recommended, a first phase where ship waves freely reach the bank for terrace creation, responding to local lithologies, and a second phase with lowered erosive loads, facilitated by slightly submerged pre-banks. The latter phase increases the possibilities for vegetation, and likely other living organisms, to develop.

The knowledge and tools now available create new possibilities for improved management of re-naturalized banks in navigable rivers. The progress made helps to better understand the contribution of different drivers to bank erosion and to identify which factors control retreat at different bank types, stages of development, and settings. The new insights explain how to apply SfM-UAV to monitor bank erosion processes along river reaches, interpret bankline patterns, assess the role of isolated trees in bank retreat, and manage expectations regarding bank retreat and the role of vegetation to control erosion. The understanding of erosion processes in regulated navigable rivers and the possibility to estimate final erosion magnitudes open future opportunities to analyse the river system from a holistic perspective and to find creative ways to balance diverse river functions.

SAMENVATTING

Oevers vormen belangrijke zones voor rivierecologie aangezien zij een veelheid aan gunstige omstandigheden leveren voor flora en fauna. De hydromorfologische diversiteit die deze overgangszones tussen water en land typeert, en de daarmee verbonden processen van erosie en aangroei, maken rivieroevers van vitaal belang voor vele aquatische en riviergebonden terrestrische planten en dieren. In recente decennia resulteerde het groeiende bewustzijn van het ecologisch belang van rivieren en waterlichamen in de geleidelijke uitvoering van omvangrijk herstel van beken, rivieren en uiterwaarden. In de EU wordt deze praktijk gereguleerd door de Kaderrichtlijn Water. Een belangrijke en wijd en zijd toegepaste maatregel voor natuurherstel in strak vastgelegde waterlopen is het verwijderen van oeververdedigingen om erosieprocessen te reactiveren en habitatdiversiteit te bevorderen.

In rivieren die als vaarweg gebruikt worden, kunnen scheepsgolven een belangrijke oorzaak zijn van oevererosie en ecologische verstoring. De toelevering van sediment als resultaat van oevererosie kan vaardieptes, waterkwaliteit en hoogwaterafvoercapaciteit wijzigen, waarvoor versterking van de hydromorfologie een uitdaging is in multifunctionele rivieren. Als gevolg van een dringende noodzaak om riviergebonden habitats te verbeteren, zijn grootschalige herstelwerken uitgevoerd gebaseerd op conceptuele schema's zonder uitgebreide kennis van golferosieprocessen of een nauwkeurige schatting van de terugschrijding van oevers op lange termijn. De rivier de Maas in Nederland vormt een opvallend voorbeeld van systematisch herstel, waar oeververdedigingen tussen 2008 en 2020 over 100 km verwijderd zijn.

Gegeven dat scheepsgeïnduceerde erosie nog slecht begrepen is, zou het beheer van bevaarbare rivieren en de planning van herstelmaatregelen baat hebben bij een solide en diepgaander begrip van de door scheepsgolven aangedreven dynamica van natuurlijke oevers, om zowel economische als ecologische redenen. Bovendien zouden nauwkeuriger schattingen van de terugschrijding van oevers op lange termijn helpen om verschillende functies te optimaliseren en conflicten tussen verschillende belangen

te verminderen. Daarom is de hoofddoelstelling van dit onderzoek het begrijpen en voorspellen van erosieprocessen en de morfologische ontwikkeling van natuurlijke oevers in gestuwde bevaarbare rivieren.

Het onderzoeksdoel wordt nagestreefd door grondig onderzoek van een riviertraject dat na de verwijdering van oeververdedigingen een breed bereik aan erosiesnelheden te zien geeft. Deze hoofdcasestudie bestaat uit een 1,2 kilometer lang recht traject van de rivier de Maas, nabij Oeffelt in Nederland, waarvan de linkeroever in 2010 weer natuurlijk was gemaakt door verwijdering van de steenbestorting. De Maas is een middelgrote rivier met een regenregiem, die gekanaliseerd is en gereguleerd wordt door een serie stuwen om scheepvaart mogelijk te maken. Hier worden veldtechnieken en complementaire laboratoriumtests gebruikt inclusief opnames van de topografie met UAV, golfmetingen met ADV, grondboringen, grondmechanische tests, en profielopnames met RTK GPS. Verwerking en analyse van data wordt uitgevoerd met MATLAB.

Er worden vier stappen in het onderzoek uitgevoerd. Ten eerste wordt een methodologie bepaald voor snelle opname van de 3D oevertopografie langs een middelgroot riviertraject om oevererosieprocessen te meten. Ten tweede worden onderscheiden oevererosiepatronen onderzocht die langs de rivier de Maas optraden. Het doel is om de oorzaken te ontrafelen van de afmetingen, de locatie en de asymmetrie van grote inhammen alvorens erosieprocessen bij afzonderlijke riviersecties te analyseren. Ten derde worden oevererosieprocessen in gereguleerde bevaarbare rivieren gekarakteriseerd en geconceptualiseerd. Ten vierde wordt een instrument ontwikkeld om de langjarige of uiteindelijke terugschrijding te schatten van weer natuurlijk gemaakte oevers in gestuwde bevaarbare rivieren.

De resultaten van de eerste onderzoekscomponent laten zien dat toepassing van structure-from-motion-fotogrammetrie op vanuit een UAV genomen foto's een praktische en nauwkeurige methode is om de erosie van rivieroevers te meten. Door controlepunten op de grond met voldoende onderlinge afstanden vanaf de oever de uiterwaard in te verdelen, worden digitale oppervlaktemodellen van geografische coördinaten voorzien met voldoende nauwkeurigheid om oeverprofielen tussen achtereenvolgende opnames te vergelijken. Het identificeren van controlepunten op de grond op foto's wordt vergemakkelijkt door schuine platen op de uiterwaard te plaatsen, die de noodzaak van een andere kijkhoek langs de oevers verminderen. Een enkele UAV-vlucht met een schuine kijkhoek op de oever wordt dan voldoende om haar driedimensionale complexiteit te vangen. Acht overlappen tussen achtereenvolgende beelden zijn het minimum aantal om het potentieel aan nauwkeurigheid van een enkele UAV-vlucht niet te reduceren. De voorgestelde methodologie is snel in het

veld in te zetten en neemt rivieroevers op trajectschaal met voldoende resolutie en nauwkeurigheid op om terugschrijding van oevers te kwantificeren en om morfologische kenmerken van de volledige erosiecyclus te identificeren, hetgeen het mogelijk maakt om oevererosie op processchaal te karakteriseren.

Ten tweede verklaart de scheve oriëntatie van heterogene sedimentlagen ten opzichte van de belijning van de gekanaliseerde rivier de Maas de vorming en asymmetrie van grote inhammen. Afzettingslagen van variërende samenstelling, gestructureerd door de vorming van kronkelwaardruggen tijdens het voorheen optredende meanderen van de rivier, leidden tot wijd uiteenlopende erosiesnelheden binnen een betrekkelijk kort traject, hetgeen onderscheiden oeverlijnpatronen vormde dwars door verschillende lithologieën en boven het stuwpeil van de rivier. Het veelvuldige voorkomen van deze waterstand en de voortdurende aanval door scheepsgolven vormde oeverprofielen van variërende sterktes met een flauw hellend terras. De aanwezigheid van geïsoleerde bomen op de uiterwaard vertraagt erosiesnelheden slechts lokaal. Snelheden waarmee oevers in individuele dwarsprofielen terugschrijden hangen primair af van de lithologie bij het laagste stuwpeil.

Ten derde legde de ontwikkeling van oeverprofielen de actieve rol bloot van scheepsgolven in de progressie van erosie, zelfs bij goed ontwikkelde terrassen. Stromingen dragen aanvankelijk bij aan alle fases van de erosiecyclus, maar zij oefenen geleidelijk minder schuifspanningen uit op het bovenste deel van de oever als het terras langer wordt. Hun latere rol bij tussenstadia van de ontwikkeling wordt teruggebracht tot het destabiliseren van steile hoge oevers door fluctuaties in de waterstand, zonder capaciteit om afgeschoven oeverblokken te transporteren. De weerstand van de oeverlithologie tegen erosie definieert de geometrische afmetingen van het terras en het tempo van de morfologische ontwikkeling van oeverprofielen. Bijvoorbeeld, op een bepaald tijdstip na verwijdering van verdediging kunnen minder cohesieve oevers bij tussenstadia van de ontwikkeling aanwezig zijn terwijl meer cohesieve oevers blijven bij vroege stadia. Die laatste laten kortere en minder diepe terrassen zien terwijl het tegenovergestelde geldt voor de eerstgenoemde. Begroeiing beschermt het bovenste deel van de oever tijdelijk tegen bezwijken en teenerosie, maar haar blijvende aanwezigheid is onderworpen aan terrasstabiliteit en effectiviteit in het dempen van golven. Biofilms zijn in staat om goed ontwikkelde terrassen gedeeltelijk te bedekken, waarbij ze de drempelwaarden voor het meenemen van deeltjes veranderen.

Ten vierde werd, gebaseerd op het bovengenoemde conceptuele raamwerk voor de ontwikkeling van oeverprofielen, een model ontwikkeld dat de waargenomen niet-lineaire morfodynamica vangt die wordt aangedreven door scheepsgolven in gestuwde omgevingen. Dit nieuwe instrument schat de terugschrijding op lange

termijn door rekening te houden met de voornaamste aandrijvingen van erosie en essentiële mechanismen. Evenwichtsoeverprofielen worden bereikt zodra door golven geïnduceerde schuifspanningen beneden de drempelwaarden vallen voor het meenemen van deeltjes van cohesieve bodems. Anders dan bij voorgaande modellen van scheepsgeïnduceerde erosie, maakt de op processen gebaseerde aanpak het mogelijk om de erosiebijdrage van elke factor te onderscheiden. Gevonden wordt dat primaire golven de hoogste belastingen op het terras uitoefenen, waarmee ze de profielen op lange termijn vormen en de uiterste terugschrijding definiëren. Om het model toe te passen is het nodig om de grootste primaire golf en de cohesie van de grond te meten of te schatten bij het stuwpeil, bij voorkeur in het bereik van -1.00 m tot +0.50 m ten opzichte van dit peil.

Bovenstaande bevindingen zijn gebaseerd op cohesieve oevers in een recht traject van een gestuwde rivier. De aanwezigheid van grindlagen in de oevers verandert de morfologische respons op scheepsgolven als gevolg van het afpleisteren van lager gelegen lagen. In zulke gevallen kan het oeverterras een dwarshelling bereiken in een door korrelgrootte bepaald dynamisch evenwicht, zolang stromingen in lengterichting het grind niet naar lagere delen van de oever transporteren. De lager gelegen nietcohesieve laag van samengestelde oevers reageert op een vergelijkbare manier en bereikt uiteindelijk een dynamisch evenwicht, waarna de laatste terugschrijding van de hoger gelegen cohesieve laag mogelijk is. De ligging van de oevers in de plattegrond van de rivier beïnvloedt de grootte en de duur van de bijdrage van stromingen aan erosie van het bovenste deel van de oever. Hun directe impact kan, vooral tijdens hoge hoogwaters, gedurende lange periodes de oeverterugschrijding domineren als de stroming aanhoudend tegen de bovenste oever wordt gestuurd, zoals bij buitenbochten. Ongestuwde rivieren vertonen hogere schuifspanningen dan die met gestuwde peilen. Hun zandige lagen van samengestelde oevers worden normaal blootgesteld aan stromingen en golven, zodat ze grotere morfodynamica scheppen en meer uitdagende omstandigheden voor vegetatiegroei.

Het nieuwe model om de eindterugschrijding van cohesieve oevers te schatten kan gebruikt worden om een strategie op trajectschaal voor te bereiden die de handigste aanpak definieert voor stukken rivier met vergelijkbaar morfologisch gedrag en beschikbare ruimte om zich te ontwikkelen. Op deze manier wordt van tevoren de eventuele noodzaak bepaald om erosie te reduceren of te stoppen in secties met een toekomstig teveel aan terugschrijding. Om het meeste te halen uit weer natuurlijk gemaakte oevers in termen van hun baten voor ecologische processen en habitatdiversiteit in bevaarbare rivieren, zouden waar mogelijk de voordelen gezocht moeten worden van ondiepe gebieden met minder verstoorde zones. Twee interventiefases worden aanbevolen, een eerste fase waarin scheepsgolven de oever

vrij bereiken voor het vormen van een terras, in reactie op lokale lithologieën, en een tweede fase met verlaagde erosieve belastingen, gefaciliteerd door net onder water gelegen vooroevers. De laatstgenoemde fase verhoogt de mogelijkheden voor vegetatie, en waarschijnlijk andere levende organismen, om zich te ontwikkelen.

De nu beschikbare kennis en instrumenten scheppen nieuwe mogelijkheden voor verbeterd beheer van weer natuurlijk gemaakte oevers langs bevaarbare rivieren. De gemaakte vooruitgang helpt om de bijdrage van verschillende aandrijvende mechanismen aan oevererosie beter te begrijpen en om te identificeren welke factoren de terugschrijding bepalen bij verschillende oevertypes, ontwikkelingsstadia, en omgevingen. De nieuwe inzichten leggen uit hoe SfM-UAV toegepast kan worden om oevererosieprocessen langs riviertrajecten te monitoren, hoe oeverlijnpatronen geïnterpreteerd kunnen worden, hoe de rol van geïsoleerde bomen in oeverterugschrijding bepaald kan worden, en hoe verwachtingen gemanaged kunnen worden ten aanzien van oeverterugschrijding en de rol van vegetatie voor het beheersen van erosie. Het begrip van erosieprocessen in gestuwde bevaarbare rivieren en de mogelijkheid om de uiteindelijke erosiegroottes te bepalen openen toekomstige kansen om het riviersysteem vanuit een holistisch perspectief te analysen en om creatieve manieren te vinden om de verschillende rivierfuncties in balans te brengen.



INTRODUCTION



1.1. CONTEXT AND RELEVANCE

Natural rivers migrate across their floodplains forming fascinating shapes that captivated the wonder of many (Figure 1.1), offering diverse natural environments while providing fertile areas and corridors for economic development. The dynamic behaviour of rivers is determined by processes that involve both inert elements and living organisms. The interplay between water and sediments shape the river bed by scour and deposition (Garcia, 2008). These processes commonly interact with vegetation, which in turn grows under specific conditions given by sediment characteristics and flow dynamics (Curran and Hession, 2013). These mechanisms and exchanges create a diversity of habitats where different species flourish (Amoros, 2001), often conflicting with human requirements such as navigation and flood control (Jansen et al., 1994), for which a balance between all functions has become a need for a sustainable use of rivers.



Figure 1.1. "The Banks of a River" painted by Jacob Isaacsz van Ruisdael in 1649, inspired on the landscape of the Nederrijn near Rhenen, province of Utrecht, the Netherlands.

Alluvial river channels migrate as a result of two processes occurring at their margins: bank erosion and bank accretion (Figure 1.2). Bank erosion is typically a cyclic process that comprises the collapse of a soil mass after flowing water scours the bank toe and steepens the bank front. The fallen material gradually disaggregates and is transported away, which enables subsequent erosion of bank material until another failure occurs (Thorne and Tovey, 1981). Bank accretion involves several factors and processes, including lateral deposition of sediments in sequences of high and low flows, and colonization by vegetation of emerging surfaces to form new floodplain areas (Page et al., 2003; Wintenberger et al., 2015).

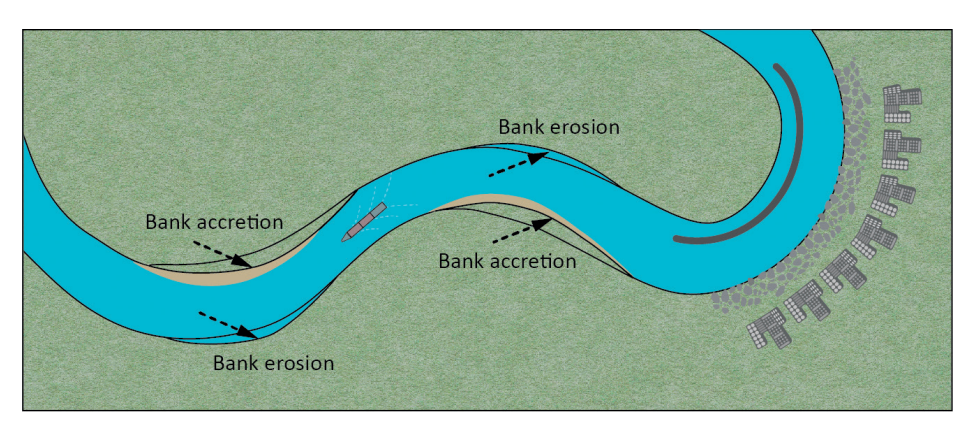


Figure 1.2. Schematic navigable river with naturally evolving banks and a stabilized stretch.

Banks are important areas for the river ecology, since they provide a diversity of favourable conditions for flora and fauna (Naiman et al., 1993; Beechie et a., 2010), particularly along middle and low river reaches where riparian habitat availability and physical heterogeneity are higher (Vannote et al., 1980). Moreover, banks represent an important ecotone between aquatic and terrestrial ecosystems that provide habitats for invertebrates, amphibians, reptiles, birds and mammals (Florsheim, et al., 2008). It is then both the hydromorphological diversity and the processes involved that make riverbanks vital for many aquatic and riparian plants and animals.

Over the last centuries, however, technical and economic developments led to the progressive adjustment of rivers without sufficient consideration of nature preservation (Wohl, 2014). For instance, in the Netherlands, river training was motivated to ensure navigable water depths and safety against floods, especially considering the silting up of the riverbeds that was occurring as a natural process typical of lowland rivers in a delta (Nienhuis, 2008). As a consequence, major Dutch rivers like the Waal, the IJssel, the Nederrijn-Lek and the Meuse were regulated and canalized through the construction of weirs, ship locks, series of groynes, meander cut-offs, and revetments. These waterways, together with a vast network of dug canals, were the main routes to transport goods and people until early 20th century, and remain essential until today.

During the last decades, the awareness of the ecological importance of rivers, streams and canals significantly increased (Brookes et al., 1983; CUR, 1994; Brierley and Fryirs, 2005; Best, 2018). This resulted in the gradual implementation of extensive stream, river and floodplain restoration (Verdonschot and Nijboer, 2002; Bernhardt et al., 2005; Gumiero et al., 2013; Theiling et al., 2015; van Denderen, 2019). These measures were supported and regulated by national and international legislation that provide common environmental policies, such as the Clean Water Act in the USA and the Water

Framework Directive (WFD, 2000) in the EU. Following the latter, diverse measures were taken in EU countries to improve the water quality and habitat diversity (Kallis and Butler, 2001; Pearce, 2013; RESTORE, 2020).

In this context, scientific knowledge is crucial to provide a basis for the success of restoration practices, e.g. on hydromorphology, ecological processes, or physical-biological feedbacks (Dufour and Piégay, 2009; Wohl et al. 2015; Gurnell et al., 2016). To improve the natural value of trained rivers, the traditional revetments protecting the banks against currents or ship waves (see e.g., scheme in Figure 1.2) were recently changed for nature-friendly alternatives searching to balance technical and ecological requirements (Boeters et al., 1997; Rauch et al., 2014; Heibaum and Fleischer, 2015). Particularly after the WFD (2000), several countries across the EU implemented bioengineering protections or the complete removal of revetments, such as Austria (Liedermann et al., 2014), Germany (Schmitt et al., 2018) and France (ONEMA, 2018). In the Netherlands, the Meuse River constitutes an outstanding example of systematic rehabilitation, where bank protections were removed along 80 km between 2008 and 2020 (www.rws.nl/maasoevers). An example of the latter is shown in Figure 1.3.



Figure 1.3. Re-naturalized bank in the Meuse River (right-hand side) opposite to the port of Gennep.

Nevertheless, the execution of bank re-naturalization measures were based on conceptual schemes (Peters et al., 2005), without a comprehensive understanding of ship-induced erosion or a precise estimate of long-term bank retreat. For instance, vegetation and slump blocks can reduce erosion (Parker et al., 2011; Vargas-Luna et al., 2019) but it is unclear under which conditions and to what extent these could control bank retreat. Ship waves can be an important driver of bank erosion (Nanson et al.,

1994, Liedermann et al., 2014; Larson et al., 2017), with economic (Rapaglia et al., 2015) and ecological implications (Gabel et al., 2012). Furthermore, ship-induced erosion not only concerns riverbanks but also shorelines of navigable lakes, estuaries and coasts, where morphological, economic and ecological consequences are significant (Houser, 2010; Parnell et al., 2007; Gabel et al., 2012; Rapaglia et al., 2015; Zaggia et al., 2017; Scarpa et al., 2019; Styles and Hartman, 2019). A solid and deeper understanding of natural bank dynamics induced by ship waves would allow managers and practitioners to optimize diverse functions that are crucial for sustainable waterways.

This investigation is part of the RiverCare programme (2014-2019, www.rivercare.nl) that studies the consequences of interventions in order to improve the design and maintenance of multifunctional rivers. Before stating the specific research objectives, this chapter presents a review of processes and factors affecting riverbank erosion, a description of technical-biological protections, and available tools to predict ship-induced erosion.

1.2. RIVERBANK EROSION

1.2.1. PRIMARY CAUSES AND SCALE OF ANALYSIS

The primary drivers of riverbank erosion can be distinguished between those natural and human-induced. Natural causes are essentially driven by climate, which defines a precipitation regime in a given basin and a discharge regime at a river reach, as well as riparian vegetation characteristics. Currents then act with different intensities against channel boundaries and produce bank erosion when and where shear stresses exceed the thresholds for material entrainment. In addition, climate produces subaerial erosion through freeze-thaw and wetting-drying cycles. The anthropogenic origins of bank erosion are direct and indirect. A direct cause are ship waves generated by commercial and recreational navigation. Indirect causes are those perturbating the preceding conditions of a river system, such as damming causing sediment discontinuity (Kondolf, 1997), land-use changes that increase discharge and thus shear forces on banks (e.g., Dragicevic et al., 2012), or sediment mining from the riverbed that can later produce channel incision and bank instability (e.g., Rinaldi et al., 2005).

The indirect anthropogenic and climate-dependent causes generally act at large spatial scales affecting entire river reaches. The consequent morphological changes often occur at large temporal scales too. The approach of understanding the river system as a whole to identify and tackle erosion problems from their source has a high practical importance. However, smaller scales of analysis provide better insights into the spatial and temporal variability of bank erosion at single river cross sections, even when boundary conditions are changed for entire reaches. This thesis then focuses on

the process scale to understand the mechanisms and factors that locally control bank retreat.

1.2.2. BANK EROSION CYCLE

The process of bank erosion typically occurs in cycles of fluvial entrainment of the bank and near-bank bed material, bank collapse, and slump-block disintegration and removal (Thorne and Tovey, 1981). Figure 1.4 illustrates these phases for homogeneous cohesive banks with varying water levels. Entrainment occurs when shear stresses exerted over soil particles and near-bank bed material exceed the threshold for detachment and initiation of motion, respectively (Arulanandan et al., 1980; Clark and Wynn, 2007; Kimiaghalam et al., 2016). This process steepens the bank that eventually fails due to geotechnical instability (Osman and Thorne, 1988; Langendoen and Simon, 2008). The wasted bank material lying at the bank toe, in the form of a wedge or blocks, needs to be removed before further entrainment can happen (Wood et al., 2001; Parker et al., 2011; Patsinghasanee et al., 2018).

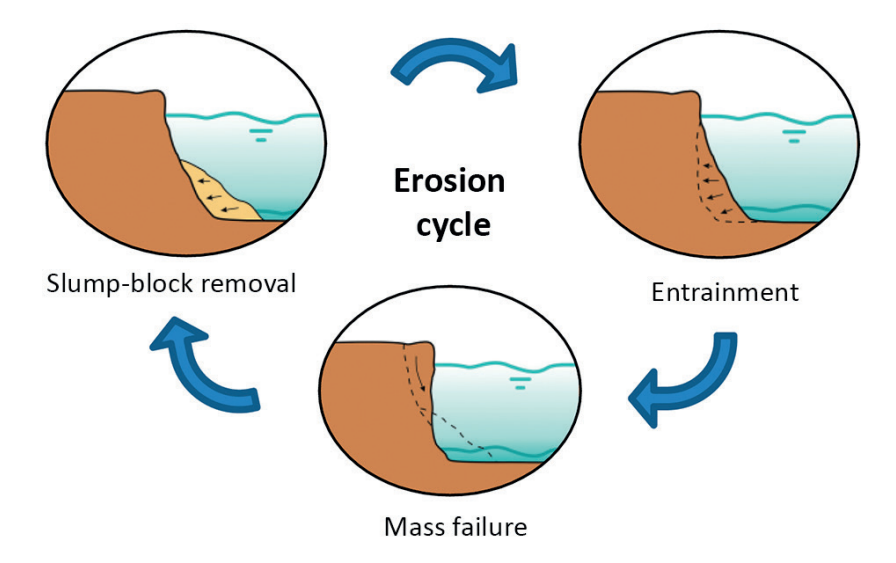


Figure 1.4. Schematic bank erosion phases: Slump-block removal (left), entrainment of bare bank (right), and incipient mass failure (centre).

Entrainment

Flowing water entrains soil particles when the drag and lift forces surpass the stabilizing forces of the boundary sediment. In case of non-cohesive sediments, the critical Shields parameter q_c (Equation 1.1) is used to characterize the stochastic process of initiation of motion, whose dependence on the grain size (or the dimensionless particle Reynolds

number $R_{ep} = \sqrt{g\Delta D}D/\upsilon$) is empirically obtained (Buffington, 1999; Zuo et al., 2017).

$$\theta_c = \frac{\tau_c}{\rho g \Delta D} \tag{1.1}$$

where τ_c (Pa) is the time-averaged critical bed shear stress, ρ (kg/m³) the water density, g the gravitational acceleration, $\Delta = (\rho_s - \rho)/\rho$ (-) the submerged specific gravity of the sediment, ρ_s (kg/m³) the sediment density, D (m) is the mean grain diameter, and u (m²/s) the kinematic viscosity of water. Non-cohesive sediments are found in meandering rivers at the lower layers of banks, deposited in a fining-upward sequence during the channel lateral migration (Nanson and Crook, 1992). Fine cohesive sediments are then found in the upper layers of alluvial banks.

The resisting forces of cohesive sediments depend on interparticle physicochemical bonds and biological processes that are difficult to accurately quantify and parameterize (Reddi et al., 1997; Grabowski et al., 2011; Karamigolbaghi et al., 2017). Four modes of erosion have been observed and characterized in cohesive beds as shear stress and erosion rates increase (Winterwerp and van Kesteren, 2004): particle by particle erosion, floc erosion, surface erosion (layer detachment), and mass erosion (undrained detachment). In fluvial environments, the most used approach to represent erosion by entrainment has been the excess shear stress formula (Equation 1.2) ascribed to Partheniades (1965) (Rinaldi and Darby, 2007), despite its limitations. The latter include the lack of time-dependency of erosion rates and considerations on the stochastic nature of the involved phenomena (van Prooijen and Winterwerp, 2010).

$$\frac{dz}{dt} = \varepsilon \left(\tau_b - \tau_c\right)^a \tag{1.2}$$

where τ_b (Pa) is the boundary shear stress, a is a dimensionless empirically-derived exponent generally assumed equal to one, and ε (m/s/Pa) the erodibility coefficient establishing the consequent linear relation between excess shear and erosion rate. τ_c and ε can be estimated through laboratory or field measurements, e.g. with the cohesive strength meter (Tolhurst et al., 1999), the JET method (Hanson and Cook, 2004), or the erosionometer (Salem and Rennie, 2017). However, the methods to estimate e and τ_c encompass high uncertainty and require careful assessments (Vardy et al., 2007; Grabowski et al., 2010; Karamigolbaghi et al., 2017). It is also common practice to use e and τ_c for calibration purposes (Julian and Torres, 2006; Crosato, 2007; Rinaldi and Darby, 2007; Constantine et al., 2009).

Failure

The bank size, geometry, geotechnical parameters (mainly internal friction angle and cohesion), stratigraphy, and erodibility of each sedimentary layer in alluvial rivers lead to different geotechnical failure mechanisms (Thorne and Tovey, 1981; Thorne and Osman, 1988b; Thorne, 1990; Darby and Thorne, 1994; Langendoen and Simon, 2008; Midgley et al., 2012). For instance, rotational failures are common in high banks because shear stresses in the soil increase faster over the depth than soil shear strength (Terzaghi et al., 1996). Planar failures occur with steep slopes, e.g. higher than 60°, that are often present in cohesive soils and river bends (Osman and Thorne, 1988). These failures can happen in any plane along the bank height and not necessarily passing through the bank toe. Toppling is typical of low banks, where tension cracks occupy a significant extent of the bank height and stability depends more on tensile than shear strength (Thorne and Tovey, 1981). Figure 1.5 provides examples of different types of failures.







Figure 1.5. Signatures of different types of mass failures: (a) rotational slip, (b) toppling, (c) incipient cantilever (note the man is one meter away from the bank edge).

The conditions for failure are analysed with the limit equilibrium method that accounts for resisting and mobilizing forces over a potentially collapsing soil mass. The factors and conditions under analysis have significantly increased in the literature over the

last decades. At present, models consider saturated and unsaturated zones, different soil layers, root reinforcement, seepage, different failure modes, and dynamic water tables (Osman and Thorne, 1988; Simon and Curini, 1998; Simon et al., 2000, Simon and Collison, 2002; Pollen and Simon, 2005; Darby et al., 2007; Langendoen and Simon, 2008; Pollen-Bankhear and Simon, 2010; Zong et al., 2017). Although current mechanistic models of mass failure include a comprehensive range of variables, they also inherit a considerable uncertainty from the variability of their input parameters (Samadi et al., 2009; Klavon et al., 2017; Lammers et al., 2017).

Slump blocks

The slump-block disintegration and removal, phase termed *basal endpoint control* after Carson and Kirkby (1972), has a duration that depends on the resistance of the waste material to hydraulic erosion (Langendoen and Simon, 2008), on their disaggregation (Wood, 2001), and on the available capacity to transport the blocks away from the toe (Osman and Thorne, 1988; Simon et al., 1999). The temporal protection of the bank face is particularly important for cohesive and composite banks because they form large blocks and offer high resistance to erosion (Thorne, 1982; Lawler, 1992; Parker et al., 2011). In contrast, loose waste material from non-cohesive banks is generally transported away relatively quicker by the river flow, leaving the bank sooner unprotected (Fukuoka, 1994). River currents typically exert shear stresses on blocks, but in navigable rivers ship waves can also significantly contribute to entrain particles and remove and disaggregate blocks.

The key distinction between this phase and the entrainment phase of the erosion cycle is the possibility of slump blocks to be transported away by the flow, whereas having a higher specific surface area for particle entrainment than the vertical bank likely plays a secondary role. The entrainment of slump blocks by the flow was estimated by Simon et al. (1999) with a Shield's type of equation (see Equation 1.1), although Wood et al. (2001) showed its inadequacy when apparent cohesion adheres blocks to the underlying slough-line materials. In addition, the armouring effect of slump blocks was suggested dependent on the river size (Motta et al., 2014), due to lower transport capacities as rivers decrease in size, and vice versa. It appears that the type of mass failure also affects the layout of waste material and thus the exposure of blocks to currents (Figure 1.6).





Figure 1.6. Slump blocks at (a) Geul and (b) Meuse Rivers, the Netherlands, respectively resulting from planar and toppling failures.

For long-term meandering models, the reduction of bank retreat rates due to slump-block armouring was considered dependent on the cohesive-soil fraction over the bank height, a characteristic block size, and a characteristic block decay time (Parker et al., 2011; Motta et al., 2014). Eke et al. (2014) proposed a block decay time as function of the near-bank Shields number and flood frequency, being consistent with Ikeda et al. (1981) erosion law. Even with these efforts, determining a characteristic block size or distribution together with its temporal disaggregation and rearrangement remains a challenge for slump-block modelling. Such an approach would allow morphodynamic models to eventually consider block transport and achieve a comprehensive process-based approach for basal clean-out. Existing methods, for instance, represent mass waste as non-cohesive sediments at the bank toe (Patsinghasanee et al., 2017) or a planar wedge at repose angle (Rousseau et al., 2017) despite accounting for complex algorithms for either cantilever or rotational and planar failures, respectively.

1.2.3.DRIVERS OF BANK EROSION

<u>Flow</u>

Currents act during the entrainment and block removal phases of the erosion cycle by inducing shear stresses due to the velocity gradients in the near-bank region. The distribution of horizontal velocities in a river cross-section is strongly influenced by water depth when rivers have large width-to-depth ratios (say W/h > 10), which are typical of lowland rivers (Uijttewaal, 2014). These flow conditions are normally described with depth-average schematizations. However, the near-bank region always presents three-dimensional flow features with a significant vertical-velocity component (Knight and Shiono, 1990; Knight, 2013). This responds to secondary flows and turbulent coherent structures, as observed in the field by Thorne (1978) and Anwar (1986) and in laboratory experiments by Blanckaert et al. (2010, 2012). These features have different intensities depending on the river planform and become stronger at sharp bends (Figure 1.7).

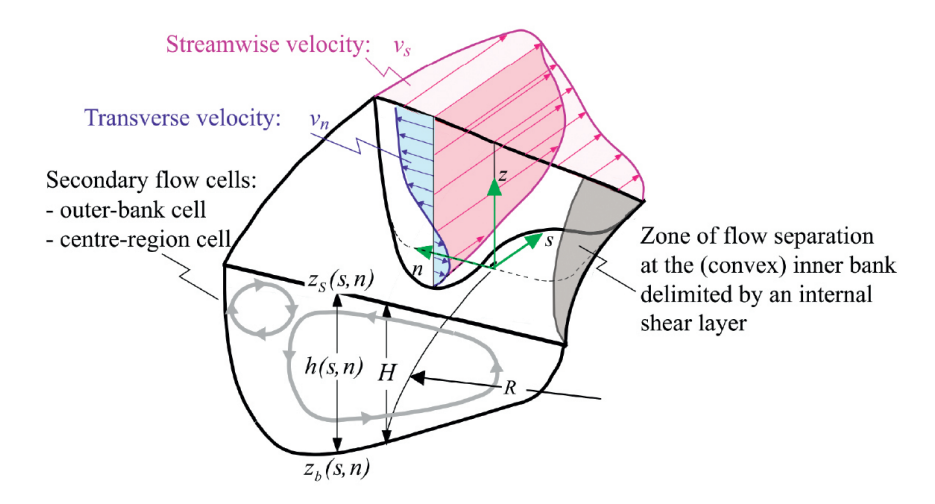


Figure 1.7. Conceptual scheme of flow features at channel bends (source: Blanckaert et al., 2012). Note the secondary flow cell forming at the top of the outer bank, typical of sharp bends.

The boundary shear stresses are also affected by bank roughness. A higher bank roughness, when continuous along the bank, enlarges the near-bank flow cells and confines the centre-region mean flow (Konsoer et al., 2016a), increasing the turbulent kinetic energy between these zones and the energy consumption from the mean flow (Blanckaert et al., 2012). This results in lower velocities and shear stresses against the bank, which also lowers the channel discharge capacity (Masterman and Thorne, 1992). Isolated macroscale irregularities along banks create local energy losses from recirculating zones, increasing shear stresses when protruding (Koken and Constantinescu, 2008) or decreasing them in cavities (Sanjou and Nezu, 2013). Intermediate situations in between discontinuous and continuous irregularities have different impacts on local shear stresses and the mean-flow energy loss depending on the magnitude and spacing of cavities (Meile et al., 2011).

In natural settings, shear stresses and near-bank velocities vary for different riverbank shapes that depend on the erosion phase, e.g., inclined banks (Blanckaert et al., 2010), undermined banks (Roy et al., 2019), or with slump blocks near the toe (Hackney et al., 2015). Natural macro-roughness elements appear, for instance, in the form of embayments (Hackney et al., 2015), large woody debris (Manners et al., 2006) or tree root plates (Rutherfurd and Grove, 2004). With the purpose of quantifying boundary shear stresses that consider the form drag of small-scale bank irregularities, Kean and Smith (2006a, 2006b) proposed a model based on parametrized roughness elements. This model applied in the Mekong River by Darby et al. (2010) showed that small-scale

form drag was a major fraction of the total shear stress, significantly reducing the skin friction that drives soil entrainment.

Ship waves

Ship waves can impose significant loads onto banks and affect all phases of the erosion cycle, depending on the location of their impact. Sailing vessels generate waves classified as primary and secondary (CIRIA et al., 2007), which act at the level of the river stage. The primary wave consists of a water level depression caused by increased flow velocities around the ship after the Bernoulli principle, with associated front and stern waves (Figure 1.8a). This wave increases as the vessel breadth, draught, length and speed increase, and as the distance to the bank reduces (Bhowmik et al., 1982). Secondary waves are created by the hull discontinuity in the flow and typically propagate at 35° with respect to the sailing direction (CIRIA et al., 2007). Primary and secondary waves can cause bank erosion by steering shear stresses onto banks throughout their propagation and breaking (Figure 1.8a,b).

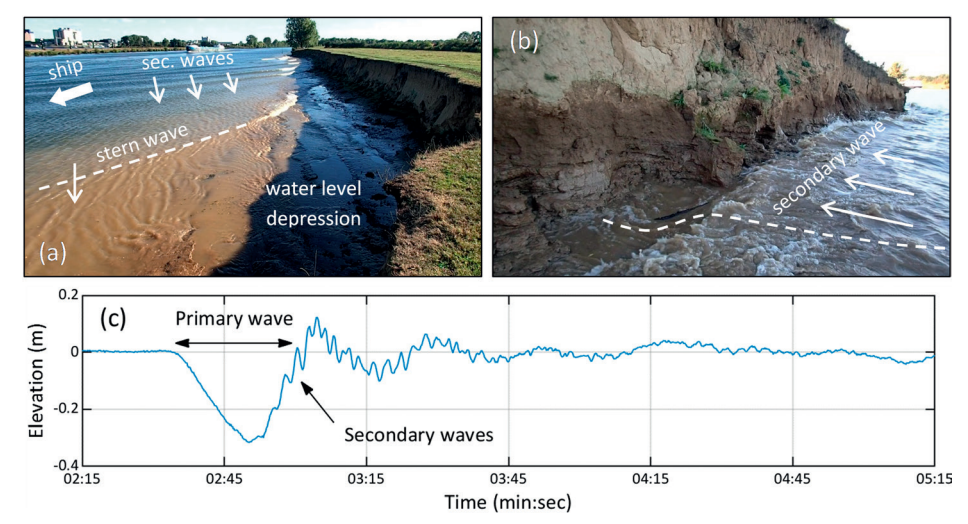


Figure 1.8. (a) Primary and secondary waves after a ship passing. (b) Secondary wave impacting a bank with signatures of erosion and undermining. (c) Example of water level fluctuations with respect to river stage due to a passing ship.

The load distribution of ship waves along banks depends on wave type and energy, but also on wave propagation and breaking location, which interact with the bank geometry (Torsvik et al., 2006). For instance, Figure 1.8a shows a primary wave propagating over a shallow area, where the water level is being restored by the stern wave after the depression, creating a current towards the bank. Both primary and secondary waves are usually, but not necessarily, induced by a sailing vessel. The amplitude, period and

number of waves depend on every hull design and sailing condition. Furthermore, primary waves are sometimes followed by damped oscillations (Figure 1.8c).

Bank hydrology: rainfall, water level changes and seepage

The increase of water content in riverbanks due to prolonged rainfall may result in mass failure due to a higher soil specific weight, the loss of apparent cohesion created by negative pore-water pressure (matric suction), and the generation of positive pore-pressure (saturation) that reduces the frictional strength (Simon et al., 2000). Water level changes in the river can also trigger the failure of banks (Rinaldi and Nardi, 2013). During the rising limb of hydrographs, this can happen due to lateral seepage into the soil that removes negative pore-pressure and increases the unit weight (Casagli et al., 1999; Simon et al., 2000). In addition to these effects, during the falling limb of hydrographs, banks can become unstable due to the loss of confining pressure available at high water levels and the development of positive pore pressures that reduce effective stresses (Rinaldi et al., 2004; Darby et al., 2007).

Groundwater seepage can be a direct erosive agent too, undercutting banks by soil-particle entrainment or by tension failures (Hagerty, 1991; Heibaum, 2002; Chu-Agor et al., 2008a). The basic mechanism occurs when sufficiently large hydraulic gradients along a permeable layer is able to detach and mobilize particles by exceeding critical shear stresses (Wilson et al., 2018). The effectiveness of this process depends on topography, climate and weather (Bernatek-Jakiel and Poesen, 2018), and especially on bank composition, stratigraphy, and hydraulic conductivity (Fox et al., 2007; Chu-Agor et al., 2009; Fox et al., 2010). Seepage undercutting contribute to destabilize banks, particularly with low water levels and low root reinforcement (Cancienne et al., 2008; Chu-Agor et al., 2008b). Although seepage can be an important erosion driver, mainly when acting together with currents, it is generally not uniformly distributed and its contribution to total bank erosion is challenging to determine (Fox et al., 2007; Midgley et al., 2013; Rinaldi and Nardi, 2013).

Subaerial erosion

Subaerial erosion results from the weathering of the bank surface, typically under wet-dry or freeze-thaw cycles (Hooke, 1979; Lawler, 1993). These processes, especially important for soils with high silt-clay content (Couper, 2003), can act as direct agents of erosion (Couper and Maddock, 2001) or weaken the bank surface which facilitates later entrainment (Thorne, 1990; Green et al., 1999). In the former case, the magnitude of erosion per cycle is usually small (in the order of centimetres), but depending on the river reach location, a high frequency of occurrence may account for significant contributions within short periods of time (Lawler, 1992; Couper and Maddock, 2001).

As preparatory process for entrainment, weathering can affect the bank erodibility and critical shear stress (Rinaldi and Darby, 2007; Kimiaghalam et al., 2015), presenting seasonal variations (Wynn et al., 2008). Despite great changes in material erodibility, the depth over which weathering affects the bank surface is normally shallow, e.g. 5 cm as observed by Konsoer et al. (2015).

1.2.4. BANK VEGETATION

The presence of vegetation (grass, bushes, saplings, trees) on a riverbank, can affect all phases of the erosion cycle (Section 1.2.2) and hence retreat rates (e.g., Beeson and Doyle, 1995). Entrainment rates of bank material change in the presence of roots, canopies and large woody debris. Bank stability is affected by mechanical reinforcement of roots permeating the bank, surcharge (mainly from trees), and vegetation hydrological effects. Slump blocks held by roots take longer to disaggregate. Furthermore, the bank height, root depth and vegetation position on the bank alter the effectiveness of vegetation on reducing erosion rates.

Hydraulics and entrainment

Vegetation affects fluvial hydrodynamics at different spatial scales depending on its distribution and density within the channel (Nepf, 2012; Curran and Hession 2013). The dynamics of in-channel vegetation, including growth and uprooting, interacting with the river flow and sediment transport shape from local bed morphologies to channel patterns (Gurnell et al., 2012; Gurnell, 2014). Bank vegetation in particular, in the form of emerging canopies and roots or large woody debris lying on the bank slope, affects the near-bank flow by increasing roughness and reducing velocities and shear stresses (see Section 1.2.3, *Flow*). This depends on vegetation type (Hopkinson and Wynn, 2009) and occurs when those features cover a sufficient bank extent (Thorne, 1990), such as river bends (Thorne and Furbish, 1995; Daniels and Rhoads, 2004; Konsoer et al., 2016a). On the other hand, local obstructions with a sufficient density accelerate the flow at their side and reduce downstream velocities, as vegetation patches (Bennett, 2004) or debris jams (Manners et al., 2006).

Furthermore, soil resistance to erosion increases when permeated with roots. Roots and rhizomes of plants create additional bonds within the soil that reduce the weakening and loosening mechanisms that precede detachment (Thorne, 1990). As a result, entrainment rates induced by jet tests on soil samples with grass roots significantly drop compared to bare soils, as root density, length and biomass increases (Pollen-Bankhead and Simon, 2010). Khanal and Fox (2017) showed that this mainly happens through an increase of critical shear stress for detachment. Vannoppen et al. (2017) further demonstrated a dependency on root and soil types, so that taproots are more

effective in reducing entrainment rates in cohesive soils than in sandy soils, whereas fibrous roots exhibit the opposite effect, they are more efficient in reducing erosion rates in sandy soils than in cohesive substrates.

Resistance against failure

The soil resistance against failure rises due to the presence of roots, which was considered in stability analyses as an apparent cohesion increase (Wu et al., 1979; Simon and Collison, 2002). This is because surfaces across the soil mass that can potentially fail are intercepted by roots, increasing the shear strength (Ghestem et al., 2014). This strengthening depends on the diameter and density of roots which vary in space and time (Pollen, 2007). Root growth and architecture, including the distribution over depth, depends on plant species, soil type, and water table fluctuations (Docker and Hubble, 2009; Pollen-Bankhead and Simon, 2009; Polvi et al., 2014; Gorla et al., 2015). Besides reinforcing against shear, the presence of vegetation adds extra weight on the bank, for which the net contribution to stability may result slight (Van de Wiel and Darby, 2007) or substantial (Abernethy and Rutherfurd, 2000a) depending on the case.

Vegetation also affects the pore-water content of the soil by intercepting rainfall and extracting moisture for transpiration, which reduces positive pore-water pressure and increases matric suction, resulting in higher shear strength (Simon and Collison, 2002; Pollen-Bankhead and Simon, 2010). These effects are seasonal due to variations in canopy density and evapotranspiration, which, for instance, can be higher during spring and summer (Langendoen et al., 2009). Moreover, canopy interception and stemflow can locally concentrate pore-water pressures (Durocher, 1990) as roots allow water to percolate deeper into the ground, which is especially relevant for large rainfall events. The net effect of vegetation on the stability of a given bank thus results from the partial influence of the aforementioned factors in a given time. Models that account for this complexity can evaluate measures for erosion control (Simon et al., 2011) or advice on convenient vegetation types for bank stabilization (Polvi et al., 2014).

Slump block degradation

The degradation of slump blocks extends in time due to root-reinforcement (Parker et al., 2011) and increased cohesion (Thorne, 1990), as they decrease entrainment rates (see above Subsection *Hydraulics and entrainment*). Blocks keep their original size for longer time, reducing their mobility (Gray and MacDonald, 1989). The necessary time for these effects to become ineffective depends on root decomposition, which in turn depends on root species and diameter (Vergani et al., 2017).

Bank height, root depth and vegetation position on the bank

The effectiveness of vegetation to retard the erosion cycle or control erosion depends on bank height, root depth, and position of vegetation on the bank profile. First, bank height not only determines the available volume of material to erode but also relates to failure type (Thorne and Tovey, 1981), failure timing (Osman and Thorne, 1988; Samadi et al., 2009), and distance of mass displacement (Fujita et al., 2000). In fact, bank height is utilized in numerical models as crucial parameter to predict bank erosion (Mosselman, 1995, 1998), being both practical to determine and independent of grid resolution (Stecca et al., 2017).

Root reinforcement against failure is effective over the depth that roots extend through the bank height (Thorne, 1990). Furthermore, the root structure, especially the density distribution over depth, influences bank stability at low banks due to the variation of root density intercepting failure planes (Pollen-Bankhead and Simon, 2009). Moreover, entrainment rates are higher below the extent of roots leading to undermining of root plates (Rutherfurd and Grove, 2004). Different combinations of bank height and vegetation type, with respective root depths, thus result in contrasting effects on bank stability (Tengbeh, 1989; Lammers et al., 2017) and retreat rates (Rood et al., 2015; Konsoer et al., 2016b).

Root depth also conditions the size of slump blocks or failure block, being larger the deeper a soil mass is reinforced. This aspect is particularly relevant in relation to stream power and river size, to which the bank height can be related if the channel is not incised or aggraded (Wilkerson and Parker, 2011). Those two factors influence the transport capacity of slump blocks and dislodged vegetation at the bank toe, and therefore the duration of the slump-block removal phase, as expressed by Motta et al. (2014). For instance, streams with low banks may experience a drastic change in lateral mobility once vegetation establishes on floodplains and permeates the full extent of the bank height (Vargas-Luna et al., 2018). The latter is not only in response to relative large blocks compared to bank height but also a consequence of the increased stability against failure and little undermining (Figure 1.9a).



Figure 1.9. Examples of different types of root-reinforced banks in lowland rivers in the Netherlands. (a) Grass, herbaceous plants (trimmed), and saplings, with roots reaching bank toe (Lunterse Beek, 05/04/2016). (b) Closely spaced trees at bank toe (Geul River, 17/04/2016). (c) Undermined large tree with shallow roots and smaller trees at bank toe (Geul River, 17/04/2016). (d) Closely spaced trees with continuous roots along the bank reaching the bank toe (Geul River, 17/04/2016). (e) Isolated tree with shallow roots (Meuse River, 19/07/2016).

The contribution of roots to bank stability depends on the vegetation position across the bank profile, being highest near potential failure planes, either on the floodplain or at the bank toe (Abernethy and Rutherfurd, 2000b; Van de Wiel and Darby, 2007). Figure 1.9b shows an example of the latter, where a group of trees grew at the bank toe, presenting a strong resistance against failure (Thorne, 1990). Such more stable root system i.e. staying longer before mass failure or dislodgement, enables a longer

entrainment phase of the erosion cycle, which in turn benefits from the reduction of shear stresses against the bank face offered by roots. This is a double benefit of vegetation at bank toe. On the other hand, trees on the floodplain can be more easily undermined, as for example shows Figure 1.9c, where root density is lower at deeper elevations.

Figure 1.9d shows a continuous and deep root reinforcement of an outer bank, where trees have imbricated roots along the bend while reaching the bank toe. Such combination of vegetation density (tree spacing) and root depth compared to bank height appears very effective in delaying erosion (Google Earth, E 5.930° N 50.759°). In contrast, isolated trees with shallow roots compared to bank height can be faster undermined and, if river size and transport capacity allows for it, be carried downstream after eventual dislodgement (e.g., Figure 1.9e presents a large tree with shallow roots in a midsized river). Finally, even if river size and stream power may transport large trees, these may offer great resistance to erosion if roots are deep enough, as it is the case for some Australian species whose deep rooting evolved to cope with the extended droughts (Hubble et al., 2010).

1.2.5. NAVIGABLE RIVERS AND TECHNICAL-BIOLOGICAL BANK PROTECTIONS

The primary requirement of navigable rivers is having sufficient water depths over a certain width for vessels to sail. Depending on the catchment hydrology, a discharge regime may or may not provide that condition throughout the year. Large rivers, as the Parana in South America, have sufficient discharge and water depths along hundreds of kilometres, naturally enabling commercial navigation. On the other hand, rivers with more restrictive conditions need to regulate the discharge, water levels, width, or planform to facilitate navigation. Examples of important European rivers with regulated water levels include the Meuse, Main, Rhine, and Danube. Hereafter in this work, regulated rivers refer to those with controlled water levels, resulting impounded especially during low flows, whereas unregulated rivers indicate those whose water levels respond to available discharge.

In navigable rivers, revetments were traditionally applied to prevent bank erosion, whereas more recently, technical-biological protections have been also considered (Section 1.1). Nature-friendly bank protections have the dual function of not to erode in an uncontrolled manner and to provide improved ecological conditions compared to revetments. On the other hand, these measures usually require more available space to be implemented, in addition to maintenance where erosion occurs or vegetation needs care. Moreover, it is a challenge to precisely quantify the additional strength provided by vegetative elements, for which experience and test cases are of great

value to better understand and promote these alternative practices. For example, stretches with different nature-friendly protections were tested in the Rhine River near Worms (Schilling et al., 2013; Heibaum and Fleischer, 2015). These include pre-banks and willow branch cuttings (Figure 1.10a), willow brush mattresses (Figure 1.10b), dead wood fascines and individual stones (Figure 1.10c), reed gabions and plant mats (Figure 1.10d), riprap with soil alginate and hydroseeding (Figure 1.10e), and pavement with reeds (Figure 1.10f).



Figure 1.10. Nature-friendly bank protections in test sections on the Rhine River near Worms, on 12/04/2016, after 4.5 years of installation. (a) Stone pre-bank, shallow water zone with dead trunks, and bank with riprap, willow branch cuttings, living fascines, and brush and hedge layers. (b) Willow brush mattresses transversally installed. (c) Riprap with gravel fill, groups of individual stones, and dead wood fascines. (d) Reed gabions and stone mattresses on granular filter, plant mats and hedge layers (note riprap with dead wood on the left). (e) Riprap with top soil alginate mixture, hydroseeding, and individual plants. (f) Riprap and pavement with reeds. Descriptions based on Heibaum and Fleischer (2015).

Pre-banks, in particular, reduce or stop ship waves before reaching the actual bank depending on the water level. They act as longitudinal barriers between the fairway and the bank (Figure 1.10a) and can be made of stones or sheet piles (Boeters et al., 1997; van Ballaer et al., 2010). These indirect protections provide a quieter area for littoral species, which is especially beneficial for young fish and nest-building species (Söhngen et al., 2008). Figure 1.11 shows an example of a submerged pre-bank constructed to

protect a dike against erosion at an inner bend of the Meuse River. In the opposite left bank, riprap was removed from the upper bank, above 0.5 meters beneath the minimum regulated water level. This bank presented a steep scarp approaching the trees after three years of protection removal. The long-term erosion of unprotected banks in waterways is currently uncertain. Monitoring is then required to check erosion and determine whether interventions are needed. A better understanding of technical-biological protections or of freely eroding banks would also serve to optimize future practices.



Figure 1.11. Example of a submerged pre-bank protection at Balgoij, the Meuse River, constructed in 2012 to reduce erosion in front of the dike on the right-hand side (28/09/2016). The left eroding upper bank had the riprap removed in 2013 from 0.5 meters beneath the regulated water level. Source: Rijkswaterstaat/J.v.Houdt.

1.2.6. BANK EROSION PREDICTION FOR NAVIGABLE RIVERS

There are two available tools to estimate bank erosion driven by ship waves. Glamore (2008) proposed a methodology based on some key elements, as bank properties and ship-wave energy, to assess the susceptibility to erosion of a river reach with the aim to manage sailing conditions. This approach is qualitative in essence, despite considering some physical quantities. The other method is a model called Bank Erosion Model (BEM, Verheij, 2000), which was adapted to tidal rivers (Stolker and Verheij, 2001a), calibrated for the Meuse River (Stolker and Verheij, 2001b) and translated into Excel sheet format (Verheij et al., 2007). The formulation for bank retreat is:

$$BR = \frac{1}{2\mu} \ln \left(2\mu c_E H^2 t + 1 \right) \tag{1.3}$$

where BR is the bank retreat or terrace length (m), H is a wave height at the terrace toe (m), t is time (s), μ is a coefficient for wave attenuation over the terrace (m⁻¹), and c_{ε} is a coefficient for bank material erodibility (m⁻¹s⁻¹). H is taken as a characteristic largest secondary wave height (CIRIA et al., 2007, p440; Stolker and Verheij, 2001b, annex E). t is the cumulative duration of secondary ship waves during a specified period at a river section, typically one or more years, so that $t = T_s * n * N$, where T_s is the secondary wave period (e.g. estimated as $5.1 * v_s / g$, with v_s the sailing speed), n is the number of secondary waves per ship passing, and N is the number of ships per year or specified period.

The wave damping μ was computed with the 1D model ENDEC, developed by Delft Hydraulics in 1990, for a set of boundary conditions to later tabulate the results. These conditions included different wave steepness (0.02, 0.03, 0.04), bank (terrace) slopes (1:10, 1:20, 1:33, 1:50, 1:100) and relative water depth to wave height (0.1-3.0). Waves were assumed to propagate perpendicular to the bank, and no primary waves were considered. BEM offers the possibility to account for additional wave attenuation due to a pre-bank protection (e.g., see Figure 1.11) and reed growth on the terrace, and for periodic erosion delay due to slump blocks. These three elements are integrated in Equation 1.3 by adjusting μ .

This model assumes a constant water level, a protected (fixed) lower bank, a homogeneous soil, no erosion due to currents, and no variations in longitudinal direction. An important aspect of BEM is that the user needs to set a priori the terrace slope, conditioning the output through μ , to which the model has a high sensitivity (Stolker and Verheij, 2001b). The high degree of uncertainty for the user to determine the input parameters of BEM, mainly the terrace slope and bank erodibility (c_E), is an significant limitation to accurately estimate ship-induced bank retreat. Furthermore, primary waves are not included in the model, which can particularly have large effects on shoreline erosion (Zaggia et al., 2017).

BEM was integrated with the two-dimensional hydrodynamic model Waqua (RWS/RIKZ, 2009), resulting in a sub-module named WAQBank (Sligte et al., 2012). This functionality determines the potential bankline shift along entire river reaches, using the flow field computed in Waqua to account for flow erosion and the formulae of BEM to account for ship-wave erosion. However, an important limitation is the lack of interaction between bank retreat and hydrodynamics, i.e., there is no morphological update and the bank is assumed in equilibrium. Such approach serves to estimate short-term bankline shifts and eroded volumes with respect to the initial condition defined in Waqua (Spruyt et al., 2012). This tool can also be used to identify stretches with relative higher erosion rates, having a strong dependence on the input soil type (Spruyt et al., 2012).

1.3. RESEARCH OBJECTIVE

Given that i) the management of multifunctional navigable rivers and the planning of restoration measures would benefit from a deeper understanding of the morphological evolution of riverbanks subject to ship-induced erosion, for both economic and ecological reasons, and that ii) less uncertain estimates of long-term bank retreat would help to better manage conflict of interests within the river system, this investigation has the following main objective:

Understand and predict erosion processes and the morphological evolution of natural banks in regulated navigable rivers

1.4. APPROACH AND RESEARCH COMPONENTS

This thesis pursues the main goal through the comprehensive investigation of a river reach that presents a wide range of erosion rates since bank protections were removed. Field studies are chosen, instead of laboratory or numerical experiments, to avoid scale effects and simplified schemes of erosion processes and factors, while benefiting from unaltered natural bank compositions and the presence of complete physical processes. The main focus of analysis is then on a 1.2-km stretch in the Meuse River near a village called *Oeffelt*, the Netherlands (Figure 1.12). A second case study named *Noordereiland* is also investigated, albeit in less detail, located upstream of the main case with a extent of 1.0 km.

The most important study site, hereafter called *Oeffelt*, is the left bank of a straight reach that was re-naturalized in 2010 by extracting the riprap. Oeffelt was chosen because it presents different bank erosion magnitudes, as shown in Figure 1.12. The case at *Noordereiland* has other bank retreat patterns, for which it is considered to complement the former case (see Chapter 3). Afterwards, the research results are validated on other riverbanks, having different compositions, locations, and boundary conditions (Chapter 5, Discussion).

The Meuse River has a pluvial discharge regime with low flows during the summer, reaching 40 m³/s, and floods during the winter, commonly reaching 1,200 m³/s and exceptionally 3,100 m³/s (100 years of return period) as occurred in 1993 (Descy et al., 2009). Its rich geological history defined different channel patterns, the last of which consists of an incised low-sinuosity meandering channel (Tebbens et al., 1999; Rixhon et al., 2011). The reach under study meandered before its canalization between 1940s and 1960s, fixing the banks to their current positions. The river width was then normalized to 120 meters and water levels were regulated for commercial navigation by means of

weirs. The minimum regulated water level at Oeffelt thereafter remained at 8.0 m NAP (Dutch reference sea level).



Figure 1.12. Re-naturalized bank near Oeffelt in the Meuse River: upstream view of first 300 m (a) and downstream view of middle 500 m (b). Note the series of embayments formed after protection removal.

In order to analyse and characterize bank erosion at the process scale, it is necessary to account with topographic surveys throughout the hydrological year that could provide sufficient temporal and spatial resolution. Given the 3D complexity and large extent of the banks at the study sites, and the recent availability of low-cost Unmanned Aerial Vehicles (UAV) and Structure from Motion (SfM) photogrammetry techniques that proved useful to survey a variety of geomorphic settings (Eltner et al., 2016), the application of UAV-SfM to measure bank erosion processes along a midsize river reach is first investigated. The goal is to determine a methodology that saves time and equipment costs compared to available techniques such as terrestrial laser scanning (Brasington et al., 2012).

Furthermore, the wide-range of erosion rates at the case studies form peculiar bankline patterns after seven years of protection removal (Figure 1.12), with oblique embayments significantly larger than individual mass failures (Leyland et al., 2015), but smaller than a river bar or a meander bend (Klosch et al., 2015). In addition, the presence of trees does not provide a comprehensive explanation about the location of these embayments. It is therefore of primary importance to disentangle the causes of the size, location and asymmetry of these embayments before analysing erosion processes at single river sections.

The aforementioned objectives are two essential steps to build a solid basis for the later understanding and interpretation of bank erosion processes. The main objective is also subdivided in two partial goals to organize the steps that guide this work. This results in four specific objectives of this thesis that are summarized as follows:

 Determine a methodology to quickly measure the 3D bank topography along a midsize river reach.

- 2. Unravel the causes of distinct bankline patterns in the navigable regulated Meuse River.
- 3. Characterize bank erosion processes in regulated navigable rivers.
- 4. Develop a tool to estimate long-term or final bank retreat of re-naturalized banks in regulated navigable rivers.

1.5. THESIS OUTLINE

The contents of this thesis are organized in the following way:

- Chapter 2: Measurement of reach-scale bank erosion processes with SfM-UAV (objective 1).
- Chapter 3: Explanation of distinct patterns of bank erosion in a regulated navigable river (objective 2).
- Chapter 4: Conceptualization of bank erosion processes in regulated navigable rivers and prediction of final bank retreat (objectives 3 and 4).
- Chapter 5: Discussion of the findings at the main case study for other type of banks in regulated and unregulated rivers. Chapter 5 also elaborates on the implications for the management of re-naturalized riverbanks. This chapter finally compares the model developed in Chapter 4 with the existing BEM model and discusses its potential application to unregulated rivers and to estimate erosion rates.
- Chapter 6: Conclusions and recommendations.



REACH-SCALE BANK EROSION PROCESSES MEASURED WITH UAV-SFM



This chapter analyses the application of Structure from motion (SfM) photogrammetry with imagery from an unmanned aerial vehicle (UAV) to measure bank erosion processes along a 1.2 km long reach of the Meuse River. This technique offers a unique set of characteristics compared to previously used methods to monitor banks, such as high resolution combined with a relatively fast deployment in the field. However, vertical scarps lying on a straight reach present specific challenges to the UAV-SfM application. A method to survey complex riverbanks with the aim to identify erosion processes and quantify erosion rates is proposed and evaluated. The accuracy of the digital surface models (DSMs) is assessed with real-time kinematic (RTK) GPS points and an airborne laser scanning of the whole reach.

The contents of this chapter are published in *Earth Surface Dynamics 6* (2018) under the title: "Bank erosion processes measured with UAV-SfM along complex banklines of a straight mid-sized river reach". Authors: Duró, G., Crosato, A., Kleinhans, M. G., and Uijttewaal, W. S. J.

2.1. INTRODUCTION

Bank erosion, as a fundamental process in morphologically active river systems, has been studied from disciplines such as engineering, geomorphology, geology and ecology to understand, quantify and model it (e.g., Hooke, 1979; ASCE, 1998; Rinaldi and Darby, 2007; Osterkamp et al., 2012; Siviglia and Crosato, 2016). Predicting and monitoring bank erosion is necessary for sound river management strategies and important for both socio-economic problems, e.g. preventing material losses (Nardi et al., 2013), and environmental challenges, e.g. promoting habitat diversity through river restoration and improving water quality (Reneau et al., 2004; Florsheim et al., 2008).

Bank erosion can be monitored with different spatial resolutions, time frequencies and accuracies. The techniques that identify the temporal change in vertical bank profiles detect and quantify the different phases of the erosion cycle (Thorne and Tovey, 1981). This characteristic helps distinguishing the factors influencing bank erosion and their relative role in the whole process (e.g., Henshaw et al., 2013). On the other hand, a simple record of sequential mass failure events (see Fukuoka, 1994, for a graph of failure-driven retreat) is sufficient to track rates of local bankline retreat and estimate eroded volumes, but does not provide further information on the role of single factors governing the bank erosion process. In navigable rivers, for instance, it is important to differentiate the effects of vessel-induced waves from the effects of river flow, as well as those of high flows and water level fluctuations. This requires high spatial resolution and relatively frequent measurements that usually involve expensive equipment and field logistics when monitoring large extensions. In this context, structure from motion (SfM) photogrammetry appears a promising easy-to-use technique to measure bank erosion processes along extensive distances (Fonstad et al., 2013).

SfM with imagery from a low-cost multi-rotor unmanned aerial vehicle (UAV) is here applied to measure horizontal and vertical bank alignments at the process scale along a mid-sized river reach with a standard workflow. In order to do that, the digital surface model (DSM) produced by SfM algorithms is compared with real-time kinematic (RTK) GPS measurements and airborne laser scanning (ALS), to later analyse erosion features in bank profiles. The erosion cycle is used as reference to distinguish this study from approaches that measure bank erosion in qualitative terms. A minimum required resolution and accuracy of 1/25 times the bank height is thus defined for quantitative analysis. The case study is a 1.2 km straight river reach with complex vertical scarps. This type of linear domain with vertical surfaces represent challenges to the UAV-SfM application, since special UAV paths and camera angles may be needed to capture the bank area and rather aligned ground-control points (GCPs) along banks may result in rotated solutions during the model linear transformation.

Next, this chapter presents the framework under which bank erosion is here analysed (Section 2.2) and a summary of available techniques to measure bank erosion (Section 2.3), considering the broader context of other disciplines dealing with this topic. Section 2.4 describes the adopted approach to apply UAV-SfM to measure bank erosion processes. Sections 2.5.1 and 2.5.2 show the precision of the digital surface models relative to other techniques, Section 2.5.3 an analysis of the particular errors that may arise from the use of UAV-SfM to survey long riverbanks, and Section 2.5.4 the features and processes identifiable from the derived bank profiles. Section 2.6 discusses the precision and error sources of UAV-SfM with the adopted approach, the differences found between two reach-scale techniques, and the particular challenges and recommendations to apply UAV-SfM for bank erosion. Section 2.6.4 finally discusses advantages and limitations of UAV-SfM compared to other available methods to measure bank erosion processes.

2.2. FRAMEWORK OF ANALYSIS

Bank erosion can be analysed and measured at two different scales, i.e. the fluvial process and the river cross-section. The measurement at the process scale considers the bank face disintegration over time with evidence of erosion phases (Figure 1.4): the mechanisms of erosion develop and are captured at the vertical dimension of the bank. The measurement of bank erosion at the cross-sectional scale, which can be referred to as bankline retreat, consists of tracking banklines over time. In this case, the focus is on the planimetric changes of the bank edge and estimations of eroded volumes and sediment yield. The former approach deals with processes and mechanisms (e.g. Rinaldi and Darby, 2007), whereas the latter with landscape development at larger spatial and temporal scales. Bank erosion studies determine the survey method based on their aims and scales of interest, whereas a given methodology constraints the scope of the findings (Massey, 2001; Couper, 2004). Thus, it is important to identify capabilities and limitations of each survey technique in the context of river banks, which are inherently steep features with small-scale irregularities independent of the scale of the river.

2.3. TECHNIQUES TO MEASURE BANK EROSION AT DIFFERENT SCALES

Measuring techniques have four essential characteristics: the extent, resolution, quality and frequency of measurements. Extent refers to the area or distance along the river covered by each survey; resolution indicates the distance between surveyed points; quality is the precision of position of each surveyed point; and frequency derives from the time interval between consecutive surveys of the same spatial extent or point. The scale of interest may vary among disciplines (e.g. geomorphology, engineering, and ecology), so that a diversity of techniques is available with varying spatiotemporal

windows of inquiry (Lawler, 1993). Even though the methods currently adopted to measure riverbank erosion range from photo-electric erosion pins to terrestrial laser scanning, they only have high resolution in either time or space (Couper, 2004; Rinaldi and Darby, 2007).

The methods to determine bankline retreat and to estimate eroded volumes are typical of remote sensing, for instance, ALS and aerial photography. The former technique has typical resolutions of 1 and 0.5 metres, and covers up to hundreds of square kilometres per day. Bailly et al., (2012) indicate decimetre vertical precision, which depends on several factors including beam footprint size, aircraft inertial measuring system, onboard GPS, vegetation cover and filtering technique. ALS has been successfully applied to identify river morphological features, such as bar tops (Charlton et al., 2003) and riffle—pool and step—pool sequences (Cavalli et al., 2008; Bailly et al., 2012). In addition, sequential ALS was used to quantify volumes of eroded banks to subsequently estimate pollutant loads, achieving reasonable results for those aims (Thoma et al., 2005). However, banks are particularly steep areas where this technique tends to increase the elevation uncertainty (Bangen et al., 2014). Therefore banks are regions where lower ALS accuracies are expected compared to horizontal and flat areas.

Bank retreat can be estimated through approaches such as those described by Lawler (1993) that include planimetric resurveys for intermediate timescales (years) and sedimentological and botanical evidence for long timescales (centuries to millennia). Aerial photography interpretation has also been applied to measure bank migration, which is a useful source of information, especially if historical imagery is available over extended periods of time. Nevertheless, it provides only limited information on bank heights, for which this planform survey technique requires other methods to estimate eroded volumes. For example, photogrammetry can serve complementary to quantify volumetric changes from overlapping photographs (Lane et al., 2010); or ALS to provide recent topographic elevations and reconstruct past morphologies (Rhoades et al., 2009).

Measuring bank erosion at the process scale involves measuring the evolution of the vertical bank profile over time and several other techniques are currently available to that end. Traditional methods include erosion pins and repeated cross-profiling, which provide two-dimensional information with resolutions that, respectively, depend on the number of pins and points across the profile (Lawler, 1993). Erosion pins are simple and effective, but their accuracy may be affected by several factors, such as subaerial processes (Couper et al., 2002). More advanced versions are the photo-electric erosion pins that automatically track the bank face during different erosion phases (Lawler, 2005). Cross-profiling can be done with GPS or total stations with point accuracies of

a few centimetres or millimetres, yet with spatial and temporal resolutions that may not be sensitive to very localized or intermittent erosion (e.g., Brasington et al., 2000).

Bank geometries can currently be surveyed at the process scale with their threedimensional complexity through a number of techniques, whose geomorphic applications are broader than bank erosion studies: terrestrial photogrammetry, terrestrial laser scanning (TLS), boat-based laser scanning and SfM photogrammetry. Terrestrial photogrammetry has shown detailed bank representations, with approximate resolutions of 2 cm and precision within 3 cm, covering up to 60 metres of banks (Barker et al., 1997; Pyle et al., 1997). At the same time, this method can be labour-intensive and requires an accessible bank (Bird et al., 2010), known camera positions and sensor characteristics, and ground-control points, among other considerations (Lane, 2000). TLS has shown detailed erosion patterns from sequential surveys, with millimetre resolutions, which in practice are usually reduced to 2-5 centimetres, and approximate final accuracies of 2 cm (Resop and Hession, 2010; Leyland et al., 2015). O'Neal and Pizzuto (2011) proved the advantages of 3D TLS in capturing patterns (e.g. overhanging blocks) and quantifying eroded volumes over 2D cross-profiling. Even though TLS could cover thousands of metres, in practice the extents are generally smaller due to accuracy decrease, large incidence angles, occlusion, etc. (Telling et al., 2017), so several scans are necessary to measure long distances. For instance, Brasington et al. (2012) surveyed a 1 km river reach scanning every 200 m along the channel. Alternative boat-based laser scanning can continually survey banks with comparable resolutions and accuracies to those of TLS, with great time reduction but involving other field logistics, resources, and post-processing (Alho et al., 2009).

2.3.1.STRUCTURE FROM MOTION PHOTOGRAMMETRY

Bangen et al., (2014) matched the resolution and practical extent of SfM photogrammetry to those of TLS, when SfM photogrammetry is used to survey river topography through aerial platforms (e.g., Fonstad et al., 2013). From terrestrial platforms, this technique has been applied to measure banks to show its potential use as survey technique with different sensors and processing systems (Micheletti et al., 2015; Prosdocimi et al., 2015). Micheletti et al. (2015) indicated root mean square errors (RMSEs) within 7 cm, when combining a 5-megapixel (MP) smartphone or a 16MP reflex camera with either PhotoModeler or 123D Catch processing systems. Prosdocimi et al. (2015) identified eroded areas of a collapsed riverbank and computed eroded and deposited volumes with a precision comparable to that of TLS.

The relatively recent and fast development of UAV technology to take airborne photographs has greatly expanded the applications of SfM photogrammetry (Eltner et

al., 2016). Recently, SfM has been applied to quantify bank retreat in streams and small rivers with a fixed-wing UAV along several kilometres with 12 cm resolution (Hamshaw et al., 2017). This study showed the UAV-SfM capabilities to produce extensive 2.5 D DSM from a 100 m high nadiral view, which achieved 0.11 m mean error and 0.33 m RMSE compared to TLS. However, this work generated DSMs similar to those of ALS, which allow for volume computations and bankline retreat but did not use the full 3D capacities to investigate undermined banks or identify erosion processes.

Applications of this combined technology span in scale and complexity, covering glacial dynamics (Immerzeel et al., 2014), landslides (Turner et al., 2015), agricultural watersheds (Ouédraogo et al., 2014), fluvial topography (Woodget et al., 2015), etc. The precision achieved relative to the camera—object distance for the mentioned diverse settings was approximately 1:1000, with distances ranging from 26 to 300 m and different cameras, lighting conditions, and surface types. Interestingly, this precision was also found for terrestrial SfM photogrammetry at different scales by James and Robson (2012). Other experiences showed lower accuracies, e.g. ~1:200 for morainemound topography (Tonkin et al., 2014) and, on the other hand, higher ones, such as ~1:2100 for fluvial changes after a flood event (Tamminga et al., 2015). Although it is not possible to generalize a precision for all settings, ~1:1000 seems an encouraging reference (RMSE of 10 cm for 100 m camera—object distance) to consider for unexplored conditions.

Several factors affect the precision of DSM obtained from UAV-SfM, such as surface textures at the field site (Cook, 2017), lighting conditions (Gómez-Gutierrez et al., 2014b), camera characteristics (Prosdocimi et al., 2015), GCP characteristics (Harwin and Lucieer, 2012), SfM algorithms (Eltner and Schneider, 2015), and photo overlaps, resolutions and perspectives (James and Robson, 2012; Micheletti et al., 2014). Knowledge to improve the quality of SfM digital surface models keeps expanding by investigating isolated variables, for example, assessing the influences of number and distribution of GCPs (Clapuyt et al., 2016; James et al., 2017) or optimizing camera calibration procedures to manage without GCPs (Carbonneau and Dietrich, 2017). The flexibility, range, high resolution and accuracy that UAV-SfM proved in other conditions shows promise for analysing bank erosion processes throughout the scale of a mid-sized river.

The monitoring of bank erosion processes in the case study herein has two specific challenges for the UAV-SfM technique. First, the bank has steep, vertical and undermined surfaces along the domain. Second, the target area is a straight reach with a large length-to-width ratio. The first aspect may require non-conventional UAV paths and camera angles to be able to adequately capture the bank area. The second matter introduces a challenge to georeference the model with rather aligned GCPs, which may result in

false solutions rotated around the GCP axis during the model linear transformation. This could be the case since GCPs are to be placed in the bank surroundings to be captured from the UAV, and this target area consist of an overall linear domain. Therefore, the GCP distribution and the image network geometry particularly have key roles in the UAV-SfM workflow applied to measure bank erosion at the process scale.

2.4. METHODOLOGY

A flexible multi-rotor UAV platform was used to capture photographs from different perspectives along 1200 m of Oeffelt reach (see later Figure 2.2) and SfM photogrammetry was later applied to derive the DSMs. Grassy fields used for grazing cover the riparian zone, followed by crop fields across the floodplain. In the near-bank area there are poplar trees every 100 m, some of which have been dislodged during erosion progression. Eight surveys done in 2017 are used in this chapter. Particularly, an extraordinarily low water level provided the opportunity to compare the SfM photogrammetry with ALS and RTK GPS not only for the banks and floodplain, but also for the sub-aqueous terrace at the bank toe (see schematic cross-sections in Figure 1.12). This terrace was composed of bare soil, without vegetation or obstructions, which adds an extra surface for the comparative analysis. This extraordinary exposure was the consequence of a ship accident against the downstream weir of Grave (on 29th December 2016). All cross sections along the Meuse are identified by their distance in kilometres from the Dutch-Belgium border.

Section 2.4.1 describes the UAV paths for photo acquisition and Section 2.4.2 the SfM imagery processing. Four steps are taken to assess the capabilities of this survey technique with the adopted approach to measure bank erosion at the process scale. First, the elevation precision is verified against 129 RTK GPS points of several DSMs obtained with diverse number of photographs and camera orientations. In this way, an effective number of images to acquire the bank topography with high accuracy is identified. Second, the chosen DSM is compared with airborne lidar points to analyse elevation precision over the whole river reach, differentiating between areas of bare ground, grassland and banks. Third, the georeferentiation accuracy is verified regarding the model rotation around GCP axis. Fourth, bank features are searched in SfM-based profiles and analogous ones from ALS, as well as signatures of erosion processes along sequential SfM surveys. All data used herein are publicly accessible (Duró et al., 2018c).

For the first step, the analysis of the minimum number of photographs needed to achieve the highest DSM accuracy, the DSMs is compared with RTK GPS measurements to quantify vertical precision. A Leica GS14 RTK GPS was deployed to take 129 points across eight profiles on 18-01-2017 (see Figure 2.2), whose root mean square precisions

according to the manufacturer specifications are 8 mm + 0.5 ppm in horizontal and 15 mm + 0.5 ppm in vertical directions. On the same date, the UAV was flown along the bank four times with different camera angles and perspectives. A total of eight photograph combinations were considered to derive eight DSMs. Then, the comparisons were done with the elevation differences between the GPS points and the corresponding closest ones of the DSM point clouds (e.g. Westoby et al, 2012; Micheletti et al., 2015). CloudCompare software (Girardeau-Montaut, 2017) was used for these computations.

In the second step, the selected DSM from the previous analysis was compared with ALS, to analyse topographic differences over the whole river reach. The ALS data were acquired on 17-01-2017 from an airplane at 300 m above the ground level. The laser scanner, a Riegl LMS-Q680i, measured a minimum of 10 points per square metre with an effective pulse rate of 266 kHz. The raw data was not accessible so that the automatically generated 0.5 m grid was used. The ALS elevation precision was tested against the 129 RTK GPS points using the vertical component of the closest distance to a local Delaunay triangulation of the ALS grid, due to the different resolutions between both datasets. Then, the distances between the ALS grid points and the corresponding nearest ones of the DSM point cloud were computed. Both computations were done with the standard cloud/cloud distance tool of CloudCompare, distinguishing between surfaces of grassland, bare ground, and bank.

Third, the DSM spatial stability with respect to the potential axis of rotation around the GCPs was analysed. The GCPs distributed over the floodplain along the near-bank area defined the linear transformation from an arbitrarily scaled coordinate system to the real-world coordinates. In order to verify that the DSM was stable and the tendency to rotate around co-linear solutions did not affect the accuracy beyond the survey target, a regression line with the GCPs was computed to identify the potential axis of rotation for the DSM domain. Then, the DSM elevation errors corresponding to the GPS points were projected onto the plane perpendicular to the regression line. Afterwards, a second regression line with those points was computed to evaluate the alignment of errors across the potential axis of rotation.

Fourth, profiles across six sections of dissimilar erosion rates were made to contrast the bank representations of i) the SfM DSM, ii) the triangulated ALS grid, and iii) the RTK GPS points. The profiles were extracted with MATLAB using i) the Geometry Processing Toolbox (Jacobson et al., 2017) adapted to slice triangle meshes, ii) a linear interpolation across the triangulated ALS grid, and iii) a projection of the RTK GPS points onto the exact cross-section locations. Then, a cross-section with sequential SfM-UAV surveys was selected and analysed to show different stages of the erosion cycle, since the bank

erosion cycle was used as a reference to distinguish between techniques capable of measuring at either the process or the cross-sectional scale.

2.4.1. UAV FLIGHTS FOR IMAGE ACQUISITION

The consumer-grade UAV DJI Phantom 4 was used to take images of the banks. It has a built-in camera with a 1/2.3" 12MP sensor and a 94° horizontal angle of view. Prior to the image acquisition, a network of GCPs was distributed on the floodplain to georeference the DSMs (see Figure 2.2). The GCP were spaced approximately every 50 metres along the reach, roughly following the tortuous bankline and avoiding proximity to trees, to simplify the field work and facilitate the GCP visibility from the UAV paths (see Figure 2.1-Figure 2.2). This approach did not include GCP locations at different elevations, as, for instance, at the bank toe, and relied on the cross-sectional GCP distribution for the stability of the DSM georeferentiation (see Section 2.4.2). The GCPs were 40 by 40 cm black ceramic tiles (Figure 2.1c) fixed to the ground with a circular reflector (12 cm CD) at its centre for their fast recognition in the photographs (Figure 2.1d-e show how a GCP is seen from tracks 1 and 2). The GCP coordinates were measured using the Leica GS14 RTK GPS unit, which was also deployed for the cross-profiling.

An initial flight plan was designed using Universal Ground Control Station (UgCS) software to photograph the banks from four different perspectives, to later compare the results of diverse combinations and find a convenient photo set to survey the target topography in subsequent campaigns. The UAV flew four times in straight parallel lines along the banks (Figure 2.1a,b,f) to simplify the setup and save flying time, compared to paths that follow changes in bankline or include paths across the domain. The first track took oblique photos from above the river at a height of 25 metres and an average (oblique) distance to the bank of 40 metres (~25 m from the least retreated bankline). The second track had a top view from 40 metres above the floodplain level along the tree line (Figure 1.12-Figure 2.2). The third and fourth tracks followed the same path as the second one in respective upstream and downstream directions, but the camera angle was 50 degrees forward inclined from the horizontal plane (see photo footprints in Figure 2.2). These perspectives were thought to capture the tortuous and complex bank surface (Figure 1.12, Figure 2.1a and Figure 2.2), including undermined upstreamand downstream-facing scarps, with an average ground resolution of 2.1 cm per pixel. A minimum resolution and accuracy of 1/25 times the bank height of the river was considered as a requirement to detect erosion processes, which resulted in a maximum acceptable precision of 14 cm for the maximum bank height of 3.5 m at the case study.

Five specific combinations of photographs from the different UAV tracks were tested. Test 1 corresponds to the photo set of the first track only, which has the side view with

the optimal coverage of the bank. Test 2 uses the nadir view alone, which is similar to the viewpoint of classic aerial photography. Test 3 is a combination of the previous two sets. Test 4 combines tracks 3 and 4, i.e. both paths from above the bank with the oblique forward perspectives in upstream and downstream directions, which allows views on all parts of the irregular banks. Finally, test 5 utilizes the four tracks with all photographs (Table 2.1).

The first oblique track was also used to evaluate the minimum longitudinal photo overlap to efficiently capture the bank relief. The photo overlap along the river is a function of the UAV speed and distance to the bank, for a given maximum photo sampling frequency, which in the case of the deployed UAV is one every 2 seconds. Then, flying at 2 m/s along track 1 resulted in 20 photo overlaps for the most retreated areas and 16 for those zones with least bank retreat, which corresponds to 95% and 93.7% image overlap, respectively. Afterwards in the processing phase, a decreasing number of overlaps by twos were successively selected, resulting in four DSMs. These were test 1a when using all photos from track 1 (which is the same set as the aforementioned test 1), test 1b when using half of them, and so forth for test 1c and test 1d (see Table 2.1).

Table 2.1. Number	of photographs and	overlaps for the tests.

	Test 1a	Test 1b	Test 1c	Test 1d	Test 2	Test 3	Test 4	Test 5
Track 1	293	147	73	37		147		293
Track 2					232	232		232
Track 3							232	232
Track 4							232	232
Min. overlaps	16	8	4	2	7	15	26	49
Max. overlaps	20	10	5	2	7	17	26	53

2.4.2. SFM WORKFLOW

The principles of SfM photogrammetry are similar to those of digital photogrammetry, but camera positions and lens characteristics are not specified in the former to reconstruct 3D structures. The camera extrinsic and intrinsic parameters are automatically estimated via tracking and matching pre-defined features in overlapping photos and an iterative bundle adjustment procedure, which results in a sparse point cloud (Hartley and Zisserman, 2003; Snavely et al., 2008; Westoby et al., 2012). Afterwards, the (dense) point matching is done at pixel scale to generate a detailed point cloud of the scene that has the final survey resolution.

GCPs are commonly used to reference the model to a geographical coordinate system, to compute erosion rates and processes through sequential surveys. The

georeferencing process involves the Helmert transformation of the point cloud through seven parameters that adjust its scale, position, and rotation in a linear and rigid way (Fonstad et al., 2013). The estimation of these parameters is done through a least-squares regression with the GCPs identified in the UAV images. The propagation of linear errors is thus given by the accuracy with which the GCPs were measured (in this study with the RTK GPS) and then identified in the photographs. Further in the workflow, GCPs can be used to refine the camera parameters estimated during the bundle adjustment, to reduce the non-linear errors that the estimation of the camera parameters may induce (Carbonneau et al., 2017). Ideally, well-distributed, precisely measured, and accurately identified GCPs avoid excessive linear and non-linear errors in the point cloud. Yet, a third type of error given by the automated image matching process cannot be prevented with GCPs. These are local and random errors and represent the classic concept of precision.

Agisoft PhotoScan software was used to process the imagery. The camera yaw, pitch, and roll recorded during the UAV flight from different perspectives (Table 2.1) were input to ensure that the image matching assigned all photos into a single model (Stöcker et al., 2015). For this step, three GCPs were used along the reach, two at the extremes and one in the middle, all close to the bank and easily visible from tracks 1 and 2. These approximate orientations and a priori known ground points helped obtain a consistent sparse point cloud of the bank along the entire reach. The resulting camera positions and orientations of the photo alignment are visible in Figure 2.1a, evidencing the UAV tracks. This figure also shows the DSM textured with colours from the photographs, in which the green area on the left side with white patches corresponds to the floodplain partially covered with snow (see also Figure 2.1d-f) and the right brownish area is the terrace at the bank toe, with snow remains as well.

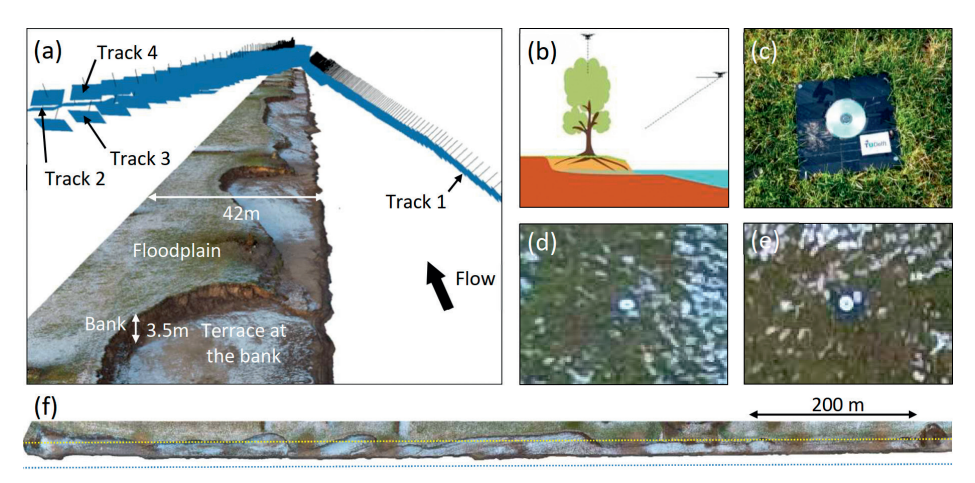


Figure 2.1. (a) Camera positions and orientations in perspective view. The digital surface model shows the low water condition during January 2017, which exposed a terrace at the bank toe. (b) Cross-sectional scheme of UAV paths. (c) Ceramic plaque with CD as ground-control point on the floodplain. (d) GCP in photograph from track 1. (e) Same GCP from track 2. (f) Top view of DSM with UAV track 1 in blue and tracks 2-4 in yellow.

After obtaining the sparse point cloud, the remaining 15 GCPs we identified (Figure 2.2) in the photographs, helped by their estimated locations in the model. Then, the camera parameters were refined by minimizing the sum of GCP reprojection and misalignment errors, i.e. using the camera optimization option in PhotoScan. This adjusts the estimated point cloud by reducing non-linear deformations. Once the dense point cloud was computed, the points outside the area of interest were removed, as well as those points at the water surface, tree canopies and individual bushes at the floodplain. Finally, the point cloud was triangulated and interpolated to generate a TIN, through the arbitrary surface option and the highest number of mesh faces suggested in PhotoScan. This mesh consisted of a non-monotonic surface that was later processed in MATLAB to plot 2D cross-sections.



Figure 2.2. Study reach of the Meuse River with GCPs, RTK GPS measurements with cross-section locations and numbers, and some image footprints for all UAV tracks.

2.5. RESULTS

2.5.1. DSM PRECISION: IDENTIFYING NECESSARY PHOTOGRAPHS

The sequentially decreasing photo overlaps of Track 1 (Table 2.1) produced four DSMs, tests 1a-1d, whose elevation differences with the 129 RTK GPS points are presented in the histograms of Figure 2.3. The elevation errors mostly ranged within 10 cm in all tests, but the mean and standard deviation (SD) presented some differences (Table 2.2 and dot with bar in Figure 2.3). Tests 1a, 1b and 1c presented mean values smaller than 1 cm and SD within 3-4 cm, while for test 1d these values increased to 4 cm and 7 cm respectively (Table 2.2, rows 1-2). The mean errors on the bank area alone for test 1a, 1b and 1c were lower than 1 cm (Table 2.2, row 5), but test 1c had a higher SD of 7 cm compared to 4 and 3 cm of tests 1a and 1b respectively (Table 2.2, row 6). Then, tests 1a and 1b had the highest precisions and showed little error differences between them: less than 1 cm for all values in Table 2.2. Consequently, test 1b with eight photo overlaps was as effective as test 1a with 16 overlaps to achieve the highest DSM accuracy. In addition, test 1b fully covered the tortuous bank area in contrast to test 1c, especially at the perpendicular stretches of embayments (Figure 2.1-Figure 2.2), which assured the choice of eight image overlaps over four, despite the general close performance of the latter in terms of accuracy (Table 2.2, all rows). Therefore, test 1b became the reference for tests 1 and was used in combination with test 2 to generate test 3.

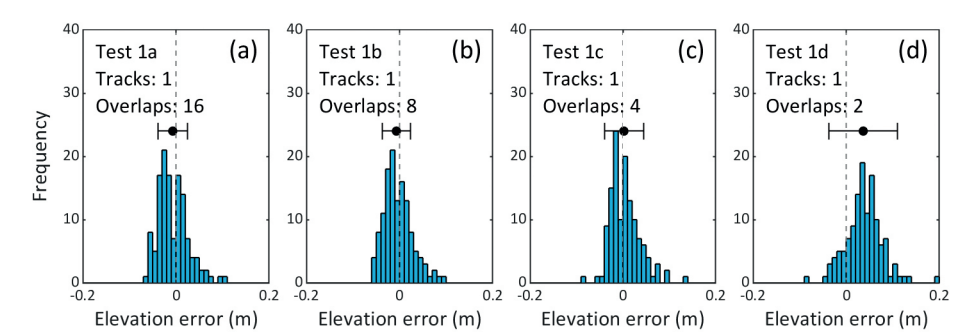


Figure 2.3. Elevation error distributions for SfM tests 1a, 1b, 1c, and 1d, assuming that the RTK points are correct and without error. Indicated overlaps are the minimum.

Table 2.2. Mean and standard deviation of elevation differences between SfM DSMs and GPS points. Colour intensity indicates the deviation from zero value with minimum/maximum of ± 0.13 m.

Surface	Error (m)	Test 1a	Test 1b	Test 1c	Test 1d	Test 2	Test 3	Test 4	Test 5
All	Mean	-0.01	0.00	0.00	0.04	0.03	-0.01	-0.05	0.00
	Std. dev.	0.03	0.03	0.04	0.07	0.03	0.03	0.05	0.03
Grassland	Mean	0.02	0.01	0.01	0.02	0.02	0.01	0.01	0.02
	Std. dev.	0.03	0.03	0.04	0.04	0.03	0.02	0.02	0.02
Bank	Mean	0.00	0.01	-0.01	-0.01	0.05	0.01	-0.03	0.01
	Std. dev.	0.04	0.03	0.07	0.13	0.03	0.03	0.04	0.03
Terrace	Mean	-0.02	-0.02	0.00	0.06	0.03	-0.02	-0.09	-0.01
	Std. dev.	0.02	0.03	0.03	0.06	0.03	0.02	0.03	0.02

Figure 2.4 shows the error distributions of the remaining four DSMs, i.e. tests 2–5, which also were mostly within 10 cm, except for Test 4. This test had evident higher errors than the rest, mostly concentrated at the terrace (Table 2.2, row 7). Tests 3 and 5 had the lowest mean elevation errors, both lower than 1 cm, with the same SDs at all surfaces that were lower than 3 cm. Test 2 presented a similar SD, but the mean was biased 3 cm. This test in combination with test 1b slightly reduced the SD errors of the latter (Table 2.2, rows 7 and 6), but without significant overall improvements. All in all, tests 1b, 3 and 5 had the best performance with average errors lower than 1 cm and standard deviations within 3 cm, however with increasing number of photographs (Table 2.1). The most efficient one was then test 1b that used the lowest number of photographs to achieve similar precision, especially on banks.

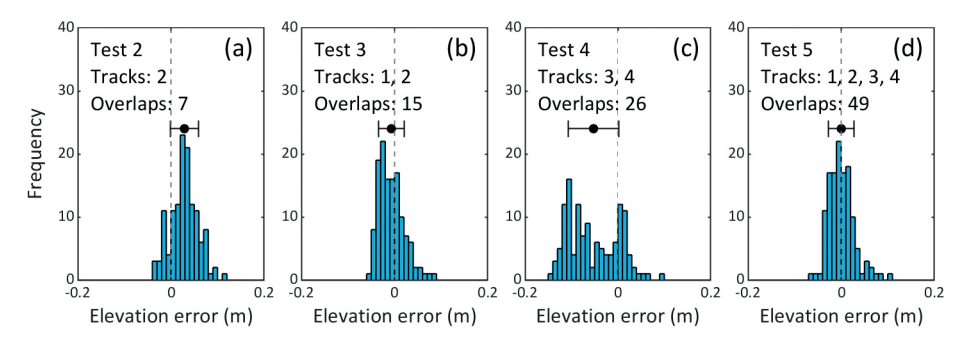


Figure 2.4. Elevation error distribution for tests 2, 3, 4, and 5. Ordinates indicate number of GPS points in each bin.

Interestingly, if we consider all tests, the elevation errors on grassland were similar to each other (Table 2.2, rows 3 and 6), means between 1 and 2 cm and SD between 2 and 4 cm, whereas the bank and terrace did not present this behaviour. Furthermore, while

the bank values (Table 2.2, rows 4 and 7) did not correlate with those of all grounds (Table 2.2, rows 1–2), the terrace mean elevation differences (Table 2.2, row 5) linearly correlated with those of all grounds (Table 2.2, row 1) with $R^2 = 0.97$. Therefore, the error biases for all grounds throughout the tests were most likely due to the biases from the points over the terrace.

To conclude, despite virtually doubling the number of images in comparison with test 1b, the test 3 setup with a nadir track and a side-looking track was chosen for subsequent UAV surveys on the basis of two findings. First and most important, growing vegetation at the bank toe occluded parts of the target surface from the oblique camera perspective. Second, the GCPs on the floodplain laid almost horizontal, which made them easier to identify from the top view during an initial phase of GCP recognition in the photographs. Moreover, at later surveys it was found that growing grass on the floodplain was sometimes blocking GCP plaques from the angle of vision of UAV track 1, for which using the nadir view of track 2 was advantageous to locate the plaque centres, preventing the otherwise disuse of some GCPs.

2.5.2. DSM PRECISION OVER THE REACH: COMPARISON WITH ALS

Compared to the ALS grid, test 3 point cloud showed a good agreement over most of the reach. This is observable from Figure 2.5a, corresponding to the blue areas that indicate elevation differences lower than 5 cm. However, two notable regions surpassed this difference: the bank and the extremes of the reach. The latter were zones beyond the GCPs, where higher errors in the DSM are expected when using parallel image directions due to inaccurate correction of radial lens distortion (James and Robson, 2014; Smith et al., 2014). Consequently, the results outside the GCP limits were not considered as reliable as those within, where distortion is minimal, and thus were discarded for the subsequent statistical comparisons (beyond the dashed lines in Figure 2.5). Within the GCP bounds, the bank area presented relatively high elevation differences, which makes the bankline visible in Figure 2.5. Moreover, another sloped area at end of the terrace also presented higher differences than surrounding areas, which is visible as a thin light-blue line at the bottom of the domain in Figure 2.5a (see also Figure 2.1a-b for other perspectives of this slope toward the channel bed).

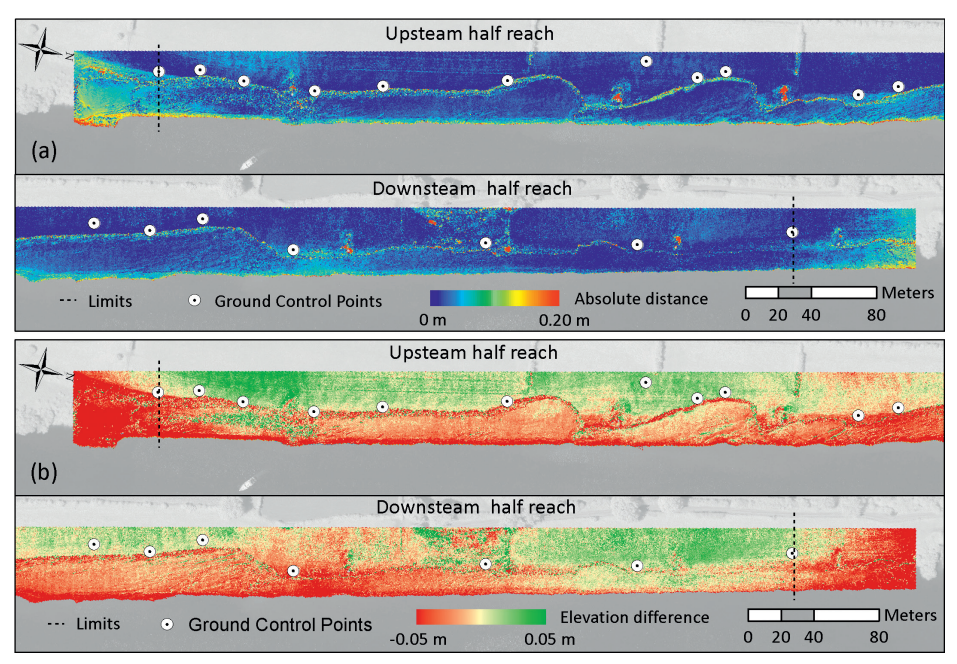


Figure 2.5. (a) Absolute elevation differences between SfM and ALS along the reach. (b) Signed elevation differences between SfM and ALS with a smaller scale range.

Figure 2.5b presents signed elevation differences with a smaller scale range to highlight areas with positive and negative deviations between techniques. Green zones indicate higher ground elevations on the SfM DSM than in the ALS grid, red zones indicate the opposite, and yellow shows elevation matches. The upstream half domain presented a general tendency of SfM to overestimate elevations on the floodplain, and in turn underestimate them on the terrace. This trend is also observed in the upper part of the downstream reach. Nevertheless, these zones showed exceptions, such as a green patch at the terrace close to the dashed limit, and a red patch on the floodplain at the end of the upstream half reach. Despite the described general opposed behaviour between floodplain and terrace, the downstream reach evidenced two zones with consistent trends across the domain, covering both the floodplain and terrace. First, lower SfM elevations at the end of the largest embayment (downstream half reach), and second, SfM higher elevations at the end of the reach, before the dashed limit.

Figure 2.6 presents the relative frequency distributions of the elevation differences divided into three regions: the grassy floodplain, the steep bank, and the bare-ground terrace. Over the grassland, both SfM and ALS had rather similar results (Figure 2.6b), with 1 cm mean difference and 2 cm of standard deviation (Table 2.3). In contrast, the bank had a bias between techniques of 6 cm (Table 2.3) and a relatively high standard deviation of the same value. Finally, the terrace showed a slightly higher deviation

than over the grassland (Figure 2.6 and Table 2.3) but with a bias of -4 cm. The bank area together with the terrace induce an overall small negative bias in the elevation difference distribution (Figure 2.6a and Table 2.3). The former has a small contribution to the total number of measurements and the latter has a greater number but a lower magnitude.

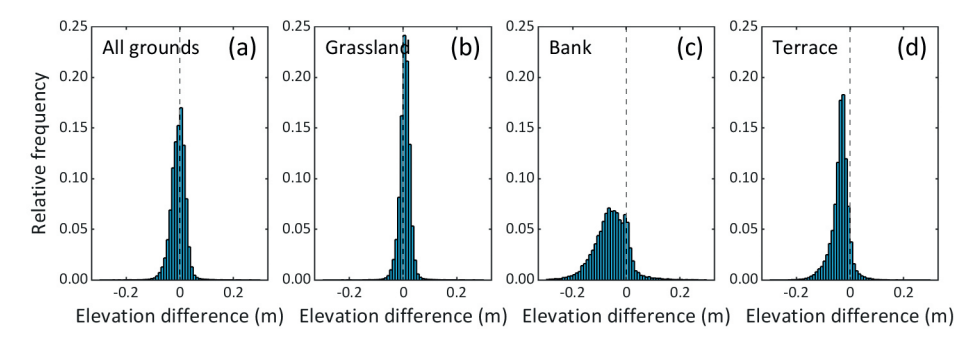


Figure 2.6. Comparison of elevation differences between SfM and ALS for distinct surface types.

Table 2.3 also indicates the differences of SfM DSM and the ALS with the 129 RTK GPS points. Interestingly, the ALS presented a constant bias of 1 cm across all surfaces, but the standard deviation did change significantly among them: the bank had a standard deviation of 9 cm, which doubled the deviation of the terrace and tripled that of the grassland. While the SfM DSM had comparable absolute biases than those of ALS, the standard deviations were all respectively lower. Particularly at banks, the standard deviation of the SfM DSM was only 3 cm in contrast to the 9 cm of the ALS, which makes the former approach considerably more accurate than the latter. This could explain the relatively large elevation differences between the two methods in the bank area (Figure 2.6c), occurring due to a lower precision of the ALS, and not vice versa.

Table 2.3. Mean and standard deviation of elevation differences between SfM, ALS and RTK GPS. Colour intensity indicates the deviation from zero value with minimum/maximum of ± 0.09 m.

Subtraction		All grounds	Grassland	Bank	Terrace
SfM - ALS (m)	Mean	-0.01	0.01	-0.06	-0.04
	Std. dev.	0.03	0.02	0.06	0.03
ALS - GPS (m)	Mean	0.01	0.01	0.01	0.01
	Std. dev.	0.05	0.03	0.09	0.05
SfM - GPS (m)	Mean	-0.01	0.01	0.01	-0.02
	Std. dev.	0.03	0.02	0.03	0.02

2.5.3. DSM ACCURACY: ROTATION AROUND GCP AXIS

A regression line was computed with the locations of the GCPs to analyse with respect to this axis the rotational tendency of the model. The GCP distributions around the regression line and the bankline are shown in Figure 2.7a. The adopted GCPs spanned 19.7 m across the reach and 1.6 m in the vertical direction (Figure 2.7, right). The bank scarp along the reach, which is the target survey area, covered 26.9 m in the cross-sectional direction due to the wide-ranging erosion magnitudes of the case study, with maximum bank heights of 3.5 m, indicated with a grey area in Figure 2.7b. This side perspective of the domain evidences the potential plane of rotation, whose stability depends on the position of the GCPs.

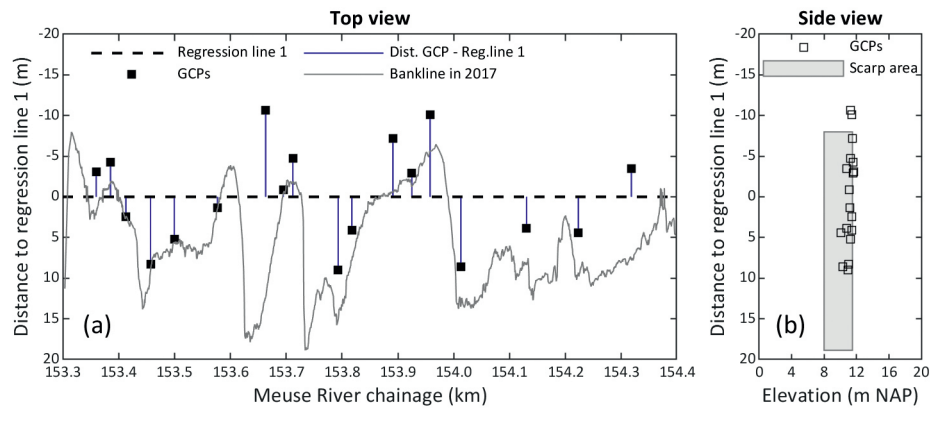


Figure 2.7. (a) GCP horizontal distances to the regression line and (b) respective positions in potential rotation plane from the regression line.

The rotation potential of the model is evaluated comparing SfM DSM elevations with those of the 129 GPS points (Figure 2.2). Figure 2.8a presents the locations of the GPS points used for accuracy control projected at the potential rotation plane, showing that they covered the domain across the channel (abscissa axis) and different elevations along the scarp area (ordinate axis), resulting in a reasonable sample to assess the model georeferentiation stability. Figure 2.8b presents the DSM elevation errors distributed across regression line 1. In this plane, a second regression line was computed with all 129 points, represented with a dashed black line in Figure 2.8b. This line is tilted from the horizontal suggesting that the model was rotated with a magnitude equal to the respective slope.

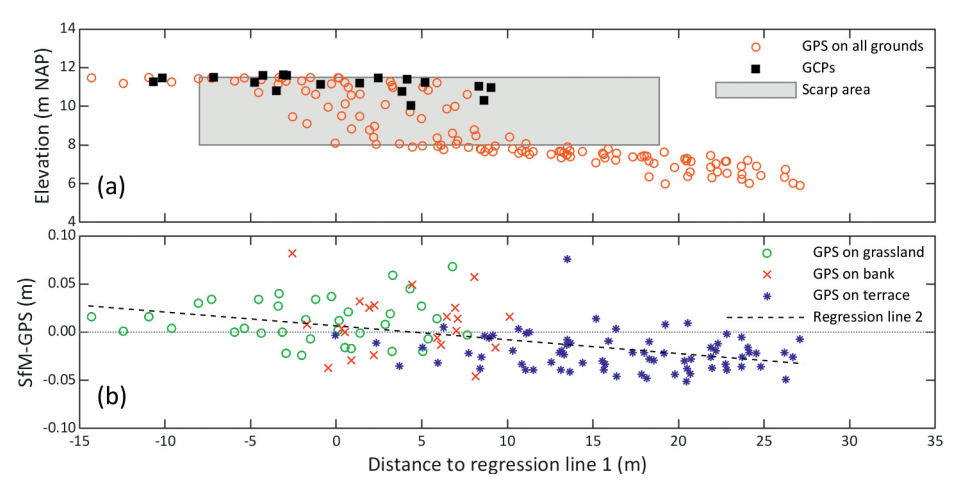


Figure 2.8. (a) Location of GPS measurements in potential rotation plane around regression line 1. (b) SfM DSM elevation errors across regression line 1, distinguished among areas of grassland, bank and terrace.

The GPS points corresponded to difference surface types, shown with different point markers in Figure 2.8b. It is clear that on the left side of the regression line 2 down-crossing, errors mostly had a positive bias, whereas on the right they mostly presented a negative bias. At the same time, those errors with positive bias were generally over ground covered with grass, and those with the negative trend were measured on slightly sloped bare ground (see also Table 2.2, column for Test 3). Then, these tendencies could also be ascribed to the overestimation of the grass cover in the former case, and a non-linear transverse deformation beyond the GCP bounds, for the latter. Regardless of the causes, the results showed an overall transverse DSM inclination with respect to the GPS points used for accuracy control. Regression line 2, when evaluated at the extremes of the bank scarp area (-7.99 m and +18.87 m), yielded an elevation difference between these points of 3.9 cm.

2.5.4. BANK EROSION FEATURES AND PROCESS IDENTIFICATION

Six bank profiles were selected among those surveyed with GPS on January 2017 (Figure 2.2) to compare the bank representation with the different survey techniques. Figure 2.9 shows the bank profiles at sections 1, 2, 4, 6, 7, and 8. These sections presented distinct erosion magnitudes and features after 7 years of restoration: for example, section 8 (Figure 2.2 and Figure 2.9) appeared close to the original condition, with a mild slope and nearly no erosion, whereas sections 6 and 7 had vertical scarps. The SfM DSM profiles are represented by continuous lines, the ALS profiles with dashed lines, and GPS points with circles. The SfM representation had better proximity to the GPS points than the ALS in almost all cases. What is more, ALS generally overestimated the

elevation corresponding to the GPS points, which confirms the bias observed in the comparison of bank elevations shown in Figure 2.5. and Figure 2.6.

SfM profiles showed detailed bank features, such as a collapsed upper bank lying at the toe (section 2), an overhang at the bank top (section 1), small-scale roughness on scarps (sections 6 and 7), and slump-block deposits (section 4). These features appeared as simple shapes in the profiles but they were confirmed with field observations. The ALS depicted simpler profiles, smoothed by coarser resolution, which made it difficult to identify characteristic features of the erosion cycle in them. Yet, ALS profiles had enough point spacing to capture gentle bank slopes with reasonable precision (section 8), but for steeper ones (sections 1, 2 and 4) and especially at scarps (sections 6 and 7), this technique provided lower accuracies.

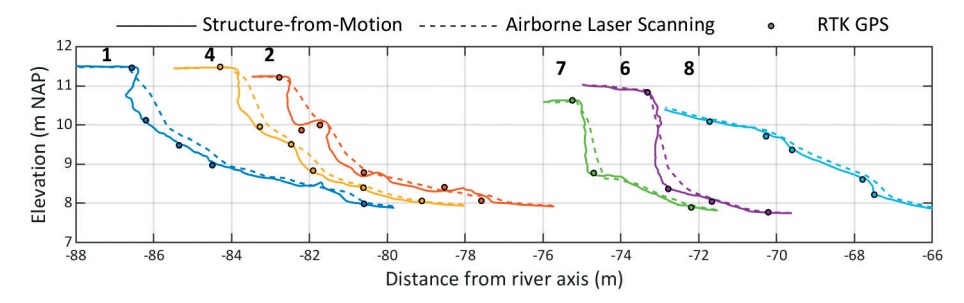


Figure 2.9. Banks measured with SfM (continuous lines), ALS (dashed lines) and GPS (circles) on 17–18 January 2017. Cross-sections are located from left to right, at river kilometres 153.4, 153.9, 153.5, 154.2, 154.1, and 154.3 (see Figure 2.2 for locations).

The temporal development of section 4 (Figure 2.2 and Figure 2.9) is illustrated in Figure 2.10a by a sequence of SfM-UAV surveys. The initial stage corresponds to the survey of Figure 2.9 on 18 January 2017. The consecutive surveys showed the evolution of the vertical bank profile through which different processes can be inferred. The bank profile, initially characterized by a top short scarp and slump blocks along the bank face, experienced a mass failure and a further removal of blocks between January 18 and March 15 2017. Between March 15 and April 26, only toe erosion occurred. By June 21, another mass failure happened, which left slump blocks along the lower half of the bank. On July 19, these blocks were removed, leaving a steep bank face. Then, further toe erosion caused a small soil failure at the lower bank whose remains laid at the toe. On October 11, this wasted material was removed. Then, until the last survey on November 22, entrainment occurred at the lower half of the bank profile, further steepening the bank. In light of the results, the methodology resolution and accuracy are high enough to identify different phases of the erosion cycle, enabling the analysis of bank erosion processes in conjunction with data on potential drivers.

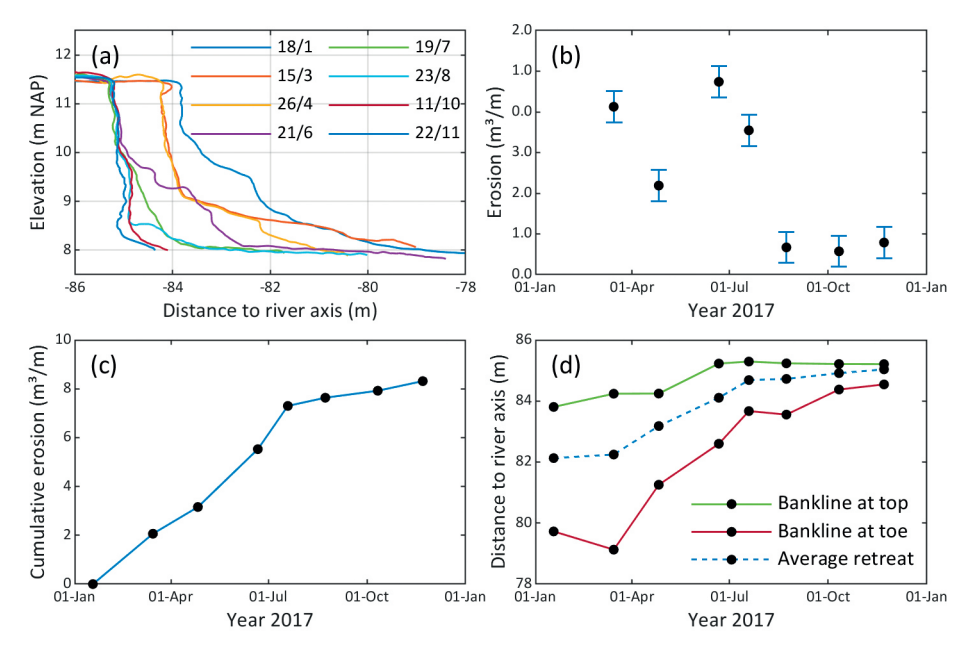


Figure 2.10. Sequential surveys at cross-section 4, Meuse River kilometre 153.9, over 2017. (a) Bank profiles from DSMs. (b) Eroded volume per unit width between consecutive surveys. (c) Cumulative erosion along surveys. (d) Bankline locations at the top and toe of the bank.

In addition to process description, eroded volumes can be quantified by computing the net area between sequential bank profiles. For example, Figure 2.10b shows eroded volumes per unit width between consecutive surveys plotted at the end of each time interval, with an error bar based on the RMSE of test 3. Evidently, there were different erosion rates during the year and the highest ones happened in the first part of it. Figure 2.10c presents the respective cumulative eroded volumes per unit width, where the two trends can be distinguished: a gentle slope towards the end and higher rates of sediment yield during the first half of the year. Given that the topographic measurements are limited to a single year, it is not possible to state whether this behaviour is recurrent on a yearly basis. However, this case exemplifies the possibilities to quantify eroded volumes throughout different phases of the erosion cycle.

The bankline retreat as a measure of bank erosion involves the identification over time of the bank top, but this concept could be extended, for instance, to the bank toe. Figure 2.10d shows the temporal progression of the bankline distance from the river axis for both the bank top and the toe, which was arbitrarily defined for this case at 11.1 m and 8.1 m, respectively. The top bankline showed a major jump between April and June and a smaller one between the first two surveys, corresponding to mass failure

events. The bank toe presented a more gradual retreat, with events of slumping and temporal accretion that were timely captured along the surveys. This alternative bank retreat representation provides evidence of the development of bank erosion at every survey. The contrast of bankline retreat at the top and toe of the bank illustrates how different processes on their own represent dissimilar erosion evolutions, since they constitute different phases of the erosion cycle, i.e. at the top mass failures and the toe slump-block removal and entrainment. Finally, the average bankline between bank toe and top would best represent the real retreat (dashed line in Figure 2.10d), despite not necessarily indicating an actual bank location for a specific elevation. This approach logically considers all erosion phases and follows a similar trend to the cumulative erosion of Figure 2.10c.



Figure 2.11. Zoomed-in UAV photos from track 1 at section 4, kilometre 153.9, showing diverse bank erosion stages: (a) slump blocks at bank toe on June 21, (b) clean bank face after block removal on July 19, and (c) undermining on August 23.

Finally, the availability of the UAV imagery provides additional information to analyse and interpret bank evolution through direct observation. Figure 2.11 shows photographs from the three consecutive surveys on June 21, July 19 and August 23 at section 4, kilometre 153.9. At this bank area, the sequence shows on the left side of the panels only entrainment at the bank toe, and from the centre (kilometre 153.9) to the right, one or more erosion cycles. Cross-section 4 presented on June 21 (Figure 2.11, left panel) slump blocks lying at the bank toe that were removed by July 19. Then on August 23, this cross-section had incipient undermining at the lower bank and block deposition at the toe. The bank area at the right of section 4 experienced a second mass failure after June 21, completing one erosion cycle, and further downstream it is more difficult to keep track of the cycles due to faster erosion rates. The UAV photos also evidence the progressive growth of grass over the floodplain, especially observable next to the walking path, which was captured along the surveys (Figure 2.10a).

2.6. DISCUSSION

2.6.1. UAV FLIGHT AND SFM PRECISION

In general, there were no large differences in accuracy between the DSMs derived with different photo perspectives and overlaps. The precision of the tests, except for test 4, was approximately 10 cm complying with the target precision and resolution

of 14 cm, and they all represented characteristic features of the erosion cycle, such as slump blocks deposited at the bank toe and mass failures. Other topographic features that were hidden from the nadir UAV perspective, such as undermining, were only captured from oblique camera perspectives. For instance, the area below the top overhangs visible at cross-sections 1 and 2 (Figure 2.9) was not captured in test 2, and were represented with a lower resolution in test 4. The UAV viewpoint of track 1 not only had the largest bank area coverage compared to the other camera perspectives proposed in this work but also achieved the highest elevation precision without the need for other tracks. Nevertheless, the nadir view of track 2 contributed to cover an additional bank area behind trees and bushes growing at the bank toe along the first 200 m of the reach (Figure 1.12a), for which it was complementarily used with track 1. Since vegetation can occlude the bank face, if denser and more abundant, it could prevent the usage of the survey technique, in a similar way as high water levels do.

The results herein show that, in the absence of bank toe vegetation, a single oblique UAV track with eight photo overlaps and visible GCPs appears effective to survey banks with the highest precision and coverage, for the given sensor size and resolution, camera—object distance and lighting conditions. This number of photo overlaps agrees with the laboratory experiment of Micheletti et al. (2015), who found that above eight the mean error was only slightly decreased, in contrast to increasing overlaps within the range below eight. Nonetheless, they showed that overlaps higher than eight reduced the number of outliers, a trend which in this study is evident for less overlaps: test 1c (four overlaps) mainly differed from test 1b (eight overlaps) in a higher RMSE but not in the mean. This difference may arise from the distinct texture and complexity of each surface, which presumably requires different number of images for a similar performance (James and Robson, 2012; Westoby et al., 2012; Micheletti et al., 2015).

A RMSE of 2.8 cm to measure a riverbank with the photo combination of test 3 results in a relative precision with respect to the average camera—surface distance of 0.0007 or ~1:1400. This relative precision ratio is somewhat higher than ~1:1000 achieved by James and Robson (2012) for steep irregular features at kilometre scale in a volcanic crater and decametre scale in a coastal cliff, whereas the precision herein is somewhat lower than ~1:2000, which those authors proved at metre scale. More precise results could be possible using a bigger and higher-resolution sensor, flying closer to the bank, or even trying other oblique bank perspectives. However, this endeavour would only be reasonable if such data are needed for research purposes and if GCP positioning had also according higher precisions, since registration errors translate into the DSM accuracy during camera parameter optimization (Harwin and Lucieer, 2012; Javernick et al., 2014; Smith et al., 2014).

A precision of 10 cm has implications for the representation of small-scale features at bank scarps. Despite the presence of features in the order of decimetres, their accuracy could not be assessed given the discrete GPS points and the 0.5 m ALS grid used to assess the DSM precision. For instance, Figure 2.10a shows an upper bank scarp along the last four surveys that, if assumed unchanged, would indicate a maximum distance of 20 cm between surveys, which still would remain within the ±10cm error estimated by the GPS comparison. Although these differences could have been caused by weathering processes or growing grass on the bank face, potential sources of error at such scale could be given, for instance, by registration errors or occlusions caused by the surface roughness (Lague et al., 2013). Then, further research is needed to evaluate the precision at the roughness scale to, for example, analyse form drag at the bank face (Leyland et al., 2015).

The analysis made for test 3 on model rotation evidenced a linear trend with increased surface elevations on the floodplain side of the domain and decreased elevations on the main channel side (Figure 2.8b). This tendency was probably caused by a rotation of the DSM around co-linear GCPs that may lead to rotated solutions of the Helmert transformation (Carbonneau and Dietrich, 2017). Yet, the areal SfM-ALS comparison within ± 5 cm range (Figure 2.5b), did not evidence a clear axis along the whole domain that could suggest a rigid rotation of the DSM, since the ALS did have a constant mean accuracy across all surface types (Table 2.3). The linear rotation tendency, then, might have been obscured by the error range that was larger across the domain (Figure 2.4b and 10b) than the mean rotation magnitude, whose elevation difference between the extremes of the cross-sectional domain was 6 cm, and 4 cm within the bank area. Thus, other sources of error were also present that resulted in the obtained error range.

The comparative analysis of the DSM elevation errors from different photo combinations showed that the ground surfaces surveyed in the case study had different precisions. The grassland presented similar errors with a positive bias throughout all tests. The positive elevation differences are typical of vegetated surfaces (Westoby et al., 2012; Micheletti et al., 2015), whereas the similar performance of different photo combinations might be due to the presence of sufficient and well-distributed GCPs in this area (the floodplain). The terrace at the toe of the bank, in contrast, presented different error skewness throughout the tests, which affected the error distribution for all grounds. Interestingly, the error deviation of test 1 increased as the overlaps decreased, which in turn implies that more overlaps created more robust models. The linear errors cannot explain this behaviour because the same GCP locations were used for all tests, and only the camera parameters were optimized for each.

The error skewness at the terrace throughout the tests could be related to the fact that this area was the most distant from the GCPs and it was not surrounded by them, so that errors in lens distortion corrections could have especially increased here (James and Robson, 2014; Javernick et al., 2014; Smith et al., 2014). This effect was clear at the reach extremes (Figure 2.5), where the elevation differences increased with respect to the ALS survey further from the GCPs, for which it is called "dome" effect. While James and Robson (2014) showed that using different (convergent) camera angles is effective to mitigate the "dome" effect, the herein results showed that the DSM precision with eight photo overlaps along a single UAV track did not substantially improve by adding the extra perspective of track 2. This may imply that the chosen number of overlaps and used GCPs were sufficient to avoid distortions in the bank area that exceed the required accuracy, together with the fact the track had oblique and not nadiral perspective.

It is most likely that all the mentioned types of error were present in the SfM DSM, i.e. linear errors given by rotation (linear trend of errors across potential rotation plane; Figure 2.8b), non-linear errors given by the estimation of camera parameters (patches of higher or lower SfM elevations across the domain compared to ALS; Figure 2.5b), overestimation of ground elevation with grass cover (Table 2.2, Figure 2.5b, Figure 2.10a), and random errors given by the bundle adjustment that could not be assessed in this work. Although the adopted workflow was effective to measure bank erosion processes with the target accuracy, linear and non-linear errors could have been reduced, for instance, using a larger cross-sectional GCP distribution or better visible and bigger GCP targets. Other possibilities are also open, such as combining two oblique perspectives with a second angle better capturing the floodplain, GCPs, and bank area.

2.6.2. COMPARISON OF TWO REACH-SCALE TECHNIQUES: SFM AND ALS

The elevation bias at the bank between the SfM-based DSM and the ALS grid (Figure 2.6) was caused by the topographic overestimation of ALS (Table 2.3 and Figure 2.7). This ubiquitous error is ascribed to a known limitation of ALS systems related to the laser beam divergence angle, which locates the closest feature within the laser footprint at the centre of the footprint. This increases the ground elevation at high-slope areas (Bailly et al., 2012), which is the case for riverbanks. Still, the ALS resolution and precision were enough to identify bank slopes, in accordance with other studies (e.g. Tarolli et al., 2012; Ortuño et al., 2017). Furthermore, despite the ALS capability to estimate volume changes of eroded banks (Kessler et al., 2013), the method omits information related to the phases of the erosion cycle by not surveying erosion features smaller than its resolution (in this case, 0.5 m), apparent in contrast with SfM profiles (Figure 2.9). Moreover, if finer ALS resolutions are available, for instance, using higher

frequency lasers or working with the raw data, more ground details can be captured, but still vertical or undermined profiles would be missed.

The elevation differences between the methods observed for grassland (Figure 2.6b) were probably caused by dissimilar ground resolutions, because a larger elevation scatter is expected in the SfM-based DSM when capturing grass with 2 cm resolution, compared to the interpolated ALS samples into a 50 cm grid, even when derived from 0.16 m beam footprints. Nonetheless, the mean difference was zero (Table 2.3), so that both methods overestimate in the same way the real ground elevation due to grass cover. The effect of this is visible, for instance, in the increasing surface elevations on the floodplain over a year (Figure 2.10a), which happens after the mowing period in October. The terrace at the bank toe presented a similar scatter as grassland but had a small negative bias that could be explained by a DSM rotation or a slight transverse "dome" effect of the SfM DSM.

The distance covered by the SfM-UAV method depends on the flight autonomy. The deployed UAV had autonomy of approximately 25 minutes, which limited the maximum bank survey extent to approximately 2 km for the tested UAV height and speed, and camera resolution and shutter frequency. This practical limit will change with the progressive development of UAVs, but the distance covered by a single flight is currently significantly smaller than the one covered by ALS. Although a larger camera—object distance and speed than those used in this work would increase the surveyed area, decreasing the ground resolution and the UAV stability may result in the loss of sufficient detail to capture erosion features, and what is more, decrease the DSM precision that depends on the image scale (James and Robson, 2012; Micheletti et al., 2015). Therefore, further investigations would be required to explore the practical limits of UAV bank monitoring in views of extending the survey coverage.

2.6.3. UAV-SFM CHALLENGES TO MEASURE BANK EROSION PROCESSES

The use of UAV-SfM to measure bank erosion processes presents specific challenges, since bank areas usually have vertical surfaces and lengths can be much larger than the other two dimensions. Furthermore, the reach under analysis was particularly straight, introducing additional complexity to apply the technique.

Vertical surfaces

The bank presented steep, vertical and undermined surfaces that required an oblique camera perspective to adequately capture it, whereas GCPs needed sufficient visibility from this angle too. Logically, the visualization and accessibility of GCPs depend on where and how they are placed across the bank profile. In the herein proposed approach, GCP

targets were horizontally placed over the floodplain and close to the bankline, covering 20 m across the channel, which was convenient for a fast field campaign. However, GCPs were not placed at the bank toe or over the bank face, so a very limited vertical extent was covered (Figure 2.7-Figure 2.8), and the target area was not surrounded by GCPs along the three dimensions. Although a larger vertical range may be effective to reduce potential non-linear errors at the bank, the linear errors may not significantly be reduced with GCP at the toe, given the relatively short bank height (~3.5 m) and corresponding horizontal extent. In the case study, there were no clear non-linear effects at the bank area that could justify the placement of GCPs along the bank face.

The apparent cross-sectional extent of a GCP is proportional to the cosine of the viewing angle with respect to the normal of the plane in which the GCP lies (say δ), which increased the uncertainty to locate the target centre along the transverse direction, thus hindering the model georeferentiation when a single UAV track was used. On the other hand, targets were not always distorted in the longitudinal direction from oblique angles, i.e. when the camera was near the GCP cross-section, so horizontal errors were not as sensitive along the river axis as they were across the channel. Linear positioning errors in the transverse direction directly affect the accuracy to quantify erosion rates since this is based on the change of bank face positions over time. Moreover, the error introduced by a coarser resolution translated into elevation errors, and these directly affect rotational errors. On the other hand, the lateral view helped to compensate for this, since this elevation errors decreased with the cosine of δ

Linear domain

Banks, considered from the reach scale, are linear domains that extend along the river with the other two dimensions much shorter than their length. The choice of UAV tracks parallel to the river axis simplifies the mission setup and shortens the flying time too. However, this configuration does not provide additional stabilization to the DSM because it is closely aligned with the potential axis of rotation. The adopted approach relied on GCPs to georegister the DSM, which proved effective for the target accuracy. Since parallel UAV tracks tend to increase doming effects (James and Robson, 2014), GCPs were also important preventing excessive non-linear errors for the required accuracy. Figure 2.5b showed no significant DSM deformations within the GCPs, but increasing errors outside the GCP bounds, for which they need to be carefully distributed.

Recommendations

Although the adopted approach attained the required DSM accuracy, further refinement in the workflow could improve the model quality. First, it is advisable to use inclined targets perpendicular to the line of sight of the camera, placing them somewhat parallel

to the bank surface, to reduce linear errors as discussed above in the Subsection *Vertical surfaces*. This could be done, for example, with a back stand on rigid plaques (Figure 2.12). Second, utilizing two sets of GCPs is recommended, one set aligned close to the bankline and another set far away from it. For instance, if the first GCP line is 40 m from the UAV camera in the oblique direction (Figure 2.1b), the second line could be placed 51 m further inland from the first line to be 80 m from the UAV sensor (twice as far). The latter would need targets 4 times as big as those next to the bankline to linearly compensate for the decrease in the image resolution (although no linear trend was found between errors and sensor—object distance; Eltner et al., 2016), but these targets in turn could be spaced with double distance while keeping the same number of photo overlaps that capture them. In this example, the rotational error would decrease 2.5 times compared to the results presented here, given by the increase in the cross-sectional GCP footprint and considering similar elevation errors (from GPS and image identification).



Figure 2.12. Example of oblique plaque supported by a back stand.

In the proposed approach, GCPs were manually identified in the photographs based on three concentric geometries: the inner and outer circles of the CD reflective area and the tile perimeter. The errors introduced during the target identification affect the georeferentiation, and although errors may compensate if not systematically biased, their influence is higher with narrower cross-sectional GCP span due to the rotation tendency of elongated domains. This source of error can be reduced with wider GCP patterns as suggested above, but also through other improvements, such as

automated identification of GCP and Monte Carlo tests (James et al., 2017), to identify more accurately the GCPs and optimize the number of GCPs and minimize DSM errors.

The camera could be manually set to optimally capture the texture of the bank scarp. In this respect, GCP targets should ideally have a similar reflecting surface to project to the camera a similar amount of light for their later identification. A tilted target would also contribute to having similar reflecting conditions after comparable orientations to the bank with respect to the Sun. Furthermore, if the date of the survey campaign is flexible, then overcast but bright days are advisable whenever possible. This is to avoid overexposed or underexposed bank areas due to direct sunlight and shades that result in lower image textures within each of these zones and thus in a lower number of detected image features (James and Robson, 2012; Gómez-Gutierrez et al., 2014a). For example, note in Figure 2.11b that there were no textural differences due to shades but only due to the bank surface.

2.6.4. SURVEYING BANK EROSION WITH UAV-SFM AND OTHER TECHNIQUES

Sequential surveys allowed to capture different phases of the erosion cycle (Figure 2.10a), which demonstrates that quantitative detection of processes is feasible. Previous studies on bank erosion proved the capabilities of SfM for post-event analysis (Prosdocimi et al., 2015), e.g. representing block deposition, or for 2.5 D bank retreat quantification (Hamshaw et al., 2017), whereas herein all erosion phases were sequentially captured, demonstrating the 3D potentialities over the complete process of erosion. Of course, the ability to monitor banks at the process scale depends on the time interval with which the method can re-survey the exposed part of banks and will only cover pre- and post-flood conditions. The survey frequency and the duration of a full cycle of erosion determine the temporal resolution with which the development of processes is captured. Then, the bank retreat rate of each case determines the necessary frequency of surveys to capture erosion processes within a single cycle. Bank erosion rates naturally depend on each site, after different river sizes, hydraulic conditions, bank materials, etc. In the presented study site, erosion rates varied enormously (Figure 2.1), but still the performed eight surveys within a year successfully captured bank processes within a single erosion cycle in areas of fast retreat such as section 4.

The study site with a regulated water level and recently restored actively eroding banks was a perfect example for the application of this technique, because banks were exposed and erosion rates were compatible with the proposed average sampling frequency of 6 weeks. For other types of rivers, where erosion mainly occurs during floods when banks are not exposed, this method would allow measuring pre- and post-event conditions only. Given the high resolution achieved, the method is applicable to

all river sizes. However, with the accuracy of the adopted workflow, the application is only advised in cases where bank retreat is larger than approximately 30 cm between consecutive surveys.

Erosion processes happening at small spatial scales, such as weathering, would be hardly or not measurable with the precision achieved in this investigation. For this, other methods are already available, for instance, TLS and boat-based laser scanning, that provide higher precisions (millimetres before registration errors, e.g. O'Neal and Pizzuto, 2011) and comparable resolutions (centimetres, e.g. Heritage and Hetherington, 2007). In addition, close-range terrestrial photogrammetry can also offer the necessary precision for such endeavours, e.g., from a tripod (Leyland et al., 2015) or a pole on the near-bank area (Bird et al., 2010), at the expense of covering shorter bank lengths. Another alternative is erosion pins, which may also provide higher accuracies, yet with point resolution.

UAV-SfM appears a suitable survey method for both process identification and volume quantification in bank erosion studies, given the decimetre precision range with 3 cm RMSE and the 3D high resolution achieved with a low-cost UAV. As Resop and Hession (2010) suggested, high-resolution three-dimensional capabilities offer great possibilities when spatial variability of retreat is critical compared to traditional cross-profiling methods. In addition, the reduced deployment time of UAVs in the field is advantageous in relation to cross-profiling, while it also improves identification of complex bank features (Figure 2.9) and volume computations as other 3D high-resolution techniques (O'Neal and Pizzuto, 2011). Nonetheless, UAV-SfM requires longer post-processing times at the office, which should not be underestimated (Westoby et al., 2012; Passalacqua et al., 2015).

This technique remains less expensive than TLS or MLS, which is more convenient for cases where roughness is beyond the scale of interest, and target bank lengths are smaller than 3000 m. This would approximately be the longest distance for a single UAV flight in this case study. For longer reaches, MLS would then compete with UAV-SfM from a practical perspective, since more than one survey/flight would be needed. In all TLS, MLS and UAV-SfM would have limitations to survey the bank surface in presence of dense bank vegetation (Hamshaw et al., 2017). In these cases, ALS provides an alternative, albeit with significant lower resolution and higher costs (Slatton et al., 2007).

For large river extents, i.e. several kilometres, Grove et al. (2013) showed that process inference is possible combining ALS with high-resolution aerial photography, two techniques that are typically applied for eroded volume estimations and bank migration

(Khan and Islam, 2003; Lane et al., 2010; De Rose and Basher, 2011; Spiekermann et al., 2017). In that work, the scale of the river (banks higher than 6 m) allowed a spatial resolution of 1 m to capture features that together with photo inspection provided information on mass failure type and fluvial entrainment. To date, UAV-SfM covers smaller extents (Passalacqua et al., 2015), but provides much higher resolutions, allowing for process identification (such as undermining) and more precise volume computations (see Figure 2.9 for profile differences between ALS and SfM). For a similar (or higher) accuracy and resolution than those of UAV-SfM and large distances, boat-based laser scanning becomes an attractive, but more expensive, solution.

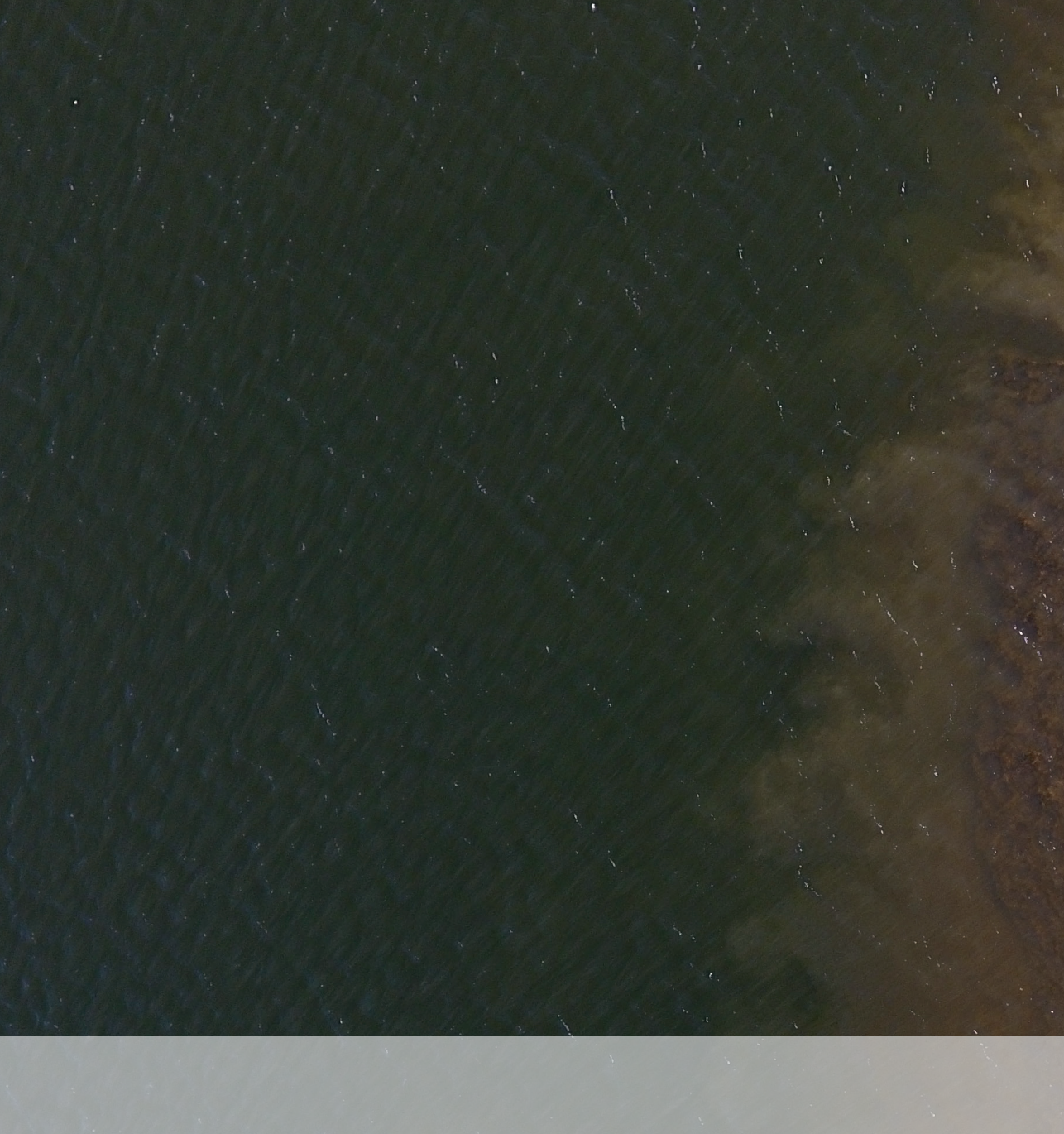
2.7. CONCLUSION

This chapter evaluated the capability of structure from motion photogrammetry applied with low-cost UAV imagery to monitor bank erosion processes along a river reach. The technique's precision was investigated by comparison with GPS points and airborne laser scanning. Vertical bank profiles were analysed to identify stages of erosion and infer processes. By means of a consumer-grade UAV, straight flight paths, and a standard SfM workflow, a sufficient accuracy and resolution was achieved to recognize and quantify the different phases of the bank erosion cycle from bank profiles. Further refinements to the workflow are possible which could reduce linear errors and increase accuracy.

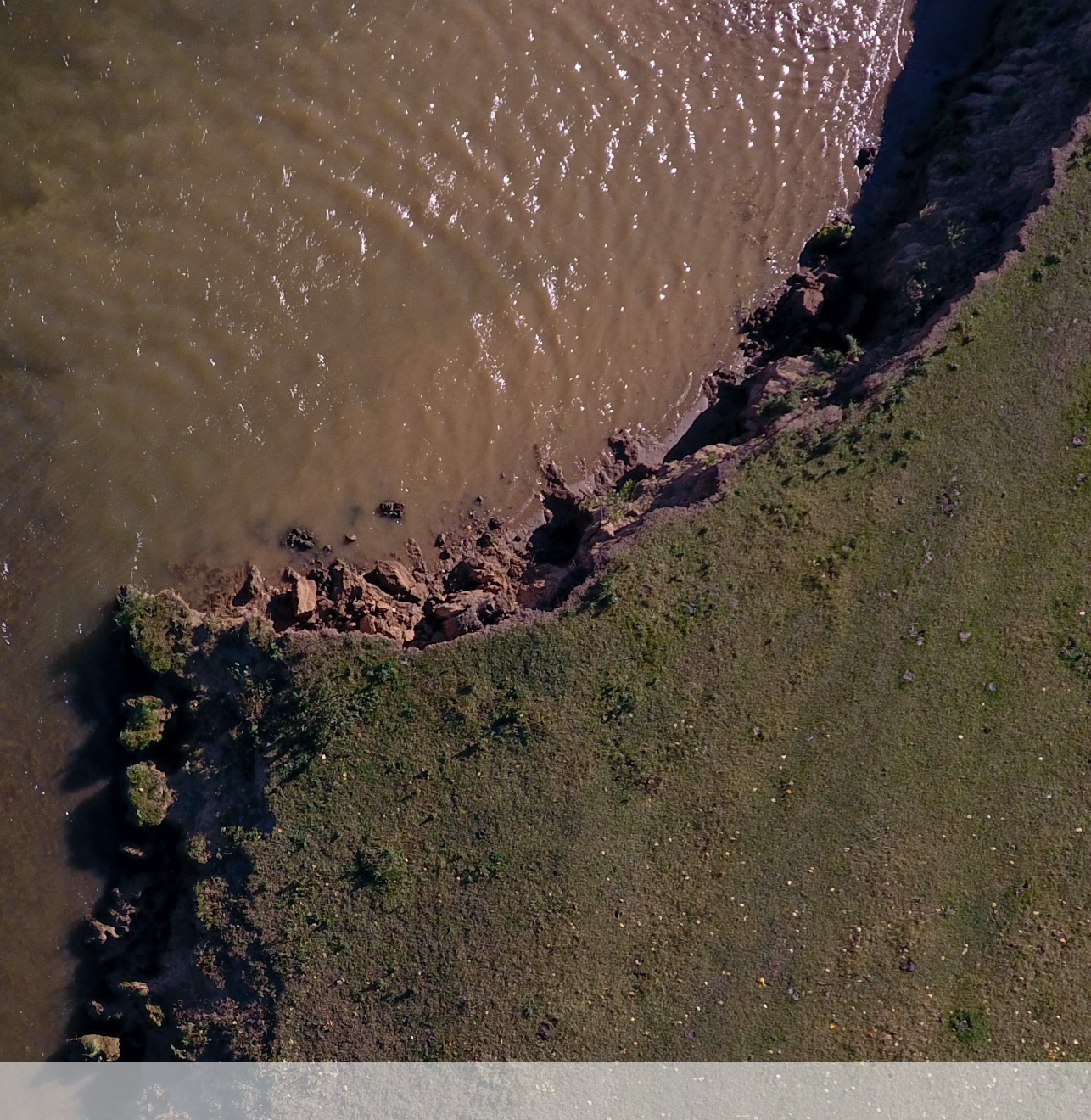
For the adopted approach, the accuracy of the DSM constructed with the SfM technique did not significantly increase with more than eight photo overlaps along a single oblique UAV track. The coverage of bank area behind bank toe vegetation, on the other hand, was increased by adding a vertically oriented perspective, albeit without a significant accuracy increase. As a result, banks were surveyed with 2 cm resolution and a 10 cm elevation precision, whose mean was 1 cm and standard deviation 3 cm (~1:1400 relative to camera—object distance, in line with previous SfM topographic applications). This accuracy was confirmed along the river reach with airborne laser scanning, although the latter overestimated elevations over bank slopes. Higher SfM errors were observed in areas beyond the extent of ground-control points, showing that control points should also be placed outside the monitoring reach and close to the bankline. Furthermore, the GCP distribution across the floodplain proved important in preventing model rotation along GCP axes, so a second line of GCPs located further inland is recommended together with proper targets, to reduce model errors as much as possible.

This investigation demonstrates the capabilities of a low-cost UAV to monitor banks at the process scale, while covering a mid-sized river reach of 1.2 km length in a single campaign. The combination of UAV and structure from motion photogrammetry can

provide relevant information of the spatial structure of bank erosion processes and, with sufficient frequency of acquisition, represent the temporal evolution of morphological processes within the erosion cycle. This method can also be used to compute eroded volumes throughout different phases of the cycle and analyse the contribution of each mechanism to overall retreat. The applied technique is most suitable when measuring bank lengths not exceeding 3000 m, and its flexibility, fast deployment, and high resolution are especially convenient for surveying highly irregular banks. While this method can survey the full cycle of erosion, and not only pre- and post-event conditions, its main limitations are dense riparian vegetation and high water levels, as for most survey techniques.



DISTINCT PATTERNS OF BANK EROSION IN A NAVIGABLE REGULATED RIVER



This chapter unravels the drivers of the bank erosion patterns that appeared along the Meuse River and provides insights on their contribution in regulated navigable rivers. The hypothesis is that ship waves, floods, trees and bank composition have different roles on the bankline pattern formation. The methods to analyse each factor and disentangle the dominant ones include measured river data, aerial photographs, soil tests, field observations, historical maps, and UAV-SfM bank topography. An extraordinary low-water-level event generated by a ship accident provided the unique opportunity to thoroughly analyse the subaqueous bank topography.

The contents of this chapter are published in *Earth Surface Processes and Landforms 45* (2020) under the title: "Distinct patterns of bank erosion in a navigable regulated river". Authors: Duró, G., Crosato, A., Kleinhans, M. G., Winkels, T. G., Woolderink, H. A., and Uijttewaal, W. S. J.

3.1. INTRODUCTION

Ten years after the first reaches were exposed to bank erosion, the new channel margin appears non-uniform at several locations, where it is often characterized by the presence of oblique embayments. In particular, two reaches near the city of Gennep present either deep embayments (Figure 3.1) or uniform bank alignment. By analysing sequential airborne laser scanning, Duró et al. (2018a) showed that the sediment yield varied greatly in these reaches due to wide-ranging erosion rates, and that the erosion patterns formed above a terrace or bench, consisting of a flat surface with elevation close to the minimum water level. Yet, the factors determining the terrace and observed patterns of erosion remain unknown.

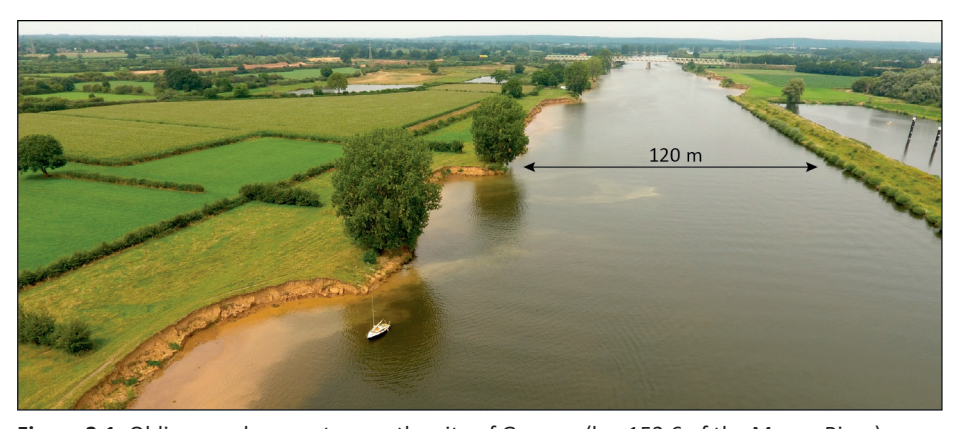


Figure 3.1. Oblique embayments near the city of Gennep (km 153.6 of the Meuse River).

Heterogeneous bankline patterns occur at different spatial scales. At the scale of the channel depth, irregularities appear due to mass failures and slumping, leaving irregular sediment deposits at the bank toe (Darby et al., 2010), or due to roots that create and support protrusions (Rutherfurd and Grove, 2004). These features are typically associated with variations in bank roughness (Kean and Smith, 2006, Darby et al., 2010). At the bend or bar scale, banklines are curved, sometimes sharply, associated to bar and bend dynamics (Klösch et al., 2015; Thorne et al., 1993) and secondary flow (Kleinhans et al., 2009; Ottevanger et al., 2012). Bank irregularities at an intermediate scale are not common, and none of the mentioned physical processes can explain their formation. Finally, embayments of similar size to those in the Meuse River appeared in the Mekong River (Hackney et al., 2015), but the size of the latter is substantially larger than the former.

The causes of the erosion patterns observed along the Meuse River are not easily discernible. Tree roots typically delay erosion by increasing the resistance against bank instability (Pollen and Simon, 2005; Wiel and Darby, 2007) and by reducing effective

shear stresses over the soil when protruding in the flow (Khanal and Fox, 2017). However, not all embayments are delimited by trees. Ship-induced waves exert oblique loads onto banks (CIRIA et al., 2007), but the directions of embayment evolution are not consistent with ship movements. Composition and stratification of riverbanks do affect erosion rates and bank failure (Thorne and Tovey, 1981; Parker et al., 2008), whose variabilities are also found along single meander bends (Konsoer et al., 2016b). Yet, no evidence of longitudinal changes of soil compositions have been reported to create oblique embayments. The formation of a terrace abutting banks in rivers used as waterways has been reported (e.g., Bonham, 1983; Nanson et al., 1994; Liedermann et al., 2014; Murray–Darling Basin Authority, 2017), but the contribution of ship waves to erosion is usually unclear due to other factors that may play a role, such as floods (De Roo and Troch, 2015), sapping (Hagerty et al., 1995; Van Balen et al., 2008), or wind waves (Houser, 2010). This is partially due to the difficulties to quantify small amounts of erosion produced by single ship passings (Bauer et al., 2002), for which prolonged monitoring of erosion is necessary for accurate yet cumulative measurements.

The objectives of this chapter are to unravel the drivers of the bank erosion patterns that have appeared along the Meuse River and to provide insights on their contribution in regulated navigable rivers. The hypothesis is that ship waves, floods, trees and bank composition have different roles on the formation of the bankline patterns, and thus each factor is analysed to disentangle the dominant ones. This chapter analyses and integrates field measurements of flow, ship waves, bank composition, bed topography and historical maps to explain the observed patterns along two reaches of the river. Particularly, the low-water-level event generated by a ship accident is used to analyse the subaqueous bank topography in detail.

3.2. STUDY SITES AND EROSION PATTERNS

The Meuse River is characterized by a pluvial regime with peak flows in winter/spring reaching 3100 m³/s, and discharges during summer/autumn as low as 40 m³/s (Descy et al., 2009). In the past, the Meuse used to meander across its floodplains (Woolderink et al., 2019). The river was trained during 1940s to 1960s to facilitate navigation and increase water conveyance. Poplar trees were planted every one hundred metres along the banks to guide ships during overbank flow conditions. The main channel was then canalized with a regular cross section (120 m wide, 1:2.5 bank slope), bends were cut off, and several weirs with ship locks were constructed (e.g., Sambeek is visible in Figure 3.2a). The relatively recent restoration removed several of those rip-rap revetments and transverse groynes, to promote natural processes and riverine habitat diversity.

The study reaches are located near the city of Gennep (Figure 3.2), the Netherlands, where the current riverbed is composed by sand and gravel and the floodplains are covered by grassland and by agricultural fields further away from the main channel (Figure 3.1). On both sites, the protection works were removed only along the left bank (Figure 3.2). Reach A was restored in two stages, first in 2008 along 750 meters and then in 2010 over the upstream 250 m. Reach B extends over 1.2 km downstream of reach A and was restored in 2010. The bankfull depth at both sites ranges between 10 and 11 metres, with minimum regulated depths of c. 7 m.

Since the restoration works, banks retreated in both reaches at wide-ranging rates, resulting in distinct erosion patterns (Figure 3.2b-e). Notably, the largest embayments along each reach had either consistent upstream or downstream asymmetrical orientations. Some bank stretches presented a rather uniform bankline and others show symmetrical embayments with somewhat smaller dimensions than the asymmetric ones. All stretches evolved forming either parallel banks or embayments over the years. In addition, a bench at the bank toe was present all along these reaches, showing that the bank retreat mainly occurred above the terrace level (Duró et al., 2018a,b).



Figure 3.2. Bankline evolution of restored reaches presenting uniform retreat and embayments with different asymmetry. (a) Location of reaches. (b-c) Reach A at Noordereiland. (d-e) Reach B near Oeffelt and Gennep.

3.3. METHODS

The role of factors which could produce the observed bankline patterns were examined through analyses of available data. The capability of flow and ship waves to produce a load distribution that could match the observed bank retreat patterns over the years was first studied. Then, the bank strength was analysed through its composition, at a local scale with deep cores and a larger scale with surface samples, and considering also the presence of trees. The mechanisms of upper-bank erosion were examined in detail over a year, in addition to past river dynamics, in order to infer processes related to lithological characteristics. Finally, the contribution of other factors was considered, such as groundwater sapping erosion, cattle and rainfall-induced erosion.

The causes of bank patterns were inferred (Kleinhans et al., 2010) distinguishing between initial conditions, such as inherited geology or planted trees, and mechanisms, such as rain- or ship-driven, spatially-varying erodibility. The role of currents, ship waves and bank composition were analysed through field data of reach B, which are described in detail in the following subsections. The channel migration in the last period preceding canalization was studied through historical maps and recent aerial photos. The influence of trees, sapping, cattle and rainfall was evaluated based on field observations along both study reaches.

The data used for the analysis came from three different sources. First, the Dutch Ministry of Transport, Water Management and Public Works (Rijkswaterstaat) provided measured and validated time series of discharge at Venlo and of water levels at Gennep and Sambeek, the river bathymetry and yearly aerial photographs. Second, the terrace and upper-bank topographies were surveyed, ship-induced waves measured, soil samples collected and analysed, deep cores in the floodplain performed, and photographs and videos taken from the field sites. Third, the National Archive of the Netherlands made available historical maps where the case studies are located, which was facilitated by courtesy of Rijkswaterstaat. All elevations in this work refer to NAP (Dutch reference sea level).

3.3.1. MECHANISMS FOR EROSION

A cross-analysis was conducted of i) discharge and water level series and ii) the timing and magnitude of average current-induced bed shear stresses, at a location with active erosion and relatively large bank retreat. For that, the channel cross section at km 153.940 of reach B (Figure 3.2a) was taken as reference, due to the relatively high erosion rates during 2017. The average bed shear stress was calculated as

$$\tau_b = \rho g h S_0 \tag{3.1}$$

assuming hydraulic radius equal to average water depth (h) since width/depth > 10, with ρ =water density (kg/m³), g=gravity acceleration (m/s²), S_o =average energy slope. Energy slopes and water depths were computed based on a linear interpolation between the two nearest known water stages.

An acoustic Doppler velocimeter (ADV) placed at km 154.0, before the beginning of the terrace measured water levels for a period of three weeks, with a frequency of 8 Hz to capture short waves. Typical wave characteristics were identified, such as period and height of both primary and secondary waves. Observations were made of the generation, propagation and breaking of ship waves across the channel and over the terrace in reach B during several field visits, and analysed their relation with the

morphological features of the bank area. In order to compare the order of magnitude of current- and ship-induced shear stresses, wave-induced bed shear stresses at the start of the terrace were estimated with the linear-wave theory and Jonsson's (1966) concept of wave friction factor f_{ω} , as explained next.

The maximum bed shear stress induced by secondary waves using the friction factor results in

$$\tau_b = \frac{1}{2} \rho f_w u^2 \tag{3.2}$$

with u=velocity amplitude near the bed (m/s). The amplitude of the near-bed velocity is

$$u = \omega \frac{H}{2\sinh(kh)} \tag{3.3}$$

with ω =angular frequency= $2\pi/T$ (1/s), T=wave period (s), H=wave height (m), k=wavenumber= $2\pi/L$ (1/m). The wave length L (m) is obtained through the dispersion relationship

$$L = \frac{gT}{2\pi} \tanh(kh) \tag{3.4}$$

The friction factor as expressed by Swart (1974) reads

$$f_w = e^{-5.977 + 5.213(\zeta/r)^{-0.194}}$$
(3.5)

with a threshold of 0.3 when (ξ/r) < 1.59; ξ is the particle displacement equal to $\xi = U_0/(2\pi/T_0)$; r is the bed roughness taken as 2 cm for the Meuse to account for bottom irregularities.

The upper bank topography was measured using an unmanned aerial vehicle in combination with structure from motion photogrammetry (Westoby et al., 2012; Clapuyt et al., 2016), following the methodology of Duró et al. (2018b) to measure riverbanks. This methodology was applied in nine surveys along 2017. A DJI Phantom 4 was used, with 18 ground control points to georeference the model and Agisoft PhotoScan to process the imagery. The resulting digital surface model achieved a resolution of 2 cm and a root-mean square error of 3 cm by comparison with RTK GPS points.

3.3.2. FACTORS AFFECTING BANK RESISTANCE

The subaqueous topography was measured down to 2.5 m below the minimum stage and seven surface samples were taken along reach B (Figure 3.2) on 18^{th} January 2017. Following the studies of Kimiaghalam et al. (2016), cohesion (Co) was used as an indication of the material erodibility to make a hierarchy of erosion resistance between different areas. Then, critical shear stresses for entrainment (τ_c) were estimated through the linear relation

$$\tau_c = 0.89Co - 0.1 \tag{3.6}$$

with units of Pa for τ_c and kPa for Co.

The digital topography of the terrace was used to identify lithological layers along the reach and measure their ridges, which were validated through observations in the field. The stratum ridges that presented varying elevations were not included in the analysis because their superficial appearance might be shaped by erosion, not corresponding to actual stratum strikes and dips. Those banklines at large embayments that have asymmetrical orientations with respect to the channel axis were also marked.

Furthermore, stratum dips were also computed by the theory of Struiksma et al. (1985) adapted by Talmon et al. (1995), similarly to van de Lageweg et al. (2014). The prediction of the dip for lateral accreting deposits in an infinitively long bend reads:

$$\tan \frac{\delta z}{\delta n} = 9 \left(\frac{D_{50}}{h}\right)^{0.3} \sqrt{\theta} \frac{2}{\kappa^2} \left(1 - \frac{\sqrt{g}}{\kappa C}\right) \frac{h}{R}$$
 (3.7)

where z=bed elevation, n =transverse direction in a curvilinear channel for damped conditions, $\theta = \tau/((\rho_s - \rho)gD)$ Shields mobility parameter, κ =von Karman's constant, C=Chézy coefficient (m $^{0.5}$ /s) calculated as 18*log(12h/D $_{90}$), and R=bend radius of curvature (m).

The material at the terrace surface was analysed at 7 locations, chosen to cover areas of different erosion magnitudes, from the least to the most retreated banks (see later Figure 3.4). Coring was done with a 15 cm-long cylinder and after removing the top 10 cm. All surface samples were subjected to direct shear tests to derive the internal friction angle and cohesion of the soil by least-squares linear regression over a range of normal loads of 17, 36 and 73 Pa and shear rates of 0.01 mm/sec. Later, all samples were dried in the oven at 105° C and mechanically sieved and weighed to obtain the particle-size distribution. For all fractions smaller than 63 κ m the granulometric curves were extended to 2 κ m by hydrometer analyses to distinguish silt from clay fractions,

measuring relative density changes of water as the mud settles. All test were done according to the standard: BS 1377-2:1990.

In total three deep corings were performed near locations were both minimal and large bank retreat has occurred (Figure 3.4). Borehole levels were measured using a RTK GPS. In total two different coring techniques were used to retrieve sediments namely i) Edelman corer (above groundwater levels) and ii) Van der Staay suction corer (below groundwater levels). Sediments were logged in the field at a 10 cm interval in terms of lithology (USDA classification) and other sedimentary characteristics (Berendsen, 1982).

The river dynamics during the last years of free migration were analysed through two historical maps that indicate positions of the main channel prior to the canalization. A map from the preliminary project for the Meuse River canalization (Nederlandsch-Belgische Commissie, 1912) was used, which also indicates the extent of a large flood that occurred during 1880. A second map was also considered, dating from 1950 and belonging to a series of national river surveys (Netherlands Nationaal Archief, 1952). Both maps were georeferenced in ArcGIS with several landmarks that served as fixed points in time, such as churches, roads, and bridge piles. The channel banklines were then digitized at all distinguishable angle changes.

3.4. RESULTS

3.4.1. CURRENTS

Both study sites are rather straight and submerged bars are absent in the channel, meaning that bend flows are negligible (Papanicolaou et al., 2007). The pluvial regime of the river is evident in Figure 3.3a through the winter/spring peak flows that stand out over the summer/autumn low discharges. Since 1940s, water levels have been strongly regulated to ensure navigability, which results in regular and extended periods of rather constant stages during low discharges. As a consequence, bed shear stresses become significant only during floods, i.e. for a relative short time during the year. Therefore, current-induced shear stresses at the bank are expected to have similar durations but lower magnitudes, as for instance, 60-80% of the bed shear stress (ASCE, 1998).

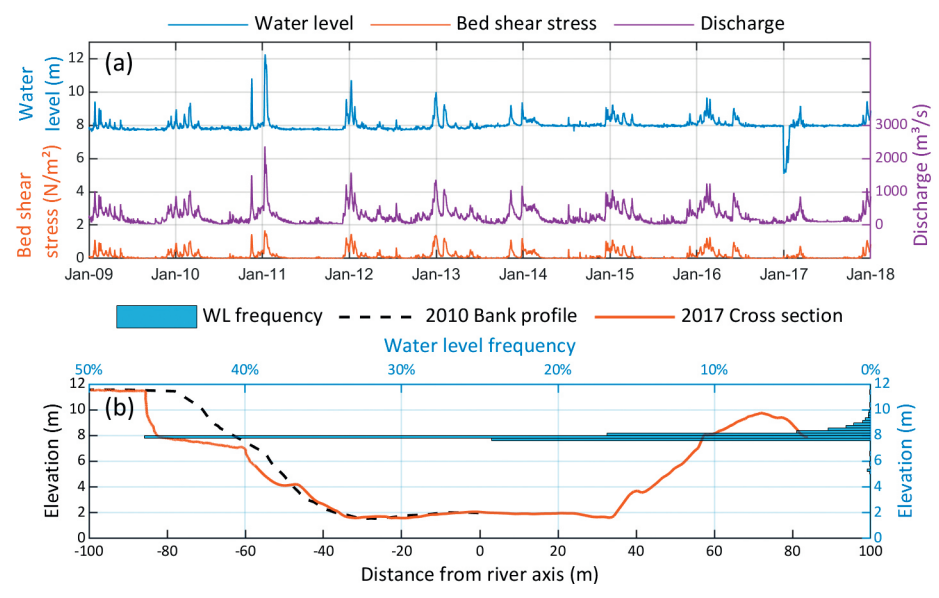


Figure 3.3. (a) Discharge, water level and bed shear stress in the period 2009-2017. (b) Water level frequency distribution over the same period, bank profile of mid-2010 and cross-section of January 2017 at km 153.940. Note vertical distortion of cross section.

Figure 3.3b presents the river a cross section located in the longest embayment of reach B. The left bank had the rip-rap protections removed in 2010. At that time, the bank profile had a 1:2.5 slope from the toe up to the floodplain level. Currently, the bank presents a terrace at an elevation of 7.0-8.0 m that extends over 20 m inland, before encountering a 3.5 m bank scarp. The submerged part of the bank presents a c. 3 m high notch that was dredged in 2012 for ship manoeuvring, whose remains partially rest at the toe. The right bank is still protected by rip-rap and belongs to a breakwater that divides the main channel from the harbour (Figure 3.2a).

The water level frequencies in the period 2009-2017 are plotted on the right axis of Figure 3.3b, overlaying the river cross section. For more than 70% of the time, the water level fluctuated within a range of 0.50 m, which coincides with the elevation range of the terrace (7.5-8.0 m). The terrace extends over the entire reach and defines the toe of the bank scarps. The bankline patterns visible in Figure 3.1 and Figure 3.2 formed above this bench. Water level frequencies also show that overbank flows rarely occurred in 7 years. Since 2009, the floodplains were inundated only at the peak of the largest flood event in January 2011 (Figure 3.3a).

3.4.2. SHIP WAVES

Navigation in the study reaches, located between Sambeek and Grave ship locks, accounts for about 35,000 passings of commercial vessels and recreational boats every year. The water level measurements indicate that primary waves have periods ranging from 25 to 65 seconds and amplitudes up to 0.45 m. Secondary waves have shorter periods, namely 1.25 to 3 seconds, with typical values of 2.25 seconds and amplitudes of 0.10 m. The maximum recorded amplitude of secondary waves was 0.45 m. According to linear wave theory, the low but frequent waves with height of 10 cm and period of 2 seconds induce a maximum bed shear stress of approximately 0.6 Pa through orbital velocities. As water stage is highly controlled (Figure 3.3b), the generated waves mostly impact banks at a narrow range of elevations.

3.4.3. LITHOLOGICAL SUCCESSION AND STRATIFICATION

The topography of the terrace has a mild slope towards the lower bank and presents stratification at certain locations, exposed after the erosion of the bank material above (Figure 3.4). A downstream view from km 153.950 clearly shows the stratification (Figure 3.5a). Here, the sedimentary layers crop out as minor scarps and form an angle of 12 degrees with the main channel axis, similar to the orientation of the bankline next to it. At other embayments, the layer orientation is more similar to those of the banklines (see dashed lines in Figure 3.4c), lying approximately parallel to each other. Ridges in Figure 3.5a are more irregular in the background, probably due to the longer time this area was exposed to erosion.

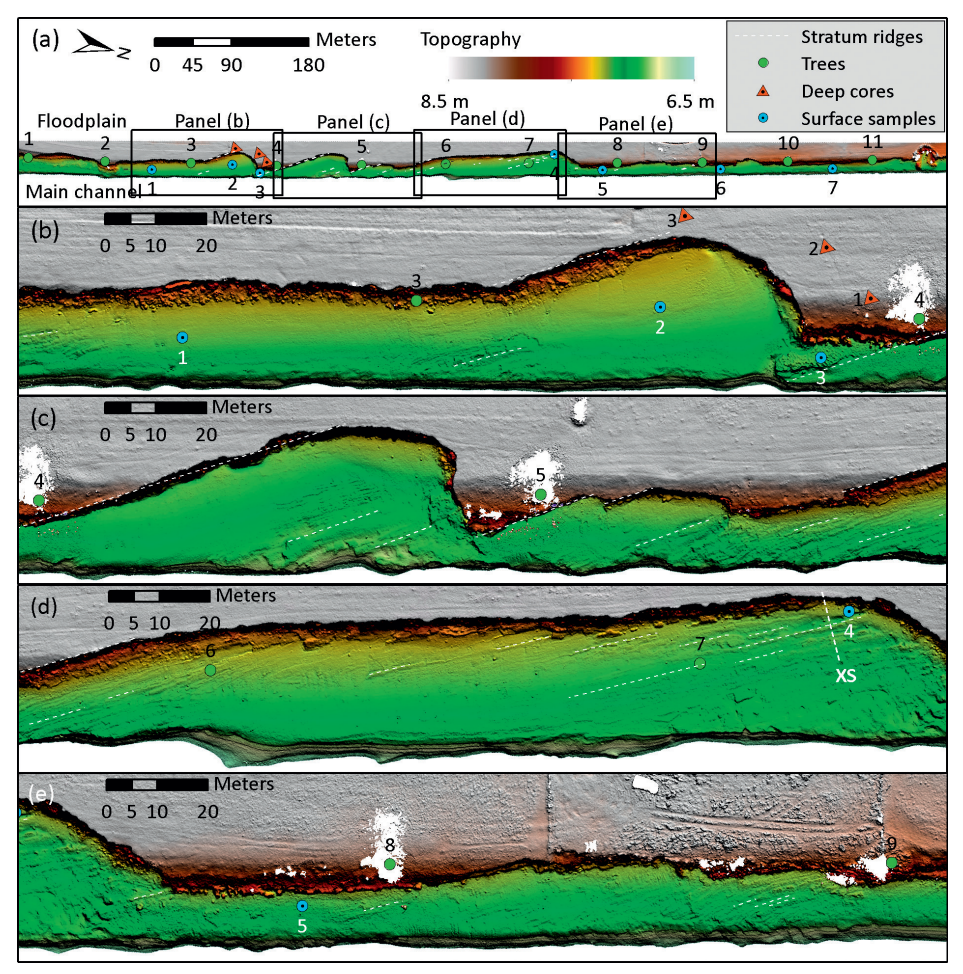


Figure 3.4. Topography of terrace evidencing stratification of the subsurface.

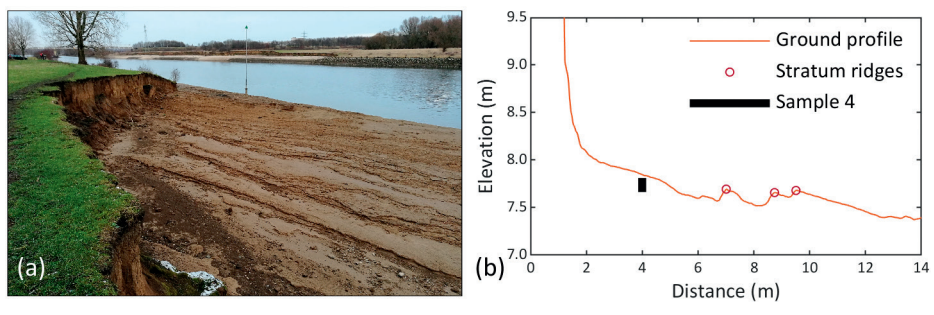


Figure 3.5. (a) Stratification visible on terrace from km 153.950. (b) Measured strata and ridges close to upper-bank toe at km 153.975 (see XS in Figure 3.4d), where Sample 4 is projected (note factor 4 vertical distortion).

Figure 3.5b presents an elevation profile of the terrace across layer strikes where some of the strata in Figure 3.5a are recognizable. In this profile, the strata are inclined by 5 degrees with respect to the horizontal plane. The predicted dip based on Struiksma et al. (1985) ranges between 4 and 6 degrees, in agreement with the measured one. This range considers a constant water depth of 8 m, a Chézy coefficient of 59 m^{0.5}/s with D₉₀=0.05m, and a variation of the Shields parameter between 0.7 and 1.8. The θ range results from either considering τ =1 Pa and D₅₀=0.09 mm or τ =2 Pa and D₅₀=0.07 mm, which account for possible values of shear stresses during high flows and mean particle size of soil samples (see next).

The samples along reach B present wide-ranging compositions at the terrace level. Clay contents range from 8% to 25% and silt from 23% to 75%, thus sand content is also diverse, ranging from 9% to 68% (Table 3.1). Such heterogeneity in grainsize results in different textures according to the USDA soil classification. Samples 1, 2 and 4 are sandy loams, 3 is a loam, and 5-7 are silty loams. In addition, critical shear stresses for entrainment, which are linearly related to cohesion, follow a trend with the texture classes. Sandy loams present lower critical shear stresses than silty loams and loams.

The location of samples with the highest cohesion, and thus highest critical shear stresses, correspond to the least retreated banks. Sample 3 is located between deep embayments (Figure 3.4b) and belongs to a protruding but submerged soil layer, higher than the surrounding terrace elevation. Samples 5, 6 and 7 belong to the uniform stretch of reach B (Figure 3.4a). These four samples have Co > 14 kPa and $\tau_c > 12$ Pa. Samples 2 and 4 belong to deep embayments, and sample 1 to an area with intermediate retreat. These samples have $Co \le 13$ kPa and $\tau_c \le 11$ Pa, corresponding to the lowest range of the sampled materials. Consequently, there is a reasonable correlation between relative erosion rates at key areas of reach B and the compositions of the different layers at the terrace level, especially regarding their cohesion.

Table 3.1. Properties of surface samples and corresponding bank retreats in 2017.

Sample number	1	2	3	4	5	6	7	8
Location (km)	153.5	153.6	153.627	153.975	154.025	154.175	154.3	154.1
Elevation (m)	7.62	7.69	7.50	7.74	7.53	7.39	7.36	8.03
% Sand	60.6	68.5	37.9	55.0	9.7	15.1	14.7	10.8
% Silt	29.2	23.1	45.3	34.9	75.6	66.1	60.1	63.2
% Clay	10.2	8.4	16.8	10.1	14.7	18.9	25.2	25.9
Cohesion (kPa)	12.43	7.33	20.92	9.87	19.6	14.29	14.04	13.4
Friction angle (°)	24.6	34.9	19.5	29.9	22.1	16.3	13.7	22.8
USDA soil class	SaLo [†]	SaLo	Lo [‡]	SaLo	SiLo§	SiLo	SiLo	SiLo
$ au_{_{ m c}}$ (Pa)	11.0	6.4	18.5	8.7	17.3	12.6	12.4	13.4
Bank retreat (m)	18.5	27.7	6.7	23.5	3.2	4.5	3.5	8.3

[†]Sandy loam, [‡]Loam, [§]Silt loam

The lithology around the embayment of Figure 3.4b also presents varying classes throughout the floodplain depth (Figure 3.6). The upstream core located next to the oblique bankline, number 3, mostly displays silty-clay loam from the bank top down to 9.0 m. The next 2 metres are mainly composed by loam. From 7.0 m down to 5.3 m, there is a mixture of loam and sand layers. Below 5.3 m, the core shows sand with some gravel contents. Core 2, located in the direction of the embayment evolution (Figure 3.2d and Figure 3.5b), presents variations between silty loam and silty-clay loam down to 9.0 m, followed by a loam layer of 0.5 m. Then, from 8.5 m down to 6.2 m, there are several sediment layers ranging from sand to loam. Deeper than 6.2 m, the lithology is mainly sand with some traces of gravel. Core 1, located near tree 4 and the least retreated bank area, has a mixture of silty loam and silty-clay loam at the top bank down to 8.5 m. The following 2 metres display loam and sandy loam layers, the former having traces of organic matter. From 6.5 m down to 5.4 m, the main composition is loam, presenting some variations within thinner layers and traces of organic matter. Below 5.4 m, sand is ubiquitous with the exception of thin loam layers and traces of gravel.

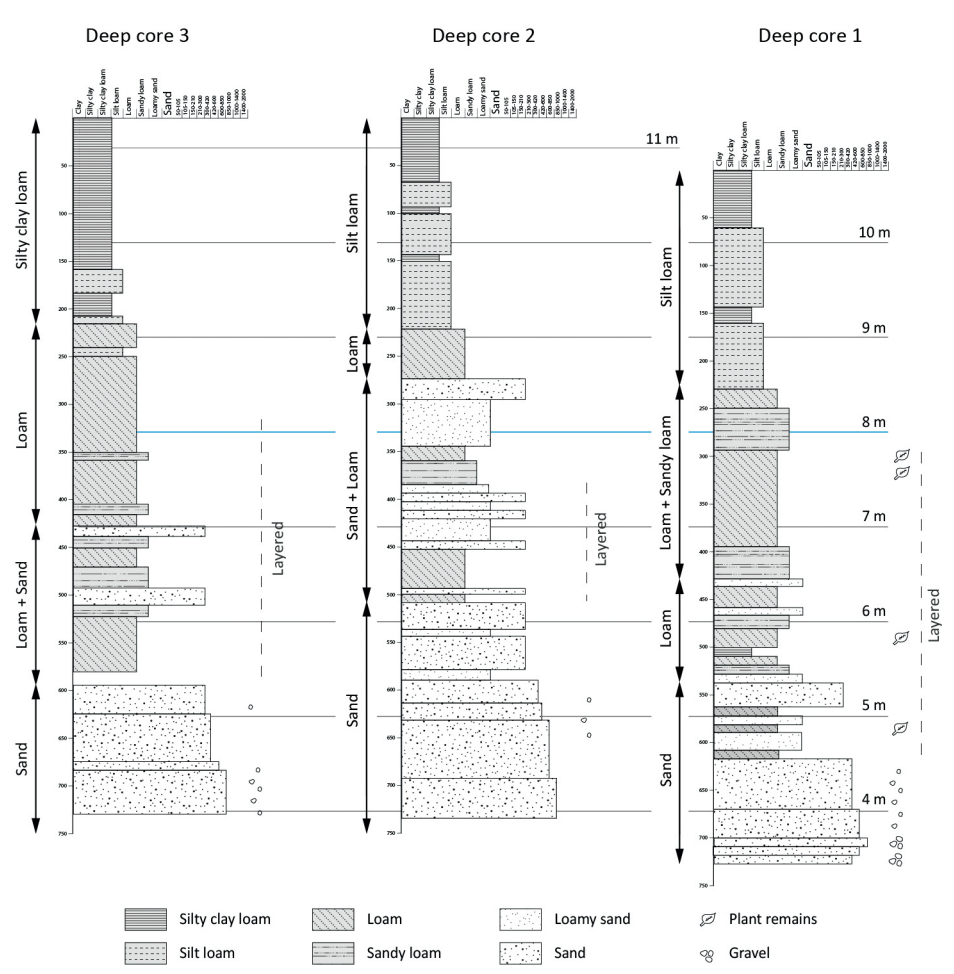


Figure 3.6. Stratigraphy of the deep cores (see Figure 3.4b for location) with references to dominant classes.

3.4.4. UPPER-BANK EROSION

Between February and November of 2017, bank erosion at km 153.940 progressed uninterruptedly (Figure 3.7). Between the first two surveys there was a flood event having a duration of two weeks (Figure 3.3a) that raised the water level up to 9 m. During the rest of the time, the water level remained at 8 m.

The difference between the first two topographic surveys show erosion throughout almost the whole bank height. From March 15 to April 26, only toe erosion occurred. Afterwards, a mass failure happened. Subsequently, from June 8 until August 23, slump blocks and the toe progressively eroded, reaching an incipient undermining of the bank.

Between August 23 and October 11, the bankline retreated and the wasted material was removed. The last survey on November 23 shows minor toe erosion.

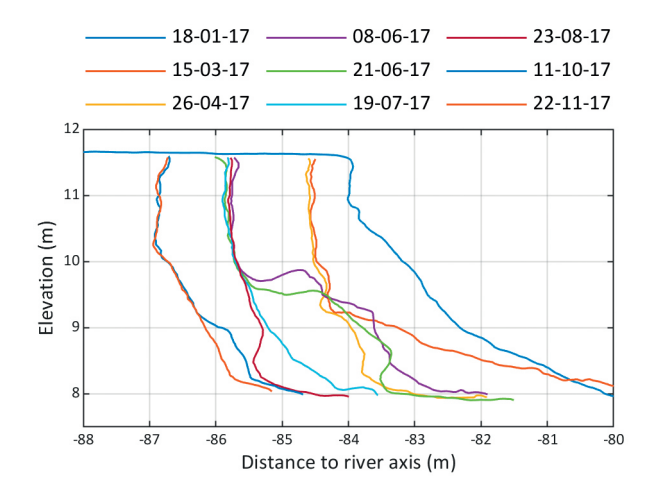


Figure 3.7. Upper-bank profiles at KM 153.940 over 2017.

3.5. INTERPRETATION OF RESULTS

3.5.1. CURRENTS

The flow structure in the near-bank area is complex and three-dimensional (Rhodes and Knight, 1994; Blanckaert et al., 2010), particularly at the sharp expansions of embayments. Here, the boundary layer could detach (Simpson, 1989), triggering a different type of erosion mechanism, as scour holes in river beds develop due to turbulent mixing layers (Hoffmans and Booij, 1993). Similarly, embayments could grow in the horizontal plane from initial bank irregularities due to recirculating flow (Hackney et al., 2015).

Since 2009 floods occurred over relatively short periods, with water levels below bankfull. The mechanism of vortex shedding within an embayment needs to act at different spatial scales to produce the erosion patterns, from initial stages of bankline retreat until full development of the embayments (Figure 3.2). Yet, this hypothesis neither explains different directions in embayment evolution nor the formation of the patterns only above the terrace level. Furthermore, flow-induced bed shear stresses at peak discharges are lower than the critical shear stresses of all soil samples (6.4-18.5 Pa). Hence, the contribution of currents to embayment growth and terrace formation was likely minor.

3.5.2. SHIP WAVES

The estimated bed shear stress induced by propagating secondary waves of average height is smaller than the flow-induced bed shear stress at peaks (0.6 versus 2.0 Pa), but occurs much more frequently. However, the assumption of linear wave theory leads to underestimated shear stress, because ship waves are steep and shear stresses exceed soil entrainment thresholds. The latter is indicated by the plumes of suspended sediments that originate from the banks during low flows (Figure 3.1). Therefore, waves explain the gradual terrace advance during low flows (Figure 3.7).

Moreover, the planform evolution of the restored banks presents four characteristic types of bank retreat that could be related to the load distribution exerted by ship waves. Banks retreat a) parallel to the channel centreline (e.g., between trees 4-5, Figure 3.2b, or trees 10-11, Figure 3.2e); b) creating embayments that grow without a clear trend towards neither upstream nor downstream (between trees 3-4, Figure 3.2b, or trees 9-10, Figure 3.2e); c) creating embayments that evolve asymmetrically towards either upstream or downstream (those with arrows in Figure 3.2b-e); d) creating embayments that evolve asymmetrically and with a certain degree of irregularity (between trees 4-5, Figure 3.11d). All these types are schematized in respective panels of Figure 3.8.

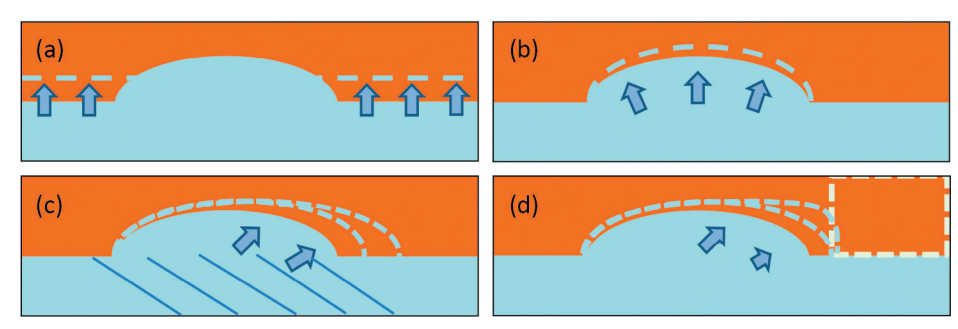


Figure 3.8. Types of bank retreat observed in the case studies. (a) Uniform retreat besides initial perturbation. (b) Symmetric embayment growth. (c) Asymmetric embayment growth. (d) Irregular asymmetric embayment growth.

Considering that ship waves dissipate over the distance as they propagate, the longer they travel the lower energy they carry. In addition, a terrace with shallow water creates higher resistance for wave advance than deeper areas, especially if waves break. These considerations promote faster bank erosion at least retreated areas (Figure 3.8a) than inside the embayments (Figure 3.8b), where longer and shallower areas are present and waves refract and diffract lowering the specific energy. Yet, this contradicts the greater bank erosion rates observed at embayments compared to uniformly retreated stretches (see bankline evolution after two years of restoration, Figure 3.2b-d), which

is coherent with the evidence of active erosion at the embayment presented in Figure 3.7 after six years of restoration.

At the terrace and in the presence bay-shaped banklines, waves refract or diffract before they break. Sharp and smooth bankline changes influence wave propagation and in turn bank retreat, which may result in non-linear interactions affecting bay formation. Once an initial perturbation grows into an embayment, asymmetric evolution (Figure 3.8c) can be related to primary and secondary waves. Deep primary waves create strong localized currents along sharp bankline changes at embayment extremes, acting like bores and locally increasing the load due to momentum change along their path.

In addition, secondary waves may enhance bays at extremes since here they approach banks at approximately right angles (see Figure 3.8c). The asymmetric evolution could thus be caused by a higher number of loaded ships in one direction (e.g., downstream) due to higher waves impacting a given bay extreme. However, this cannot explain different evolution directions of the embayments in reaches A and B, both located on the left riverbank.

The last type of bank evolution (Figure 3.8d) presents a change in the rounded shape of embayments that results in sharp bankline change. This particular morphology does not follow the typical evolution of other embayments, for which it can be related to local conditions (dashed box in Figure 3.8d). These are elaborated in the next sections, including strong root systems (Figure 3.2d, tree 5) or low erodible sediment layers. To conclude, ship-induced waves are incapable of a explaining the different bankline retreat modes in a comprehensive way, despite concentrated loads at embayment extremes may promote their growth.

3.5.3. TREES

Root growth in fluvial environments is mostly dependent on water and oxygen availability driven by water table fluctuations, which are conditioned by the river flow regime (Rood et al., 2003; Tron et al., 2015). At the case studies, all trees grew approximately 30 m above ground level and developed their roots under the same weather and water table fluctuations, which are particularly limited by the minimum regulated level in the river. Since these controlling factors for root growth were similar for all trees, then similar root size and structures are likely among them. Figure 3.9 shows trees 10 and 11 of reach B at two different stages of erosion.





Figure 3.9. Poplar trees showing (a) incipient undercutting and (b) erosion almost up to the trunk.

Despite the presence of extended roots in the upper bank, the response to erosion of trees was disparate. On the one hand, the surroundings of large embayments (Figure 3.1) present areas with relatively low retreat, which coincide with the location of the 30 m high trees, such as trees 4 and 5 in Figure 3.2d. This could result from root-reinforced soils and associated chemical strengthening by extra-cellular polymeric substances. On the other hand, in other areas erosion surpassed the location of trees (e.g., trees 7 and 10 in reach A, and trees 3,6 and 7 in reach B). Also, some embayments are not confined by trees, as tree 8 is 40 m from the end of the largest embayment of reach B (Figure 3.2e), whose bank scarp does not present any roots. As a consequence, the presence of trees in the upper bank does not offer an exhaustive explanation for the planform patterns of erosion.

3.5.4. LITHOLOGICAL SUCCESSION AND STRATIFICATION

The floodplain indeed presents highly heterogeneous compositions arranged into tilted strata along the reach, whose strikes are oblique to the current channel position. Figure 3.10 shows two channel positions before the canalization works of the 1960s to infer possible depositional processes during floodplain formation (e.g., Lewin and Ashworth, 2014). In 1912, the river main channel presented two clear meanders connected to a rather straight reach (Figure 3.10a). The latter bend migrated from 1912 until approximately 1950 smoothing the curvature while shifting downstream and to the right (Figure 3.10c-d), involving processes of erosion along the outer bank and accretion at the inner bank. The channel was then fixed with revetments and groynes, and later canalized cutting the bends off, resulting in the present channel alignment (dashed lines in Figure 3.10).

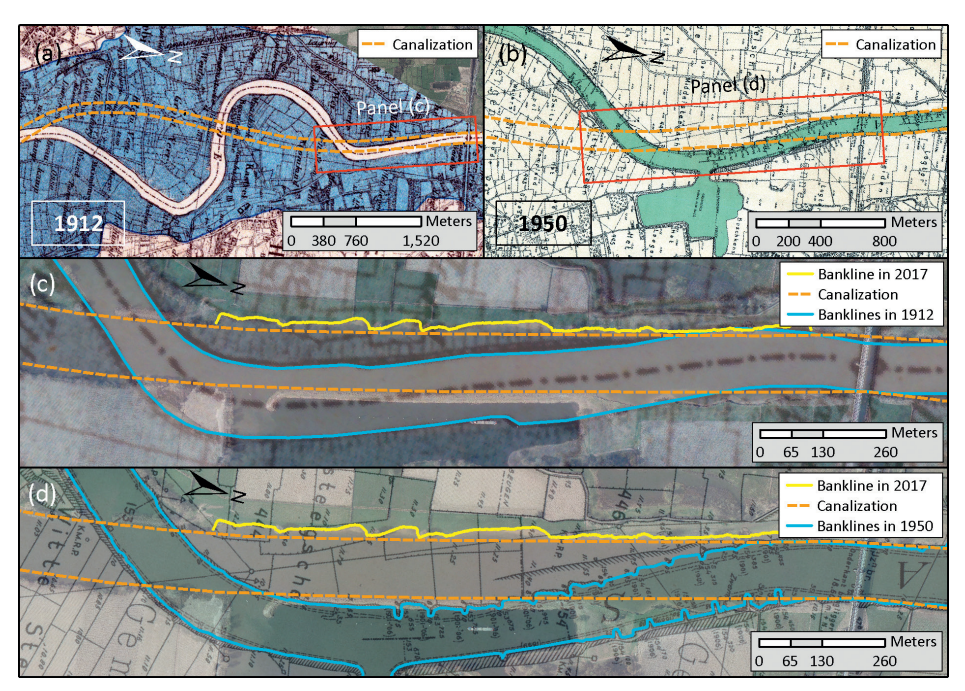


Figure 3.10. (a) Meuse River position in 1912 and later canalization. (b) Meuse River in 1950 and later canalization. (c) Reach B with 2017 banklines along canalized river and 1912 channel position. (d) Reach B with 2017 banklines along canalized river and 1950 channel position. Background images corresponds to aerial photo of 2017 and translucent maps of 1912 and 1950.

Figure 3.11 compares the orientations of the inner banklines in 1912 with the layer strikes identified on the terrace (Figure 3.4), including also the current bankline orientation of asymmetric embayments.

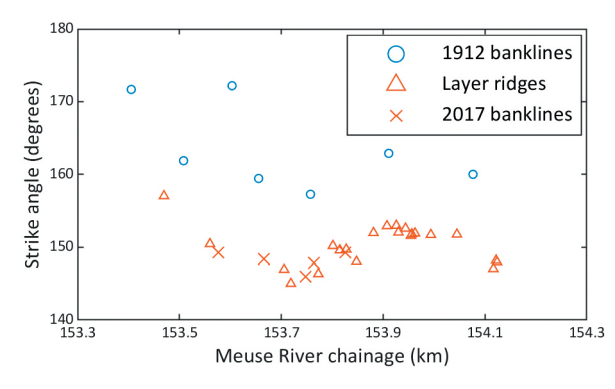


Figure 3.11. Orientation comparison of ridge strikes on terrace, banklines in 1912, and banklines at asymmetric embayments in 2017.

The orientations of strata and the 2017 banklines at embayments match the orientations of the 1912 inner bank along the reach, except for an outlier at km 153.6, which could be the consequence of a local discontinuity in the bank resistance, forming a mild abutment. The series have an average orientation difference of 11 degrees and a 45 metre downstream shift. This correspondence suggests that the meander bend migrated to the 1912 position passing through the current channel location, depositing sediments in sequences that determined the observed strata. What is more, the channel migrated from 1912 to 1950 with a similar drift towards the downstream-right direction, also with rotation and translation of banklines from an absolute reference system.

This downstream shift of the inner bankline can be interpreted as the result of scroll bar deposits (Wu et al., 2016; Candel et al. 2018). The measured dip of the strata is within the range of predicted angles based on Struiksma et al. (1985), for lateral accreting deposits of meandering rivers (Gibling and Rust, 1993). Moreover, the deep cores around the embayment present lithological successions that vary in elevation and thickness, which is explained by successive scroll bar formation. Figure 3.12 interprets the ridge-swale morphology from the deep cores and illustrates the planform layout of former and current channels.

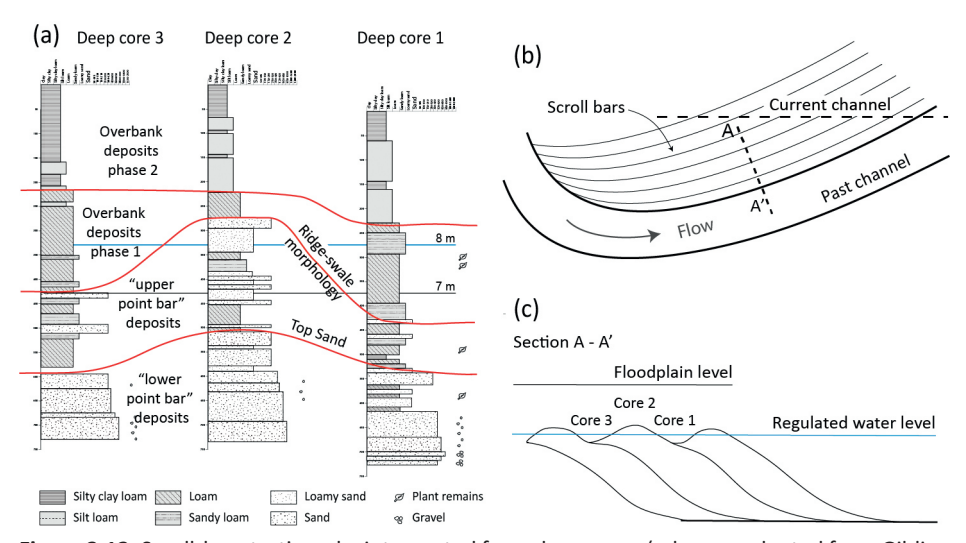


Figure 3.12. Scroll-bar stratigraphy interpreted from deep cores (schemes adapted from Gibling and Rust (1993) and Morrison (2017)).

The depositional sequence follows the direction of the past river migration, which is oblique to the current channel position, so embayments appear as a consequence of these varying compositions along the present channel (Figure 3.12b). Importantly, the elevation of the point-bar deposits especially varies at the water level range (7-8 m) where primary and secondary waves normally attack the banks (Figure 3.12c). Above

these variations, overbank deposits fill the top bank with fine sediments, dominated by the presence of loam up to 9 m and above that by silt, levelling the floodplain morphology (Nanson and Croke, 1992). These spatial variations agree with the different lithologies observed at the terrace along reach B (Table 3.1). Therefore, bank retreat rates and patterns are controlled by the nature of the deposits, producing faster erosion at sandy deposits and lower at loams, whose spatial disposition is defined by the structure and orientation of strata.

The asymmetry of embayments is caused by the obliqueness of sedimentary layers with respect to the canalized channel. The consistent but opposite asymmetric orientations of embayments in reaches A and B correspond to scroll bar formation in different directions during meander migration (Figure 3.2a,10a). On the other hand, parallel bank retreat, such as the straight bankline in the downstream end of reach B, responds to a relative strong layer at the minimum regulated level lying almost parallel to the current channel position (Figure 3.10c). Finally, the different embayment lengths are most likely the result of varying layer thicknesses and strike angles with the main channel, which create a variation of the projected length along the channel (see Figure 3.12b,c).

The layer that protrudes at the upper bank near tree 4 exemplifies the control exerted by lithology and stratification on bank retreat (Figure 3.13a). This layer with relatively high clay content (sample 3, Table 3.1) is aligned with the subsequent downstream bankline on the right, corresponding to the beginning of the next embayment (Figure 3.4). Its oblique orientation with respect to the canalized channel defines the asymmetry of the downstream bay. Even though tree 4 locally delays erosion rates by root reinforcement, the response of bank retreat follows the location of this cohesive layer (Figure 3.13b), except where shear stresses are highest due to less wave dissipation and high currents. The upstream bay results from the erosion of the scroll-bar ridge composed by sand at the regulated water level (sample 2 and Figure 3.12), whose development rate reduces at the encounter with the downstream scroll-bar swale, filled with loam at the controlled water stage.

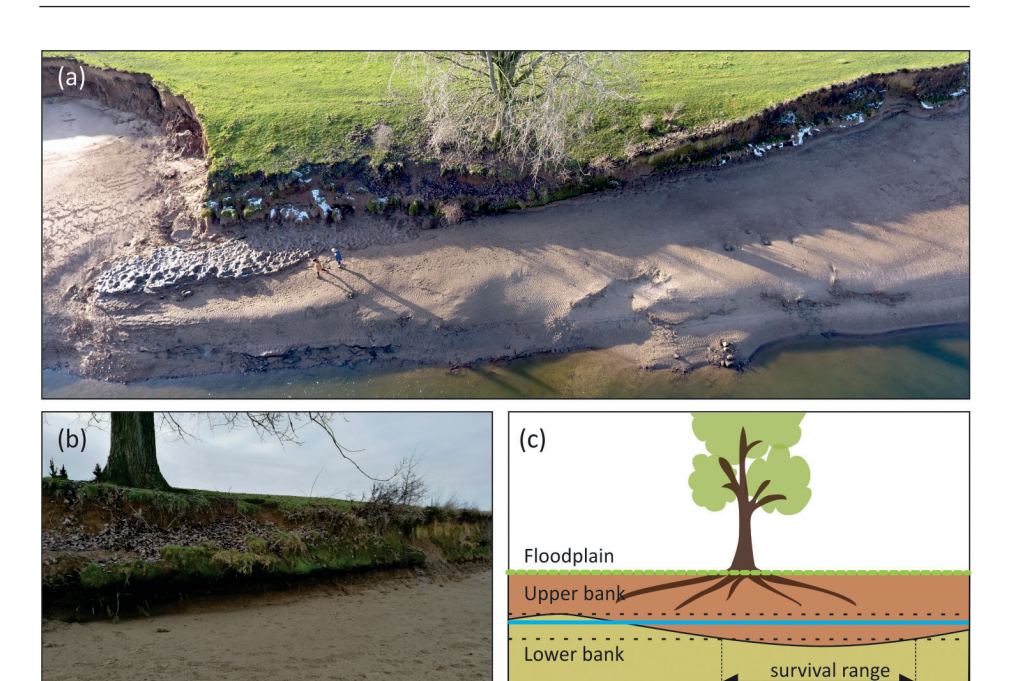


Figure 3.13. Terrace and upper bank at extraordinary low water level. (a) Cohesive layer along the upper-bank toe delaying erosion near tree 4 (note two people on terrace for scaling). (b) Tree 4 with incipient undermining along the oblique bankline. (c) Relative position between tree roots at the upper bank and strong cohesive layer at toe.

The disparate erosion at the location of trees is then explained by the erodibility of the layers at the upper-bank toe, and the relative position of the trees across them. Figure 3.13b schematizes the horizontal extent along which a strong layer delays erosion rates in front of a tree, called "survival range" to refer to its short-term fate. This range depends on the layer thickness, tilt and position with respect to the tree, but also on the elevation range of wave action (between dotted lines) propagating at controlled stages (upper limit of green area). Those trees over a weak stratum are dislodged after few years, while those partially covered by a strong one (e.g., tree 3 of reach B) are later outflanked.

3.5.5. OTHER FACTORS

No evidence of sapping was observed along the hydrological year in the study reaches, neither in the form of regular cavities at bank scarps nor through deposits of dislocated particles (Hagerty, 1991). Cattle grazing on floodplains may widen small streams by progressively breaking banks down (Trimble, 1994), but in the study sites banks heights reach 3.5 m and cow pathways were always observed far enough from the edge to avoid mass failures. Rainfall events can increase the soil specific weight and induce bank mass

instability (Simon et al., 2000), but only a few local and isolated failures were observed at the beginning of the rainy season.

3.6. DISCUSSION

3.6.1. SHIP-INDUCED WAVES AND TERRACE FORMATION

The relative contribution of waves on eroding banks depends on vessel frequencies and characteristics and on the natural forces also acting on the banks. The case studies present highly regulated water levels that allow ship waves to attack banks at a narrow range of elevations. These conditions are sufficient to develop a terrace across riverbanks during low flows, despite the erosion produced during floods. Furthermore, the fact that the water does not surpass a minimum stage impedes some mechanisms of erosion to act on the lower bank, such as drawdown (Simon et al., 2000) and subaerial processes (Wynn et al., 2008), which further increases the differential retreat between the lower and upper bank.

Detailed monitoring of the upper-bank erosion showed that floods were not necessary for the basal clean-out of failed material (Dorava and Moore, 1997), and ship waves acted disaggregating and removing slump blocks, as observed in the Ohio River (Hagerty et al., 1995). The role of ship waves extend over the whole erosion cycle, including undermining and destabilization of the bank top. In the most erodible stretches, the terrace presents mild slopes of c. 1:25, unlike situations with more frequent water level changes that display steeper bank profiles (Maynord et al., 2008). Therefore, highly regulated rivers with high ship traffic set the conditions to form a mild extended terrace across banks, which reduces erosion rates over time due to wave energy dissipation in shallow waters, but continues developing after 8 years of protection removal.

3.6.2. EFFECTS OF TREE ROOTS ON BANK EROSION

Uniformly vegetated banks can significantly reduce near-bank velocities along entire river bends (Konsoer et al., 2016a). At a smaller scale, Pizzuto et al. (2010) suggested that the joint effect of nearby trees on flow detachment could reduce erosion rates similarly to small-scale roughness (Kean and Smith, 2006), based on short-term observations of sequential abutments on sandy-loams. Rutherfurd and Grove (2004) demonstrated that isolated trees locally delay erosion rates in sandy-loams, which is shown by root-plate abutments in the bankline, but their effect is negligible for the migration rate of the meander bend, in agreement with the results of this study.

The combination of large woody roots and different substrates led to disparate erosion resistances. The effect of trees located on highly erodible layers in the study reaches (e.g. tree 7 over sandy loam, Figure 3.4) appeared negligible at yearly intervals of

bank retreat, even at a local scale. On the other hand, trees with cohesive substrates presented high erosion resistance. Vannoppen et al. (2017) showed that the additional resistance against concentrated flow erosion of soils with thick taproots increases as the cohesion increases, but decreases with increasing sand content. Hence, the mechanism through which woody roots reduce bank erosion rates is more effective with less erodible substrates.

This positive feedback between the presence of vegetation and cohesive soils during the entrainment phase of the erosion cycle (Thorne and Tovey, 1981) can explain the divergent fates of trees in the study cases. Cohesive soils permeated by deep roots hold steeper banks (Thorne, 1990) by increasing the resistance against instability (Pollen-Bankhead and Simon, 2009). This delays the failure mechanism compared to the case without root reinforcement, allowing for a longer phase of entrainment within the erosion cycle, which is also extended by the effect of roots through delaying entrainment rates. In contrast, more erodible soils fail at earlier stages even if root-reinforced, which reduces the time scale of the entrainment phase and thus the period along which roots reduce shear stresses onto the soil. As a consequence, this positive feedback enlarge further the difference of erosion rates between sandy and loam soils in presence of woody roots.

3.6.3. FLOODPLAIN HETEROGENEITY ON BANK EROSION AND RIVER MIGRATION

The angle between past and present river channels, the stratification of the floodplain, and the regulation of the water levels, created the conditions for wide-ranging erosion rates along relatively short distances. The resulting scale of the embayments is not common in rivers where channels normally follow abandoned paths (Gautier et al., 2007; Constantine et al., 2010) or cut previous paths at large angles (Hooke, 1995; Slingerland and Smith, 2004). Yet, as expected, large embayments also arose in other reaches of the Meuse River, for instance, upstream of the city of Hedel, the Netherlands (51°44'21"N, 5°16'50"E, July 2017).

Previous studies proposed flow patterns and their interaction with bank shape as the main factors for the formation of embayments (Hackney et al., 2015). However, the appearance and growth of the embayments in the Meuse River are dominated by floodplain stratification, under relatively uniform and highly delimited loads induced by ship waves. Therefore, in cases where flow velocities are not affected by stage regulation, bank stratigraphy and composition may also have a significant role in shaping banklines into large embayments. This hypothesis is supported by the fact that the bank bathymetric surveys performed by Hackney et al. (2015) in the Mekong River presented

clear strata, and that critical shear stresses ranged significantly from the weakest to the strongest soil samples, with respect to acting shear stresses.

This work indicates that structured along-channel variability in lithology defines erosion patterns within a river reach, at a scale which has not been identified before. Previous works have shown the control that floodplains with heterogeneous erosional resistance exert on meander migration, through both field observations (Hudson and Kesel, 2000) and numerical models (Güneralp and Rhoads, 2011). Further numerical analyses and field cases showed that meander planform complexity increases with floodplain soil heterogeneity (Motta et a., 2012b; Vermeulen et al., 2014). Konsoer et al. (2016b) found that vertical heterogeneity in bank resistance significantly changes bank erosion rates and mechanisms in the Wabash River, in agreement with Motta et al.'s (2014) long-term meander simulations, which included a physically-based erosion model for stratified banks.

This work highlights the importance of floodplain formation and related channel dynamics for later morphological developments. The complexity of the processes involved during floodplain formation (Nanson and Croke, 1992, Kleinhans 2010, Kleinhans et al. 2018) limits the use of uniform bank erosion coefficients for predictive purposes, even considering complex hydrodynamics (Motta et al., 2012a). Moreover, Schwendel et al. (2015) showed significant changes in migration rates and sinuosity of a large meandering sand-bed river driven by clay bodies, presumably caused by pedogenic processes. Bogoni et al. (2017) demonstrated that numerical models that account for floodplain formation, including key geomorphic units as scroll bars and oxbow lakes, achieve realistic meander planforms thanks to heterogeneous bank resistances. The morphological features within a river reach, even when developing in the short term (<10 years), may have an impact for further developments and latter affect landscape formation, stressing the relevance of process-based numerical modelling.

3.7. CONCLUSIONS

Distinct bankline patterns, presenting several oblique embayments with different angulations, arose along two reaches of the Meuse River after removing bank protections. These patterns were analysed by considering the processes and factors affecting bank erosion rates in the study area. The results show that floodplain heterogeneity controls the bankline irregularities in magnitude and orientation, in combination with ship waves hitting the bank at regulated water levels. Past river alignments and floodplain stratigraphy indicate that scroll bar depositions modulate the erodibility along the channel. Different strata thicknesses and orientations with respect

to the river channel can explain the different embayment lengths and the stretches with parallel bankline retreat.

On the bank strength side, the effectiveness of isolated tree roots on reducing bank erosion rates depends on soil characteristics, which define a primary control over erosion rates. Locations with sandy deposits vanished the contribution of mature poplar trees over yearly intervals, whereas loam layers seem to allow tree roots to significantly increase the resistance against entrainment and reduce bank erosion rates. On the load side, floods induce relatively low bed shear stresses during short periods, whereas ship waves regularly exert similar to higher loads. The difference in frequency and duration between these loads, and the fact that water levels are strongly regulated, create the conditions for ship waves to form a long mild terrace across the banks.

This research highlights the importance of underlying mechanisms that act at large spatial scales and control future responses of eroding riverbanks. This supports the idea that process-based long-term meandering models should account for processes that form floodplains to improve the representation of natural planforms and their eventual predictive accuracy, advancing statistical approaches. Furthermore, short-term and process-based bank erosion models applied to navigable rivers need to consider heterogeneous floodplain properties, but also have the challenge to represent the magnitude of loads exerted by ship waves over different phases of bank evolution.





Ship passages contribute to the erosion of unprotected banks in waterways but their short and long term impacts remain unclear. This chapter characterizes the effects of ship waves and floods on bank erosion along Oeffelt reach in the Meuse River. The role of vegetation growth at the bank toe is also considered. The approach to analyse the progression of bank retreat after riprap removal uses 17 topographic surveys with UAV-SfM, RTK-GPS bank profiles, ship waves measured with acoustic Doppler velocimetry, systematic aerial and terrestrial photography, soil tests, and multibeam echo sounding. Once the consequences of ship-generated waves and currents, floods, and vegetation dynamics on bank erosion are explained and integrated in a conceptual framework, a process-based model is proposed to estimate the long-term bank retreat in regulated rivers.

The contents of this chapter are published in *Journal of Geophysical Research: Earth Surface 125* (2020) under the title: "Bank erosion processes in regulated navigable rivers". Authors: Duró, G., Crosato, A., Kleinhans, M. G., Roelvink, D., and Uijttewaal, W. S. J.

4.1. INTRODUCTION

Many and complex interacting factors are involved in the erosion process of riverbanks, especially when ship waves are present. Banks commonly erode due to currents while other factors may also destabilize banks, such as seepage and water level changes during flood events (Fox et al., 2010; Nardi et al., 2012; see Section 1.2.3). Ship waves exert additional loads onto banks that may induce mass failures through impinging loads or gradual undermining. Waves can also simultaneously act with other drivers enhancing erosion rates. This was observed, for instance, by Dorava and Moore (1997) with currents in bank embayments during peak flows.

The complexity of factors affecting erosion rates involve i) waves and currents induced by ships that vary in size, speed, loading, and travelling distances from the bank (e.g., Nakos and Sclavounos, 1990), ii) spatially-varying bank geotechnical characteristics (Samadi et al., 2009; Pollen-Bankhead and Simon, 2009); iii) entrainment rates of bank material (Rinaldi and Darby, 2007), and iv) vegetation dynamics on eroding banks (e.g., Bertoldi et al., 2011; Edmaier et al., 2011). It is particularly difficult to isolate the effects of the single factors due to their simultaneous occurrence and mutual interactions (e.g., Maynord et al., 2008; Laderoute and Bauer, 2013). In addition, the episodic nature of ship passages hinders the use of survey techniques to measure the effects of single events (Bauer et al., 2002).

One of the aims of river restoration is to increase habitat suitability for fish, invertebrates and plants by offering a diverse morphology (Wohl et al., 2015) including shallow areas and varied bank slopes. Eroding riverbanks in waterways show a characteristic terrace (Hagerty et al., 1995; Liedermann et al., 2014) which is formed by the combined action of ship-induced waves and stage regulation to facilitate navigation. Banks are hit at approximately the same level over prolonged periods and, as a result, retreat at different rates below and above this level. For this, the lower bank is hereafter distinguished from the upper bank (Figure 4.1). The lower bank connects the riverbed and the terrace, which are normally submerged due to stage regulation. The upper bank is usually exposed and links the terrace with the floodplain level.

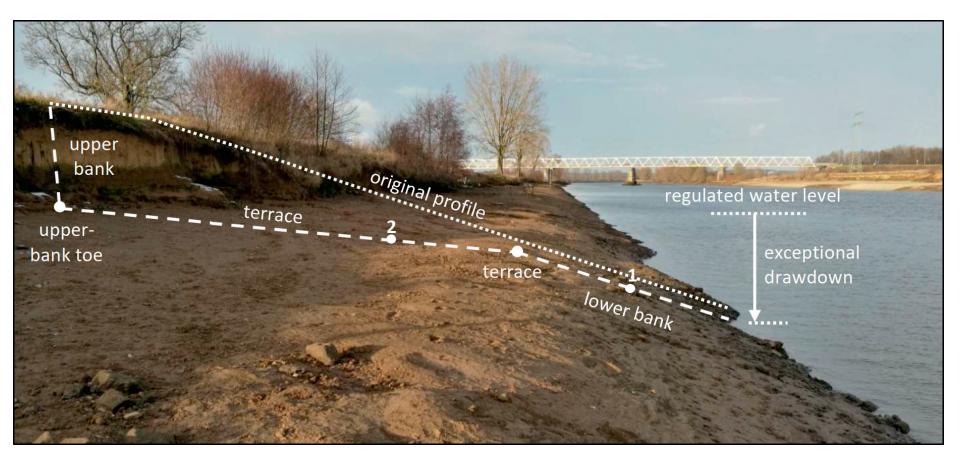


Figure 4.1. Bank terrace of Meuse River (km 154.1), visible after a ship accident that lowered the water level by 2.6 m from the regulated stage.

Even though ship waves contribute to terrace formation, increasing the morphological diversity of the river bank, they also negatively affect the local ecosystem through increased bed shear stresses, sediment resuspension, mobilization of nutrients and chemicals (Gabel et al., 2017). The plants that are able to grow at the upper-bank toe are beneficial for functional diversity (Wollny et al., 2019). Still, their ability to control bank erosion is uncertain (Coops et al., 1996; Koch et al., 2009). A better understanding of bank evolution and long-term response is thus important to define potential ecological improvements, estimate land loss, and evaluate management strategies. The goals of this chapter are to characterize the processes that determine the evolution of unprotected banks in navigable regulated rivers, integrate them in a conceptual model, and propose a numerical approach to estimate the maximum extension of bank retreat that can be expected. The following aspects are given special attention: relative role of ship waves and floods; role of vegetation growth on bank erosion.

4.2. METHODS

Bank processes, bank material, ship waves, water flow, and vegetation growth are analysed on the left bank of Oeffelt reach (right-hand side of Figure 4.2). This river reach is characterized by rather intense ship traffic, presenting a wide variety of erosion rates at the re-naturalized bank. For practical reasons, three parts of the vertical bank profile are differentiate: upper bank, terrace, and lower bank. Upper-bank erosion processes are studied focusing on the fastest eroding area located within the biggest embayment (Figure 4.2). Bank retreat at locations with dissimilar behaviour are analysed and compared, particularly considering the distribution of erosion before and after a flood event. The terrace geometry is analysed at eight locations, each one having its own physical characteristics. Ship waves are characterized based on field measurements

and observations. The results are integrated with the aim to define a conceptual model of bank evolution and develop a numerical model to estimate the final bank retreat for different locations.

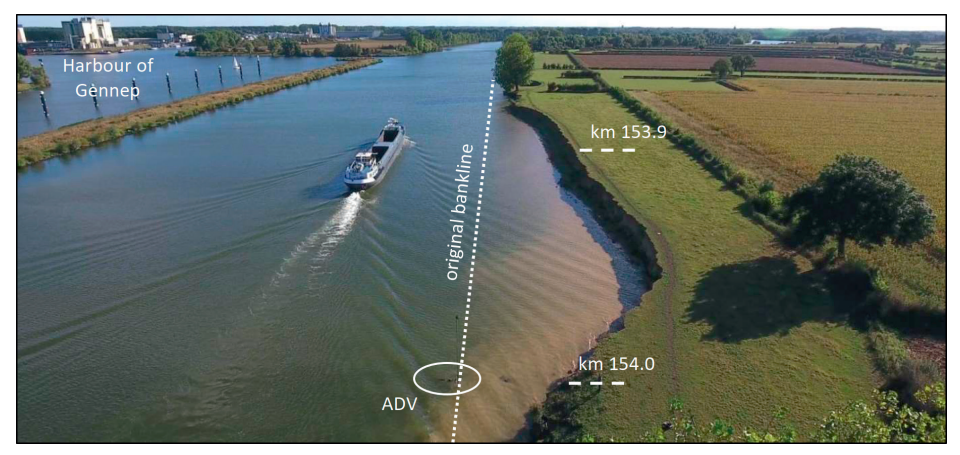


Figure 4.2. Upstream view of study site. Secondary waves of empty ship propagating over terrace and reaching upper-bank toe. Acoustic Doppler velocimeter (ADV) fixed to frame and navigation pole.

4.2.1. WAVE MEASUREMENTS

Water pressure and flow velocity components were measured with an Nortek Vector acoustic Doppler velocimeter (ADV) between June 21st and July 13th 2017 with a frequency of 8 Hz. The ADV head and pressure sensor were placed 0.50 m below the regulated water level near the terrace toe where the water depth was 1.60 m (Figure 4.2). At that location, waves with typical lengths of 3 m were not affected by bottom friction due to deep water conditions. The data were processed with MATLAB scripts. The pressure was converted into water level assuming hydrostatic pressure distribution over the depth. After subtracting the mean level, water level fluctuations were processed with a third-order median filter to identify primary and secondary waves. The primary waves were separated from secondary waves by keeping only frequencies below 1/8 Hz (Figure 4.3a). The secondary waves were isolated by keep only frequencies higher than 1/8 (Figure 4.3b).

The quantification of the period and height of primary and secondary waves from the water level series was done through the identification of key points. Primary waves were first identified through the downward zero-crossing at the threshold of -0.05 meters from the minimum regulated level (P1). Then, the minimum water level reached by the subsequent trough was determined (P2). This point was used to compute the primary wave height (or depth). After P2, the following upward zero-crossing was identified (P4).

Finally, the first upward zero-crossing before P1 was located (P3). The time duration from P3 to P4 was computed to quantify the primary wave period.

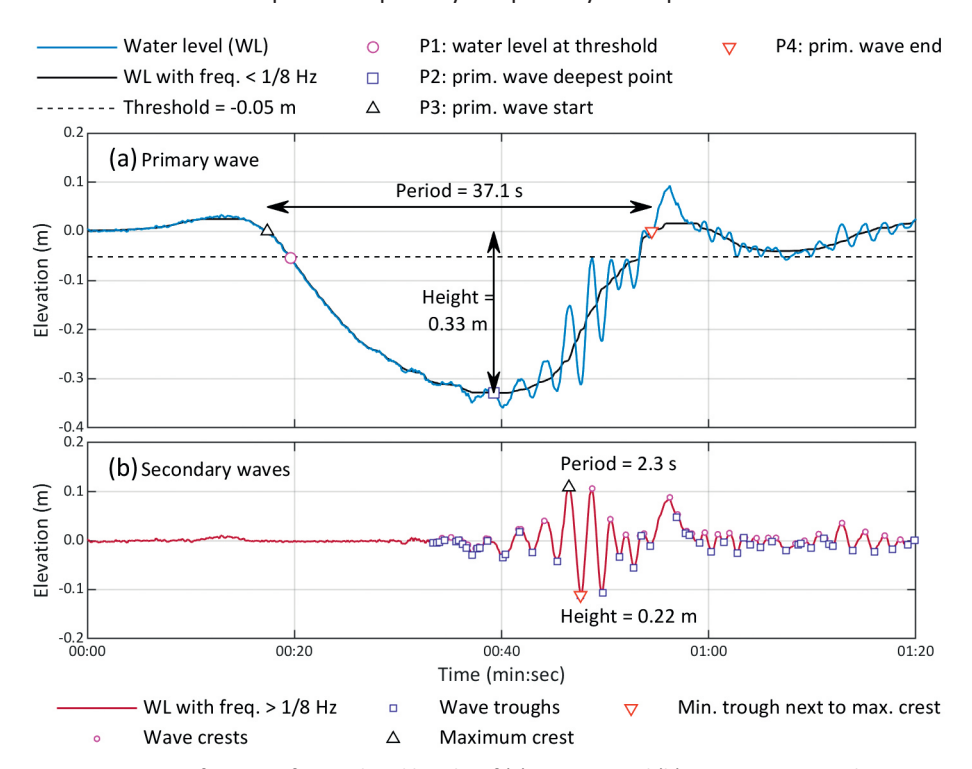


Figure 4.3. Quantification of period and height of (a) primary and (b) maximum secondary wave.

The maximum secondary wave height was considered representative for the erosive potential of each secondary wave train (Nanson et al., 1994), so the focus of analysis was only on those (Sheremet et al., 2013). First, the crests and troughs of all secondary waves during and after the main primary wave were determined. Then, the highest crest was identified. In the following step, the minimum trough between the previous and the next trough with respect to the maximum crest was determined. The maximum secondary wave height was computed from the difference between the maximum crest and the minimum trough next to it. The period was quantified by multiplying by two the time duration between the two points defining the maximum wave height.

The Dutch Ministry of Transport, Water Management and Public Works (Rijkswaterstaat) provided ship passing records at Sambeek lock, 5 km upstream of the ADV location (Figure 4.2), from 2013 to 2018 and historical water level series, which were used to verify the ADV measurements and characterize the water levels during floods.

4.2.2. UPPER BANK

Sequential topographic surveys of the upper bank were carried out using an Unmanned Aerial Vehicle and Structure from Motion photogrammetry with the methodology described by Duró et al. (2018) to measure riverbanks. The reach was surveyed 17 times from January 2017 to February 2019, deploying 18 ground control points to georeference the digital models, UgCS software to control the UAV, and Agisoft PhotoScan to process the imagery. The surface models had a resolution of 2 cm and root-mean-square error of 3 cm, verified with RTK-GPS. On 29th December 2016, a ship accident against the weir located downstream of the study area caused an exceptional water level drawdown (Figure 4.1) which allowed surveying also the terrace topography.

The resulting digital topography was used to compute the area between sequential vertical bank profiles to quantify eroded volumes and progression of bank erosion between successive surveys. With high water levels, the submerged part of the profile was assumed at the same position as in the subsequent survey. The airborne surveys, complemented with terrestrial photographs taken from the floodplain, were also used to register the development of vegetation on the upper bank. Finally, yearly banklines were delineated in ArcGIS over aerial photos taken during summer by Rijkswaterstaat.

4.2.3. TERRACE AND LOWER BANK

The topography of the terrace was measured on 18th January 2017 and December 11th 2018. The first survey was made with UAV-SfM during the exceptional water level drawdown that exposed the otherwise subaqueous terrace. The second survey consisted of cross-profiling with RTK-GPS at 10 locations (Figure 4.4). The bathymetry of the lower bank was measured every year with a multibeam echosounder by Rijkswaterstaat, who already provided the point cloud on a 0.5 m grid.



Figure 4.4. Location of study reach and analysed cross sections.

Lithological characterization along the terrace was done taking eight cores at 10 cm from the soil surface, seven of which were already presented by Duró et al (2020a). All samples were tested with direct shear box to obtain the internal friction angle and

cohesion, using a range of normal loads of 17, 36 and 73 Pa and shear rates of 0.01 mm/ sec. The samples were dried at 105° C, sieved, and the fractions under 63 κ m subject to hydrometer test, to classify each lithology according to USDA (see Table 3.1).

The critical shear stresses for entrainment for each sample were then estimated. Despite the complexity of determining this parameter through soil properties (Thoman and Niezgoda, 2008), cohesion has proved a simple but key property to estimate it (Kimiaghalam et al., 2016). Therefore, Kimiaghalam et al. (2016) regression based on cohesion is used (see Equation 3.6). The resulting critical shear stresses vary greatly between textures, ranging between 6.4 and 18.5 Pa (Table 3.1) and matching measured values on other cohesive banks, as for instance on the St. Lawrence River (Gaskin et al., 2003).

The characterization of the transverse terrace geometry requires the definition of its boundaries in the field. Particularly, the identification of the terrace toe is complex, because of the different shapes that this transition zone presents. Therefore, a common point among cross sections is first defined at the lower bank, which is not affected by wave erosion (point 1, Figure 4.1). For that, this point was located at half wavelength from the regulated level, at the start of the shoaling zone of typical secondary waves, i.e. 1.5 m deep corresponding to 3 m wavelengths (see e.g., Figure 4.2). A second point was then identified (point 2, Figure 4.1) at a distance of two wavelengths onshore from point 1, so that i) the slope transition is surpassed and point 2 lays on the terrace slope, and ii) the water depth near the terrace toe can be measured and compared among cross sections. The midpoint between points 1 and 2 defines the terrace toe, visually lying at the inflexion point between the lower bank and the terrace. The terrace length is then measured from this midpoint to the upper-bank toe (Figure 4.1).

4.3. RESULTS AND INTERPRETATION

4.3.1. SHIP-WAVE CHARACTERISTICS

In the study area, commercial shipping has regular frequency (Figure 4.5a), for both loaded and empty vessels. Recreational boats, on the other hand, show a seasonal behaviour, with peak traffic concentrated in the summer. Considering only waves with amplitude larger than 5 cm, between June 21st and July 13th 2017, a total of 1,224 passing ships producing primary waves were recorded (Figure 4.5d), of which 1,013 also produced secondary waves (Figure 4.5e, circles). In the same period, another 905 ship passages produced secondary waves but induced primary waves smaller than 5 cm (Figure 4.5e, triangles). Primary wave heights reached 0.45 m, inducing return currents up to 1.2 m/s near the terrace toe. The highest secondary waves also reached 0.45 m, generating orbital velocities up to 0.60 m/s (Figure 4.5e). Recreational boats and

commercial vessels produced similar secondary waves, but the former usually did not produce significant primary waves (deeper than 5 cm). An example of typical primary and secondary wave patterns produced by a passing ship is available in the dataset by Duró (2020d).

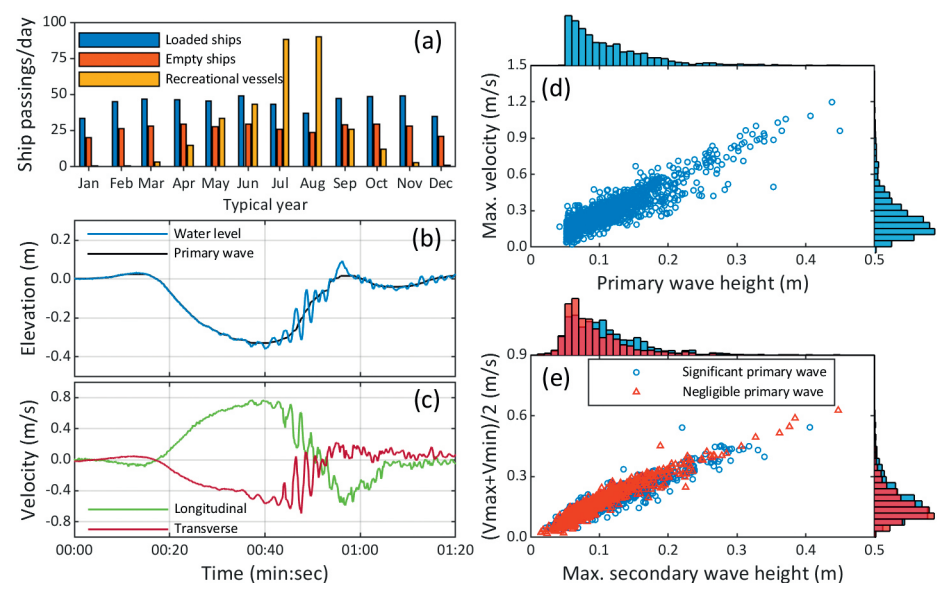


Figure 4.5. (a) Daily ship passings during a typical year. (b) A primary wave with secondary waves during the rising limb. (c) Longitudinal and transverse components of the velocity evidence overlapping water motions, with positive signs in downstream direction and towards the bank, respectively. (d) Maximum horizontal velocities induced by primary waves near terrace toe. (e) Amplitude of the horizontal orbital velocity near terrace toe produced by the highest secondary wave per ship.

The results confirm that the generation of primary and secondary waves by vessels are not necessarily correlated, given their different geneses (Söhngen, 2008). When both types of waves are produced, their relative timing also varies among vessels. The train of stern-secondary waves may happen during the rising limb of the primary wave, as shown in Figure 4.5b, or after the main primary wave depression (see for instance, movie S1 in Duró, 2020d). The former case presents coupled water motions consisting of a longitudinal current with overlapping orbital velocities (Figure 4.5c). These cases allow secondary waves to break at elevations that are lower than regulated levels, i.e. over the terrace and below the upper-bank toe (Figure 4.6a).

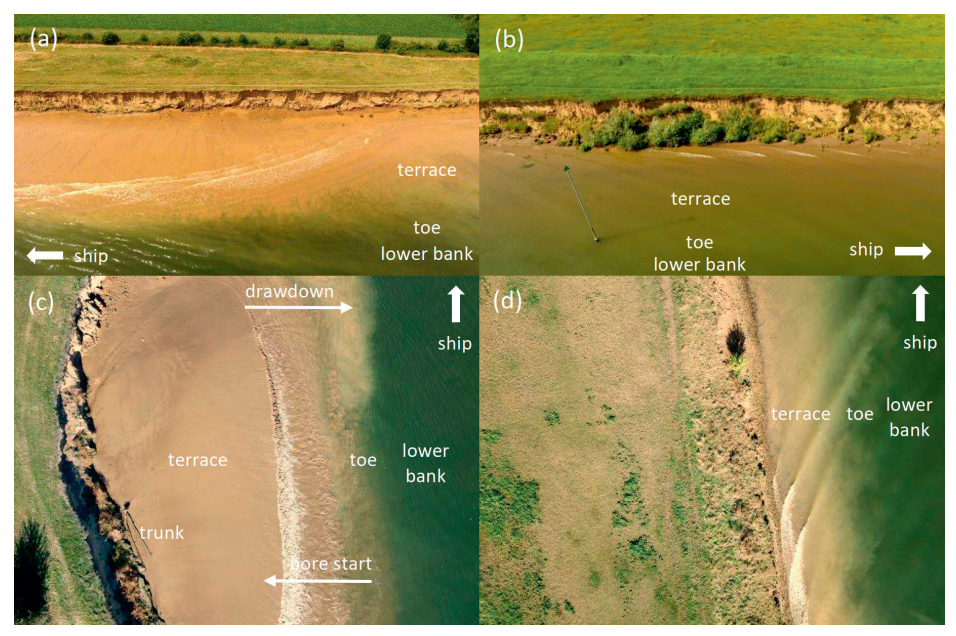


Figure 4.6. (a) Primary wave propagating over terrace as secondary waves break over it, km 153.9 on 21/06/2017. (b) Secondary waves breaking near the upper-bank toe, km 153.5 on 23/08/2017. (c) Primary wave ejecting sediments from terrace, km 153.6 on 10/10/2018. (d) Secondary waves breaking at upper-bank toe over gravel layer, km 154.3 on 10/10/2018.

At low flows, the breaking location of secondary waves also depends on terrace elevation at the upper-bank toe. If this level is higher than the regulated water level, then secondary waves dissipate on the terrace without reaching the upper-bank toe (Figure 4.6b, area on the right). On the contrary, secondary waves hit the upper bank when the toe level is submerged or close to the regulated level (Figure 4.6b, centre left area with vegetation). Secondary waves entrain sediments mostly during breaking, as indicated by the higher concentrations of suspended solids observed near the upperbank toe. Figure 4.6d shows secondary waves breaking close to the upper bank, and previously entrained sediments covering the terrace.

Primary waves exert shear stresses during drawdown through the current induced by the transverse energy gradient (i.e., flow towards the main channel), entraining and transporting sediment in suspension (Figure 4.6c). The rising limb of deep primary waves turns asymmetric when propagating in shallow water (Parnell et al., 2015), as above the terrace, with rear slope 2-3 times steeper than the front slope (e.g., Figure 4.6b). The uprush propagates towards the upper bank as a bore, starting from the lowest water level reached during the depression, subsequently returning the water to the preceding level.

4.3.2. UPPER-BANK EROSION PROCESSES

The cumulative erosion along the largest embayment from January 2017 until March 2019 shows an uneven distribution (Figure 4.7b). The upper bank lost 25 m³/m of volume on average at km 153.900-153.950, 17 m³/m at km 153.960-153.970, and approximately 10 m³/m at km 153.840-153.860. These differences are detectable from the bankline shift from 2017 to 2018 (Figure 4.11a), when the bankline migrated to form a more uniform retreat from a break at km 153.930, which was caused by a less erodible layer at the upper-bank toe (Duró et al., 2020a).

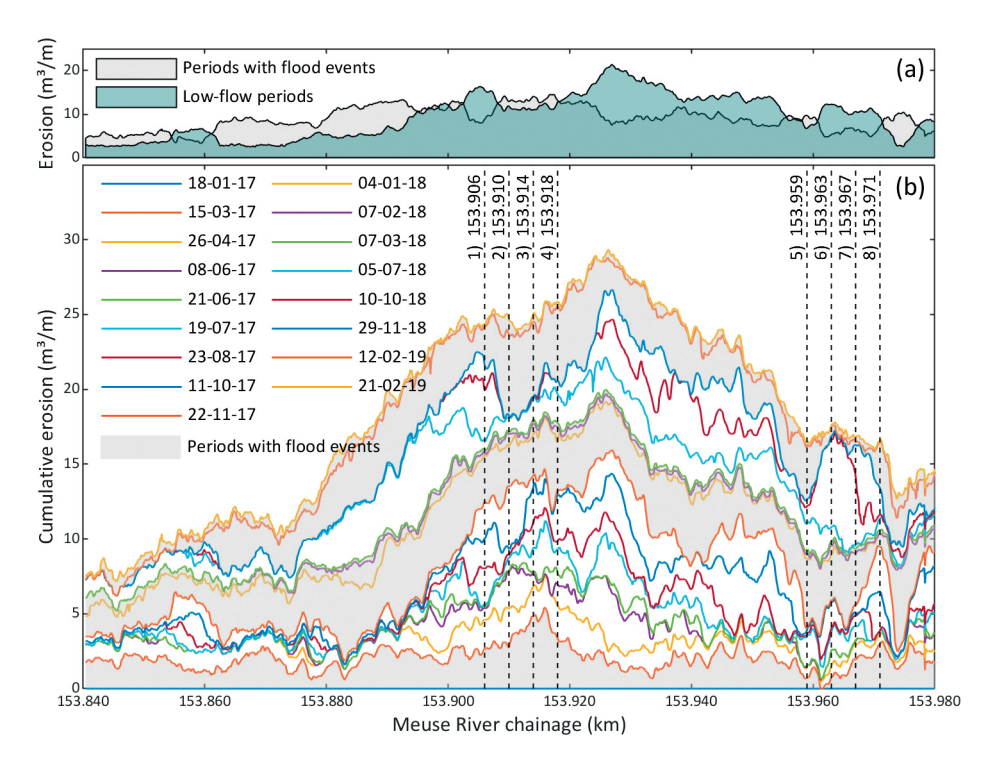


Figure 4.7. (a) Upper-bank erosion during periods with and without floods at largest embayment from 18-01-17 to 21-02-2019. (b) Upper-bank cumulative erosion at largest embayment throughout 17 surveys (note 18-01-17 series lying on x axis). This stretch can be located in Figure 4.11a and Figure 4.4 based on chainage, i.e. the reference kilometres along the River.

The relative quantities of material eroded during low flows and flood periods varied along the reach (Figure 4.7a,b). Erosion during low-flow periods is associated to wave action only, given the very-low flow velocities at the bank toe, absence of seepage erosion, and rainfall events only producing few local and isolated failures (Duró et al., 2020a). During flood events, currents may produce significant shear stresses to contribute to bank erosion (Duró et al., 2020a), in addition to ship wave action and water level fluctuations. From km 153.860 to km 153.885, more bank erosion occurred during

4

periods with flood events than during low flows. From km 153.920 to km 153.955, higher erosion occurred during low flows than in flood periods. Along the rest of stretches, bank erosion happened similar quantities during high- and low-flow periods.

Figure 4.8 presents the evolution of two sets of upper-bank profiles, indicated with dashed lines in Figure 4.7b. Each group has four cross sections separated by 4 m with similar final cumulative erosion. The upstream set (Figure 4.8b-e) shows that during flood periods banks failed, which normally happened at the rising limb of the hydrographs (e.g., 12-2-2019 and 21-02-2019 banklines had similar positions). The downstream profile set had lower erosion rates showing intermediate erosion stages. Notably, despite the failure of the upper bank, the net erosion during the last flood period at km 153.963 and 153.967 (Figure 4.8g,h) was negligible (Figure 4.7b).

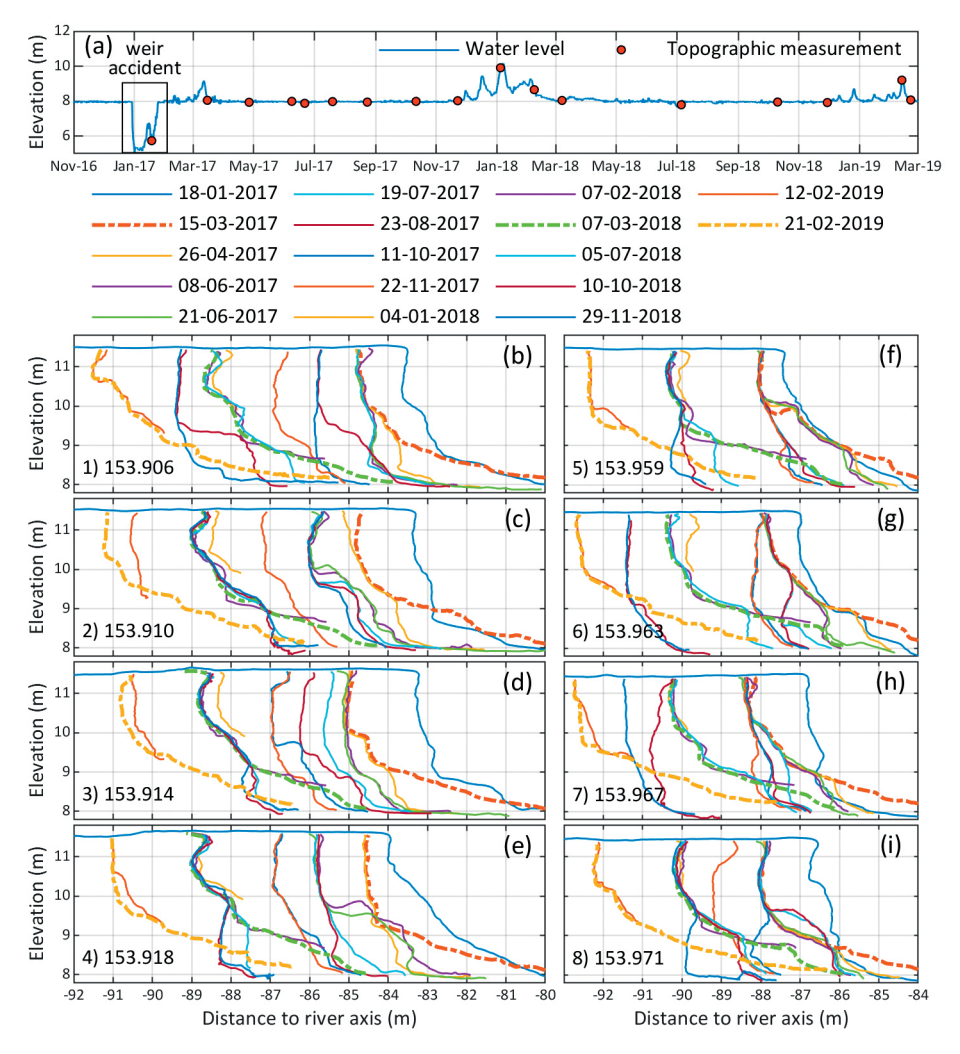


Figure 4.8. (a) Water level at km 153.940. (b-i) Upper-bank profile evolution of sections indicated in Figure 4.7b (dashed profiles indicate post-flood surveys).

These sections show that the material deposited at the upper-bank toe was not eroded or transported either by currents or waves (km 153.961-153.969, Figure 4.7b). Near-bank currents were too low at embayments for producing significant sediment entrainment (estimated below 0.3 m/s at the 2018 flood peak while at the channel axis were 1.5 m/s). Waves did not erode the upper bank likely due to the protection of nearby slump-block deposits (km 153.959 and 153.971, Figure 4.8f,i), implying a lateral connectivity and modulation of erosion phases along banks (e.g., see out-of-phase erosion phases of slump-block deposits and undermining in Figure 4.10b). To conclude, at embayments,

floods redistributed the bank material across sections, reshaping the profile with a mild slope ($^{\sim}$ 1:3).

4.3.3. DIFFERENCES IN BANK RETREAT

Top-bank retreat shows different behaviours along the studied reach. First, the variety of erodibilities resulted in diverse erosion rates. For instance, Km 153.9 evolved twice as fast as 154.1 (Figure 4.9a) due to different dominant lithology, i.e., sandy loams vs. silty loams. Moreover, transitions between lithological layers changed erosion rates. For example, rates decreased at km 153.8 at the start of a less erodible layer (Figure 4.9b), whereas erosion rates increased at km 154.0 after 2014, when a low-erodible layer was surpassed (Figure 4.9c, section at pole location).

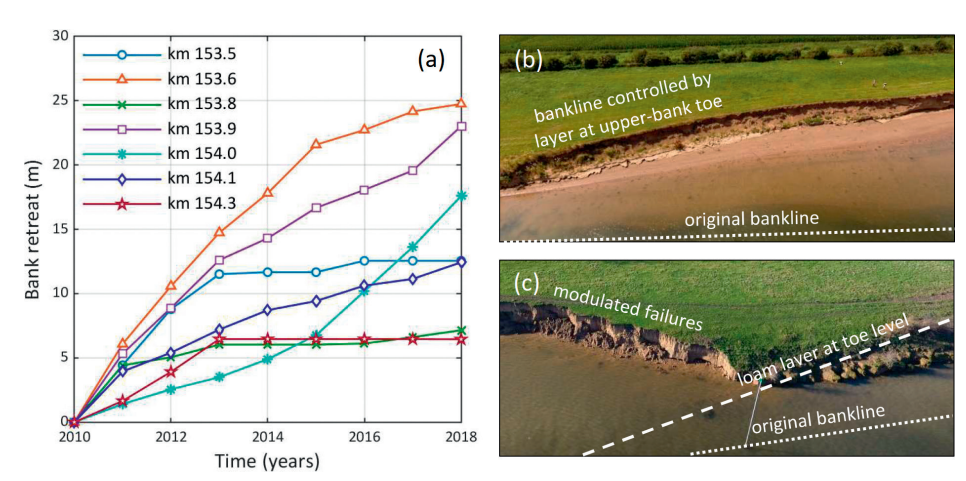


Figure 4.9. (a) Different cumulative bank retreats at key locations affected by floodplain heterogeneity and vegetation at upper-bank toe. Examples of (b) encounter of less erodible layer at km 153.8 and (c) encounter of more erodible layer at km 154.0.

Uneven distribution of bank retreat also occurred in the largest embayment where floods produced extensive bankline shifts (Figure 4.7). Figure 4.10a shows the topographic changes in that area between the first two measurements, which included a flood event. At the embayment upstream end (around km 153.8), the bank was not eroded. The strong layer at the upper-bank toe (Figure 4.9b) prevented toe erosion from wave action during regulated water levels. This enabled a rather stable upper-bank slope and profile, also because water level fluctuations did not destabilize banks once a mild slope was reached, despite the wave attack at higher levels during floods. Similar conditions apply to the upstream ends of the other embayments (Figure 4.11a), where layers with relatively low erodibility shaped the banklines.

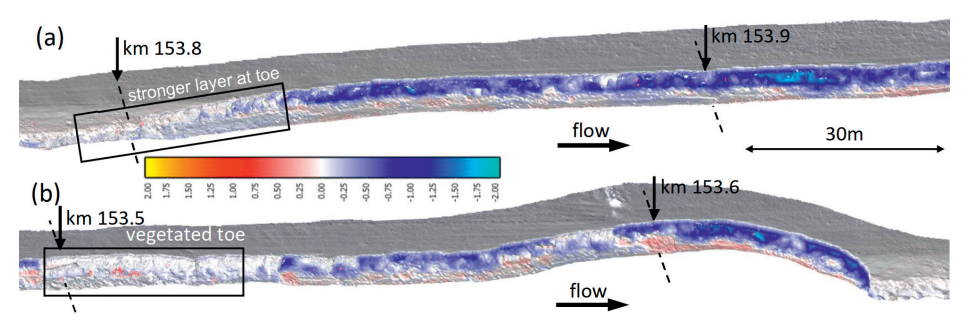


Figure 4.10. Erosion (blue) and deposition (red) between 18-01-2017 and 15-3-2017, represented over the latter bank topography, at (a) km 153.790-153.930 and (b) km 153.490-153.630.

At the downstream end of embayments, banklines crossed layers of different compositions. Here, low-erodibility layers created sharp angles in the bankline that were gradually smoothed by waves and currents (Figure 4.11a). The flow downstream of protruding banks (see e.g., km 153.630 in Figure 4.11a) detached from the upper bank, generating recirculation zones with low velocities over the terrace. At the largest embayment in particular (Figure 4.2 and Figure 4.9c), currents eventually reattached to the upper bank during floods, due to its length. The reattached currents flowing over the terrace converged at the bay end generating high velocities (up to 1 m/s at the 2018 flood peak). This increased the erosion and transport capacity compared to more retreated areas, inducing higher shear stresses over protruding low-erodible layers. Nevertheless, bank erosion rates were relatively low, solely attributed to the presence of more resistant layers given the absence of trees at this location.

Vegetation at the upper bank toe was also found to affect bank retreat rates. Figure 4.10b shows an area that did not present upper-bank erosion after the 2017 flood because of the presence of sufficiently grown vegetation (km 153.5, Figure 4.6b, box in Figure 4.10b). Here, the upper-bank toe remained undisturbed for a sufficiently long time for vegetation to grow thanks to bank retreat rate reduction in 2013 (Figure 4.9a), possibly due to the encounter of a less erodible layer, and the wave dissipation over a developed terrace. Pioneer plants were first observed in 2015 (Figure 4.10b and Figure 4.13b). As a consequence, mass failures were temporarily prevented in stretches where vegetation was able to grow, thanks to relatively low perturbations at the upper-bank toe.

The presence of a gravel armouring layer at the upper-bank toe is another factor that affects erosion rates in the study area. Although erosion rates were controlled by the dominant lithology, the gravel layer at upper-bank toe between km 154.275 and km 154.325 (Figure 4.6d) reduced the erosion produced by secondary waves after 2013 (Figure 4.12d).

4.3.4. TERRACE AND LOWER-BANK EVOLUTION

The terrace topography after seven years of protection removal presents diverse lengths and water depth at the toe (Figure 4.11b) that generally correlate with the different upper-bank retreat rates (Figure 4.11a, 2017 bankline). However, each area presented its own variability of terrace toe water depths and lengths. Figure 4.11, c and d, shows the Kernel density function of terrace toe water depths and retreats related to sub-surface soil cohesion at 8 selected areas. The areas are then grouped into low, middle and high cohesion: C1, C2 and C3, respectively. Subsurface cohesion shows a general correlation with the two main parameters defining the terrace geometry, since the lowest values correspond to fast retreating areas with the deepest terrace toes, and vice versa.

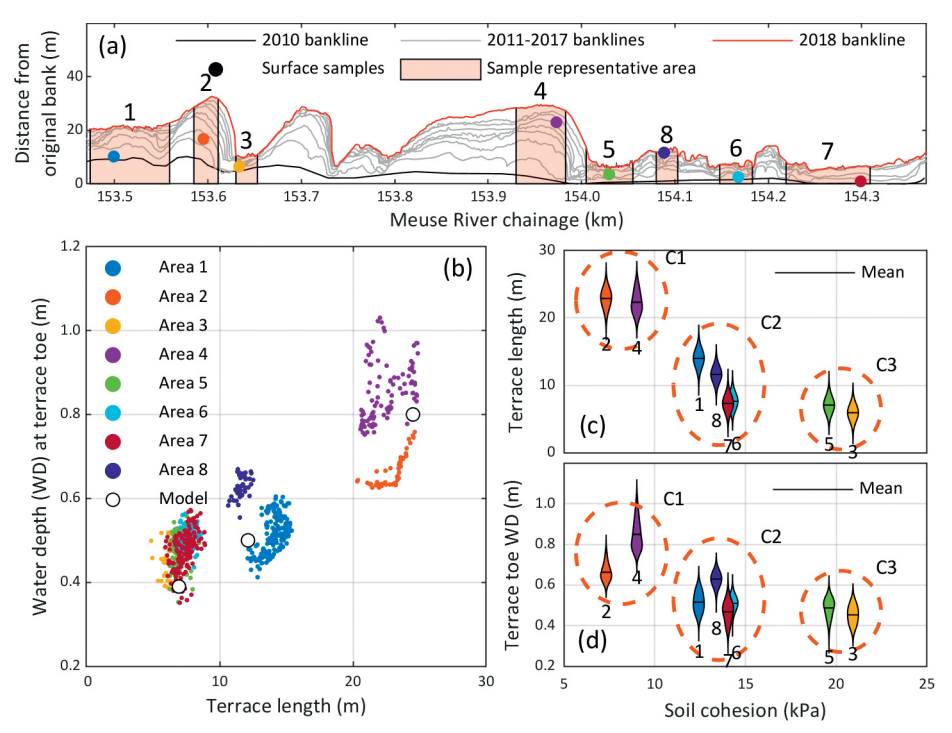


Figure 4.11. Terrace characteristics at zones with different lithologies after seven years of development. (a) Location of surface samples and respective representative areas, with bankline evolution. (b) Terrace length (see Section 4.2.3) and toe water depth (point 2, Figure 4.1) after seven years. (c) Kernel density function of terrace length per lithological cohesion, bandwidth = 0.20. (d) Kernel density function of water depth at terrace toe per lithological cohesion, bandwidth = 0.03.

Figure 4.12a-c shows characteristic profiles of clusters 1-3 (C1-C3 in Figure 4.11c) in 2010, 2017 and 2018. In 2017 and 2018, low-cohesion areas (C1, Figure 4.12a) present a mildly-sloping terrace and considerable upper-bank erosion, whereas high-cohesion areas (C3, Figure 4.12c) have steeper terrace slopes and low upper-bank erosion. Mid-

erodible areas (C2, Figure 4.12b) show intermediate slopes and upper-bank erosion. Erosion rates across terraces are higher at higher elevations, i.e. near the upper-bank toe, and lower near the terrace toe (Figure 4.12d), except for km 154.3 with an armour layer. Moreover, low-erodible lithologies (C3) present the highest terrace erosion rates while high erodible substrates (C1) have the lowest ones.

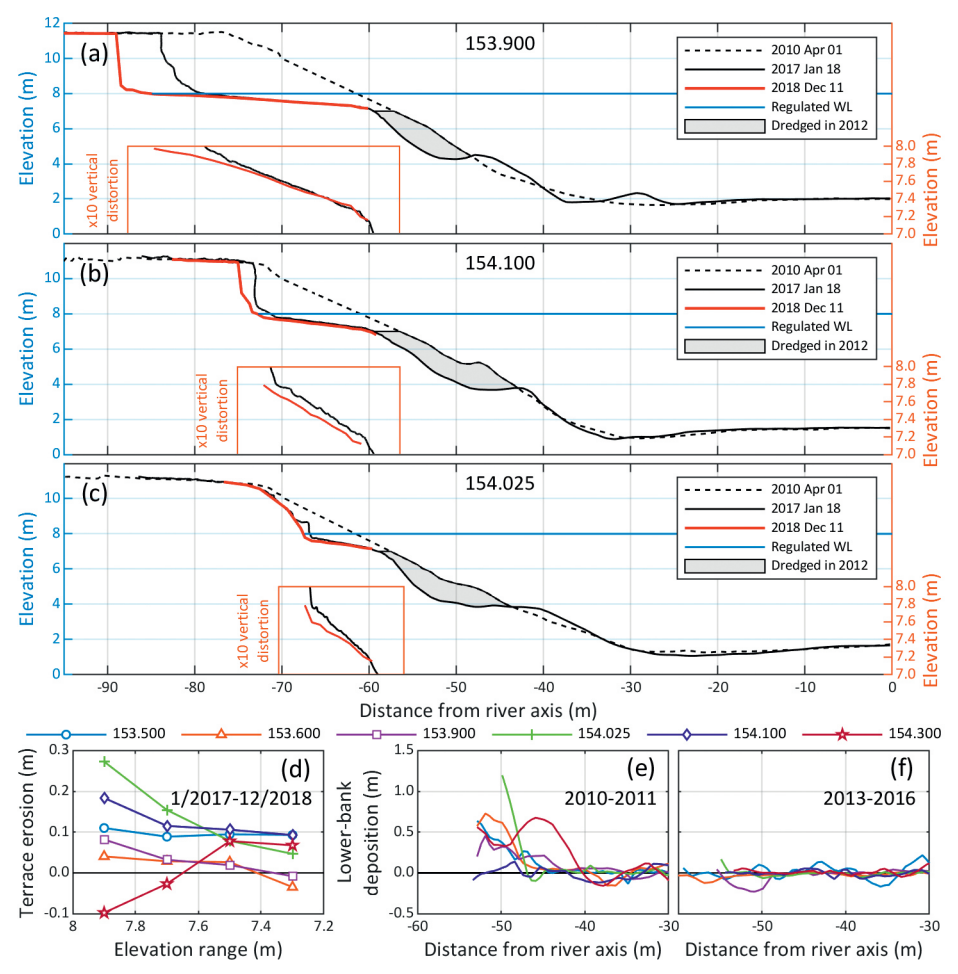


Figure 4.12. Characteristic bank profiles of areas with (a) high, (b) middle, and (c) low erodibilities. Morphological changes of (d) terrace and (e-f) lower-bank at key cross sections (indicated by chainage km).

Different critical shear stresses for entrainment (τ_c) can explain the variety of erosion rates across terrace types. For instance, high-erodible areas (C1) responded faster to wave-induced shear stresses, falling already below τ_c in seven years at the terrace toe, but not at the upper-bank toe where still sufficient wave energy arrives to exert shear stresses above τ_c . On the other hand, C3 areas had slow erosion due to high τ_c , which

combined with still high wave-induced shear stresses result in current relatively high erosion rates. Despite the differences in erosion rates among clusters, terraces evolve in length and depth with a similar spatial and temporal sequence, deepening first the terrace toe and later the subsequent areas across the terrace as it elongates. Final configurations, once shear stresses fall below τ_c along the terrace, thus depend on the strength of each lithology.

Other factors, however, seem to influence the terrace development. The presence of the armour layer in area 7 (Figure 4.11a) can explain the relative short terrace and shallow toe depth compared to areas 1 and 8 of C2, resulting with similar geometrical characteristics to those of cluster C3 (Figure 4.11a-c). Area 6, with a similar terrace geometry to area 7, is possibly affected by bushes on the floodplain that delay upperbank retreat. Moreover, areas 3 and 5 belonging to C3 are both downstream of long embayments, where currents flowing on the terrace converge (see e.g. Figure 4.9c and section 4.3.3) and produce high flow velocities, and thus locally higher erosion rates during floods. It is thus likely that C3 profiles would have shallower and shorter terraces if belonging to homogenous stretches with a uniform exposure to currents.

The morphological changes of the lower bank occurred in three phases after protection removal. During the first phase, between 2010 and 2011 (Figure 4.12e), accretion occurred at the upper part of the lower bank, likely resulting from upperbank erosion. The uneven distribution of sediment yield (Figure 4.11a, 2010-2011 banklines) and transport during the 2011 flood event explain the downstream uneven but general increase of deposits. The second morphological phase consisted of erosion due to artificial dredging of the upper half of the lower bank (2012) by the waterway maintenance authority, to prevent sedimentation from hindering navigation. During the third phase from 2013 to 2016 (Figure 4.12f), the lower bank did not present substantial changes.

4.4. DISCUSSION

4.4.1. SHIP-WAVE AND FLOOD CONTRIBUTIONS TO BANK EROSION

The analysis of data indicates that the terrace is shaped by the regular action of ship waves hitting the bank at regulated water levels during low flows, whereas currents are incapable of entraining sediment once a well-developed terrace is formed. Primary waves shear the terrace during drawdown as a current directed towards the channel, and during their rising limb, as a bore traveling on the terrace towards the bank. During low flows, secondary waves regularly act at regulated levels and less frequently at the depression level of the primary waves. During high discharges, secondary waves do not dissipate over the terrace and hit the upper bank.

During early development stages, when the terrace is relatively short, floods appear to contribute to terrace and upper-bank erosion through current-induced shear stresses (Darby et al., 2007). This implies currents entraining bank material and disaggregating and transporting slump blocks after bank failure (Osman and Thorne, 1988). Furthermore, the presence of ship waves simultaneously attacking banks at high elevations, with low or negligible previous dissipation, promotes further mass failures and block degradation and removal, as observed by Dorava and Moore (1997).

Such a process is more effective than either factor acting alone. The transport capacity of near-bank currents could move blocks without the need to degrade them (Parker et al., 2011). This is also intensified by the high transverse slopes of the terrace at initial stages (Thorne and Tovey, 1981; Baar et al., 2018). The higher downstream and downslope transport of slump blocks and bank material explains the lower-bank deposits observed between 2010 and 2011 (Figure 4.12e), when a large flood occurred soon after riprap removal.

Once the terrace develops so that currents on terrace and bank are sufficiently reduced (Shiono and Knight, 1991), the flow becomes incapable of removing slump blocks. At this stage, currents and waves decouple their effects on bank erosion and lose their feedback mechanism. At this point, floods operate through water level fluctuations, destabilizing steep banks particularly during the rising limb of the flood wave. The latter likely happens at the banks of the study site composed by silty-clay loam to loam due to loss of negative pore-water pressure, with the consequent loss of apparent cohesion and reduction of effective friction angle (Thorne and Tovey, 1981; Casagli et al., 1999; Simon et al., 2000; Duró et al., 2020a).

Failed material accumulates at the toe of the upper bank as slump-block deposit. At the same time, waves not only contribute to destabilize steep banks impinging normal forces (Oumeraci et al., 1993), but also rework the slump-block deposits at varying levels during flow recession. These processes of breaking and moving blocks towards the channel are facilitated by their lighter submerged weight. Once the regulated level is reached again, the blocks that are partially or fully submerged on the terrace are sheared by primary and secondary waves. This gradual process, which occurs with mild terrace slopes, progresses until blocks disintegrate and transform in suspended sediment or wash load (ASCE Task Committee, 1998a). This mechanism explains the absence of substantial lower-bank deposits between 2013 and 2016 (Figure 4.12f), despite the continuous upper-bank erosion that occurred during that period (Figure 4.11a), together with the plumes observed over the terrace.

At this stage, upper-bank erosion occurs with a longitudinal alternation of mass failures and block deposits (herein called modulated failures). This is associated with an increase in form drag during high flows (Leyland et al., 2015), thought to delay erosion rates (Parker et al., 2011). Yet, the actual effect remains an open discussion, since it depends on the simultaneous occurrence of modulated failures and the permanence of block deposits. The observations of this study show the modulation during low flows when slump blocks are not easily removed (see e.g. Figure 4.9c), but it may not be the case during flood events where currents clean the toe relatively fast and bank irregularities seem to smoothen during submerged conditions (Konsoer et al., 2017). This would lead to more random and not modulated failures, increasing instead erosion rates by concentrating shear stresses on isolated block deposits.

In deep embayments, variations in volume of eroded material between low flows and flood periods (see Figure 4.7) are related to variations in erodibility of the lithological layer that surfaces at the upper-bank toe. Low-flow periods define the duration of the time when ship waves attack the upper-bank toe. The steepness and stability of the upper bank before a flood event depends on previous toe erosion. If the toe is not significantly eroded over two or three years, as for instance between km 153.840 and 153.860, upper-bank erosion mainly occurs during floods at the bank top level, decreasing the bank slope by mass failures. In this case the top bank level retreats, but not the toe position.

The development stage at which flow and waves decouple their effects depends on three factors. First, river planform, since the highest velocity is found near outer banks (Thorne and Hey, 1979; Dietrich and Smith, 1984). Here, the flow near the upper bank becomes negligible with a longer terrace; and viceversa for inner banks. Second, longitudinal flow detachment at outcropping low-erodible layers or trees. This requires a certain length before the shear layer develops and flow reattaches to the upper bank (van Prooijen et al., 2005), as observed in the longest embayment of the study reach (Figure 4.2). Third, water depth at the terrace toe, which affects the momentum exchange between main channel and terrace (Knight and Shiono, 1990).

4.4.2. VEGETATION AND BIOFILM EFFECTS ON BANK EROSION

Pioneer vegetation growing at the upper-bank toe has been observed at certain locations along the reach nine years after bank protection removal. It appears that vegetation can only survive the first years of growth under certain conditions. Three locations in the reach presented young trees in July 2019, all of them having a certain degree of protection from wave action, offered for instance, by the presence of rocks on the terrace, which provide extra wave dissipation (km 153.4), or by a groyne

placed upstream to stabilize an outlet (km 154.45). In one case, a less erodible layer (intermediate erodibility: cluster 2) provided both a well-developed terrace and a dry higher ground at the toe, out of the reach of waves during low flows for a couple of years (Figure 4.6b, km 153.5).

At this location, the upper-bank toe presents an even more resistant soil. Possibly, the availability of a loamy texture also provided favourable physical conditions for plant growth, irrespectively of the necessary preceding seed dispersal (Gurnell, 2014) that naturally happened on the study site. The spatial complexity of propagule dispersal (e.g., Gurnell et al., 2008) could explain the absence of vegetation on other locations with similar conditions to the described above. Km 153.5 particularly did not present adjacent hard structures, and the height of colonizing plants at the toe surpassed the floodplain level (c. 3 m) in approximately three years (Figure 4.13b,c).

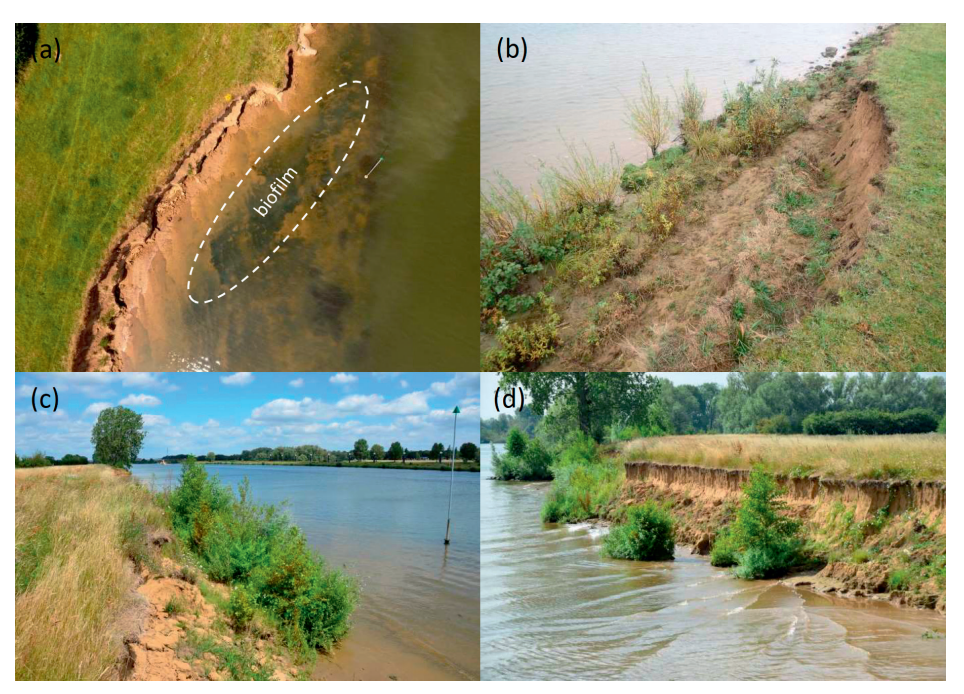


Figure 4.13. (a) Biofilm growing on terrace (July 2018). (b) Plants growing on upper-bank toe at km 153.5 (Nov. 2016). (c) Vegetation at same location reaching ~3 m high on July 2019. (d) Vegetated patches showing different erosion rates than bare soil.

The arrival of waves to the vegetated upper-bank toe depended on terrace elevation. Between January 2017 and December 2018, Km 153.5 presented a terrace lowering similar to km 154.1 (Figure 4.12b,d). Wave dissipation was progressively less effective over the terrace, increasing the wave energy arrival at the upper-bank toe. Figure 4.13d shows waves reaching the upper bank toe where a layer of moderate to low erodibility

lays, which holds a sapling on the centre right of the photograph. On the centre left, a patch with younger vegetation was outflanked by waves, showing higher resistance compared to unvegetated surroundings, and on the other hand, anticipating its removal, as occurred to other young trees in the same stretch (note trunk of dislodged tree on Figure 4.6c).

It appears that plants could grow on relatively low-erodible soil in the presence of either a well-developed terrace (>12 m) or external wave dissipation, generating a time window without much wave disturbance against the bank. Shorter terraces (cluster 3) are subject to shear stresses at the upper-bank toe that are too high for plant colonization, whereas longer ones (cluster 1) present too high erosion rates (due to low τ_c). Low disturbance is necessary for seedling establishment and root growth in other systems too, as for instance on tidal flats (Balke et al., 2011). Even when these conditions occur, subsequent terrace erosion could eventually remove toe vegetation. This agrees with measurements and modelling of salt marshes, which relate marsh retreat to bed level dynamics of the adjacent flat (Mariotti and Fagherazzi, 2013; Bouma et al., 2016; Willemsen et al., 2018), subject to wind waves among other factors.

Vegetation at the upper-bank toe delays the entrainment phase of the erosion cycle by reinforcing the soil through the root system (Khanal and Fox, 2017). Its presence also protects the upper bank from failing once the repose angle of the slump material is reached (Figure 4.10; Simon et al., 2011). However, the duration of these effects depends on the terrace stability. Eroding terraces cannot sustain a positive feedback between bank morphodynamics and riparian vegetation dynamics, typical of fluvial and estuarine environments (Gurnell and Petts, 2006; D'Alpaos et al., 2016). Finally, vegetation persistence also depends on the duration of flood events (Glenz et al., 2006).

After eight years, the terrace presented extended areas covered by biofilms (Figure 4.13a), likely as a result of shallow water conditions during spring and summer, when high shear stresses are only intermittently induced by ships and light easily penetrates to the bed (Thom et al., 2015). Biofilms reduce the local bed roughness and thus wave dissipation on the terrace. On the other hand, biofilms increase the critical shear stress for sediment entrainment (Fang et al., 2014; van de Lageweg et al., 2018; Cheng et al., 2018), but when this threshold is passed clumps detach abruptly removing the membrane cover (Vignaga et al., 2013). The penetration of biofilms into the sedimentary bed results in greater erosion resistance over depth, which is sustained over longer time than with superficial layers (Chen et al., 2017a; Chen et al., 2017b). Biofilms then affect the development of the terrace (Piqué et al., 2016; Fang et al., 2017a; Kakeh et al., 2016).

4.4.3.CONCEPTUALIZATION

The factors governing bank erosion in regulated waterways are different for each evolution stage of the terrace. Initial stages are characterized by a relative high contribution of currents to terrace and upper-bank erosion and high wave impact. Intermediate stages do not present a significant influence of currents on upper-bank dynamics and waves arrive at the upper-bank toe with significant lower energy than in the previous stage. The final stage of terrace development presents a morphology with negligible upper-bank retreat and terrace erosion, when exerted shear stresses gradually reduce to the critical values for entrainment (final configuration). Figure 4.14 schematizes the first two settings.

Initial stages (Figure 4.14a) are characterized by relatively high shear stresses induced by both waves and currents during floods, which drive the upper-bank erosion cycle and terrace erosion. Slump block dynamics are relatively fast, facilitated by downhill transport. In particular, blocks are generally transported to the lower bank before they are completely disaggregated, contributing to lower bank accretion. Vegetation could hardly grow in this context, due to either the relatively fast erosion of the upperbank toe or the frequent high shear stresses at this area. The presence of trees on the floodplain reduces bank retreat rates but the contribution of trees depends on substrate erodibility at the terrace and upper-bank toe elevation range (Duró et al., 2020a).

Intermediate stages (Figure 4.14b) present lower shear stresses at the upper-bank toe and thus smaller erosion rates, which are more favourable conditions for vegetation growth. Slump blocks are sheared near this area for longer times, due to milder transverse bed slopes and negligible currents, disaggregating until the material is entrained, mainly as suspended load. Blocks only contribute to lower bank dynamics through their sand fraction, which is rather low in the case study, the upper bank material being mostly silty loam. Small, but continuous, terrace and upper-bank toe erosion results in slow upper bank retreat, after vegetation decay or removal. Biofilms are able to grow on areas with low erosion rates, temporally influencing critical shear stresses for soil entrainment, but at the same time reducing wave dissipation on the terrace.

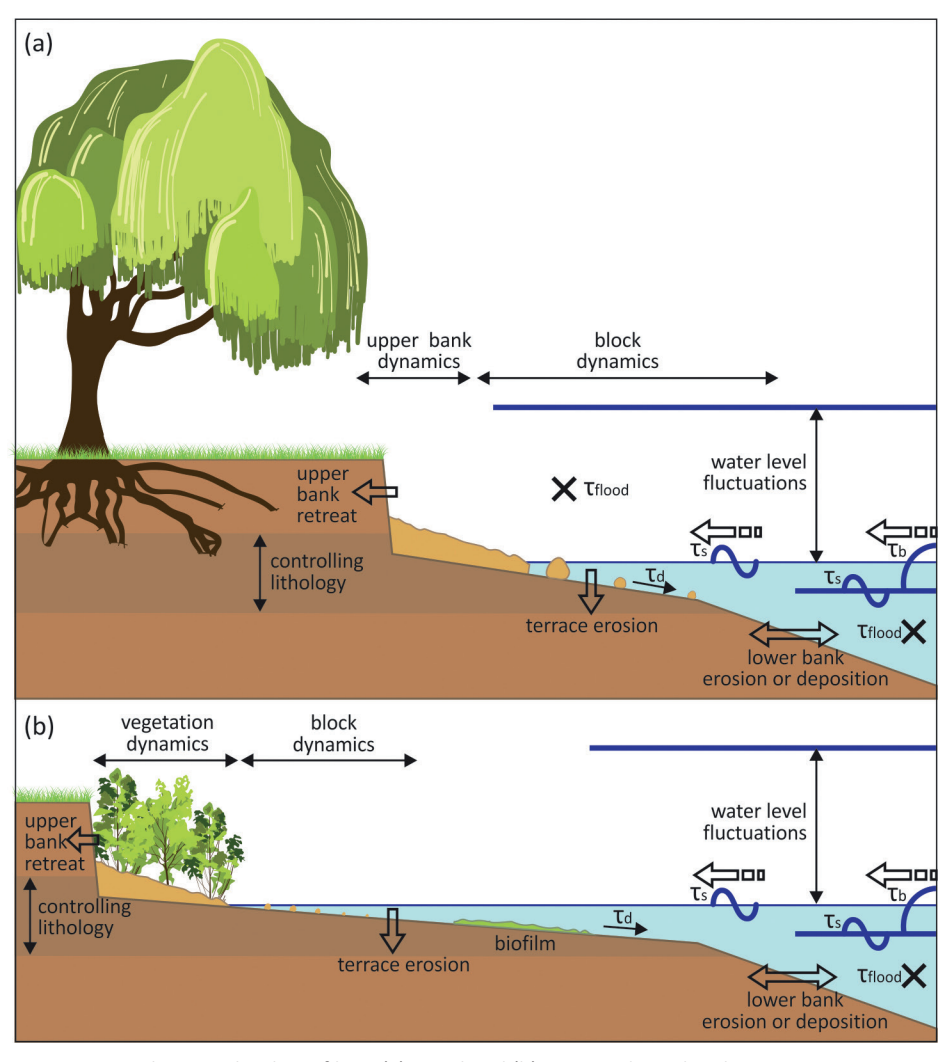


Figure 4.14. Schematic bank profile at (a) initial and (b) intermediate development stages. $\tau_{a'}$, $\tau_{b'}$, and τ_{s} stand for shear stresses respectively induced by primary wave drawdown, primary wave bore, and secondary waves.

Other factors influencing the temporal evolution of the bank profile in the study area are floodplain heterogeneity and the presence of gravel layers. The encounter of a low-erodible layer can drastically change erosion rates, whereas in the opposite case faster rates are triggered. In the latter cases, longitudinal processes driven by flow contribute to smoothen protruding layers. A gravel layer on the upper-bank toe can resist high shear stresses, especially from secondary waves breaking. This creates an armouring effect which delays the upper-bank retreat.

In general, the stability of the terrace depends also on lower bank stability, which is governed by the shear stresses produced by the flow and return currents of ships. The latter depend on waterway sailing conditions, so, as long as they remain constant, the lower bank could eventually achieve a stable configuration. However, intense floods might always produce erosion. Therefore, the stability of the upper bank depends on terrace stability, which in turn depends on lower-bank stability.

Since the terrace is formed due to the persistent action of ship waves at a close range of water levels, unregulated rivers may have a different morphological evolution due to a load distribution spread over a wider range of water levels. This may also have implications for the long-term development of the bank, especially if vegetation is able to regenerate and reproduce thanks to a low frequency of loads at different elevations. A larger window of opportunity also holds for rivers with a lower ship traffic or milder waves than in the case study (e.g. with larger river cross sections). Nevertheless, the impact of floods under unregulated conditions may be larger due to the proximity and exposure of the bank to currents in the deeper channel. Waves would also not dissipate on a mild sloping terrace, so the net impact on the bank could be even higher. Further research is needed to assess the role of ship waves, floods and vegetation dynamics in unregulated rivers.

4.4.4. LONG-TERM EROSION PREDICTION

The final extension of bank retreat is determined by a balance between the exerted shear stresses and the resistance of both the terrace and the upper bank, if the lower bank remains stable. At minimum regulated water levels, ship waves dissipate on the terrace, exerting progressively lower shear stresses as the terrace extends over time. During floods, both current and waves act directly on the upper bank, destabilizing steep slopes and easily transporting slump blocks away. As the terrace extends, currents gradually lose transport capacity of slump blocks and sediments at the upper-bank toe. The final configuration would therefore suppose a terrace that is long enough to dissipate waves during regulated flows and to substantially reduce near-bank flow during floods, with an upper bank either with a mild (e.g., 1:3) repose slope, or a steeper one if the bank is colonized by vegetation. The presence of biofilm might affect the final configuration by changing the local soil resistance against erosion and the bed roughness, but quantifications of these effects encompass high uncertainties since they depend on several conditions and vary with the season (Fang et al., 2017b).

To get an insight on the final configuration of the bank, a model is developed to simulate the bed shear stress distribution induced by ship waves at the most unfavourable conditions, i.e., the largest wave heights acting at the lowest levels. The model computes the shear stresses induced by primary and secondary waves during their propagation, breaking and running-up over a homogeneous terrace, with initial uniform slope. The model updates the terrace morphology with a Partheniades (1965)-type of formula (Equation 4.1), so that erosion stops when bed shear stresses τ_b (Pa) fall below the critical threshold for sediment entrainment τ_c . The erodibility coefficient ε is taken as a calibration coefficient.

$$\frac{\delta z_b}{\delta t} = \varepsilon \left(\tau_b - \tau_c \right) \tag{4.1}$$

 ε is the erodibility coefficient in m/s/Pa. The critical value τ_c (Pa) is estimated after Kimiaghalam et al. (2016) formula based on soil cohesion (Equation 3.6). The bed shear stresses are computed considering primary and secondary wave action as described below.

Primary wave drawdown

The model considers a constant water level gradient during the primary wave drawdown, given by the maximum depression Hp (m) and the terrace length L (m) to estimate flow velocities through the momentum balance in non-dimensional form:

$$\frac{d\left(z_b + h\right)}{dx} + \frac{d\left(U^2 / 2g\right)}{dx} = \frac{U^2}{hC^2}$$
(4.2)

with

$$\frac{d\left(z_{b}+h\right)}{dx} = -\psi \frac{H_{p}}{L} \tag{4.3}$$

 z_b is the bed elevation (m), h the water depth (m), U the average velocity over the depth (m/s), g the gravitational acceleration (m/s²), C the Chézy coefficient (m¹/²/s), and ψ =1/4 an attenuation coefficient (-). The x axis follows the cross-sectional direction and starts at the terrace toe (see later Figure 4.15a). Since the steady flow assumption with maximum linear water level gradient was found too conservative to estimate flow velocities, y compensates for U overestimation, which was estimated by trial and error considering measured velocities. During early development stages, primary waves reach the upper-bank toe before the maximum depression is reached at the terrace toe. As a consequence, the actual maximum energy gradient is lower than the estimated with H_p . These cases consider then an effective primary wave height $H_{p,eff}$ (m) instead of H_p , computed as

$$H_{p,eff} = H_p \frac{T_{UTt}}{T_p/2} \tag{4.4}$$

with
$$T_{UBt} = \int_{0}^{L} \frac{x}{\sqrt{gh}} dx$$

where $T_{\it uBt}$ is the time the primary wave takes to reach the upper-bank toe (sec) and $T_{\it p}/2$ is half the primary wave period. Friction losses are estimated with the Chézy formula, assuming that the flow resistance at a given section is the one of uniform flow with the same depth and velocity. The Chézy coefficient given by White-Colebrook formula was adopted (Equation 4.5), with a Nikuradse roughness height $K_{\it s}$ of 0.02 m. The bed shear stress is computed with Equation 4.6.

$$C = 18\log_{10}\left(\frac{12h}{k_s}\right) \tag{4.5}$$

$$\tau_d = \frac{g}{C^2} \rho U^2 \tag{4.6}$$

with ρ water density (Kg/m³).

Primary wave surge

The primary wave propagates as a bore on the terrace during the rising limb. Bore propagation and dissipation is modelled based on energy balance (Battjes and Jansen, 1978, Equation 4.7), considering refraction and shoaling from an incident angle of χ = 20° normal to bankline (CIRIA et al., 2007) and Snell's law. The water level during propagation is given by the maximum depression reached during the primary wave recession (H_p), assumed horizontal. Since H_p was measured from the regulated level, the stern wave (bore) height is H_b = 1.5 H_p , taken as upper limit considering measured values and CIRIA et al. (2007) formulation. After breaking, Lamb's (1932) dissipation model for fully developed bores is used (Equation 4.10).

$$\frac{dEC_g\cos\chi}{dx} = D_b \tag{4.7}$$

$$E = B_0 \rho g H_b^2 \tag{4.8}$$

$$C_g = \sqrt{gh} \tag{4.9}$$

$$D_b = \frac{1}{4} \rho g \frac{1}{T_b} \frac{H_b^3}{h} \tag{4.10}$$

The primary wave bore is assumed steady with a constant saw-tooth shape, resulting in a variance of the wave surface elevation B_o of 1/12. The bore period (T_b) is taken as 1/3 of the primary wave period (T_p) due to the wave asymmetry in shallow water that steepens the rear slope (Parnell et al., 2015). Tp is taken equal to 25 seconds for deep waves, which corresponds to the deepest recorded of 0.45 m. The breaker criterion for nonlinear waves was also consider, so $\gamma = H_b/h_B = 5/9$ (Didenkulova et al., 2006; Zahibo et al., 2008). The mean velocity under the trough is estimated through Hansen's (1990) regression for experimental data (Equation 4.11), and the simplified velocity profile of Svendsen (1984a):

$$\overline{u_w^2} = \beta^2 C_w^2 \left(\frac{H_b}{h}\right)^2 B_0$$
 (4.11)

where β is the ratio between measured and calculated velocities given by:

$$\beta^2 = 0.8 - 0.5 \tanh \left[2.5 \left(\frac{h}{h_B} \right)^2 \right]$$
 (4.12)

with h_B being the water depth at breaking. C_w is the wave celerity taken as the velocity of the bore (C_B , Hansen and Svendsen, 1987), estimated by Svendsen et al. (1978) as:

$$C_b^2 = gh \frac{d_c d_t}{h^3} \frac{(d_c + d_t)}{2}$$
 (4.13)

with d_c being the water depth at the bore crest and d_t the water depth at the trough. The bed shear stress is computed with a Chézy-type formula (Equation 4.14, Jonsson, 1966), with f_w a friction coefficient for oscillatory flows computed with Equation 4.15, the Colebrook formula (O'Donoghue et al., 2016; Briganti et al., 2018).

$$\tau_b = \frac{1}{2} f_w \rho U^2 \tag{4.14}$$

$$\frac{0.5}{\sqrt{f_w}} = -2\log_{10}\left(\frac{k_s}{14.9h} + \frac{2.51}{\text{Re}\,2\sqrt{f_w}}\right) \tag{4.15}$$

where Re = $u_w h/v$ is the Reynolds number for instantaneous depth and velocity, with v being the water kinematic viscosity (m²/s).

Wave run-up

Assuming a steady bore, the energy dissipation becomes unrealistic near the upper bank toe (Putrevu and Svendsen, 1991), for which the formulation changes into run-up for $h/h_g < 0.15$. The maximum run-up height R_v above the location of the bore collapse is estimated with Equation 4.16 after Bergsma et al. (2019):

$$R_{v} = \frac{\left[\left(Fr_{b,c} + \alpha \right) \sqrt{gH_{b,c}} \right]}{2g} \tag{4.16}$$

where $Fr_{b,c} = U_{b,c}/(gH_{b,c})^{1/2}$ is the bore Froude number at the moment of collapse, being $U_{b,c}$ and $H_{b,c}$ mean velocity and height respectively. α is an empirical coefficient equal to 0.889 accounting for the conversion efficiency of potential to kinetic energy during collapse. The distribution of maximum shear stresses $\tau_{b,\max}$ is then computed using Pujara et al. (2015) non-dimensional relation with the distance along the run-up, based on measurements with different types of breaking waves. The upper-limit linear relation of these measurements reads:

$$\frac{\tau_{b,\text{max}}}{\left(\rho U_{b,c}^2 / 2\right)} = 0.01 \left(1 - \frac{x_R}{R_h}\right) \tag{4.17}$$

with X_R (m) distance over the run-up horizontal length R_h (m).

Secondary waves

The shoaling, refraction and dissipation of secondary waves is computed with Equations 4.7-4.8, with $B_o = 1/8$ for sinuous waves, and group celerity $C_g = NC_w$. N is computed with Equation 4.18 and the wave celerity $C_w = L_s/T_s$ through the dispersion relation of linear waves (Equation 4.19).

$$N = \frac{1}{2} \left(1 + \frac{2\pi}{L_s} \frac{2h}{\sin\left(2h\frac{2\pi}{L_s}\right)} \right)$$
(4.18)

$$L_s = \frac{gT_s^2}{2\pi} \tanh\left(\frac{2\pi}{L_s} 2h\right) \tag{4.19}$$

 L_s is the secondary wave length. The wave period T_s equals 2.25 seconds and the incident angle normal to bankline χ = 45°, being both the average values from the measurements.

The breaker criterion for secondary waves is $\gamma = H_s/h_B = 0.8$, and dissipation is only considered after breaking. Once $h/h_B < 0.15$, run-up shear stresses are computed with Equations 4.16-4.17.

Morphological update

The initial topography consists of a 1:2.5 slope for the lower bank ($s_{l,B}$), in correspondence with the 2010 profile of the case study (Figure 4.12a-c), with 2.5 m water depth at the downhill boundary. The terrace has a $s_{l,B}/4$ slope, equal to the computed maximum (see below). It starts at a depth equal to 0.40 m, after rounding the deepest recorded primary wave. Nevertheless, the computed profiles have a very low sensitivity to the initial bank slope. The model estimates development stages based on a simplified approach of single wave heights (one for primary and one for secondary waves), not representing actual erosion rates. In this way, each time step Δt accounts for the erosion of single events, i.e. ship passings. After each computational step, the terrace elevation is updated resulting in a new geometry for the input waves. The model is run until no morphological changes occur.

The implicit assumption of the model is that development stages are driven by the frequency of occurrence of given wave heights. The highest waves occur less frequent than the lowest ones (Figure 4.5), and thus the terrace morphology takes longer times to adapt to the former. The choice of small input wave heights is representative of initial development stages, whereas higher waves correspond to later stages. Thus, the highest wave happening at a study reach results in the final morphological stage of the bank profile.

The spatial step ΔX for hydrodynamic computations is 0.02 m. The topography is updated through Equation 4.1 with a morphological spatial step ΔX_m of 2 m, considering the mean τ_b over $-\Delta X_m/2$ and $+\Delta X_m/2$ at each point (Figure 4.15a). τ_b along the terrace results the envelope of maximum values of those induced by the primary wave drawdown, primary wave bore, and secondary waves. Those updated points are then checked for minimum (S_{\min}) and maximum (S_{\max}) slopes, whose values are 0 and 0.10 respectively (Figure 4.15a). S_{\min} corrects downhill slopes and avoids negative values considering that irregularities are eventually smoothed by erosion, as observed in the field. S_{\max} acts uphill and prevents the development of a scarp, representing the effect of upper-bank retreat without the actual processes involved. The bed elevations of points with ΔX spacing in between those morphologically updated are linearly interpolated.

Modelled conditions

The model is tested for characteristic values of τ_c for clusters 1-3, respectively taken as 8,12 and 18 Pa (Table 3.1). Two scenarios are modelled for those three cases. In the first, the model is run to represent the profiles measured on 18th January 2017, which are used to estimate e. The constant-height input wave for each case is evaluated by trial and error within the range of measured waves (Figure 4.5d-e). The waves selected as representative for 2017 profiles are those best reproducing them in terms of terrace length and depth at the toe. In the second scenario, the highest measured waves are used to estimate the maximum bank retreat for each cluster.

The input waves for every simulation are a primary and a secondary wave of independent height per event, representing a ship passing. The number of events to reach an equilibrium morphology is unknown in advance. Every simulations repeats the input primary and secondary waves until the bank morphology does not change between two consecutive time steps. For instance, the necessary number of events for clusters 1-3 for 2017 profiles were respectively 223, 93 and 77, and for final profiles 434, 291 and 95 (see the modelled profiles later in Figure 4.15).

The period of primary waves is kept constant and equal to that of the deepest recorded waves, i.e. 25 seconds. The period of secondary waves are set equal to the measured average, i.e. 2.25 seconds. Given that primary waves were found to produce much higher erosion than secondary waves (see next section), only the former were changed among simulations, while the latter were kept with a constant value of 0.45 m, which is the recorded maximum.

Model results

Predicted 2017 profiles present terrace lengths of 24.9, 12.2, 7.4 m, and water depths at the toe of 0.83, 0.59, 0.50 m for C1-C3 respectively (Figure 4.15, continuous black lines), falling within the measured ranges (Figure 4.11b-d). The results indicate that primary wave bores dominate the terrace evolution and final state because they yield the highest shear stresses throughout. This is supported by the fact that secondary waves from recreational boats concentrate in summer, but without an apparent increase of erosion rate over this period (Figure 4.7b). The 2017 profiles reasonably match the measured ones with corresponding primary wave heights of 0.30 m, 0.21 m and 0.15 m, which are within the measured wave heights (Figure 4.5d,e). Since the wave frequency of occurrence diminishes the higher the waves are (Figure 4.5d,e), the model shows that the terrace length of each soil type at a certain time, and consequently for a given wave height, depends on soil erodibility, in this case characterized by τ_c . More erodible banks have a faster morphological response to higher waves, whereas low-

erodible banks need more time to adjust to the same loads. The latter then adjusts to average loads for the given time used to test the model, i.e., seven years. The difference in depth at terrace toes for C2-C3 can be ascribed to this single-wave-height approach which lacks full wave spectra. Such approach could result in a more accurate temporal development, improving the estimate of e. The effects of currents, also relevant close to the main channel, are not included in the model. Yet, the current model is able to represent well the average behaviour and characteristic geometry of each cluster.

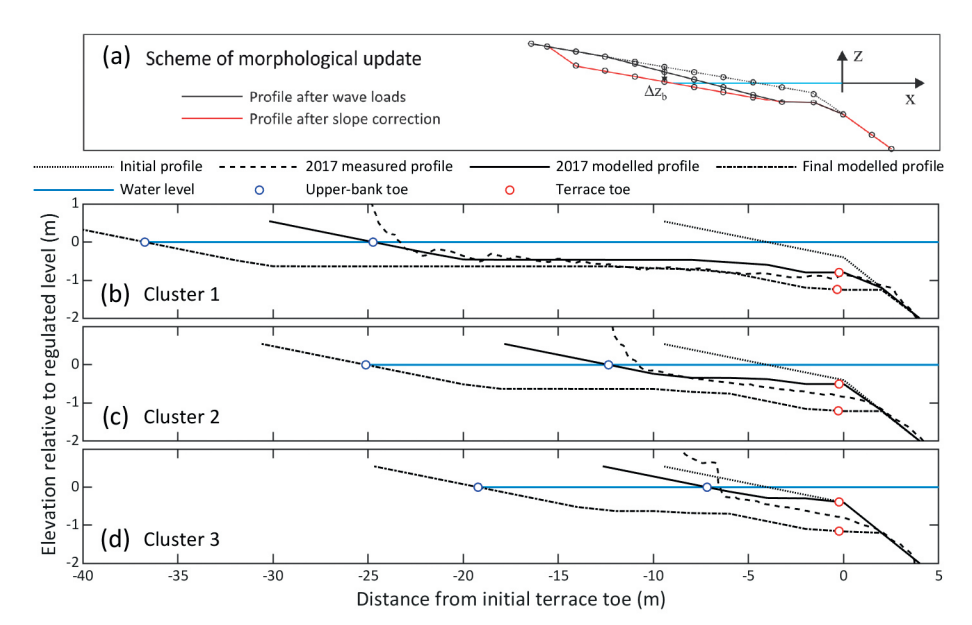


Figure 4.15. (a) Model schematization and long-term upper-bank erosion prediction for soils of clusters (b), 2 (c) and (d) 3, with τ_c = 8,12 and 18 Pa, respectively. Measured profiles on 2017 respectively correspond to km 153.975, 153.100, and 154.025, where samples 4, 8 and 5 were taken.

Discussion of model results

The model shows that for the highest measured loads, i.e. $H_{\rm p}$ = 0.45 m and $H_{\rm s}$ = 0.45 m (Figure 4.5), the final development stages are 50%, 100% and 150% larger than 2017 retreats respectively for C1-3. This suggests that the lower the erodibility the slower the terrace evolution. Furthermore, final profiles show that the lower the bank erodibility the steeper the resulting slope, in accordance with numerical experiments of Bendoni et al. (2019) on tidal flats with cohesive mud-sand mixtures. Field measurements 50 years after stage regulation in the Kanawha River exhibited diverse terrace slopes (Hagerty et al., 1995, Table 1), covering the predicted ones (1:30, 1:21 and 1:17, Figure 4.15) and exceptionally reaching 1:43 for fine sandy silt, which is comparable to the model estimate of 1:45 for the lowest $\tau_{\rm c}$ = 6.4 Pa (Table 3.1). Figure 4.16 shows the terrace

lengths for τ_c and H_p ranging 6-18 Pa and 0.15-0.45 m respectively, which cover the values of the case study, with H_s = 0.45 m assuming constant recreational boat waves and T_p = 25 s considering the lowest period of primary waves.

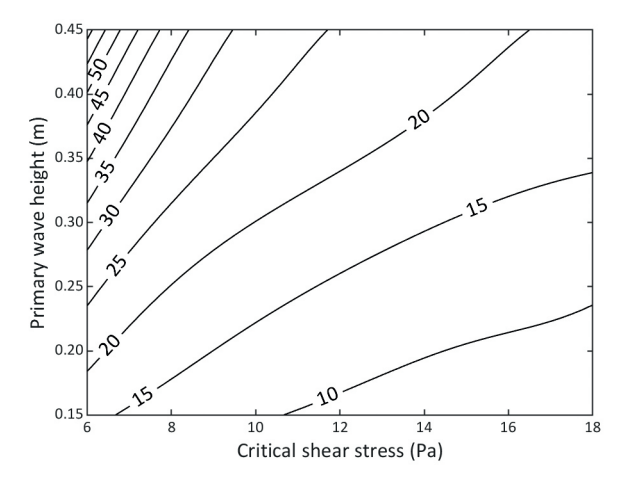


Figure 4.16. Terrace length (m) estimated by the model for varying soil strengths and wave loads.

Previous models and tools to estimate potential erosion in waterways are rational yet empirical in nature (Glamore, 2008; Spruyt et al., 2012). The model presented here addresses this challenge with a process-based approach, requiring measured wave heights and soil characteristics. The above results correspond to $e = 0.01 \,\text{m/s/Pa}$ which was used as calibration parameter to match 2017 terrace parameters. Measured values of e cover a wide range from 10^{-5} to 10^{-2} depending on the erosion mechanism, sediment characteristics and consolidation (e.g., Mitchener and Torfs, 1996; Jacobs et al., 2011). Moreover, the commonly used JET method to estimate e for consolidated soils encompass high uncertainty (Karamigolbaghi et al., 2017), and e is often used for model calibration (Crosato, 2007; Rinaldi and Darby, 2007). Yet, the sensitivity of the model to e is considerable, especially regarding the water depth at the toe, which for instance reduces to 65% with e = 0.001 m/s/Pa, whereas the terrace length reduces to 80% with respect to calibrated values (Figure 4.15).

Nevertheless, the model is able to represent with single wave heights a coherent response of the system, considering the measured profiles and long-term projections, despite the non-linearity of the terrace evolution. Future improvements may include wave statistics, which could increase the accuracy of the temporal developments and e approximations. Other possible improvements are the addition of factors acting in longitudinal direction, such as currents, considering upstream detachment or not, and heterogeneous compositions of different layers, including gravel layers. More advance

strategies could incorporate the effects of upper-bank erosion processes and vegetation dynamics.

4.5. CONCLUSIONS

This work aimed to characterize the processes that drive bank erosion in navigable regulated rivers, integrate the roles of relevant factors, and estimate the final extension of bank retreat. The waves acting on the study site were characterized, showing their dynamics and impact locations. The investigation analysed upper-bank erosion processes, distinct retreat rates across bank profiles, terrace geometry and its relation with soil lithological properties, and the evolution of terrace and lower bank. Finally, the relative contributions of ship waves and floods to bank erosion were discussed, together with observations on vegetation dynamics. This study proposed a conceptual model of bank evolution and developed a numerical model for long-term bank retreat prediction.

Several processes influence the evolution of riverbanks in regulated waterways. The characteristic terrace produced by ship waves attacking at regulated stages develops in two stages, distinguished by the contribution of floods to erosion. Currents during floods initially have significant entrainment and transport capacity, but these effects are reduced by the distance of the upper bank to the main channel. In a second stage, floods simply destabilize banks through water level fluctuations. During low flows and regulated stages, deep primary waves shear the terrace through transverse currents and bores. The latter also erode the upper-bank toe, together with secondary waves that normally attack at this level.

The terrace erodibility given by its lithological characteristics defines the range of lengths and toe elevations at a given time. Soil types have here been clustered in three categories. For each one, the terrace evolves adjusting the length and water depths across the profile, progressively from the toe to the upper bank. Floodplain heterogeneity across single profiles may cause changes from one bank type to another, leading to mixed situations. Currents and waves propagating along the navigation channel tend to smooth bank line transitions. The efficiency of the terrace to dissipate waves, which depends on its length and elevations, eventually controls the upper bank stability. In turn, the permanence of the terrace position depends on the stability of the lower bank.

Other factors affecting the terrace development include upper-bank dynamics, which present a spatial modulation of out-of-phase undermining and basal clean-out, whose occurrence or net effect with longitudinal currents is not clear yet. Slump-block dynamics also affect the terrace evolution by interacting with dissipating waves and currents, which particularly affect lower bank dynamics during initial stages. Grown

vegetation temporarily protects the upper bank from failure and toe erosion, but its permanence is subject to terrace stability and efficiency to dissipate waves. Moreover, vegetation needs sufficient wave dissipation and dry areas in order to establish at the upper-bank toe. Furthermore, the presence of gravel layers and trees on the floodplain also affect the terrace and upper-bank erosion rates.

The long-term terrace stage or final configuration is controlled by the magnitude of primary waves, inducing shear stresses during their propagation as a bore and at breaking, and by the lithological characteristics of the terrace. The necessary time to reach the final stage depends on the abovementioned factors, and is mostly influenced by terrace characteristics and ship traffic, as indicated by measurements and suggested by the model results. It appears that the final stage would asymptotically be reached over time, unless biological factors (e.g., biofilms) or anthropogenic interventions change entrainment thresholds or reduce shear stresses. Biofilm effects on cohesive environments should be further investigated to better assess their impacts on long-term morphology, particularly when penetrating into the subsurface.

The development of a terrace across banks of navigable regulated rivers is driven by the additional loads of ship waves acting at minimum stages. The longer the terrace evolves the more efficiently it dissipates waves, leading to a "self-healing" mechanism. The bank may take decades to reach a stable configuration, in which wave action becomes incapable of entraining more sediment or uprooting vegetation. The factors, mechanisms and time scales presented and discussed in the present work can help managers in their search to optimize all river functions in future strategies. For instance, protecting against the action of primary waves once a well-developed terrace is reached. Future research including unregulated rivers and non-cohesive banks is highly encouraged.



DISCUSSION



The previous three chapters focused on the measurement, patterns and processes of bank erosion along a reach of the regulated navigable Meuse River. This chapter analyses bank erosion in different settings and navigable rivers searching for other relevant processes and factors. Four different cases are considered: a bank with a gravel layer, a bank with a composite vertical structure, a bank under the influence of direct stream flow, and a group of four banks subject to unregulated water levels. This chapter then analyses practical implications for renaturalized banks. Finally, it compares the proposed model with a previous one and discusses its accuracy to predict erosion rates and applicability to unregulated settings, in view of further developments.

5.1. EROSION OF RE-NATURALIZED BANKS IN OTHER SETTINGS

Based on the findings from previous chapters, riverbanks with different characteristics and boundary conditions are analysed further with the objective to identify relevant factors and processes not present or significant in the Oeffelt case study. First, a case in the Meuse River with similar hydrodynamic conditions as Oeffelt is selected to evaluate differences in the morphological response of a bank with a gravel layer and lowerbank protection. Second, another case in the Meuse River is chosen to analyse the evolution of a composite bank in regulated water level conditions and without large effects of currents, because it is located at an inner bend. Third, a case with lower-bank protection along a free-flowing reach of the Danube River is selected to investigate the combined effects of unregulated currents and ship waves on the upper bank. Fourth, four banks in rivers with uncontrolled stages and different boundary conditions are examined to interpret their response to ship waves and other factors in a variety of settings. These differentiate from each other for: i) being located in a straight reach, with lower bank protection (Worms, Rhine River), ii) being located in a straight reach, with lower bank protection, and between transverse groynes (Steinmauern, Rhine River), iii) being in an inner bend, without direct protection, and between transverse groynes (Fortmond, IJssel River), iv) being in an inner bend, without direct protection, and behind a longitudinal training wall (Tiel, Waal River).

5.1.1. GRAVEL LAYER AND TOE PROTECTION: CASE AT SINT AGATHA, MEUSE RIVER

Five kilometres downstream of the Oeffelt reach (analysed in previous chapters), i.e. between km 159.5 and km 160.3, at a location called Sint Agatha, the left bank of the Meuse River presents a gravel layer. Here the river channel has a mild curvature with transverse groynes on the right bank and a continuous bank alignment on the left, from where riprap protections were partly removed in 2015 (Figure 5.1). Poplar trees were planted along the left bank every 100 meters, whose locations are recognizable through their shadows on the water in Figure 5.1. This river reach was not excavated as in Oeffelt. Here the channel was gradually fixed to its current location through training works, which were finalized in the 1950s (Kadaster, 2020). The ship traffic is the same as in Oeffelt, since there are no connecting canals or harbours between these locations. This section and Section 5.1.2 use topographic surveys and soil tests performed by the author in 2019. Topographic and bathymetric data prior to that year were provided by Rijkswaterstaat.

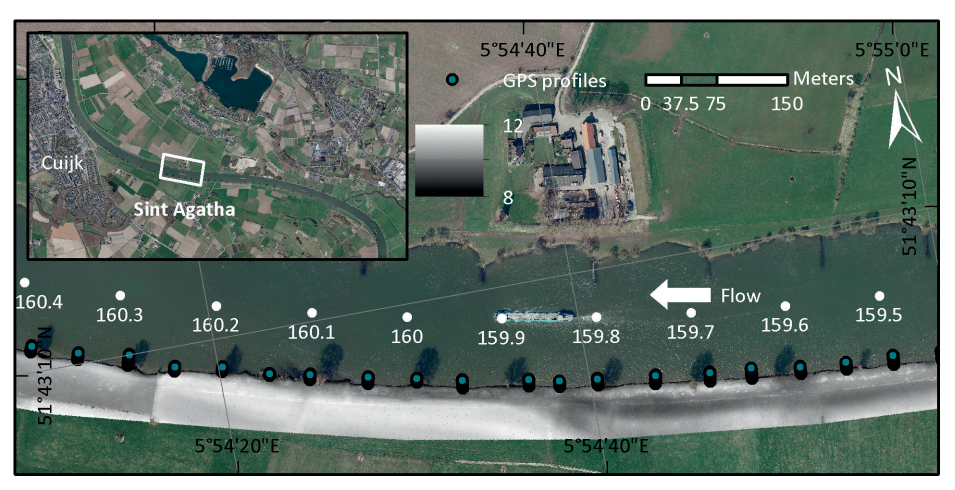


Figure 5.1. Location of Sint Agatha re-naturalized bank of the Meuse River.

Sint Agatha presents shorter upper banks compared to those at Oeffelt, i.e. the regulated water level is closer to the floodplain level (Figure 5.2a). This is because the upper-bank height mainly depends on the distance to the downstream weir, which regulates the water level, and the river longitudinal slope. As a consequence, the erodible bank volume is smaller and the terrace level reaches the root zone of bushes and grass. The upper bank is composed by 57% silt, 22% clay, 21% sand, with a cohesion of 9.1 KPa and an internal friction angle of 29.1 degrees. The upper bank presents also a significant organic material content, noticeable by the characteristic dark colour of the soil (Figure 5.2b, upper-right corner). Furthermore, the bank presents a mixture of gravel and sand (Figure 5.2b) at the elevation range where waves hit the bank and form the terrace, which is circa ±0.5 m from the regulated water level.



Figure 5.2. (a) Downstream view of re-naturalized bank at Sint Agatha, presenting an armoured terrace. (b) Terrace top soil next to upper-bank toe, composed of a gravel-sand mixture.

As a result of soil composition, the terrace evolved leaving a gravel layer at the surface where secondary waves dissipate (Figure 5.3). Moreover, the transport of this material towards the lower bank is limited by the presence of a longitudinal rock protection at the terrace toe. The riprap was left along this river reach up to an elevation of approximately 0.5 m below the regulated water level, with the intension of keeping control of the lower-bank position while reactivating upper-bank dynamics. As a consequence, the terrace toe is fixed at a depth ranging between 0.5-0.7 m, (see e.g., Figure 5.4).



Figure 5.3. Upstream view at Sint Agatha bank where ship waves dissipate over armoured terrace.

In April 2019, the analysed bank profiles (Figure 5.1) had lengths ranging between 10 and 12 meters. Figure 5.4 shows the evolution of a typical bank profile between 2017 and 2019. Within this period, the bank retreated for about one meter and the upper elevation of the terrace, an area frequently exposed to wave breaking, experienced erosion. The rest of the terrace slightly accreted, likely as a result of material redistribution from the upper bank. The general trend was thus of small terrace tilting. The terrace toe in Figure 5.4 seems to have also increased its elevation, but this is ascribed to the irregularity of the rocks and different GPS operators between surveys. Grass growth can explain elevation differences on the floodplain (airborne LIDAR surveys in 2014 and 2017).

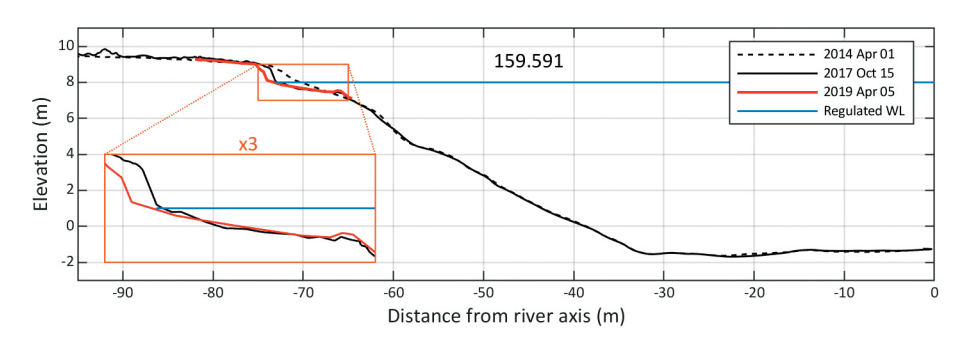


Figure 5.4. Bank profile at km 159.591, Sint Agatha, with typical length of 11 meters and 0.6 m depth at the terrace toe in 2019 (note 2:1 vertical distortion).

The toe protection intersects the elevation range where ship waves cause bank erosion, which for instance reaches depths of 1.1 m at Oeffelt (Figure 4.11), influencing the terrace development. The toe protection probably affects the propagation of deep primary waves, which are the main driver of long-term retreat, but not of secondary waves (see e.g., Figure 5.3). The combination of a gravel layer covering the terrace and a fixed toe will likely result in a gradual upper-bank retreat with an increasingly milder terrace slope, tilting around the toe. A final development stage is expected once the terrace effectively dissipates secondary and primary waves, whose slope and length will depend on the sediment size of the gravel layer. Then, the profile will arrive to a dynamic equilibrium similarly to coastal beaches (Dean, 1991), where Shields numbers may stay slightly above the threshold for mobility.

The described behaviour naturally depends on the availability of gravel deposits across the bank, which makes a different situation compared to the banks at Oeffelt reach. The non-cohesive bank material makes the terrace development dependent on transverse sediment transport and critical Shields numbers, in contrast to critical shear stresses for entrainment in the case of cohesive banks. The restricted water depth at the toe limits wave penetration, shortening the ultimate terrace length. The final configuration will then likely be in closer resemblance to cluster 3 (Figure 4.15) than other cohesive bank configurations, which an upper-bank cohesion of 9.1 kPa would instead indicate.

5.1.2. COMPOSITE BANKS: CASE AT NEERLOON, MEUSE RIVER, THE NETHERLANDS

In the Meuse River, between km 179.6 and 181.0 (Figure 5.5), i.e. between the weirs of Grave and Lith (Figure 5.5), we find the other case study reach near a village called Neerloon. This part of the river was excavated in the early 1950s, cutting a former meander off (note the oxbow lake in Figure 5.5) and creating a bend with milder curvature (Kadaster, 2020). A secondary channel was excavated in 2009 behind the right

bank, for flood safety. Then in 2015, the left bank was re-naturalized through complete removal of riprap protections. Commercial ship traffic at this location is significantly lower than at Oeffelt (Figure 4.5), because many vessels divert upstream to the Rhine River via the Maas-Rijnkanaal, resulting in 29 ship passings per day, on average (Figure 5.6).

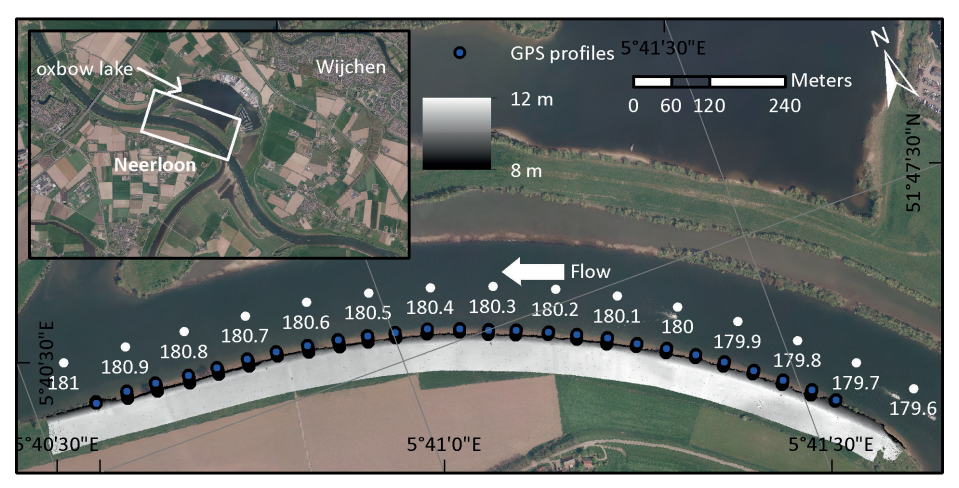


Figure 5.5. Location of Neerloon re-naturalized bank in the Meuse.

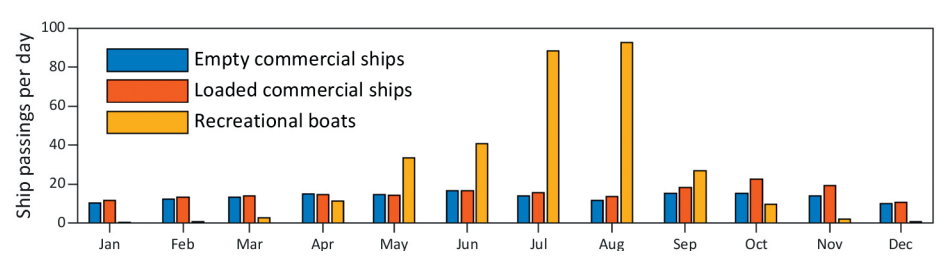


Figure 5.6. Daily ship passings at Neerloon in a typical year.

At Neerloon, the Meuse River presents composite banks with two soil layers, the upper one with cohesive and the lower one with non-cohesive behaviour (Tovey and Thorne, 1981). This type of banks typically fails as cantilevers, which happens after the faster erosion of the lower non-cohesive material, leading to the collapse of the overhanging cohesive layer. Figure 5.7a shows a situation after failure in which slump blocks from the upper layer lay on the sandy terrace. In the study site, the upper-bank cohesive layer is composed of 54% silt, 21% clay, 25% sand, with a cohesion of 14.6 kPa and internal friction angle of 21.8 degrees. The lower layer is composed of sand, whose non-cohesive behaviour is apparent comparing panels b and c of Figure 5.7, which show the collapse of the sand layer by its own weight moments after the excavation was made.



Figure 5.7. (a) Downstream view of the left bank at Neerloon, with cohesive slump blocks over a sandy terrace (April 5, 2019). (b) Composite structure with transition at the upper-bank toe. (c) Lower sand layer collapsing by own weight at same location, after few minutes of excavation. (d) Upstream view of stretch with longer terrace than panel a) on same day.

In the study site, the floodplain level ranges between 8.4 and 9.2 m NAP. The minimum regulated water level at this location is 5.2 m NAP, which is close to the transition between the cohesive and non-cohesive layers in 2017-2019 (Figure 5.8). The morphological changes between these two years show upper-bank retreat with terrace accretion, likely resulting from a cross-sectional redistribution of bank material. Between 2015 and 2017, just after riprap removal, the lower bank accreted as well, also possibly after redistribution of upper-bank material. At Neerloon, the upper-bank retreat and terrace length had significant variations between 2015 and 2017, from 6 to 15 meters (Figure 5.9), although water depths at the terrace toe remained within a relative narrow range.

The vertical heterogeneity of the bank likely formed during the past migration of the meander bend (Figure 5.5), which was interrupted after river canalization. Scroll bars across the current channel alignment determined sand deposits with a swale-ridge topography lying about the elevation of the present regulated water level.

Above these non-cohesive sediments, finer deposits filled the topography up to the higher elevations of the current floodplain. The differences in upper-bank retreat can be explained by slight variations in the elevation of the transition between these soil layers, so stretches with a deeper cohesive stratum present less retreat due to a greater erosion resistance, and on the other hand, a slightly higher interface produced faster erosion of the sand layer, causing cantilever failures and faster overall retreat.

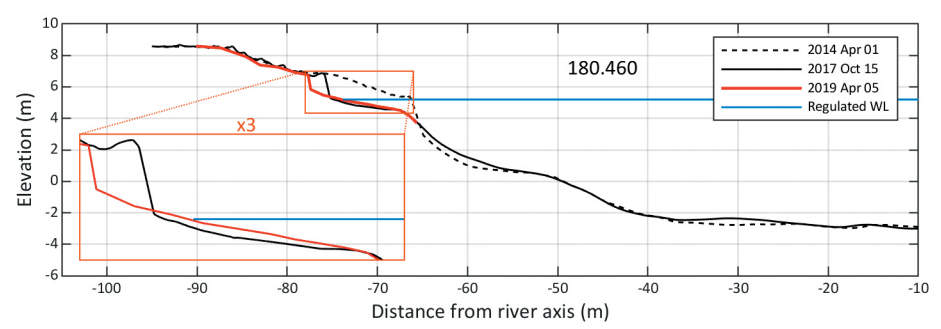


Figure 5.8. Bank profile at km 180.460, Neerloon, showing upper-bank erosion and deposition over the terrace (note 2:1 vertical distortion).

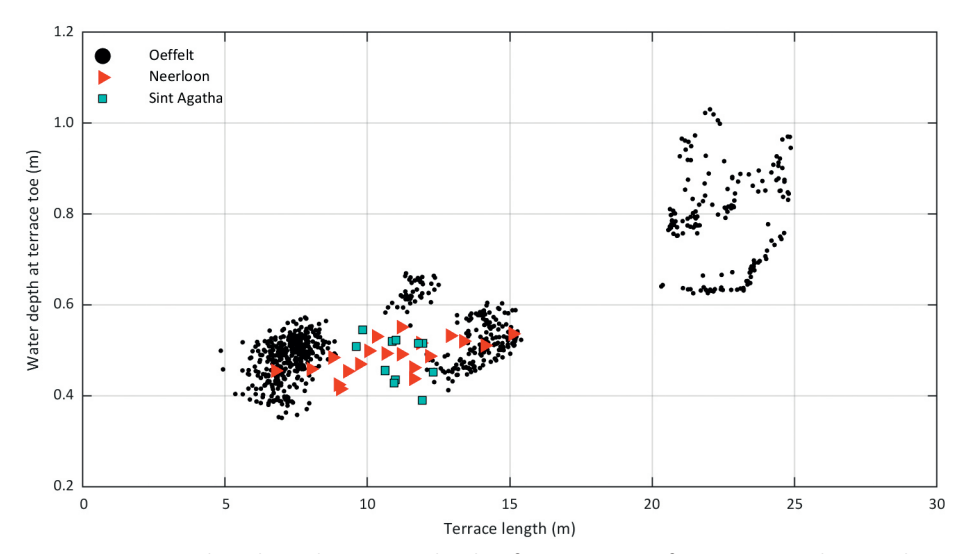


Figure 5.9. Terrace lengths and toe water depths after two years of riprap removal at Neerloon and Sint Agatha reaches, compared to Oeffelt cases after seven years of restoration (see Figure 4.11 for coloured series).

The bank morphology with moderate terrace extents and slopes (Figure 5.9) presents characteristics of an early to intermediate development stage. The upper-bank material accretes the lower bank and terrace with sand and cohesive slump blocks, which do not completely disaggregate before being transported downslope (Figure 5.7a,d). Instead, the blocks roll down over moderate slopes and are exposed to longitudinal flow and primary-wave currents, due to moderate terrace lengths and the absence of salients. The absence of vegetation growing at the upper-bank toe indicates high erosion rates, especially in areas dominated by sand-layer response, or high shear stresses, particularly important at locations where bank erosion is dominated by the cohesive-layer behaviour.

The terrace geometric relations at Neerloon differ from those at Oeffelt (Figure 5.9), especially for the longest ones. The cross-sectional redistribution of the sand deposits from the upper bank to the terrace raise the toe elevation and, in many cases, extend the terrace length through lower-bank depositions. In other words, the water depths at the toe and terrace lengths do not mainly respond to erosion processes, as in Oeffelt, but are also dependent on accretion. The dynamics of non-cohesive sediment deposits, as the case of Sint Agatha gravel layer, depend on sediment transport relations driven by flow and ship waves, so that the temporal cross-sectional development of bank profiles is affected by such processes. In addition, seepage may also increase erosion rates of the sand layer (Section 1.2.3).

Given the fact that the sand layer appears to dominate the soil composition at the minimum regulated level, the long-term bank profile development will be determined by the morphological response of such lithology to deep primary waves, while the upper layer will affect the temporal development. The resulting terrace slope will then defined by a transverse dynamic equilibrium, as described above for gravel layers (Section 5.1.1). The occurrence of floods inducing significant shear stresses at the terrace toe will affect the equilibrium depth and possibly the location of the toe across the river section, so that shear stresses remain within a range that are compatible with cycles of sediment deposition and erosion over the years.

Furthermore, depending on the extent of the ridge-swale topographic modulation of soil layers across the bank, defining the soil erodibility near the regulated water level at this reach, the equilibrium bank profile may encounter mixed regimes of terrace characteristics defined by the different soil compositions intercepted by the bank profile.

5.1.3. CURRENTS AND RIVER PLANFORM: CASE AT THURNHAUFEN, DANUBE RIVER

The re-naturalized Thurnhaufen bank is located on the left side of the Danube River, 4 km upstream of the Austria-Slovakia border. At this location, the Danube River has moderate nival regime, with mean discharge of 1,930 m³/s, a bankfull and maximum navigable discharge of 5,060 m³/s, and a 100-year return period peak of 10,400 m³/s (Liedermann et al., 2014). The average water level is 137.8 m a. A. (meters above the Adriatic), which can range from 135.25 to 144.80 m a. A. (www.noel.gv.at/wasserstand/). The river reach where Thurnhaufen is located, was channelized in the late 19th century for navigation, and yet has unregulated water levels and free flowing conditions. This area currently belongs to Donau-Auen National Park, established in 1996 and subject to several restoration projects since then. The main channel keeps serving as waterway for 14,000 passing vessels per year (Danube STREAM, 2019).

Thurnhaufen bank extends along an inner bend from km 1885,75 to km 1882,90, opposite to the town Hainburg an der Donau (Figure 5.10a). Completed in 2006, renaturalization involved the upper bank only, i.e. above 137.5 m a. A., to ensure the main channel stability. The floodplain level is at 143.0 m a. A., which means that renaturalization covers 5.5 m of bank, measured in vertical direction. Water levels stay above the protected lower bank for 60% of the time, on average. Ship waves may then frequently reach the re-naturalized bank. Here, focus is on the most upstream kilometre of the restored river reach, i.e. between km 1885.5 and km 1884.5, where erosion occurred after the removal of bank protection. In contrast, the bend apex immediately downstream is a natural depositional area (note point bar in Figure 5.10a).

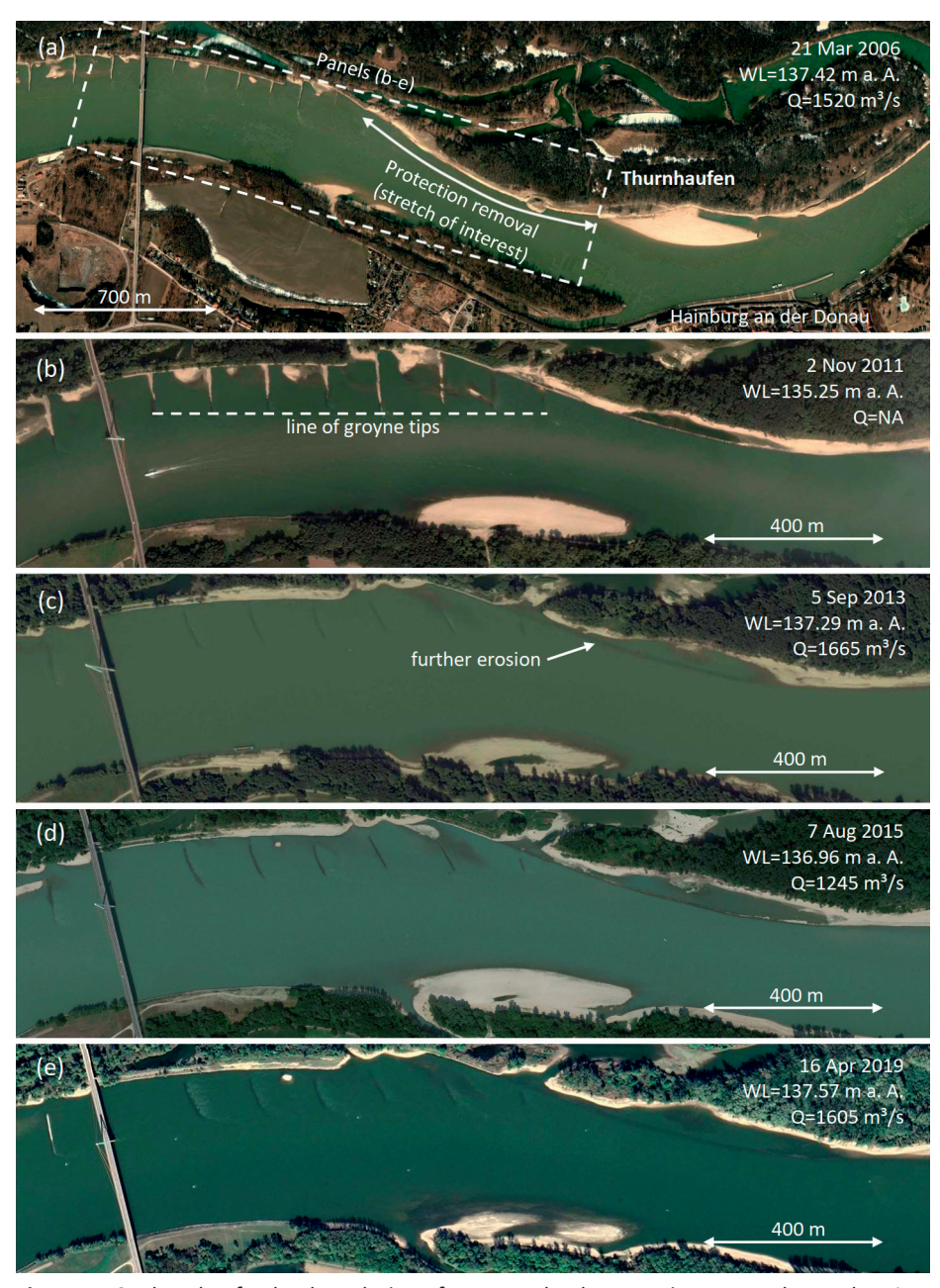


Figure 5.10. Thurnhaufen bank evolution after upper-bank protection removal, Danube River. (a) 21/03/2006. (b) 02/09/2011. (c) 05/09/2013. (d) 07/08/2015. (e) 16/04/2019. Source: Google Earth.

Figure 5.10 shows the evolution of bankline retreat as seen from aerial photographs, distinguishable between the first line of trees and the lower-bank protection along the original bankline. The latter is noticeable in Figure 5.10b-e given the relatively low water

levels. Between early 2006 and the end of 2011, the bankline presented an average retreat of 25 m at the centre area of the stretch of interest (Figure 5.10a), with a highest retreat of 35 m at the upstream part. Importantly, the bankline shape at the latter zone seems to follow the pathway of the upstream groyne tips (Figure 5.10b). Within this period, a terrace formed as the upper bank retreated (Figure 5.11).

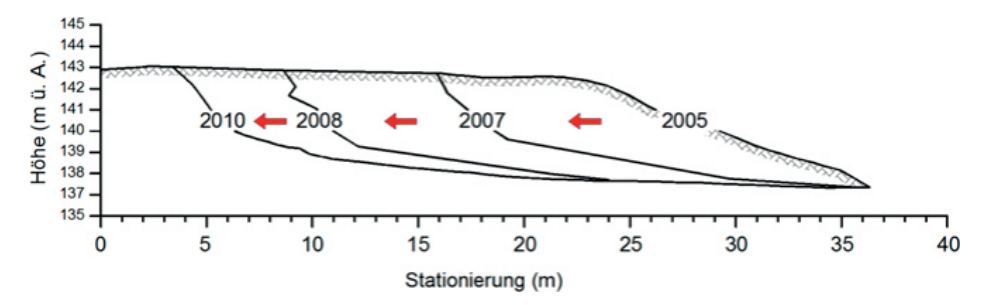


Figure 5.11. Bank retreat at Thurnhaufen, where Y axis indicates elevation in m a. A. and X axis distance in meters (from Habersack and Klösch, 2012).

In 2012, the groynes located upstream of the Thurnhaufen bank were replaced by new ones with a different shape and position (compare Figure 5.10b and Figure 5.10c), to optimize flow conveyance and reduce bed degradation (Pilot Project Bad Deutsch-Altenburg, www.viadonau.org). The latter responds to better guided streamlines by the curved groynes, which likely created a more efficient cross section with lower flow velocities in the channel centreline, reducing the sediment transport capacity. In turn, this intervention increased the flow velocity near the groyne tips and downstream bank. Figure 5.10b-c show a significant bank retreat within two years (2011-2013), reaching a total shift up to 50 m. Within this period, on 6th June 2013, a flood peak of 10,750 m³/s occurred. Once more, it is noteworthy the alignment of the new upstream groyne tips with the first half of bankline shift within the most eroded zone (Figure 5.10c).

Afterwards, the progression of bank retreat decelerated. From 2013 to 2015 (Figure 5.10c-d), the terrace lost sediments at the downstream zone but no significant bank retreat happened. From 2015-2019 (Figure 5.10d-e), the bank only eroded locally, downstream of the most retreated area in 2013 and in the direction of the groyne tips, i.e. following the previously observed pattern (Figure 5.10b-c). Between November 2013 and April 2019, flood events reached 5,000 m³/s.

Despite deep drawdowns induced by passing vessels, recorded up to 0.45 m in this river reach (Liedermann et al., 2014), the studied bankline seems to have followed a retreat pattern driven by currents. The flow impinged against the initial location of retreat (Figure 5.10b) guided by the position of upstream groyne tips, whose efficiency was

possibly improved after the new design. Bank erosion followed this straight alignment until 2019 (Figure 5.10e). The dominant role of currents on upper-bank erosion is also supported by the evolution of terrace sediments, whose erosion progressed from upstream to downstream direction. Therefore, at this stage of bank development, currents appear effective in entraining bank material, producing bank instability, and transporting slump blocks and sediment away, covering the full erosion cycle. A rather parallel bankline retreat (see e.g., Figure 5.1 or Figure 5.5) would have favoured the hypothesis of erosion dominated by ship waves. Hence, the terrace topography at this case study is not only shaped by ship waves propagating and breaking over it, but significantly by currents flowing over the lower-bank protection.

From a different perspective, the influence of oblique strata from past channel migration cannot be discarded, although in such a case a bay-shaped or rounded transition between the original bankline and a strong stratum would be expected. Nevertheless, this would not prevent currents from carving through different strata strengths if exerted sufficiently high shear stresses (see e.g., Figure 4.9c). Despite a potential influence of lithological spatial variations, which cannot be confirmed without specific data, the bankline does not seem to follow a clear pattern determined by those, as it does the path of groyne tips guiding intense currents. The latter also explains the erosion of sediments from the terrace in downstream direction.

The hypothesis presented herein suggests that currents during flood events shape the upper bankline. The location of the bank in the river planform then represents a primary cause of bankline retreat, defining the exposure to steered currents. Ship waves contribute to erosion rates and terrace evolution for as long as deep primary waves reach the upper bank, which in the long term can further shift the bankline shaped by currents. The bank in this case study presents closely spaced trees on the floodplain that increase bank stability and resistance against entrainment. An equilibrium at Thurnhaufen bank could eventually be reached with a fixed lower bank, when ship waves and current do not exert sufficient loads far behind the lower-bank protection to further surpass the upper-bank resistance, enhanced by dense root systems.

5.1.4. UNREGULATED WATER LEVELS: CASES AT WORMS (RHINE RIVER), STEINMAUERN, (RHINE RIVER), FORTMOND (IJSSEL RIVER), AND TIEL (WAAL RIVER)

This section analyses two bank profiles of the Rhine River in Germany and another two at its downstream branches, the Waal and IJssel Rivers, in the Netherlands. The main differences between unregulated and impounded rivers are the unrestricted fluctuation of water levels and higher flow velocities throughout the year. In this section, terrestrial

photographs after bank protection removal are used to identify early morphological responses under those conditions. After a description of bank profiles, observations are analysed and interpreted. The focus is on the scarp and mild sloping part of the bank, or above the lower-bank protection when existing.

Worms, Rhine River

The re-naturalized right bank of the Rhine River is located near Worms, between km 441.475 and km 441.600, in a rather straight reach. Here, the main channel is 300 m wide, with a mean discharge of 1,410 m³/s and a 100-year flood of 6,300 m³/s (http://undine.bafg.de). The mean water level is 86.25 m. a. NHN (meters above NHN, German reference level), with regular fluctuations of 4.95 meters (www.elwis.de). This bank is composed by gravelly sands covered by c. 2 m layer of alluvial clayey deposits (Heibaum and Fleischer, 2015). Bank protection was removed in December 2011 when also the bank slope was reduced from 1:3 to 1:7. In 2015, Heibaum and Fleischer (2015) reported toppled trees and a dislodged shrub caused by bank erosion, which also uncovered some old rubble part of former protection works. In April 2016, the bank presented large woody debris and some remains of the old rubble, partially protecting the mild-sloping and short (~10 m) terrace (Figure 5.12a). The scarp was slightly undermined presenting signatures of seepage erosion.







Figure 5.12. Unprotected upper banks in the Rhine River. (a) Test section near Worms on 12/04/2016, after riprap removal in 2011. (b-c) Section between groynes near Steinmauern on 23/03/2019, after protection removal in 2013 (courtesy of Petra Fleischer).

Steinmauern, Rhine River

Bank re-naturalization near Steinmauern was performed in 2013 on the right side of the Rhine River, from km 343.550 to km 343.800. The mean discharge at Maxau am Rhein, 18.5 km downstream, is 1,250 m³/s, the 100-year flood 5,300 m³/s. The mean water level in the study area is 102.79 m. a. NHN, with normal fluctuations of 4.26 m. The fairly straight river reach near Steinmauern has regularly spaced groynes of variable length at one or both banks that reduce the effective channel width from 230 m to 150 m during low flows (note one submerged in the background of Figure 5.12b), but not opposite to the re-naturalized bank. This is composed by gravel and sand, with alluvial loam at the top. In 2013, the protection above 102.3 m. a. NHN was removed, the slope changed from 1:3 to 1:7, and the surface covered with a layer of 63 mm to 180 mm stones (Petra Fleischer, personal communication). In 2019, the bank presented a milder terrace and a scarp (Figure 5.12b-c), evidencing terrace erosion and upper bank retreat.

Fortmond, IJssel River

The re-naturalized bank is located on the left side of the IJssel River, the Netherlands, to the south of the village Fortmond. Here, the IJssel River is 100 m wide between opposite groynes. The mean river discharge is 390 m³/s, the bankfull 750 m³/s, and 100-year floods reach 1,900 m³/s (Reeze et al., 2017). Water levels can range up to 6 meters. Yearly commercial ship passages are 8,000 at the nearby city of Olst. Bank protection were extracted between groynes along 1,050 m of an inner bend (Figure 5.13a), but the stretch of interest and focus of study is only on the downstream 280 m between the last two groynes, since upstream groynes have a spacing of 70 m and a stronger influence on bank morphology. This bank presents a composite structure, consisting of a top cohesive layer of 1-2 m clayey sand above a sand stratum. Figure 5.13b shows these different strata soon after protections were removed in 2010. Later in 2016, the bank showed signs of erosion through the lowering of the sand stratum, the formation of a composite scarp of c. 1.5 meters, and the partial coverage of the sandy terrace with slump blocks from the upper cohesive layer (Figure 5.13c).



Figure 5.13. Re-naturalized bank opposite to Fortmond, IJssel River. (a) Bank location, with star showing where photos of panels b and c were taken. (b) Upstream view on 13/04/2010, after protection removal (courtesy of Margriet Schoor), and (c) during site visit on 22/03/2016, with Maarten Kleinhans, Wim Uijttewaal, Margriet Schoor, and Alessandra Crosato.

Tiel, Waal River

The freely eroding bank resulted from the excavation of a side channel in the left floodplain of the Waal River downstream of the city of Tiel. It is located at the second of three consecutive longitudinal training dams constructed in 2014 along this river reach (Figure 5.14a). The main branch of the Rhine River conveys an average discharge of 1,600 m³/s and a bankfull discharge of 3,400 m³/s. Water levels can range up to 8 meters. The main channel width between groynes is typically 230 m. Commercial navigation in this reach produces 88,000 ship passages every year.

Longitudinal training dams (LTDs) can be regarded as large-scale pre-banks (see Section 1.2.5) since they separate the main navigable channel from the riverbank, particularly covering a significant extend of the river width for a distance of several river widths. The LTDs at the Waal River, in particular, generate side channels of approximately a quarter of the main channel width and extend along more than 10 main channel widths. This allows for potentially significant morphological interactions between both channels in the long term (Le et al., 2018), although the inlet of side channels conditions the entry of discharge and sediments (de Ruijsscher et al., 2020).



Figure 5.14. New bank behind longitudinal training dam near Tiel, Waal River. (a) Bank location, with star at km 917.5 indicating where photos of panels b and c were taken (source: Google Earth). (b) Upstream view on 19/12/2015 and (c) on 10/05/2016. Courtesy of Frank Collas.

The focus here is on the second kilometre of the second LTD, whose total length is 3.2 km. The bank has a composite structure with a top cohesive layer of approximately 1 meter and a lower sand stratum (Figure 5.14). Ship waves are able to reach the upper elevations of the bank, propagating over the LTD during high water stages. Figure 5.14b shows the bank profile approximately a year after construction. After winter and a part of autumn, within which a flood of 3,500 m³/s took place, the profile appeared with a steeper slope and a higher scarp (Figure 5.14c), indicating that erosion occurred during the previous five months. Slump blocks were present at the upper-bank toe, and undermined sections of the upper layer were also observed (Frank Collas, personal communication).

Interpretation of observations

The cases considered above indicate a common pattern of erosion through the lowering of the profile and the formation and retreat of an upper bank or scarp. In presence of lower-bank protection, as in the cases of the Rhine River, the lowering of the bank results in the formation of a terrace whose slope tilts around the fixed toe. Once a scarp is formed, the bankline retreats through sequential failures. In case of fully unprotected banks, as those in the IJssel and Waal Rivers, the lower bank may freely shift affecting

the upper bank morphology. For instance, the mean water depth and width of a side channel behind a LTD respond to morphodynamics at larger scales, through the exchanges between main and side channels. This process may eventually lead to an equilibrium width and a stable lower bank, from which an upper profile might evolve responding to local erosion mechanisms, such as those driven by waves or seepage.

The contribution of individual factors to the observed bank erosion cannot be quantified without detailed field data. Still, considering the different settings of the case studies, interpretations of respective effects can be done based on previous analyses. For example, considering the bank position at the downstream end of an inner bend (Figure 5.13a), the sloping bank at Fortmond (Figure 5.13c) possibly responded to the action of ship waves and currents, with a likely lower contribution of the latter. The presence of upstream groynes further reduced near-bank velocities at the stretch of interest. In such a case, primary and secondary waves were dominant drivers forming the sandy terrace. On the other hand, the Tiel case had a threshold for wave penetration given by the LTD. Therefore, the steepening of the sandy sloping bank likely resulted from erosion produced by flow, since no significant return currents were present due to absence of commercial shipping in the side channel. The upper-bank toe, however, presented a sandy scarp (e.g., Figure 5.14c) associated with wave runup in coastal beaches (van Bemmelen et al., 2020), for which wave attack during higher flows probably took place.

The presence of cohesive slump blocks and collapsed upper banks (Figure 5.12c, Figure 5.13c, and Figure 5.14c) are the indication of a bank retreat event that previously happened. The processes that can explain the erosion of composite banks include upper layer instability by wave attack or rapid water level drawdown, and faster erosion of the non-cohesive layer undermining the upper layer until failure (see Sections 1.2.2 and 1.2.3). The latter mechanism can be triggered by wave- or current-induced entrainment and by seepage erosion, particularly during flood recession. All four cases appeared with signatures of seepage erosion, such as eroded sandy layers and undermined upper cohesive layers. This erosion mechanism probably increased retreat rates at these case studies due to the composite structure of the banks, unlike the Oeffelt case where seepage did not have a significant role.

Ship waves seem to shape riverbanks with steeper slopes in absence of a prevailing water level (Figure 5.13c). In highly regulated rivers like the Meuse, a terrace was carved through cohesive banks with increasingly mild slopes as retreat progressed. The Fortmond case presents a rather steep bank slope even with a sand stratum. This may be the situation at an early stage in the bank evolution, presenting a slope that might decrease in the long term. Still, the erosive effects of ship waves can act at a larger range of elevations throughout the year, spreading the loads over a larger surface.

Ship waves do not have significant dissipation without a mild sloping terrace. It seems then reasonable to expect erosion at varying elevations that lead to steeper slopes compared to those shaped with controlled water levels, also considering that lower layers destabilize upper layers.

In the long term, freely eroding banks in unregulated rivers develop a mild terrace from a mean low water level. As non-cohesive sediments normally lay at lower levels sorted by alluvial deposition, a long-term equilibrium profile seems plausible as a transverse dynamic equilibrium with mobility close to critical values. Such system would be subject to longitudinal processes of sediment transport that in turn depend on reach-scale morphodynamics. In settings with restricted longitudinal mobility, such as groyne fields, the conditions for transverse equilibrium would be met. Stratified cohesive upper banks may reach an equilibrium with different slopes according to individual erosion resistances. Finally, the establishment of dense vegetation in the long-term or the presence of gravel layers can change ultimate retreat magnitudes by increasing thresholds for entrainment.

5.2. HOW TO COMBINE NAVIGATION, REDUCED EROSION AND MORE NATURAL BANKS?

The re-naturalization of banks aims to improve the river ecological status through an increase of hydromorphological diversity and the reactivation of bank dynamics. Freely eroding banks in navigable rivers are exposed not only to flow but also to ship waves, which are responsible for the formation of new shallow areas. In the case study at Oeffelt, long-term bank retreat induced by deep primary waves is expected in the order of tens of metres, approximately ranging from 20 to 60 m, depending on soil erodibility (Figure 4.16). During the intermediate stages of bank development, vegetation at upperbank toe is subject to high ship wave loads (Section 4.4.3), despite being at a favourable position for stability (Section 1.2.4). Waves hinder the growth and survival of vegetation in diverse lithologies, including highly cohesive banks, where ship waves exert high loads on the terrace and upper-bank toe, and weakly cohesive banks, where erosion rates dislodge or prevent vegetation establishment.

As a consequence, the possibility that eroding banks offer to diversify the hydromorphology in highly trained rivers, and to enhance habitat variety for flora and fauna, is threatened by the existence of high loads on the new shallow water areas. Furthermore, primary waves perturbate this habitat structure with a moving water line and high velocities, resulting unfavourable for young-of-the-year fish and inappropriate for early-stage larvae (Schludermann et al., 2014). Negative effects of ship waves involve shoreline ecosystems too, where invertebrates show a decrease of growth rates (Gabel

et al., 2017). However, at some river sections, the restoration of erosion processes recreated vegetation dynamics of growth and uprooting, which is considered a positive biotic response (Hetfield et al., 2007).

Vegetation cannot control erosion under these conditions, as neither do slump blocks. They extend the duration of the erosion cycle, but cannot stop it. Erosion progresses when shear stresses exceed thresholds for entrainment of reinforced soils or slump blocks. The effectiveness of the temporary delay depends on the type of substrate and roots. For example, cohesive soils significantly increase their erosion resistance when permeated by woody roots, as more sandy soils do with fibrous roots (see Section 1.2.4). Moreover, trees at floodplain level showed a primary dependence on substrate type leading to diverse responses to erosion drivers (Section 3.6.2). This implies that re-naturalization projects need to consider the local substrate in order to expect a significant reduction of erosion rates caused by grown, and preferably dense (Section 1.2.4), vegetation.

Vegetation establishment at upper banks likely takes place once a well-developed terrace forms, thus in the long term. Depending on lithological and ship traffic characteristics, that stage may take decades to be reached. From a managerial perspective, it may be convenient to reach ecological targets in shorter terms. An option for that aim is to reduce the dominant drivers of bank erosion in order to increase the windows of opportunity for plants to grow and withstand (or recover from) remaining loads. The actual establishment naturally depends on the availability of appropriate soil, nutrients and climate conditions as well.

Strategies can be specifically defined to settings with regulated levels, where ship waves are confined to a narrow range of elevations during most of the time, and currents gradually reduce exerted shear stresses on upper banks as retreat progresses. Since waves dominate upper-bank toe erosion once a well-developed terrace is formed, with deep primary waves inducing the highest loads, a sensible approach seems offered by an armoured pre-bank at the terrace toe, slightly below the regulated level (e.g., 0.20 m for Oeffelt case). A slightly submerged pre-bank has a number of positive functions:

- A significant reduction of the impact of primary waves, by limiting the highest drawdown to the submerged depth of the pre-bank, and therefore the maximum transverse energy gradient and the available volume for water exchange between the side and main channels.
- The pre-bank acts as submerged breakwater for both primary and secondary waves, reducing their energy before reaching the upper bank.

- Vegetation has a larger window of opportunity to grow at the upper-bank toe due to less hydrodynamic disturbance (Caponi et al., 2019).
- Fishes can surpass the pre-bank and reach calmer zones.
- The gap above the pre-bank enables flow exchanges during low flows.
- Low waves can surpass the pre-bank, aerating the water through breaking or reaching the upper bank toe, which possibly keeps a low degree of active bank dynamics.
- Stone pre-banks can serve as habitat for mussels providing biofiltration (Collas et al., 2020).

It is advised to optimize this type of intervention in terms of length, inlets and outlets to the secondary channel (Boeters et al., 1997), as well as for the case of LTD. Other strategies have been suggested in literature to reduce loads on banks, such as improved hull designs and speed limits for vessels (Söhngen et al., 2008; Gabel et al., 2017; Scarpa et al., 2019). The latter particularly requires consensus, legislation, and control to be implemented.

One of the consequences of eroding banks is the sediment yield to the river, which may deposit on the riverbed and affect minimum depth for navigation. The deposition on the main channel is expected larger during the initial stages of bank development, when currents still have a significant contribution in all phases of the erosion cycle (Section 4.4.3). This is due to the fact that slump blocks do not completely disaggregate on the terrace before being transported away, so that the mud fraction which could otherwise become wash load forms blocks that increase the bed level. At later stages of bank evolution, the main contribution to lower bank accretion is the sand fraction of the upper bank. If interventions such as pre-banks are planned to reduce wave loads, upper-bank erosion should be already low before implementation, so that sediment yield is not too larger before vegetation can colonize the upper bank toe.

Large-scale restoration, as those performed in the Meuse and IJssel Rivers in the Netherlands, can consider a variety of measures to set the most appropriate for each stretch. This concerns ecological targets and structural requirements for other river uses. Each stretch may present different local bank characteristics, such as lithology or location in the river planform, which make some approaches more convenient than others to optimize river functions. In this regard, an estimation of the final retreat with the proposed model (Section 4.4.4) may help to make such assessment, for instance, to differentiate freely eroding banks from those that require some degree of protection, e.g., with technical-biological alternatives (Section 1.2.5). The necessary steps to apply the current version of the model are:

- Identify soil cohesion from the range -1.00 m to +0.50 m with respect to the minimum regulated water level.
- Estimate critical shear stress for entrainment, e.g. with Equation 3.6.
- Measure ship waves at the river reach or estimate deepest drawdowns, e.g. with CIRIA et al. (2007).

5.3. MODELLING SHIP-INDUCED BANK EROSION

Modelling riverbank erosion driven by ship waves entails the representation of the characteristic terrace in regulated rivers, or a mild-sloping bank in unregulated conditions. A bank terrace evolves over time, with a decreasing slope as the upper bank retreats. This affects wave propagation and breaking, and therefore, bank retreat has a dependency on the non-linear interaction between the terrace morphology and wave transformations. These effects are not included in the schematization of BEM (Verheij, 2000), which requires a constant terrace slope as input parameter, conditioning its predictive capacity. On the other hand, the Ship-Induced Riverbank Erosion Model proposed in this thesis (SIREM for simplicity) does account for the morphological adaptation of the terrace which responds to the depth-dependent wave shear stresses, resolving the interaction between bank shape and ship waves. Furthermore, the lower bank in SIREM is not fixed as in BEM, which enables the adaptation of the terrace toe to acting loads.

The assumption of both BEM and SIREM to consider homogeneous banks is substantiated by the fact that the soil composition close to the minimum regulated water level is a decisive factor for bank retreat rates and the final bank configuration. That assumption appears then reasonable when banks present a rather homogeneous composition near the controlled level and the parameters for bank strength ($c_{\rm E}$ or $\tau_{\rm c}$ -e) are chosen to characterize this location. This is a clear advantage of modelling regulated rivers compared to unregulated cases. An important difference between BEM and SIREM, however, is that SIREM includes both primary and secondary waves as erosive agents. The former turned out to exert the highest shear stresses on the bank, defining the long-term equilibrium of the bank morphology. This is thus a fundamental factor to consider in a ship-induced bank retreat model, which is not incorporated in BEM.

The approach to represent the temporal evolution of bank retreat significantly differs between BEM and SIREM. The first explicitly proposes a temporal evolution of bank retreat (Equation 1.3) while SIREM focuses on long-term equilibrium, despite accounting for the terrace development. For that reason, the current reproduction of bank erosion rates by SIREM is poor (Duró et al., 2020c) and requires further changes and calibration to improve the prediction of temporal bank retreat. The next section discusses possible

improvements to achieve a more realistic estimation of bank retreat rates, and in turn a potentially more accurate prediction for long-term equilibrium. Section 5.3.2 later analyses how this model can be extended for its application to unregulated rivers.

5.3.1. BANK EROSION RATES IN REGULATED RIVERS

SIREM estimates the ultimate bank retreat through the temporal morphological evolution of the bank profile, in regulated rivers. Intermediate development stages result from the morphological adaptation to sequential waves. The proposed model reproduces reasonably well, both in qualitative and quantitative terms, the bank geometry of measured bank profiles by accounting for the effects of essential driving processes and factors. Single wave heights are able to represent intermediate morphological stages (e.g., 2017 profiles used for calibration in Figure 4.15), despite the simplified approach. However, in order to predict specific intermediate stages of bank retreat, it is unknown in advance what the dominant wave height or respective frequency of occurrence is. This is a major shortcoming from a practical perspective.

In order to overcome this limitation, which considers unlimited numbers of single wave heights until an equilibrium profile is reached, future improvements to SIREM can incorporate the actual number and timing of different ship waves. A possible approach is to use time intervals that capture typical intra-annual variations of ship traffic, such as monthly time series that are statistically representative of the type, height, and number of ship waves. Chronological sequences would then affect the non-linear morphological bank evolution (Southgate, 1995), for which a sensitivity analysis with different series would be desirable. This model upgrade requires the recalibration of the erodibility coefficient ε , which should be separately determined for different bank strengths (see Section 4.3.4) to obtain more accurate results. This approach would likely achieve more accurate estimates of long-term bank equilibrium too, because more realistic ranges of wave characteristics will affect ultimate bank retreat through the non-linear response of the bank morphology.

A next stage to improve the predictive accuracy of bank retreat rates is to include processes that significantly affect them, through their effects on τ_b and τ_c . There are particularly two whose inclusion would cover broader conditions and potentially result in more accurate predictions. The first is flow-induced erosion during floods. Shear stresses induced by currents during floods can be especially relevant at initial stages of bank development (Section 4.4.3). These can be estimated, for instance, over compound cross-sections following Kordi et al. (2015) and setting representative hydrographs and varying water levels, or by coupling SIREM with a hydrodynamic model as was done with other bank erosion models (e.g., Gibson et al., 2015). The second are upper-bank

erosion processes which involve three phases (Section 1.2.2). These are complex to represent and would require many more data from the banks than the current version of SIREM, which absorbs their effects in e and the maximum slope S_{max} (Section 4.4.4).

The following should be considered if the effects of upper-bank erosion processes are to be implemented in SIREM:

- The moment of geotechnical instability. The case studies showed that mass failures mostly happen due to wave-driven undermining or are induced by water level fluctuations. A model as BSTEM (Langendoen and Simon, 2008; Lammers et al., 2017) could be adapted and coupled to compute the timing, type and size of failures.
- Slump-block degradation and transport on the terrace. Wasted bank material, which could be of diverse compositions if incorporated in the mass failure module, delay bank retreat. This is especially important for long terraces where longitudinal transport during floods is low or null. This implies the computation of slump-block dynamics produced by both ship waves and currents. Such challenge could be initially addressed by a Shield's type of approach (Equation 1.1; Verheij, 2000; Eke et al., 2014). Furthermore, block degradation induced by currents and waves are important mechanisms too. This would also require new insights on the physical processes of degradation and transport of slump blocks.
- Entrainment at steep banks. Expressions that represent shear stresses by waves
 onto steep and vertical surfaces are necessary to incorporate erosive processes
 induced by impinging waves (e.g., Bullock et al., 2007). This happens at early
 development stages and notably later, once terrace level at the bank toe has
 eroded sufficiently and slump blocks are removed, so waves do not break before
 reaching the bank scarp (see, for instance, Figure 1.8b).

The presence of grown vegetation at the bank toe reduces erosion rates by attenuating wave loads and strengthening the soil (e.g., Coops et al., 1996). This was also observed in this research at banks with extended terraces (e.g., Figure 4.12b). Vegetation dynamics with their effects on hydrodynamics and soil strength may be incorporated in SIREM as understanding of those processes and conditions for vegetation growth and uprooting increases (Edmaier et al., 2011; Gorla et al., 2015; Bankhead et al., 2017; Calvani et al., 2019). For example, formulations for root growth rates, critical rooting length, and shear stress reduction by stems can be implemented (Pasquale et al., 2012; Chen et al., 2018; Bau et al., 2019). Nevertheless, biomorphodynamic models still have a high degree of uncertainty for quantitative assessments, given the complex nature of the processes involved (Bertoldi et al., 2011; Tron et al., 2015; Tinoco et al., 2020) and lack of accurate models for specific processes, such as the increased resistance of root-

permeated soils to flow erosion (Zen and Perona, 2020). As a result, incorporating vegetation dynamics will not yet result in more accurate quantitative predictions of the bank terrace temporal development.

Only at few locations of the analysed cases vegetation was found to grow at the bank toe. Relatively low hydrodynamic perturbances and erosion rates are necessary conditions for growth (Section 4.4.2), but other environmental factors such as soil type, moisture conditions, and seed dispersal are also decisive (Gurnell, 2014), for which growth becomes largely uncertainty. Incorporating vegetation dynamics on SIREM can, however, serve to assess appropriate timing to plant vegetation or cuttings at the bank toe, with the intention to increase the opportunity to colonize the upper bank or to analyse strategies to reduce or control erosion (van Batenburg, 2020).

5.3.2. BANK EROSION IN UNREGULATED RIVERS

The application of SIREM to unregulated rivers requires recalibrating the current version to improve the estimation of erosion rates, particularly through ship wave statistics, as discussed in the previous section. Given that the non-cohesive layer of composite riverbanks is normally exposed to waves and currents without controlled water levels, SIREM needs also to be further developed to account for sediment transport across the bank, and thus for mass balance. Different formulae for bedload transport could be applied, as well as expressions for suspended sediment transport, driven by both currents and waves (see e.g., Deltares, 2020). The latter mode of transport is common for mudflats, where fine sediments prevail and profiles maintain a dynamic equilibrium in a yearly time scale, despite seasonal variations (van der Wegen et al., 2019). Lower layers of riverbanks usually contain sand and gravel due to former alluvial depositional sequences, for which the inclusion of only bedload transport appears a first reasonable approach to model composite bank erosion induced by ship waves.

The addition of a non-cohesive layer in SIREM requires a new scheme for stratified banks. Although lower layers are likely responsible for the largest proportion of bank retreat at long-term equilibrium, the upper cohesive strata also affect the final retreat. Both cohesive and non-cohesive layers should then be represented, whose relative thickness will influence the shape of equilibrium profiles and retreat magnitudes. Furthermore, statistically representative water level series should be considered as model input. Over variable water stages, primary and secondary waves should propagate and impact the bank. It is particularly important to include the effects of different water depths on the generation of primary waves, since ship blockage in the river section and the distance to the bank are key factors to produce the Bernoulli

effect causing the drawdown. Empirical formulae could be used for this, such as the ones proposed by CIRIA et al. (2007).

The application of SIREM to unregulated rivers could also benefit from the inclusion of more processes, as for regulated rivers (Section 5.3.1). Relevant ones are effects of erosion processes of the cohesive layer (mass failure, slump-block dynamics, entrainment at steep slopes) and longitudinal sediment transport produced by currents. For the latter, coupling with existing hydromorphological river models may be a convenient strategy, as these can consider the river planform and flow obstructions, such as groynes. More complex versions could include other processes affecting erosion rates, such as vegetation dynamics or seepage, induced during flood recession or by excess pore water pressure during primary wave drawdown (Heibaum, 2002).

Section 5.3 shows that SIREM has the potential to increase its predictive accuracy, for both retreat magnitudes and rates, and cover different river settings. There are a number of approaches, models, and formulations already available that can be implemented. As the understanding of physical and biological processes expands, further mechanisms can be incorporated in the future. The next chapter presents the conclusions of this thesis and indicates recommendations for prospective research.





6.1. CONCLUSIONS

This thesis provided novel insights into bank erosion processes occurring in regulated navigable rivers, explained the morphological evolution of bank profiles, and developed a model that represents the observed morphodynamic behaviour and estimates long-term retreat.

To achieve these goals, a recent technique to capture geomorphic changes was successfully applied to measure the three-dimensional complexity of riverbanks along a considerable extent. Particularly, a methodology was proposed to apply structure from motion photogrammetry with photos taken from an UAV to combine two scales of analysis: the reach and process scales. The technique is fast to deploy in the field and surveys reach-scale riverbanks in sufficient resolution and accuracy to quantify bank retreat and identify morphological features of the complete erosion cycle. This enables the characterization of bank erosion at the process scale, including the spatial distribution and timing of different erosion phases. Minimum requirements of paths, camera perspectives, number of photographs, and distribution of ground-control points were identified in order not to reduce the precision potential of a single UAV flight. This methodology allows practitioners to survey banks with UAV for monitoring and design.

In a second research step, the distinct bankline patterns of the Meuse River were unravelled, linking past large-scale river migration with present geomorphological features and erosion rates at single cross sections. The oblique alignment of the river canalization with respect to the orientation of depositional layers of varying compositions, defined during former channel meandering, led to the formation and asymmetry of large embayments. The patterns appeared above the controlled water level whose frequent occurrence determined the persistent attack of ship waves at that elevation. Ship waves shaped a mild sloping terrace across bank profiles of diverse lithologies, each having own geometrical proportions. Isolated trees on the floodplain only locally delayed erosion rates, which primarily depended on the lithology near the minimum regulated water stage. The inherited geology before the canalization thus largely controlled the bank dynamics, in contrast to freely meandering rivers where banks are continuously created and eroded by contemporary fluvial processes.

The analysis of bankline evolution and erosion processes revealed the active role of ship waves on erosion progression, even at well-developed terraces. Currents initially contribute to all phases of the erosion cycle, but they gradually decrease exerted shear stresses on the upper bank as the terrace elongates. Their later role at intermediate stages of development is reduced to the destabilization of steep high banks through water level fluctuations, without capacity to transport slump blocks. Bank profiles with diverse erosion magnitudes at Oeffelt showed different stages of morphological

evolution after seven to nine years of protection removal. More cohesive banks were still at early stages of development, whereas least cohesive banks were already at intermediate stages. At the latter, biofilms covered some terrace areas, changing entrainment thresholds.

Based on the conceptual framework of bank profile evolution, a model was developed that captures the observed non-linear morphodynamics driven by ship waves in regulated settings. This new tool estimates long-term retreat by accounting for the main erosion drivers and essential mechanisms. Equilibrium bank profiles are reached once wave-induced shear stresses fall below the threshold for entrainment of cohesive soils. Unlike previous models of ship-induced erosion, the process-based approach enables to distinguish the contribution of each factor to erosion. Primary waves exert the highest loads on the terrace, shaping long-term profiles and defining ultimate retreat. To apply the model, it is necessary to measure or estimate the largest primary wave and the soil cohesion at the controlled level, preferably in the range -1.00 m to +0.50 m with respect to it.

The above findings are based on cohesive banks in a straight reach of a regulated river. The presence of gravel layers in the bank introduces a change in the morphological response to ship waves since thick-enough layers can armour lower strata. In such a case, the bank terrace can reach a transverse slope in dynamic equilibrium defined by grain size, as long as longitudinal currents do not transport the gravel to the lower bank, which is especially relevant to consider during large floods. In case of composite banks, the lower non-cohesive layer also creates a different response compared to cohesive banks, where an eventual dynamic equilibrium of the lower layer becomes necessary before a final retreat of the upper cohesive layer is reached.

Considering the above insights, it is important that the planning of bank protections removal along a navigable river considers the following aspects. First, the possibilities that river functions offer to allow the main channel to experience morphological changes and potential lateral migration. Large scale morphodynamics can occur when lower banks are allowed to erode and sediments can be transported. Fairways are normally required to maintain their dimensions and course, which keeping lower bank protections can offer. Such an approach sets the boundary for upper bank dynamics, from which morphological changes take place. The depth at which protections are removed defines the extent to which ship waves and currents shape the bank. Considering the range of analysed cases, a depth of 1.5 meters from a regulated water level enables free bank dynamics induced by ship waves. Below that threshold, removing protections does not contribute to enhance ship-induced erosion but mainly the effects triggered by currents.

Second, the position of banks in the river planform defines the magnitude and duration of the contribution of currents to erosion. The capacity of currents to act in all three phases of the erosion cycle defines the duration of early morphological stages, after which ship waves control bank erosion by elongating the terrace. The direct impact of currents, especially during high floods, can dominate bank retreat during long periods if the river planform steers flow persistently against the upper bank, as at outer bends. In such settings, it is expected that intermediate stages of evolution with negligible slump-block transport are reached with much longer terraces, and thus time, compared to those developed at straight reaches.

Third, the bank lithological composition is crucial to define expectations with respect to the speed of morphological evolution, final retreat, and possibilities for vegetation and other living organisms to develop. The knowledge of the dominant composition near the regulated water level, together with the highest expected waves at a given reach, serve to estimate final bank retreat with SIREM and accordingly prepare a reach scale strategy that defines the most convenient approach for stretches with similar morphological behaviour and available space to develop. Since closely spaced soil sampling and testing is expensive for large-scale re-naturalization, an alternative approach is to make few cores as first assessment and monitor with an UAV the unprotected banks for the first two or three years. The initial trend of erosion patterns becomes then evident (Figure 3.2) and soil samples can be targeted to stretches with different responses, saving economic resources along stretches with similar retreat rates. Once lithological types are identified, a map of future long-term retreat is possible to delineate, together with a plan to manage each stretch. In this way, the eventual need to reduce or stop erosion at sections with future excess retreat is determined in advance, for which methods such as submerged pre-banks or nature-friendly protections can be considered.

The development of vegetation at upper banks in unprotected conditions is dependent on hydrodynamic, lithological and climatic conditions. Re-naturalized banks increase the hydromorphology of rivers, but its potential to diversify and improve the habitats for flora and fauna is restricted by persistent disturbance. Therefore, the availability of new shallow bank areas does not directly translate into vegetation establishment in the short term, being one indicator of the ecological improvement. Continuous erosion processes contribute to regenerate dynamics of vegetation growth and decay (succession) at certain locations, usually associated with partial protections or a combination of a well-developed terrace (say >12 m) with proper soil and generally dry conditions.

In order to make the most of re-naturalized banks in terms of their benefits for ecological processes and habitat diversity in navigable rivers, the advantages of shallow areas with less perturbated zones should be sought. Two phases of interventions are

recommended, a first where ship waves freely reach the bank for terrace creation, responding to local lithologies, and a second with lowered erosive loads, facilitated by slightly submerged pre-banks (Section 5.2). The latter phase increases the possibilities for vegetation and fauna to develop. An assessment of when to reduce loads and switch strategies, from the erosion phase to quieter areas for nature, is possible considering as reference the different terrace lengths of the cases studied herein. Alternatively, a further development of SIREM could also provide such estimates (Section 5.3.1).

Unregulated rivers present higher challenges for vegetation to grow at erodible riverbanks due to the presence of high currents, ship traffic, and easily erodible sandy substrates. As a consequence, natural bank erosion processes have better short-term prospects at connected side channels, presenting lower shear stresses and low or none navigation. Moreover, at less exposed bank positions, such as inner bends within groyne fields or behind longitudinal training dams, the long term morphology likely enables vegetation establishment. However, given the lack of long-term observations, it could be necessary to use gravel layers or low-intensity measures to reduce erosion rates and increase the window of opportunity for vegetation growth, even after significant bank retreat.

The knowledge and tools now available create new possibilities for improved management of re-naturalized banks in navigable rivers. The progress made helps to better understand the contribution of different drivers to bank erosion and to identify which factors control retreat at different bank types, stages of development, and settings. The new insights explain how to apply SfM-UAV to monitor bank erosion processes along river reaches, interpret bankline patterns, assess the role of isolated trees in bank retreat, and manage expectations regarding bank retreat and the role of vegetation to control erosion. The understanding of erosion processes in regulated navigable rivers and the possibility to estimate final erosion magnitudes open future opportunities to analyse the river system from a holistic perspective and to find creative ways to balance diverse river functions.

6.2. RECOMMENDATIONS FOR FURTHER RESEARCH

Three aspects outside the scope of this research would expand the knowledge and applicability of the concepts and tools developed so far.

First, the proposed ship-induced riverbank erosion model (SIREM) can increase its accuracy to represent erosion rates and long-term retreat by considering statistically representative wave series to recalibrate the erodibility coefficient ε for different cohesive banks (e.g., clusters 1-3 in Section 4.3.4). Moreover, the representation of erosion rates during early development stages will benefit from including formulae

for two additional processes: i) wave breaking over steep slopes (plunging waves); and ii) current-induced erosion. Section 5.3.1 elaborates further on these and other ideas. SIREM can also expand its applicability to other settings by incorporating a new scheme for composite banks, which requires to include processes of sediment transport and mass balance. After that, the application to unregulated rivers could be done by incorporating ship wave generation with varying water depths, and bank processes such as mass failure and slump-block dynamics. Section 5.3.2 explains these concepts in more detail.

Second, fundamental research on the following topics would improve the understanding of bank erosion in rivers and estuaries:

- Dynamics of slump block driven by currents and waves, including different soil compositions, sizes with respect to wave heights or water depths, and bed slopes.
- Quantification and modelling of soil strength increase against flow erosion by root systems, including different root types and soil compositions.
- Characterization of near-bank hydraulics in presence of root-plate abutments, estimating shear stresses and flow detachment and re-attachment, under different conditions. The latter may consider various root-plate dimensions with respect to channel depth, longitudinal spacings, and root densities.
- Morphological and biological development of re-naturalized banks in unregulated rivers.

Third, research on strategies to enhance vegetation development on re-naturalized banks is recommended, in controlled conditions or test sections in the field. For instance, submerged pre-banks for wave reduction could be installed as pilots at the toe of well-developed terraces in regulated rivers to evaluate subsequent vegetation dynamics, either naturally growing or planted. Furthermore, the optimization of the design of such interventions could be done in laboratory experiments, considering different inlets, outlets, and submergence.

BIBLIOGRAPHY

- Abernethy, B., & Rutherfurd, I.D. (2000a). Does the weight of riparian trees destabilize riverbanks?. Regulated Rivers: Research & Management: An International Journal Devoted to River Research and Management, 16(6), 565-576. DOI:10.1002/1099-1646(200011/12)16:6<565::AID-RRR585>3.0.CO;2-1.
- Abernethy, B., & Rutherfurd, I.D. (2000b). The effect of riparian tree roots on the mass-stability of riverbanks. *Earth Surface Processes and Landforms: The Journal of the British Geomorphological Research Group*, 25(9), 921-937. DOI:10.1002/1096-9837(200008)25:9<921::AID-ESP93>3.0.CO;2-7.
- Alho, P., Kukko, A., Hyyppä, H., Kaartinen, H., Hyyppä, J., & Jaakkola, A. (2009). Application of boat-based laser scanning for river survey, *Earth Surface Processes and Landforms*, *34*(13), 1831-1838, DOI:10.1002/esp.1879.
- Amoros, C. (2001). The concept of habitat diversity between and within ecosystems applied to river side-arm restoration. *Environmental management*, 28(6), 805-817. DOI:10.1007/s002670010263.
- Anwar, H. O. (1986). Turbulent structure in a river bend. *Journal of hydraulic engineering*, 112(8), 657-669. DOI:10.1061/(ASCE)0733-9429(1986)112:8(657).
- ASCE Task Committee on Hydraulics, Bank Mechanics, and Modeling of River Width Adjustment (1998). River width adjustment. I: Processes and mechanisms, *Journal of Hydraulic Engineering 124*(9), 881–902, DOI:10.1061/(ASCE)0733-9429(1998)124:9(881).
- Baar, A.W., de Smit, J., Uijttewaal, W.S., & Kleinhans, M.G. (2018). Sediment transport of fine sand to fine gravel on transverse bed slopes in rotating annular flume experiments. Water Resources Research, 54(1), 19-45. DOI:10.1002/2017WR020604.
- Bailly, J. S., Kinzel, P.J., Allouis, T., Feurer, D. & Le Coarer, Y. (2012). Airborne LiDAR Methods Applied to Riverine Environments. In *Fluvial Remote Sensing for Science and Management*. P.E. Carbonneau and H. Piégay (eds.). DOI:10.1002/9781119940791.ch7.
- Balke, T., Bouma, T.J., Horstman, E.M., Webb, E.L., Erftemeijer, P.L., & Herman, P.M. (2011). Windows of opportunity: thresholds to mangrove seedling establishment on tidal flats. *Marine Ecology Progress Series*, 440, 1-9. DOI:10.3354/meps09364.
- Bankhead, N.L., Thomas, R.E., & Simon, A. (2017). A combined field, laboratory and numerical study of the forces applied to, and the potential for removal of, bar top vegetation in a braided river. *Earth Surface Processes and Landforms*, 42(3), 439-459. DOI:10.1002/esp.3997.
- Bangen, S.G., Wheaton, J.M., Bouwes, N., Bouwes, B., & Jordan, C. (2014). A methodological intercomparison of topographic survey techniques for characterizing wadeable streams and rivers. *Geomorphology, 206*, 343-361, DOI:10.1016/j.geomorph.2013.10.010.

- Barker, R., Dixon, L., & Hooke, J. (1997). Use of terrestrial photogrammetry for monitoring and measuring bank erosion. *Earth Surface Processes and Landforms*, 22(13), 1217-1227, DOI:10.1002/(SICI)1096-9837(199724)22:13<1217::AID-ESP819>3.0.CO;2-U.
- Battjes, J.A., & Janssen, J.P.F.M. (1978). Energy loss and set-up due to breaking of random waves. In *Coastal Engineering* 1978, 569-587, ASCE. DOI:10.1061/9780872621909.034.
- Bau, V., Zen, S., Calvani, G., & Perona, P. (2019). Extracting the critical rooting length in plant uprooting by flow from pullout experiments. Water Resources Research, 55, 10424-10442. DOI:10.1029/2019WR025074.
- Bauer, B.O., Lorang, M.S., & Sherman, D.J. (2002). Estimating boat-wake-induced levee erosion using sediment suspension measurements. *Journal of Waterway, Port, Coastal, and Ocean Engineering, 128*(4), 152-162. DOI:10.1061/(ASCE)0733-950X(2002)128:4(152).
- Beechie, T.J., Sear, D.A., Olden, J.D., Pess, G.R., Buffington, J.M., Moir, H., Roni, P. & Pollock, M.M. (2010). Process-based principles for restoring river ecosystems. *BioScience*, 60(3), 209-222. DOI:10.1525/bio.2010.60.3.7.
- Beeson, C.E., & Doyle, P.F. (1995). Comparison of bank erosion at vegetated and non-vegetated channel bends. *JAWRA Journal of the American Water Resources Association*, *31*(6), 983-990. DOI:10.1111/j.1752-1688.1995.tb03414.x.
- Bendoni, M., Georgiou, I.Y., Roelvink, D., & Oumeraci, H. (2019). Numerical modelling of the erosion of marsh boundaries due to wave impact. *Coastal Engineering*, 103514. DOI:10.1016/j.coastaleng.2019.103514.
- Bennett, S.J. (2004). Effects of emergent riparian vegetation on spatially averaged and turbulent flow within an experimental channel. In *Riparian vegetation and fluvial geomorphology*, 8, 29-41. Bennett S. J., Simon A. (eds.). American Geophysical Union: Washington, DC. ISBN 0-87590-357-6.
- Berendsen, H.J.A. (1982). De genese van het landschap in het zuiden van de provincie Utrecht, een fysischgeografische studie. Ph.D. thesis (with summary in English), Utrechtse GeoGeografische Studies 10, 256 pp.
- Bergsma, E.W., Blenkinsopp, C.E., Martins, K., Almar, R., & de Almeida, L. P. M. (2019). Bore collapse and wave run-up on a sandy beach. *Continental Shelf Research*, 174, 132-139. DOI:10.1016/j.csr.2019.01.009.
- Bernatek-Jakiel, A., & Poesen, J. (2018). Subsurface erosion by soil piping: Significance and research needs. *Earth-Science Reviews*, 185, 1107-1128. DOI:10.1016/j.earscirev.2018.08.006.
- Bernhardt, E.S., Palmer, M.A., Allan, J.D., Alexander, G., Barnas, K., Brooks, S., ... & Galat, D. (2005). Synthesizing US river restoration efforts. *Science*, Vol. 308, Issue 5722, 636-637. DOI:10.1126/science.1109769.
- Bertoldi, W., Drake, N.A., & Gurnell, A.M. (2011). Interactions between river flows and colonizing vegetation on a braided river: exploring spatial and temporal dynamics in riparian vegetation cover using satellite data. *Earth Surface Processes and Landforms*, 36(11), 1474-1486. DOI:10.1002/esp.2166.
- Best, J. (2018). Anthropogenic stresses on the world's big rivers. *Nature Geoscience*, 1. DOI:10.1038/s41561-018-0262-x.
- Bhowmik, N.G., Demissie, M., & Guo, C.Y. (1982). Waves generated by river traffic and wind on the Illinois and Mississippi Rivers. Illinois State Water Survey. http://hdl.handle.net/2142/72711, last access 24/07/2020.
- Bird, S., Hogan, D., & Schwab, J. (2010). Photogrammetric monitoring of small streams under a riparian forest canopy. *Earth Surface Processes and Landforms*, *35*(8), 952-970, DOI:10.1002/esp.2001.

- Blanckaert, K., Duarte, A., & Schleiss, A. J. (2010). Influence of shallowness, bank inclination and bank roughness on the variability of flow patterns and boundary shear stress due to secondary currents in straight open-channels. Advances in Water Resources, 33, 1062-1074. DOI: 10.1016/j. advwatres.2010.06.012.
- Blanckaert, K., Duarte, A., Chen, Q., and Schleiss, A.J. (2012). Flow processes near smooth and rough (concave) outer banks in curved open channels, *J. Geophys. Res.*, 117, F04020, DOI:10.1029/2012JF002414.
- Boeters, R.E.A.M., Havinga, H., Litjens, G., & Verheij, H.J. (1997). Ten years of experience in combining ecology & navigation on Dutch waterways. In 29th PIANC Congress. PIANC.
- Boeters, R.E.A.M., Havinga, H., Litjens, G., & Verheij, H.J. (1997). *Ten years of experience in combining ecology and navigation on Dutch waterways*. Paper presented at 29th PIANC Congress. PIANC.
- Bogoni, M., Putti, M., & Lanzoni, S. (2017). Modeling meander morphodynamics over self-formed heterogeneous floodplains. Water Resources Research, 53(6), 5137-5157. DOI:10.1002/2017WR020726.
- Bonham, A. J. (1983). The management of wave-spending vegetation as bank protection against boat wash. Landscape planning, 10(1), 15-30. DOI:10.1016/0304-3924(83)90025-4.
- Bouma, T.J., Van Belzen, J., Balke, T., Van Dalen, J., Klaassen, P., Hartog, A.M., Callaghan, D.P., Hu, Z., Stive, M.J.F., Temmerman, S., & Herman, P.M.J. (2016). Short-term mudflat dynamics drive long-term cyclic salt marsh dynamics. *Limnology and oceanography*, *61*(6), 2261-2275. DOI:10.1002/lno.10374.
- Brasington, J., Rumsby, B.T., & McVey, R.A. (2000). Monitoring and modelling morphological change in a braided gravel-bed river using high resolution GPS-based survey. *Earth Surface Processes and Landforms*, 25(9), 973-990, DOI: 10.1002/1096-9837(200008)25:9<973::AID-ESP111>3.0.CO;2-Y.
- Brasington, J., Vericat, D., & Rychkov, I. (2012). Modeling river bed morphology, roughness, and surface sedimentology using high resolution terrestrial laser scanning. *Water Resources Research*, 48(11). DOI:10.1029/2012WR012223.
- Brierley, G.J., & Fryirs, K.A. (2005). Geomorphology and river management: applications of the river styles framework. Blackwell, Oxford, UK. ISBN-13: 978-1-4051-1516-2.
- Briganti, R., Dodd, N., Incelli, G., & Kikkert, G. (2018). Numerical modelling of the flow and bed evolution of a single bore-driven swash event on a coarse sand beach. *Coastal Engineering*, 142, 62-76. DOI:10.1016/j. coastaleng.2018.09.006.
- Brookes, A., Gregory, K. J., & Dawson, F. H. (1983). An assessment of river channelization in England and Wales. *Science of the Total Environment*, 27(2-3), 97-111. DOI:10.1016/0048-9697(83)90149-3.
- Buffington, J.M. (1999). The legend of AF Shields. *Journal of Hydraulic Engineering*, 125(4), 376-387. DOI:10.1061/(ASCE)0733-9429(1999)125:4(376).
- Bullock, G.N., Obhrai, C., Peregrine, D.H., & Bredmose, H. (2007). Violent breaking wave impacts. Part 1: Results from large-scale regular wave tests on vertical and sloping walls. *Coastal Engineering*, *54*(8), 602-617. DOI:10.1016/j.coastaleng.2006.12.002.
- Calvani, G., Francalanci, S., & Solari, L. (2019). A physical model for the uprooting of flexible vegetation on river bars. *Journal of Geophysical Research: Earth Surface, 124*, 1018-1034. DOI:10.1029/2018JF004747.
- Candel, J.H.J., Kleinhans, M.G., Makaske, B., Hoek, W.Z., Quik, C., & Wallinga, J. (2018), Late Holocene channel pattern change from laterally stable to meandering a palaeohydrological reconstruction, *Earth Surface Dynamics*, *6*, 723-741. DOI:10.5194/esurf-6-723-2018.
- Caponi, F., Koch, A., Bertoldi, W., Vetsch, D.F., & Siviglia, A. (2019). When does vegetation establish on gravel bars? observations and modelling in the Alpine Rhine river. *Frontiers in Environmental Science*, 7, 124. DOI:10.3389/fenvs.2019.00124.

- Carbonneau, P.E. & Dietrich, J.T. (2017). Cost-effective non-metric photogrammetry from consumer-grade sUAS: implications for direct georeferencing of structure from motion photogrammetry. *Earth Surface Processes and Landforms*, 42(3), 473-486. DOI:10.1002/esp.4012.
- Carson, M.A. and Kirkby, M.J. (1972). Hillslope Form and Process, Cambridge University Press, UK.
- Casagli, N., Rinaldi, M., Gargini, A. & Curini, A. (1999). Pore water pressure and streambank stability: results from a monitoring site on the Sieve River, Italy. *Earth Surf. Process. Landforms, 24*: 1095-1114. DOI:10.1002/(SICI)1096-9837(199911)24:12<1095::AID-ESP37>3.0.CO;2-F.
- Casagli, N., Rinaldi, M., Gargini, A. and Curini, A. (1999), Pore water pressure and streambank stability: results from a monitoring site on the Sieve River, Italy. *Earth Surf. Process. Landforms, 24*: 1095-1114. DOI:10.1002/(SICI)1096-9837(199911)24:12<1095::AID-ESP37>3.0.CO;2-F.
- Cavalli, M., Tarolli, P., Marchi, L., & Dalla Fontana, G. (2008). The effectiveness of airborne LiDAR data in the recognition of channel-bed morphology. *Catena*, 73(3), 249-260. DOI:10.1016/j.catena.2007.11.001.
- Charlton, M.E., Large, A.R., & Fuller, I.C. (2003). Application of airborne LiDAR in river environments: the River Coquet, Northumberland, UK. *Earth surface processes and landforms*, 28(3), 299-306. DOI:10.1002/esp.482.
- Chen, X.D., Zhang, C.K., Paterson, D.M., Thompson, C.E.L., Townend, I.H., Gong, Z., Zhou, Z., and Feng, Q. (2017a), Hindered erosion: The biological mediation of noncohesive sediment behavior, *Water Resources Research*, 53, 4787-4801. DOI:10.1002/2016WR020105.
- Chen, X.D., Zhang, C.K., Zhou, Z., Gong, Z., Zhou, J.J., Tao, J.F., Paterson, D.M., Feng, Q. (2017b). Stabilizing effects of bacterial biofilms: EPS penetration and redistribution of bed stability down the sediment profile. *Journal of Geophysical Research: Biogeosciences*, 122, 3113–3125. DOI:10.1002/2017JG004050.
- Chen, H., Ni, Y., Li, Y., Liu, F., Ou, S., Su, M., ... & Suzuki, T. (2018). Deriving vegetation drag coefficients in combined wave-current flows by calibration and direct measurement methods. *Advances in water resources*, 122, 217-227. DOI:10.1016/j.advwatres.2018.10.008.
- Cheng, W., Fang, H., Lai, H., Huang, L., & Dey, S. (2018). Effects of biofilm on turbulence characteristics and the transport of fine sediment. *Journal of soils and sediments, 18*(10), 3055-3069. DOI:10.1007/s11368-017-1859-1.
- Chu-Agor, M.L., Fox, G.A., & Wilson, G.V. (2009). Empirical sediment transport function predicting seepage erosion undercutting for cohesive bank failure prediction. *Journal of hydrology, 377*(1-2), 155-164. DOI:10.1016/j.jhydrol.2009.08.020.
- Chu-Agor, M.L., Fox, G.A., Cancienne, R.M., & Wilson, G.V. (2008a). Seepage caused tension failures and erosion undercutting of hillslopes. *Journal of hydrology*, 359(3-4), 247-259. DOI:10.1016/j. jhydrol.2008.07.005.
- Chu-Agor, M.L., Wilson, G.V., & Fox, G.A. (2008b). Numerical modeling of bank instability by seepage erosion undercutting of layered streambanks. *Journal of Hydrologic Engineering*, 13(12), 1133-1145. DOI:10.1061/(ASCE)1084-0699(2008)13:12(1133).
- CIRIA, CUR, & CETMEF (2007). The rock manual: The use of rock in hydraulic engineering (2nd edition). Vol. 683. C683, CIRIA, London. ISBN:9780860176831.
- Clapuyt F., Vanacker V., & Van Oost, K. (2016). Reproducibility of UAV-based earth topography reconstructions based on Structure-from-Motion algorithms. *Geomorphology 260*, 4-15. DOI:10.1016/j. geomorph.2015.05.011.
- Clark, L.A. & Wynn, T.M. (2007). Methods for determining streambank critical shear stress and soil erodibility: Implications for erosion rate predictions. *Transactions of the ASABE, 50*(1), 95-106. DOI:10.13031/2013.22415.

- Collas, F.P.L., Koopman, K.R., van der Velde, G., & Leuven, R.S.E.W. (2020). Quantifying the loss of filtration services following mass mortality of invasive dreissenid mussels. *Ecological Engineering*, *149*, 105781. DOI:10.1016/j.ecoleng.2020.105781.
- Constantine, C.R., Dunne, T., & Hanson, G.J. (2009). Examining the physical meaning of the bank erosion coefficient used in meander migration modeling. *Geomorphology*, *106*(3), 242-252. DOI:10.1016/j. geomorph.2008.11.002.
- Constantine, J.A., McLean, S.R., & Dunne, T. (2010). A mechanism of chute cutoff along large meandering rivers with uniform floodplain topography. *GSA Bulletin* 122, 855-869. DOI: 10.1130/B26560.1.
- Cook, K.L. (2017). An evaluation of the effectiveness of low-cost UAVs and structure from motion for geomorphic change detection. *Geomorphology*, 278, 195-208. DOI:10.1016/j.geomorph.2016.11.009.
- Coops, H., Geilen, N., Verheij, H. J., Boeters, R., & van der Velde, G. (1996). Interactions between waves, bank erosion and emergent vegetation: an experimental study in a wave tank. *Aquatic Botany*, *53*(3-4), 187-198. https://hdl.handle.net/2066/29063.
- Couper, P.R. (2003). Effects of silt–clay content on the susceptibility of river banks to subaerial erosion. *Geomorphology*, *56*(1-2), 95-108. DOI:10.1016/S0169-555X(03)00048-5.
- Couper, P.R. (2004). Space and time in river bank erosion research: A review. *Area*, *36*(4), 387-403. DOI: 10.1111/j.0004-0894.2004.00239.x.
- Couper, P.R., & Maddock, I. P. (2001). Subaerial river bank erosion processes and their interaction with other bank erosion mechanisms on the River Arrow, Warwickshire, UK. *Earth Surface Processes and Landforms*, 26(6), 631-646. DOI:10.1002/esp.212.
- Couper, P.R., Stott, T.I.M., & Maddock, I. (2002). Insights into river bank erosion processes derived from analysis of negative erosion-pin recordings: observations from three recent UK studies. *Earth Surface Processes and Landforms*, *27*(1), 59-79. DOI: 10.1002/esp.285.
- Crosato, A. (2007). Effects of smoothing and regridding in numerical meander migration models. *Water Resources Research*, 43(1). DOI:10.1029/2006WR005087.
- CUR, Handboek Natuurvriendelijke Oevers (Ecologically Sound Banks Handbook), Gouda, 1994.
- Curran, J.C., & Hession, W.C. (2013). Vegetative impacts on hydraulics and sediment processes across the fluvial system. *Journal of Hydrology*, *505*, 364-376. DOI:10.1016/j.jhydrol.2013.10.013.
- D'Alpaos, A., Toffolon, M., & Camporeale, C. (2016). Ecogeomorphological feedbacks of water fluxes, sediment transport and vegetation dynamics in rivers and estuaries. *Advances in Water Resources*, 93, 151-155. DOI:10.1016/j.advwatres.2016.05.019.
- Daniels, M. D., & Rhoads, B.L. (2004). Spatial pattern of turbulence kinetic energy and shear stress in a meander bend with large woody debris. In *Riparian vegetation and fluvial geomorphology, 8*, 87-98. Bennett S. J., Simon A. (eds.). American Geophysical Union: Washington, DC. ISBN 0-87590-357-6.
- Danube STREAM (2019). Common Danube Report 2018. Available at http://www.interreg-danube.eu/approved-projects/danube-stream/outputs, last access 04/07/2020.
- Darby, S.E., & Thorne, C.R. (1994). Prediction of tension crack location and riverbank erosion hazards along destabilized channels. *Earth surface processes and landforms*, 19(3), 233-245. DOI:10.1002/esp.3290190304.
- Darby, S.E., Rinaldi, M., & Dapporto, S. (2007). Coupled simulations of fluvial erosion and mass wasting for cohesive river banks. Journal of Geophysical Research: Earth Surface, 112(F3). DOI:10.1029/2006JF000722.

- Darby, S.E., Trieu, H.Q., Carling, P.A., Sarkkula, J., Koponen, J., Kummu, M., Conlan, I., & Leyland, J. (2010). A physically based model to predict hydraulic erosion of fine-grained riverbanks: The role of form roughness in limiting erosion. *Journal of Geophysical Research: Earth Surface 115*(F4). DOI:10.1029/2010JF001708.
- De Roo, S., & Troch, P. (2015). Evaluation of the Effectiveness of a Living Shoreline in a Confined, Non-Tidal Waterway Subject to Heavy Shipping Traffic. *River research and applications, 31*(8), 1028-1039. DOI: 10.1002/rra.2790.
- De Rose, R.C., & Basher, L.R. (2011). Measurement of river bank and cliff erosion from sequential LIDAR and historical aerial photography. *Geomorphology*, 126(1), 132-147. DOI:10.1016/j.geomorph.2010.10.037.
- de Ruijsscher, T.V., Vermeulen, B., & Hoitink, A.J.F. (2020). Diversion of flow and sediment toward a side channel separated from a river by a longitudinal training dam. *Water Resources Research*, *56*, e2019WR026750. DOI:10.1029/2019WR026750.
- Dean, R.G. (1991). Equilibrium Beach Profiles: Characteristics and Applications. *Journal of Coastal Research*, 7(1), 53-84. www.jstor.org/stable/4297805.
- Deltares (2020). Delft3D-FLOW User Manual. Available at http://oss.deltares.nl/web/delft3d/manuals/, last access 30/07/2020.
- Descy JP, Patrick K, Everbecq E, Verniers G, Usseglio-Polatera P, Gérard P, Viroux L, Beisel J-N, Smitz J. 2009. The Meuse river basin. Rivers of Europe. EAWAG/ETH, Switzerland. Elsevier, London, 151199, 154-166.
- Didenkulova, I.I., Zahibo, N., Kurkin, A.A., & Pelinovsky, E.N. (2006). Steepness and spectrum of a nonlinearly deformed wave on shallow waters, Izvestiya Atmos. *Ocean. Phys.* 42, 773–776. DOI:10.1134/S0001433806060119.
- Dietrich, W.E., & Smith, J.D. (1984). Bed load transport in a river meander. Water Resources Research, 20(10), 1355-1380. DOI:10.1029/WR020i010p01355.
- Docker, B.B., & Hubble, T.C.T. (2009). Modelling the distribution of enhanced soil shear strength beneath riparian trees of south-eastern Australia. *Ecological Engineering*, *35*(5), 921-934. DOI:10.1016/j. ecoleng.2008.12.018.
- Dorava, J.M. & Moore, G.W. (1997). Effects of boatwakes on streambank erosion, Kenai River, Alaska. *Water Resources Investigations*, Report, 97-4105. US Geological Survey: Anchorage.
- Dragicevic, S., Zivkovic, N., Roksandic, M., Kostadinov, S., Novkovic, I., Tosic, R., Stepic, M., Dragicevic, M. & Blagojevic, B. (2012). Land use changes and environmental problems caused by bank erosion: A case study of the Kolubara River Basin in Serbia. In *Environmental Land Use Planning*, 978-953. DOI:10.5772/50580.
- Dufour, S., & Piégay, H. (2009). From the myth of a lost paradise to targeted river restoration: forget natural references and focus on human benefits. *River research and applications*, *25*(5), 568-581. DOI:10.1002/rra.1239.
- Duró, G., Crosato, A., Kleinhans, M.G., & Uijttewaal W.S.J. (2018a). On the morphological evolution of restored banks: case study of the Meuse river. In *E3S Web of Conferences 40*, 02021. River Flow 2018, Lyon, France. DOI:10.1051/e3sconf/20184002021.
- Duró, G., Crosato, A., Kleinhans, M.G., & Uijttewaal, W.S.J. (2018b). Bank erosion processes measured with UAV-SfM along complex banklines of a straight mid-sized river reach. *Earth Surface Dynamics 6*, 933-953. DOI:10.5194/esurf-6-933-2018.
- Duró, G., Crosato, A., Uijttewaal, W.S.J., & Kleinhans, M.G. (2018c). Monitoring bank erosion with Unmanned Aerial Vehicle (UAV) during a low-water event. *4TU.ResearchData*. Dataset. DOI:10.4121/uuid:4eab4339-52d6-4328-81b2-640544c05438.

- Duró, G., Crosato, A., Kleinhans, M.G., Winkels, T.G., Woolderink, H.A.G., & Uijttewaal, W.S.J. (2020a). Distinct patterns of bank erosion in a navigable regulated river. Earth Surface Processes and Landforms. DOI:10.1002/esp.4736.
- Duró, G., Crosato, A., Kleinhans, M.G., Roelvink, D., & Uijttewaal, W.S.J. (2020b). Bank erosion processes in regulated navigable rivers. *Journal of Geophysical Research: Earth Surface, 125*, e2019JF005441. DOI:10.1029/2019JF005441.
- Duró, G., Crosato, & Uijttewaal, W. S. J. (2020c). Bank erosion in regulated navigable rivers: towards a process-based model of bank retreat. River Flow conference 2020, Delft, the Netherlands. (in press)
- Duró, G. (2020). Data underlying the research of Bank erosion processes in regulated navigable rivers. *4TU. ResearchData*. Dataset. DOI:10.4121/uuid:9193985b-90ba-4d30-a882-a7f0a5fb4fb7.
- Durocher, M.G. (1990). Monitoring spatial variability of forest interception. *Hydrological Processes*, 4(3), 215-229. DOI:10.1002/hyp.3360040303.
- Edmaier, K., Burlando, P., & Perona, P. (2011). Mechanisms of vegetation uprooting by flow in alluvial non-cohesive sediment. *Hydrology and Earth System Sciences*, *15*(5), 1615-1627. DOI:10.3929/ethz-b-000029971.
- Eke, E., Parker, G., & Shimizu, Y. (2014). Numerical modeling of erosional and depositional bank processes in migrating river bends with self-formed width: Morphodynamics of bar push and bank pull. *Journal of Geophysical Research: Earth Surface*, 119(7), 1455-1483. DOI:10.1002/2013JF003020.
- Eltner, A., & Schneider, D. (2015). Analysis of different methods for 3D reconstruction of natural surfaces from parallel-axes UAV images. *The Photogrammetric Record*, *30*(151), 279-299. DOI:10.1111/phor.12115.
- Eltner, A., Kaiser, A., Castillo, C., Rock, G., Neugirg, F., & Abellán, A. (2016). Image-based surface reconstruction in geomorphometry-merits, limits and developments. *Earth Surface Dynamics*, 4(2), 359-389, DOI:10.5194/esurf-4-359-2016.
- Fang, H., Shang, Q., Chen, M., & He, G. (2014). Changes in the critical erosion velocity for sediment colonized by biofilm. *Sedimentology*, *61*(3), 648-659. DOI:10.1111/sed.12065.
- Fang, H., Chen, Y., Huang, L., & He, G. (2017a). Analysis of biofilm bacterial communities under different shear stresses using size-fractionated sediment. *Scientific reports, 7*(1), 1299. DOI:10.1038/s41598-017-01446-4.
- Fang, H., Lai, H.J., Cheng, W., Huang, L., & He, G.J. (2017b). Modeling sediment transport with an integrated view of the biofilm effects. *Water Resources Research*, *53*(9), 7536-7557. DOI:10.1002/2017WR020628.
- Florsheim, J.L., Mount, J.F., & Chin, A. (2008). Bank Erosion as a Desirable Attribute of Rivers. *BioScience*, 58(6), 519-529, DOI:10.1641/B580608.
- Fonstad, M. A., Dietrich, J. T., Courville, B. C., Jensen, J. L., & Carbonneau, P. E. (2013). Topographic structure from motion: a new development in photogrammetric measurement. *Earth Surface Processes and Landforms*, 38(4), 421-430. DOI:10.1002/esp.3366.
- Fox, G.A., Wilson, G.V., Simon, A., Langendoen, E.J., Akay, O., & Fuchs, J.W. (2007). Measuring streambank erosion due to ground water seepage: correlation to bank pore water pressure, precipitation and stream stage. *Earth Surface Processes and Landforms*, 32(10), 1558-1573. DOI:10.1002/esp.1490.
- Fox, G.A., Heeren, D.M., Wilson, G.V., Langendoen, E.J., Fox, A.K., & Chu-Agor, M.L. (2010). Numerically predicting seepage gradient forces and erosion: Sensitivity to soil hydraulic properties. *Journal of hydrology*, 389(3-4), 354-362. DOI:10.1016/j.jhydrol.2010.06.015.
- Fujita, Y., Kawaguchi, M., & Pham, T.H. (2000). A conceptual model for erosion processes of high river bank. *Proceedings of Hydraulic Engineering, JSCE, 44*, 753-758. DOI:10.2208/prohe.44.753.

- Fukuoka, S. (1994). Erosion processes of natural river bank. *Proceedings of 1st International Symposium on Hydraulic Measurement*, Beijing, Vol. 223229.
- Gabel, F., Garcia, X. F., Schnauder, I., & Pusch, M. T. (2012). Effects of ship-induced waves on littoral benthic invertebrates. *Freshwater Biology*, *57*(12), 2425-2435. DOI:10.1111/fwb.12011.
- Gabel, F., Lorenz, S., & Stoll, S. (2017). Effects of ship-induced waves on aquatic ecosystems. *Science of the Total Environment*, 601, 926-939. DOI:10.1016/j.scitotenv.2017.05.206.
- Garcia, M.H. (2008). Sediment transport and morphodynamics. In *Sedimentation engineering: Processes, measurements, modeling, and practice, 110, 21-164, DOI:10.1061/9780784408148.ch02.*
- Gaskin, S.J., Pieterse, J., Shafie, A.A., & Lepage, S. (2003). Erosion of undisturbed clay samples from the banks of the St. Lawrence River. *Canadian Journal of Civil Engineering*, 30(3), 585-595. DOI:10.1139/I03-008.
- Gautier, E., Brunstein, D., Vauchel, P., Roulet, M., Fuertes, O., Guyot, J.L., Darozzes, J. & Bourrel, L. (2007). Temporal relations between meander deformation, water discharge and sediment fluxes in the floodplain of the Rio Beni (Bolivian Amazonia). *Earth Surf. Process. Landforms*, *32*, 230-248. DOI:10.1002/esp.1394.
- Ghestem, M., Veylon, G., Bernard, A., Vanel, Q., & Stokes, A. (2014). Influence of plant root system morphology and architectural traits on soil shear resistance. *Plant and Soil*, *377*(1-2), 43-61. DOI:10.1007/s11104-012-1572-1.
- Gibling, M.R., & Rust, B.R. (1993). Alluvial ridge-and-swale topography: a case study from the Morien Group of Atlantic Canada. In *Alluvial Sedimentation*, 133-150. M. Marzo and C. Puigdefábregas (eds.). DOI:10.1002/9781444303995.ch11.
- Gibson, S., Simon, A., Langendoen, E., Bankhead, N., & Shelley, J. (2015). A physically-based channel-modeling framework integrating HEC-RAS sediment transport capabilities and the USDA-ARS bank-stability and toe-erosion model (BSTEM). In *Federal Interagency Sediment Conference, SedHyd Proceedings*.
- Girardeau-Montaut, D. (2020). CloudCompare (version 2.9; GPL software), EDF RandD, Telecom ParisTech. Available at http://www.cloudcompare.org/, last access 09/07/2020.
- Glamore, W.C., 2008. A Decision Support Tool for Assessing the Impact of Boat Wake Waves on Inland Waterways. Paper presented at International Conference on Coastal and Port Engineering in Developing Countries, Issue 1, p. 20.
- Glenz, C., Schlaepfer, R., Iorgulescu, I., & Kienast, F. (2006). Flooding tolerance of Central European tree and shrub species. Forest Ecology and Management, 235(1-3), 1-13. DOI:10.1016/j.foreco.2006.05.065.
- Gómez-Gutiérrez, Á., de Sanjosé-Blasco, J.J., de Matías-Bejarano, J., & Berenguer-Sempere, F. (2014a). Comparing two photo-reconstruction methods to produce high density point clouds and DEMs in the Corral del Veleta Rock Glacier (Sierra Nevada, Spain). *Remote Sensing*, 6(6), 5407-5427. DOI: 10.3390/rs6065407.
- Gómez-Gutiérrez, Á., Schnabel, S., Berenguer-Sempere, F., Lavado-Contador, F. & Rubio-Delgado, J. (2014b). Using 3D photo-reconstruction methods to estimate gully headcut erosion. *Catena*, *120*, 91-101. DOI:10.1016/j.catena.2014.04.004.
- Gorla, L., Signarbieux, C., Turberg, P., Buttler, A., & Perona, P. (2015). Transient response of Salix cuttings to changing water level regimes. *Water Resources Research*, *51*(3), 1758-1774. DOI:10.1002/2014WR015543.
- Grabowski, R.C., Droppo, I.G., & Wharton, G. (2010). Estimation of critical shear stress from cohesive strength meter-derived erosion thresholds. *Limnology and Oceanography: Methods, 8*(12), 678-685. DOI:10.4319/lom.2010.8.0678.
- Grabowski, R.C., Droppo, I.G., & Wharton, G. (2011). Erodibility of cohesive sediment: The importance of sediment properties. *Earth-Science Reviews*, 105(3-4), 101-120. DOI:10.1016/j.earscirev.2011.01.008.

- Gray, D.H., & MacDonald, A. (1989). The role of vegetation in river bank erosion. In *Hydraulic engineering*, Proceedings of ASCE Conference, 218-223. Ports, M. A. (ed.), ASCE.
- Green, T.R., Beavis, S.G., Dietrich, C.R., & Jakeman, A.J. (1999). Relating stream-bank erosion to in-stream transport of suspended sediment. *Hydrological processes*, 13(5), 777-787. DOI:10.1002/(SICI)1099-1085(19990415)13:5<777::AID-HYP780>3.0.CO;2-P.
- Grove, J. R., Croke J., & Thompson, C. (2013). Quantifying different riverbank erosion processes during an extreme flood event. *Earth Surface Processes and Landforms*, 38(12), 1393-1406. DOI:10.1002/esp.3386.
- Gumiero, B., Mant, J., Hein, T., Elso, J., & Boz, B. (2013). Linking the restoration of rivers and riparian zones/wetlands in Europe: sharing knowledge through case studies. *Ecological Engineering*, *56*, 36-50. DOI:10.1016/j.ecoleng.2012.12.103.
- Güneralp, İ., & Rhoads, B. L. (2011). Influence of floodplain erosional heterogeneity on planform complexity of meandering rivers. *Geophysical Research Letters*, *38*, p. L14401, DOI:10.1029/2011GL048134.
- Gurnell, A. (2014). Plants as river system engineers. *Earth Surface Processes and Landforms*, *39*(1), 4-25. DOI:10.1002/esp.3397.
- Gurnell, A. & Petts, G. (2006). Trees as riparian engineers: the Tagliamento River, Italy. Earth Surface Processes and Landforms: The Journal of the British Geomorphological Research Group, 31(12), 1558-1574. DOI:10.1002/esp.1342.
- Gurnell, A., Thompson, K., Goodson, J., & Moggridge, H. (2008). Propagule deposition along river margins: linking hydrology and ecology. *Journal of Ecology*, *96*(3), 553-565. DOI:10.1111/j.1365-2745.2008.01358.x.
- Gurnell, A.M., Bertoldi, W., & Corenblit, D. (2012). Changing river channels: The roles of hydrological processes, plants and pioneer fluvial landforms in humid temperate, mixed load, gravel bed rivers. *Earth-Science Reviews*, 111(1-2), 129-141. DOI:10.1016/j.earscirev.2011.11.005.
- Gurnell, A.M., Rinaldi, M., Buijse, A.D., Brierley, G., & Piégay, H. (2016). Hydromorphological frameworks: emerging trajectories. *Aquatic sciences*, 78(1), 135-138. DOI:10.1007/s00027-015-0436-1.
- Habersack, H. & Klösch, M. (2012). Monitoring und Modellierung von eigendynamischen Aufweitungen an Drau, Mur und Donau. Österreichische Wasser-und Abfallwirtschaft 64, 411-422. DOI:10.1007/s00506-012-0007-9.
- Hackney, C., Best, J., Leyland, J., Darby, S.E., Parsons, D., Aalto, R., & Nicholas, A. (2015). Modulation of outer bank erosion by slump blocks: Disentangling the protective and destructive role of failed material on the three-dimensional flow structure. *Geophysical Research Letters*, 42(24), 10-663. DOI: 10.1002/2015GL066481.
- Hagerty, D.J. (1991). Piping/sapping erosion. II: Identification-diagnosis. *Journal of Hydraulic Engineering*, 117(8), 1009-1025. DOI:10.1061/(ASCE)0733-9429(1991)117:8(1009).
- Hagerty, D.J., Spoor, M.F., & Parola, A.C. (1995). Near-bank impacts of river stage control. *Journal of Hydraulic Engineering*, 121(2), 196-207. DOI:10.1061/(ASCE)0733-9429(1995)121:2(196).
- Hamshaw, S.D., Bryce, T., Rizzo, D.M., O'Neil-Dunne, J., Frolik, J. & Dewoolkar, M.M. (2017). Quantifying streambank movement and topography using unmanned aircraft system photogrammetry with comparison to terrestrial laser scanning. *River Research and Applications*, 33(8), 1354-1367. DOI:10.1002/rra.3183.
- Hansen, J. B. (1990). Periodic waves in the surf zone: Analysis of experimental data. *Coastal Engineering*, 14(1), 19-41. DOI:10.1016/0378-3839(90)90008-K.
- Hansen, J.B. & Svendsen, I.A. (1987). Experimental investigation of the wave and current motion over a longshore bar. In *Coastal Engineering* 1986, 1166-1179, ASCE. DOI:10.1061/9780872626003.086.

- Hanson, G.J. & Cook, K.R. (2004). Apparatus, test procedures, and analytical methods to measure soil erodibility in situ. *Applied engineering in agriculture*, 20(4), 455. DOI:10.13031/2013.16492.
- Hartley, R. & Zisserman, A. (2003). Multiple view geometry in computer vision. Cambridge University press.
- Harwin, S. & Lucieer, A. (2012). Assessing the accuracy of georeferenced point clouds produced via multiview stereopsis from unmanned aerial vehicle (UAV) imagery. *Remote Sensing*, 4(6), 1573-1599. DOI:10.3390/rs4061573.
- Heibaum, M. (2002). Geotechnical parameters of scouring and scour countermeasures (English & German). In *Mitteilungsblatt der Bundesanstalt für Wasserbau 85,* 59-70. Karlsruhe, BAW. https://hdl.handle.net/20.500.11970/102649.
- Heibaum, M. & Fleischer, P. (2015). Technical-biological bank protection for navigable waterways on trial. In *Scour and Erosion: Proceedings of 7th International Conference on Scour and Erosion, Perth, Australia*, 2-4. Cheng, L., Draper, S., & An, H. (eds.). CRC Press.
- Henshaw, A.J., Thorne, C.R., & Clifford, N.J. (2013). Identifying causes and controls of river bank erosion in a British upland catchment. *Catena*, *100*, 107-119. DOI:10.1016/j.catena.2012.07.015.
- Heritage, G. & Hetherington, D. (2007). Towards a protocol for laser scanning in fluvial geomorphology. *Earth Surface Processes and Landforms*, 32(1), 66-74. DOI:10.1002/esp.1375.
- Helfield, J.M., Capon, S.J., Nilsson, C., Jansson, R., & Palm, D. (2007). Restoration of rivers used for timber floating: effects on riparian plant diversity. *Ecological Applications*, 17(3), 840-851. DOI:10.1890/06-0343.
- Hoffmans, G.J., & Booij, R. (1993). Two-dimensional mathematical modelling of local-scour holes. *Journal of Hydraulic Research*, *31*(5), 615-634. DOI:10.1080/00221689309498775.
- Hooke, J.M. (1979). An analysis of the processes of river bank erosion. *Journal of Hydrology, 42*(1-2):39-62. DOI:10.1016/0022-1694(79)90005-2.
- Hooke, J.M. (1995). River channel adjustment to meander cutoffs on the River Bollin and River Dane, northwest England. *Geomorphology*, 14(3), 235-253. DOI:10.1016/0169-555X(95)00110-Q.
- Hopkinson, L. & Wynn, T. (2009). Vegetation impacts on near bank flow. *Ecohydrology: Ecosystems, Land and Water Process Interactions, Ecohydrogeomorphology*, 2(4), 404-418. DOI:10.1002/eco.87.
- Houser, C. (2010). Relative importance of vessel-generated and wind waves to salt marsh erosion in a restricted fetch environment. *Journal of Coastal Research*, 26 (2 (262)), 230-240. DOI:10.2112/08-1084.1.
- Hubble, T.C.T., Docker, B.B., & Rutherfurd, I.D. (2010). The role of riparian trees in maintaining riverbank stability: a review of Australian experience and practice. *Ecological Engineering*, *36*(3), 292-304. DOI:10.1016/j.ecoleng.2009.04.006.
- Hudson, P.F. & Kesel, R.H. (2000). Channel migration and meander-bend curvature in the lower Mississippi River prior to major human modification. *Geology*, 28(6), 531-534. DOI: 10.1130/0091-7613(2000)28<531:CMAMCI>2.0.CO;2.
- Ikeda, S., Parker, G., & Sawai, K. (1981). Bend theory of river meanders. Part 1. Linear development. *Journal of Fluid Mechanics*, 112, 363-377. DOI:10.1017/S0022112081000451.
- Immerzeel, W.W., Kraaijenbrink, A., Shea, J.M., Shrestha, A.B., Pellicciotti, F., Bierkens, M.F.P., & De Jong, S.M. (2014). Highresolution monitoring of Himalayan glacier dynamics using unmanned aerial vehicles. *Remote Sens. Environ., 150*, 93-103. DOI:10.1016/j.rse.2014.04.025.
- Jacobs, W., Le Hir, P., Van Kesteren, W., & Cann, P. (2011). Erosion threshold of sand–mud mixtures. Continental Shelf Research, 31(10), S14-S25. DOI:10.1016/j.csr.2010.05.012.

- Jacobson A. et al. (2020). Geometry Processing Toolbox. Available at http://github.com/alecjacobson/gptoolbox, last access 09/07/2020.
- James, M.R. & Robson, S. (2012). Straightforward reconstruction of 3D surfaces and topography with a camera: Accuracy and geoscience application. *Journal of Geophysical Research: Earth Surface, 117*(F3). DOI:10.1029/2011JF002289.
- James, M.R. & Robson, S. (2014). Mitigating systematic error in topographic models derived from UAV and ground-based image networks. Earth Surface Processes and Landforms, 39(10), 1413-1420. DOI:10.1002/ esp.3609.
- James, M.R., Robson, S., d'Oleire-Oltmanns, S. & Niethammer, U. (2017). Optimising UAV topographic surveys processed with structure-from-motion: Ground control quality, quantity and bundle adjustment. *Geomorphology*, 280, 51-66. DOI:10.1016/j.geomorph.2016.11.021.
- Jansen, P., Van Bendegom, L., Van Den Berg, J.H., de Vries, M.B., & Zanen, A. (1994). Principles of river engineering: the non-tidal alluvial river. Reprinted 2010. VSSD: Delft. ISBN 978-90-6562-146-7. xv, 509 pp.
- Javernick, L., Brasington, J., & Caruso, B. (2014). Modeling the topography of shallow braided rivers using Structure-from-Motion photogrammetry. *Geomorphology*, 213, 166–182. DOI:10.1016/j. geomorph.2014.01.006.
- Jonsson, I.G., 1966. Wave boundary layers and friction factors. *Proceedings of 10th International Conference on Coastal Engineering, Tokyo Japan*, 127-148. ASCE.
- Julian, J.P. & Torres, R. (2006). Hydraulic erosion of cohesive riverbanks. *Geomorphology*, 76(1-2), 193-206. DOI:10.1016/j.geomorph.2005.11.003.
- Kadaster (2020). Website topotijdreis, https://www.topotijdreis.nl, last access 24/07/2020.
- Kakeh, N., Coco, G., & Marani, M. (2016). On the morphodynamic stability of intertidal environments and the role of vegetation. *Advances in water resources*, 93, 303-314. DOI:10.1016/j.advwatres.2015.11.003.
- Kallis, G., & Butler, D. (2001). The EU water framework directive: measures and implications. Water policy, 3(2), 125-142. DOI:10.1016/S1366-7017(01)00007-1.
- Karamigolbaghi, M., Ghaneeizad, S.M., Atkinson, J.F., Bennett, S.J., & Wells, R.R. (2017). Critical assessment of jet erosion test methodologies for cohesive soil and sediment. *Geomorphology*, 295, 529-536. DOI:10.1016/j.geomorph.2017.08.005.
- Kean, J.W., & Smith, J.D. (2006). Form drag in rivers due to small-scale natural topographic features: 1. Regular sequences. Journal of Geophysical Research: Earth Surface, 111, F04009. DOI:10.1029/2006JF000467.
- Kessler, A.C., Gupta, S.C., and Brown, M.K. (2013). Assessment of river bank erosion in Southern Minnesota rivers post European settlement. Geomorphology, 201, 312-322. DOI:10.1016/j.geomorph.2013.07.006.
- Khan, N.I. & Islam, A. (2003). Quantification of erosion patterns in the Brahmaputra–Jamuna River using geographical information system and remote sensing techniques. *Hydrological Processes*, 17(5), 959-966. DOI: 10.1002/hyp.1173.
- Khanal, A. & Fox, G.A. (2017). Detachment characteristics of root-permeated soils from laboratory jet erosion tests. *Ecological Engineering*, 100, 335-343. DOI:10.1016/j.ecoleng.2016.10.081.
- Kimiaghalam, N., Goharrokhi, M., Clark, S. P., & Ahmari, H. (2015). A comprehensive fluvial geomorphology study of riverbank erosion on the Red River in Winnipeg, Manitoba, Canada. *Journal of Hydrology, 529*, 1488-1498. DOI:10.1016/j.jhydrol.2015.08.033.
- Kimiaghalam, N., Clark, S.P., & Ahmari, H. (2016). An experimental study on the effects of physical, mechanical, and electrochemical properties of natural cohesive soils on critical shear stress and erosion rate. *International Journal of Sediment Research*, 31(1), 1-15. DOI:10.1016/j.ijsrc.2015.01.001.

- Klavon, K., Fox, G., Guertault, L., Langendoen, E., Enlow, H., Miller, R., and Khanal, A. (2017) Evaluating a process-based model for use in streambank stabilization: insights on the Bank Stability and Toe Erosion Model (BSTEM). *Earth Surf. Process. Landforms*, 42, 191-213. DOI:10.1002/esp.4073.
- Kleinhans, M.G. (2010). Sorting out river channel patterns. *Progress in Physical Geography 34*(3), 287-326. DOI:10.1177/0309133310365300.
- Kleinhans, M.G., Schuurman, F., Bakx, W., & Markies, H. (2009). Meandering channel dynamics in highly cohesive sediment on an intertidal mud flat in the Westerschelde estuary, the Netherlands. *Geomorphology* 105, 261-276. DOI:10.1016/j.geomorph.2008.10.005.
- Kleinhans, M.G., Bierkens, M.F.P., & Van der Perk, M. (2010). HESS Opinions On the use of laboratory experimentation: "Hydrologists, bring out shovels and garden hoses and hit the dirt". *Hydrology and Earth System Sciences*, *14*(2), 369-382. DOI:10.5194/hess-14-369-2010.
- Kleinhans, M.G., de Vries, B., Braat, L., & van Oorschot, M. (2018). Muddy and vegetated floodplain formation effects on fluvial pattern in an incised river. *Earth Surf. Process. Landforms*, *43*, 2948-2963. DOI:10.1002/esp.4437.
- Klösch, M., Blamauer, B., & Habersack, H. (2015). Intra-event scale bar-bank interactions and their role in channel widening. *Earth surface processes and landforms*, 40(11), 1506-1523. DOI:10.1002/esp.3732.
- Knight, D.W. (2013). River hydraulics—a view from midstream. *Journal of Hydraulic Research*, 51(1), 2-18. DOI:10.1080/00221686.2012.749431.
- Knight, D.W. & Shiono, K. (1990). Turbulence measurements in a shear layer region of a compound channel. Journal of hydraulic research, 28(2), 175-196. DOI:10.1080/00221689009499085.
- Koch, E.W., Barbier, E.B., Silliman, B. R., Reed, D.J., Perillo, G.M., Hacker, S.D., et al. (2009). Non-linearity in ecosystem services: temporal and spatial variability in coastal protection. *Frontiers in Ecology and the Environment*, 7(1), 29-37. DOI:10.1890/080126.
- Koken, M. & Constantinescu, G. (2008). An investigation of the flow and scour mechanisms around isolated spur dikes in a shallow open channel: 1. Conditions corresponding to the initiation of the erosion and deposition process. Water Resources Research, 44(8). DOI:10.1029/2007WR006491.
- Kondolf, G.M. (1997). PROFILE: hungry water: effects of dams and gravel mining on river channels. Environmental management, 21(4), 533-551. DOI:10.1007/s002679900048.
- Konsoer, K.M., Rhoads, B.L., Best, J.L., Langendoen, E.J., Abad, J.D., Parsons, D.R., & Garcia, M.H. (2016a). Three-dimensional flow structure and bed morphology in large elongate meander loops with different outer bank roughness characteristics. Water Resources Research, 52(12), 9621-9641. DOI:10.1002/2016WR019040.
- Konsoer, K.M., Rhoads, B.L., Langendoen, E.J., Best, J.L., Ursic, M.E., Abad, J.D., & Garcia, M.H. (2016b). Spatial variability in bank resistance to erosion on a large meandering, mixed bedrock-alluvial river. *Geomorphology*, 252, 80-97. DOI:10.1016/j.geomorph.2015.08.002.
- Konsoer, K., Rhoads, B., Best, J., Langendoen, E., Ursic, M., Abad, J., & Garcia, M. (2017). Length scales and statistical characteristics of outer bank roughness for large elongate meander bends: The influence of bank material properties, floodplain vegetation and flow inundation. *Earth Surface Processes and Landforms*, 42(13), 2024-2037. DOI:10.1002/esp.4169.
- Kordi, H., Amini, R., Zahiri, A., & Kordi, E. (2015). Improved Shiono and Knight method for overflow modeling. Journal of Hydrologic Engineering, 20(12), 04015041. DOI: 10.1061/(ASCE)HE.1943-5584.0001239.
- Laderoute, L., & Bauer, B. (2013). River Bank Erosion and Boat Wakes Along the Lower Shuswap River. British Columbia. Final project report submitted to the Regional District of North Okanagan Fisheries and Oceans Canada. Available at http://www.rdno.ca/docs/River_Bank_Erosion_Lower_Shu_River_Final_Project Report.pdf, last accessed 25/06/2020.

- Lague, D., Brodu, N., & Leroux, J. (2013). Accurate 3D comparison of complex topography with terrestrial laser scanner: Application to the Rangitikei canyon (NZ). ISPRS Journal of Photogrammetry and Remote Sensing, 82, 10-26. DOI:10.1016/j.isprsjprs.2013.04.009.
- Lamb, H. [1932] Hydrodynamics (Cambridge University Press, Cambridge), 738pp.
- Lammers, R.W., Bledsoe, B.P., & Langendoen, E.J. (2017). Uncertainty and sensitivity in a bank stability model: implications for estimating phosphorus loading. *Earth Surface Processes and Landforms*, 42(4), 612-623. DOI:10.1002/esp.4004.
- Lane, S.N. (2000). The measurement of river channel morphology using digital photogrammetry. *The Photogrammetric Record, 16*(96), 937-961. DOI:10.1111/0031-868X.00159.
- Lane, S.N., Widdison, P.E., Thomas, R.E., Ashworth, P.J., Best, J.L., Lunt, I.A., Sambrook Smith, G.H. & Simpson, C.J. (2010). Quantification of braided river channel change using archival digital image analysis. *Earth Surface Processes and Landforms*, 35(8), 971-985. DOI:10.1002/esp.2015.
- Langendoen, E.J., & Simon, A. (2008). Modeling the evolution of incised streams. II: Streambank erosion. *Journal of hydraulic engineering*, 134 (7) DOI:10.1061/(ASCE)0733-9429(2008)134:7(905).
- Langendoen, E.J., Richard Lowrance, R. and Simon, A. (2009). Assessing the impact of riparian processes on streambank stability. *Ecohydrol.*, 2: 360-369. DOI:10.1002/eco.78
- Larson, M., Almström, B., Göransson, G., Hanson, H., & Danielsson, P. (2017). Sediment movement induced by ship-generated waves in restricted waterways. *Proceedings of Coastal Dynamics 2017*, 120, 300-311.
- Lawler, D.M. (1992). Process dominance in bank erosion systems. In *Lowland floodplain rivers: Geomorphological perspectives*, 117-43. John Wiley, Chichester.
- Lawler, D.M. (1993). The measurement of river bank erosion and lateral channel change: a review. *Earth surface processes and landforms*, 18(9), 777-821. DOI:10.1002/esp.3290180905.
- Lawler, D.M. (2005). The importance of high-resolution monitoring in erosion and deposition dynamics studies: examples from estuarine and fluvial systems. *Geomorphology, 64*(1), 1-23. DOI:10.1016/j. geomorph.2004.04.005.
- Le, T.B., Crosato, A., & Uijttewaal, W.S.J. (2018). Long-term morphological developments of river channels separated by a longitudinal training wall. *Advances in Water Resources*, 113, 73-85. DOI:10.1016/j. advwatres.2018.01.007.
- Lewin, J., & Ashworth, P.J. (2014). The negative relief of large river floodplains. *Earth-Science Reviews, 129,* 1-23. DOI:10.1016/j.earscirev.2013.10.014.
- Leyland, J., Darby, S. E., Teruggi, L., Rinaldi, M., & Ostuni, D. (2015). A self-limiting bank erosion mechanism? inferring temporal variations in bank form and skin drag from high resolution topographic data. *Earth Surf. Process. Landforms*, 40: 1600–1615. DOI:10.1002/esp.3739.
- Liedermann, M., Tritthart, M., Gmeiner, P., Hinterleitner, M., Schludermann, E., Keckeis, H., & Habersack, H. (2014). Typification of vessel-induced waves and their interaction with different bank types, including management implications for river restoration projects. *Hydrobiologia*, 729(1), 17-31. DOI:10.1007/s10750-014-1829-1.
- Mariotti, G., & Fagherazzi, S. (2013). Critical width of tidal flats triggers marsh collapse in the absence of sea-level rise. *Proceedings of the national Academy of Sciences, 110*(14), 5353-5356. DOI:10.1073/pnas.1219600110.
- Massey, D. (2001). Talking of space-time, *Transactions of the Institute of British Geographers, 26*: 257–261. DOI:10.1111/1475-5661.00019.
- Masterman, R., & Thorne, C.R. (1992). Predicting influence of bank vegetation on channel capacity. *Journal of Hydraulic Engineering*, 118(7), 1052-1058. DOI:10.1061/(ASCE)0733-9429(1992)118:7(1052).

- Maynord, S.T., Biedenham, D.S., Fischenich, C.J., & Zufelt, J.E. (2008). Boat-wave-induced bank erosion on the Kenai River, Alaska (No. ERDC-TR-08-5). Engineer Research and Development Center Vicksburg Ms Coastal And Hydraulics Lab. US Army Corps of Engineers. Available at https://apps.dtic.mil/docs/citations/ADA479220, last access 24/07/2020.
- Meile, T., Boillat, J.L., & Schleiss, A.J. (2011). Flow resistance caused by large-scale bank roughness in a channel. *Journal of Hydraulic Engineering*, 137(12), 1588-1597. DOI:10.1061/(ASCE)HY.1943-7900.0000469.
- Micheletti, N., Chandler, J.H., and Lane, S.N. (2015). Investigating the geomorphological potential of freely available and accessible structure-from-motion photogrammetry using a smartphone. *Earth Surface Processes and Landforms*, 40(4), 473-486. DOI:10.1002/esp.3648.
- Midgley, T.L., Fox, G.A., & Heeren, D.M. (2012). Evaluation of the bank stability and toe erosion model (BSTEM) for predicting lateral retreat on composite streambanks. *Geomorphology, 145*, 107-114. DOI:10.1016/j.geomorph.2011.12.044.
- Mitchener, H., & Torfs, H. (1996). Erosion of mud/sand mixtures. *Coastal engineering, 29*(1-2), 1-25. DOI:10.1016/S0378-3839(96)00002-6.
- Morrison, M. J. (2017). Shallow Shear-Wave Seismic Analysis of Point Bar Deposits of False River, Louisiana. LSU Master's Theses. 4407. Available at https://digitalcommons.lsu.edu/gradschool_theses/4407, last access 24/07/2020.
- Mosselman, E. (1995). A review of mathematical models of river planform changes. *Earth Surface Processes and Landforms*, 20(7), 661-670. DOI:10.1002/esp.3290200708.
- Mosselman, E. (1998). Morphological modelling of rivers with erodible banks. *Hydrological Processes*, *12*(8), 1357-1370. DOI:10.1002/(SICI)1099-1085(19980630)12:8<1357::AID-HYP619>3.0.CO;2-7.
- Motta, D., Abad, J.D., Langendoen, E.J., & Garcia, M.H. (2012a). A simplified 2D model for meander migration with physically-based bank evolution. *Geomorphology, 163,* 10-25. DOI:10.1016/j. geomorph.2011.06.036.
- Motta, D., Abad, J.D., Langendoen, E.J., & Garcia, M.H. (2012b). The effects of floodplain soil heterogeneity on meander planform shape. *Water Resources Research*, 48, W09518. DOI:10.1029/2011WR011601.
- Motta, D., Langendoen, E.J., Abad, J.D., & Garcia, M.H. (2014). Modification of meander migration by bank failures. *Journal of Geophysical Research: Earth Surface*, 119(5), 1026-1042. DOI:10.1002/2013JF002952.
- Murray—Darling Basin Authority (2017). Bank erosion along the Murray River between Hume Dam and the Ovens Junction. ISBN (online): 978-1-925599-21-3.
- Naiman, R.J., Decamps, H., & Pollock, M. (1993). The role of riparian corridors in maintaining regional biodiversity. *Ecological applications*, *3*(2), 209-212. DOI:10.2307/1941822.
- Nakos, D.E., & Sclavounos, P.D. (1990). On steady and unsteady ship wave patterns. *Journal of Fluid Mechanics*, 215, 263-288. DOI:10.1017/S0022112090002646.
- Nanson, G.C. & Croke, J.C. (1992). A genetic classification of floodplains. *Geomorphology*, 4(6), 459-486. DOI:10.1016/0169-555X(92)90039-Q.
- Nanson, G.C., Von Krusenstierna, A., Bryant, E.A., & Renilson, M.R. (1994). Experimental measurements of river-bank erosion caused by boat-generated waves on the gordon river, Tasmania. *Regulated Rivers: Research & Management*, *9*(1), 1-14. DOI:10.1002/rrr.3450090102.
- Nardi, L., Campo, L., & Rinaldi, M. (2013). Quantification of riverbank erosion and application in risk analysis. *Nat Hazards*, *69*(1), 869-887. DOI:10.1007/s11069-013-0741-8.
- Nardi, L., Rinaldi, M., & Solari, L. (2012). An experimental investigation on mass failures occurring in a riverbank composed of sandy gravel. *Geomorphology*, 163, 56-69. DOI:10.1016/j.geomorph.2011.08.006.

- Nederlandsch-Belgische commissie ingesteld tot onderzoek van de kanalisatie van de gemeenschappelijke Maas (1912). Maas-Meuse. Rapport betreffende de werkzaamheden van de commissie: Rapport sur les travaux de la commission. Den Haag: Drukkerij Mouton.
- Nepf, H.M. (2012). Hydrodynamics of vegetated channels. *Journal of Hydraulic Research*, 50(3), 262-279. DOI:10.1080/00221686.2012.696559.
- Netherlands Nationaal Archief (1952). Algemene Rivierkaart van Nederland Tweede Herziening, 1914-1961. Serie III. Maas, Afgedamde Maas, Bergsche Maas, Amer, Nieuwe-Merwede, Hollandsch Diep, Haringvliet, c.a. (tweede herziening) - Blad no. 18: Gennep.
- Nienhuis, P.H. (2008). Environmental history of the Rhine-Meuse Delta: an ecological story on evolving human-environmental relations coping with climate change and sea-level rise. Springer Science & Business Media.
- O'Donoghue, T., Kikkert, G.A., Pokrajac, D., Dodd, N., & Briganti, R. (2016). Intra-swash hydrodynamics and sediment flux for dambreak swash on coarse-grained beaches. *Coastal Engineering*, 112, 113-130. DOI:10.1016/j.coastaleng.2016.03.004.
- O'neal, M. A., and Pizzuto, J. E. (2011). The rates and spatial patterns of annual riverbank erosion revealed through terrestrial laser-scanner surveys of the South River, Virginia. *Earth Surface Processes and Landforms*, 36(5), 695-701. DOI:10.1002/esp.2098.
- ONEMA (2018). Towards the restoration of rivers and aquatic environments. A collection of river hydromorphology restoration examples. Available at https://professionnels.ofb.fr/en/node/654, last access 24/07/2020.
- Ortuño, M., Guinau, M., Calvet, J., Furdada, G., Bordonau, J., Ruiz, A., & Camafort, M. (2017). Potential of airborne LiDAR data analysis to detect subtle landforms of slope failure: Portainé, Central Pyrenees. *Geomorphology, 295*, 364-382. DOI:10.1016/j.geomorph.2017.07.015.
- Osman, A.M. & Thorne, C.R. (1988). Riverbank stability analysis. 1: Theory. *Journal of Hydraulic Engineering*, 114(2), 134-150. DOI:10.1061/(ASCE)0733-9429(1988)114:2(134).
- Osterkamp, W.R., Hupp, C.R. and Stoffel, M. (2012). The interactions between vegetation and erosion: new directions for research at the interface of ecology and geomorphology. *Earth Surf. Process. Landforms*, *37*: 23-36. DOI:10.1002/esp.2173.
- Ottevanger, W., Blanckaert, K., & Uijttewaal, W.S. (2012). Processes governing the flow redistribution in sharp river bends. *Geomorphology*, 163, 45-55. DOI:10.1016/j.geomorph.2011.04.049.
- Ouédraogo, M.M., Degré, A., Debouche, C., & Lisein,J. (2014). The evaluation of unmanned aerial system-based photogrammetry and terrestrial laser scanning to generate DEMs of agricultural watersheds. *Geomorphology, 214*, 339-355. DOI:10.1016/j.geomorph.2014.02.016.
- Oumeraci, H., Klammer, P., & Partenscky, H.W. (1993). Classification of breaking wave loads on vertical structures. *Journal of waterway, port, coastal, and ocean engineering, 119*(4), 381-397. DOI:10.1061/(ASCE)0733-950X(1993)119:4(381).
- Page, K.J., Nanson, G.C., & Frazier, P.S. (2003). Floodplain formation and sediment stratigraphy resulting from oblique accretion on the Murrumbidgee River, Australia. Journal of Sedimentary Research, 73(1), 5-14.
- Papanicolaou, A. N., Elhakeem, M., & Hilldale, R. (2007). Secondary current effects on cohesive river bank erosion. *Water Resources Research, 43*, p. W12418. https://DOI.org/10.1029/2006WR005763.
- Parker, C., Simon, A., & Thorne, C.R. (2008). The effects of variability in bank material properties on riverbank stability: Goodwin Creek, Mississippi. *Geomorphology*, 101(4), 533-543. DOI:10.1016/j. geomorph.2008.02.007.

- Parker, G., Shimizu, Y., Wilkerson, G.V., Eke, E.C., Abad, J.D., Lauer, J.W., Paola, C., Dietrich, W.E., & Voller, V.R. (2011). A new framework for modeling the migration of meandering rivers. *Earth Surface Processes and Landforms*, 36(1), 70-86. DOI:10.1002/esp.2113.
- Parnell, K.E., McDonald, S.C., & Burke, A.E. (2007). Shoreline effects of vessel wakes, Marlborough Sounds, New Zealand. *Journal of Coastal Research*, 502-506. https://www.jstor.org/stable/26481640.
- Parnell, K.E., Soomere, T., Zaggia, L., Rodin, A., Lorenzetti, G., Rapaglia, J., & Scarpa, G.M. (2015). Ship-induced solitary Riemann waves of depression in Venice Lagoon. *Physics Letters A*, 379(6), 555-559. DOI:10.1016/j.physleta.2014.12.004.
- Partheniades, E. (1965). Erosion and deposition of cohesive soils. *Journal of the Hydraulics Division*, 91(1), 105-139.
- Partheniades, E. (2009). Cohesive Sediments in Open Channels: Erosion, Transport and Deposition. Butterworth-Heinemann. ISBN 9780080877976.
- Pasquale, N., Perona, P., Francis, R., & Burlando, P. (2012). Effects of streamflow variability on the vertical root density distribution of willow cutting experiments. *Ecological Engineering*, 40, 167-172. DOI:10.1016/j. ecoleng.2011.12.002.
- Passalacqua, P., Belmont, P., Staley, D.M., Simley, J.D., Arrowsmith, J.R., Bode, C.A., Crosby, C., DeLong, S.B., Glenn, N.F., Kelly, S.A. & Lague, D. (2015). Analyzing high resolution topography for advancing the understanding of mass and energy transfer through landscapes: A review. *Earth-Science Reviews*, 148, 174-193. DOI:10.1016/j.earscirev.2015.05.012.
- Patsinghasanee, S., Kimura, I., Shimizu, Y., Nabi, M., & Chub-Uppakarn, T. (2017). Coupled studies of fluvial erosion and cantilever failure for cohesive riverbanks: Case studies in the experimental flumes and U-Tapao River. *Journal of Hydro-environment Research*, 16, 13-26. DOI: 10.1016/j.jher.2017.04.002.
- Patsinghasanee, S., Kimura, I., Shimizu, Y., & Nabi, M. (2018). Experiments and modelling of cantilever failures for cohesive riverbanks. *Journal of Hydraulic Research*, *56*(1), 76-95. DOI:10.1080/00221686. 2017.1300194.
- Pearce, F. (2013). A Successful Push to restore europe's long-Abused rivers. *Yale Environment 360* (10 December). Available at https://e360.yale.edu/features/a_successful_push_to_restore_europes_long-abused_rivers, last access 24/07/2020.
- Peters, B.A.M. (2005). Vrij eroderende oevers langs de Maas: landschapsecologisch streefbeeld. Bureau Drift.
- Piqué, G., Vericat, D., Sabater, S., & Batalla, R.J. (2016). Effects of biofilm on river-bed scour. *Science of The Total Environment*, 572, 1033-1046. DOI:10.1016/j.scitotenv.2016.08.009.
- Pizzuto, J., O'Neal, M., & Stotts, S. (2010). On the retreat of forested, cohesive riverbanks. *Geomorphology*, 116(3-4), 341-352. DOI:10.1016/j.geomorph.2009.11.008.
- Pollen, N. (2007). Temporal and spatial variability in root reinforcement of streambanks: accounting for soil shear strength and moisture. *Catena*, *69*(3), 197-205. DOI:10.1016/j.catena.2006.05.004.
- Pollen, N. & Simon, A. (2005). Estimating the mechanical effects of riparian vegetation on stream bank stability using a fiber bundle model. *Water Resources Research*, *41*, p. W07025. DOI:10.1029/2004WR003801.
- Pollen-Bankhead, N., & Simon, A. (2009). Enhanced application of root-reinforcement algorithms for bankstability modeling. *Earth Surface Processes and Landforms*, 34(4), 471-480. DOI:10.1002/esp.1690.
- Pollen-Bankhead, N., & Simon, A. (2010). Hydrologic and hydraulic effects of riparian root networks on streambank stability: Is mechanical root-reinforcement the whole story?. *Geomorphology, 116*(3-4), 353-362. DOI:10.1016/j.geomorph.2009.11.013.

- Polvi, L.E., Wohl, E., & Merritt, D.M. (2014). Modeling the functional influence of vegetation type on streambank cohesion. *Earth Surface Processes and Landforms*, 39(9), 1245-1258. DOI:10.1002/esp.3577.
- Prosdocimi, M., Calligaro, S., Sofia, G., Dalla Fontana, G., & Tarolli, P. (2015). Bank erosion in agricultural drainage networks: new challenges from structure-from-motion photogrammetry for post-event analysis. *Earth Surface Processes and Landforms*, 40(14), 1891-1906. DOI:10.1002/esp.3767.
- Pujara, N., Liu, P.L.F., & Yeh, H. (2015). The swash of solitary waves on a plane beach: flow evolution, bed shear stress and run-up. *Journal of Fluid Mechanics*, 779, 556-597. DOI:10.1017/jfm.2015.435.
- Putrevu, U., & Svendsen, I.A. (1991). Wave induced nearshore currents: a study of the forcing, mixing and stability characteristics. Center for Applied Coastal Research, Department of Civil Engineering, University of Delaware.
- Pyle, C.J., Richards, K. S., & Chandler, J. H. (1997). Digital photogrammetric monitoring of river bank erosion. *The Photogrammetric Record, 15*(89), 753-764. DOI:10.1111/0031-868X.00083.
- Rapaglia, J., Zaggia, L., Parnell, K., Lorenzetti, G., & Vafeidis, A.T. (2015). Ship-wake induced sediment remobilization: Effects and proposed management strategies for the Venice Lagoon. *Ocean & Coastal Management*, 110, 1-11. DOI:10.1016/j.ocecoaman.2015.03.002.
- Rauch, H., Sutili, F. & Hörbinger, S. (2014). Installation of a Riparian Forest by Means of Soil Bio Engineering Techniques-Monitoring Results from a River Restoration Work in Southern Brazil. *Open Journal of Forestry*, 4, 161-169. DOI: 10.4236/ojf.2014.42022.
- Reddi, L.N., & Bonala, M.V. (1997). Critical shear stress and its relationship with cohesion for sand. kaolinite mixtures. *Canadian geotechnical journal*, *34*(1), 26-33. DOI:10.1139/t96-086.
- Reeze, B., van Winden, A., Postma, J., Pot, R., Hop J. & Liefveld, W. (2017). Watersysteemrapportage Rijntakken 1990-2015. Ontwikkelingen waterkwaliteit en ecologie. Bart Reeze Water & Ecologie, Harderwijk.
- Reneau, S.L., Drakos, P.G., Katzman, D., Malmon, D.V., McDonald, E.V., & Ryti, R.T. (2004). Geomorphic controls on contaminant distribution along an ephemeral stream. *Earth Surface Processes and Landforms*, 29(10), 1209-1223. DOI:10.1002/esp.108.
- Resop, J.P., & Hession, W.C. (2010). Terrestrial laser scanning for monitoring streambank retreat: Comparison with traditional surveying techniques. *Journal of Hydraulic Engineering*, 136(10), 794-798. DOI:10.1061/(ASCE)HY.1943-7900.0000233.
- RESTORE (2020). Restoring Europe's River. https://restorerivers.eu/wiki, last access 24/07/2020.
- Rhoades, E.L., O'Neal, M.A., & Pizzuto, J.E. (2009). Quantifying bank erosion on the South River from 1937 to 2005, and its importance in assessing Hg contamination. *Applied Geography, 29*(1), 125-134. DOI:10.1016/j.apgeog.2008.08.005.
- Rhodes, D.G., & Knight, D.W. (1994). Distribution of shear force on boundary of smooth rectangular duct. *Journal of Hydraulic Engineering*, 120(7), 787-807. DOI:10.1061/(ASCE)0733-9429(1994)120:7(787).
- Rinaldi, M. & Darby, S.E. (2007). 9 Modelling river-bank-erosion processes and mass failure mechanisms: progress towards fully coupled simulations. *Developments in Earth Surface Processes, 11*, 213-239. DOI:10.1016/S0928-2025(07)11126-3.
- Rinaldi, M. & Nardi, L. (2013). Modeling interactions between riverbank hydrology and mass failures. *Journal of Hydrologic Engineering*, *18*(10), 1231-1240. DOI:.10.1061/(ASCE)HE.1943-5584.0000716.
- Rinaldi, M., Casagli N., Dapporto S., & Gargini, A. (2004). Monitoring and modeling of pore water pressure changes and riverbank stability during flow events. *Earth Surf. Processes Landforms*, *29*, 237-254. DOI: 10.1002/esp.1042.

- Rinaldi, M., Wyżga, B. and Surian, N. (2005). Sediment mining in alluvial channels: physical effects and management perspectives. *River Res. Applic.*, 21, 805-828. DOI:10.1002/rra.884.
- Rixhon, G., Braucher, R., Bourlès, D., Siame, L., Bovy, B., & Demoulin, A. (2011). Quaternary river incision in NE Ardennes (Belgium)–Insights from 10Be/26Al dating of river terraces. *Quaternary Geochronology,* 6(2), 273-284. DOI:10.1016/j.quageo.2010.11.001.
- Rood, S.B., Braatne, J.H., & Hughes, F.M. (2003). Ecophysiology of riparian cottonwoods: stream flow dependency, water relations and restoration. *Tree Physiology*, 23(16), 1113-1124. DOI:10.1093/ treephys/23.16.1113.
- Rood, S.B., Bigelow, S.G., Polzin, M.L., Gill, K.M., & Coburn, C.A. (2015). Biological bank protection: trees are more effective than grasses at resisting erosion from major river floods. *Ecohydrology*, *8*(5), 772-779. DOI:10.1002/eco.1544.
- Rousseau, Y.Y., Van de Wiel, M.J., & Biron, P.M. (2017). Simulating bank erosion over an extended natural sinuous river reach using a universal slope stability algorithm coupled with a morphodynamic model. *Geomorphology*, 295, 690-704. DOI:10.1016/j.geomorph.2017.08.008.
- Roy, S., Das, V.K., & Debnath, K. (2019). Characteristics of intermittent turbulent structures for river bank undercut depth increment. *Catena*, *172*, 356-368. DOI: 10.1016/j.catena.2018.09.008.
- Rutherfurd, I.D., & Grove, J.R. (2004). The influence of trees on stream bank erosion: evidence from rootplate abutments. In *Riparian Vegetation and Fluvial Geomorphology*, 141-152. S.J. Bennett and A. Simon (eds.). American Geophysical Union, Washington DC. DOI:10.1029/008WSA11.
- RWS/RIKZ (2009). WAQUA/TRIWAQ two- and three-dimensional shallow water flow model Technical documentation. SIMONA report nr. 99-01. Rijkswaterstaat, the Netherlands.
- Samadi, A., Amiri-Tokaldany, E., & Darby, S.E. (2009). Identifying the effects of parameter uncertainty on the reliability of riverbank stability modelling. *Geomorphology*, 106(3-4), 219-230. DOI:10.1016/j. geomorph.2008.10.019.
- Sanjou, M., & Nezu, I. (2013). Hydrodynamic characteristics and related mass-transfer properties in openchannel flows with rectangular embayment zone. Environmental Fluid Mechanics, 13(6), 527-555. DOI:10.1007/s10652-013-9279-2.
- Scarpa, G.M., Zaggia, L., Manfè, G., Lorenzetti, G., Parnell, K., Soomere, T., Rapaglia, J., & Molinaroli, E. (2019). The effects of ship wakes in the Venice Lagoon and implications for the sustainability of shipping in coastal waters. *Scientific Reports*, *9*, 19014. DOI:10.1038/s41598-019-55238-z.
- Schilling, K., Kleinwachter, M., & Liebenstein, H. (2013). Technical-biological river-bank protection a contribution to the ecological upgrading of the banks of Federal waterways in Germany First experiences from a field test along the River Rhine. *PIANC Smart Rivers Conference 2013*, 110, Liege (BE) Maastricht (NL).
- Schludermann, E., Liedermann, M., Hoyer, H., Tritthart, M., Habersack, H., & Keckeis, H. (2014). Effects of vessel-induced waves on the YOY-fish assemblage at two different habitat types in the main stem of a large river (Danube, Austria). *Hydrobiologia 729*, 3-15. DOI:10.1007/s10750-013-1680-9.
- Schmitt, K., Schäffer, M., Koop, J., & Symmank, L. (2018). River bank stabilisation by bioengineering: potentials for ecological diversity. Journal of Applied Water Engineering and Research, 6(4), 262-273. DOI:10.1080/23249676.2018.1466735.
- Schwendel AC, Nicholas AP, Aalto RE, Sambrook Smith GH, Buckley S. 2015. Interaction between meander dynamics and floodplain heterogeneity in a large tropical sand-bed river: the Rio Beni, Bolivian Amazon. Earth Surface Processes and Landforms, 40(15), 2026-2040. DOI:10.1002/esp.3777.

- Sheremet, A., Gravois, U., & Tian, M. (2013). Boat-wake statistics at Jensen Beach, Florida. Journal of Waterway, Port, Coastal, and Ocean Engineering, 139(4), 286-294. DOI:10.1061/(ASCE)WW.1943-5460.0000182.
- Shiono, K. & Knight, D.W. (1991). Turbulent open-channel flows with variable depth across the channel. Journal of Fluid Mechanics, 222, 617-646. DOI:10.1017/S0022112091001246.
- Simon, A., Curini, A., & Abt, S. (1998). Pore pressure and bank stability: The influence of matric suction. Hydraulic engineering, 98.
- Simon, A., Curini, A., Darby S.E., Langendoen E. (1999a). Streambank mechanics and the role of bank and near bank processes in incised channels. In Incised Channels: Processes, Forms, Engineering, and Management, 123-152. Darby S.E., Simon A. (eds). Wiley: Chichester.
- Simon, A., Curini, A., Darby, S.E., & Langendoen, E.J. (2000). Bank and near-bank processes in an incised channel. Geomorphology, 35(3), 193-217. DOI:10.1016/S0169-555X(00)00036-2.
- Simon, A., Pollen-Bankhead, N., & Thomas, R.E. (2011). Development and application of a deterministic bank stability and toe erosion model for stream restoration. In Stream restoration in dynamic fluvial systems: Scientific approaches, analyses and tools. Washington, DC, USA, AGU, 453-474. DOI:10.1029/2010GM001006.
- Simpson, R.L. (1989). Turbulent boundary-layer separation. Annual Review of Fluid Mechanics 21, 205-232. DOI: 10.1146/annurev.fl.21.010189.001225.
- Siviglia, A., & Crosato, A. (2016). Numerical modelling of river morphodynamics: Latest developments and remaining challenges. *Advances in Water Resources*, 93(A), 1-3. DOI:10.1016/j.advwatres.2016.01.005.
- Slatton, K.C., Carter W.E., Shrestha R.L., & Dietrich W. (2007). Airborne Laser Swath Mapping: Achieving the resolution and accuracy required for geosurficial research. *Geophys. Res. Lett.*, 34, L23S10. DOI:10.1029/2007GL031939.
- Sligte van der, R.A.M., Weij, D., Spruyt, A., Schuurman, F. (2012). Schuivende marges 2011; casestudy IJssel en Maas: concept. Available at https://www.deltares.nl/nl/publicaties/, last access 27/05/2020.
- Slingerland, R., & Smith, N.D. (2004). River avulsions and their deposits. *Annu. Rev. Earth Planet. Sci., 32,* 257-285. DOI:10.1146/annurev.earth.32.101802.120201.
- Smith, H.G., Spiekermann, R., Dymond, J., & Basher, L. (2019). Predicting spatial patterns in riverbank erosion for catchment sediment budgets. *New Zealand Journal of Marine and Freshwater Research*, 53(3), 338-362.
- Smith, M.W., Carrivick, J.L., Hooke, J., & Kirkby, M.J. (2014). Reconstructing flash flood magnitudes using "Structure-from-Motion": A rapid assessment tool. *Journal of Hydrology*, 519, 1914–1927. DOI:10.1016/j. jhydrol.2014.09.078.
- Snavely, N., Seitz, S.M., & Szeliski, R. (2008). Modeling the world from internet photo collections, International Journal of Computer Vision, 80(2), 189-210. DOI:10.1007/s11263-007-0107-3.
- Söhngen, B., Koop, J.H.E., Knight, S.E., Rythönen, J., Beckwith, P., Ferrari, N., Iribarren, J., Kevin, T., Wolter, C., Maynord, S.T. (2008). Considerations to Reduce Environmental Impacts of Vessels. Report of PIANC InComWorking Group 27 (No. 99). PIANC, Brussels, p. 90.
- Southgate, H.N. (1995) The effects of wave chronology on medium and long term coastal morphology. Coastal Engineering, 26(3-4), 251-270. DOI:10.1016/0378-3839(95)00028-3.
- Spiekermann, R., Betts, H., Dymond, J., & Basher, L. (2017). Volumetric measurement of river bank erosion from sequential historical aerial photography. Geomorphology, 296, 193-208. DOI:10.1016/j. geomorph.2017.08.047.

- Spruyt, A., van der Sligte, R.A.M., van der Mark, C.F., Sieben, A., & Mosselman, E. (2012). Development of a rapid assessment tool for river bank erosion. *Proceeding of River Flow 2012, San Jose, Costa Rica*, 767-772. CRC Press.
- Stöcker, C., Eltner, A., & Karrasch, P. (2015). Measuring gullies by synergetic application of UAV and close range photogrammetry A case study from Andalusia, Spain. *Catena*, 132, 1–11. DOI:10.1016/j. catena.2015.04.004.
- Stolker, C. & Verheij, H.J. (2001a). Gevoeligheidsonderzoek sedimentatie en erosie in kribvakken langs de Lek, WL Delft Hydraulics, Delft. Available at http://resolver.tudelft.nl/uuid:0cc33eb6-31e2-4c37-ae2a-897fdddf6d17, last access 06/06/2020.
- Stolker, C. & Verheij, H.J. (2001b). Calibratie van een oeverafslagmodel voor de Zandmaas. Rapport nr. Q3060, WL Delft Hydraulics, Delft. Available at http://resolver.tudelft.nl/uuid:39bfdd9b-d1eb-43e1-ae86-044155b65419, last access 06/06/2020.
- Struiksma, N., Olesen, K.W., Flokstra, C., De Vriend, H.J. (1985). Bed deformation in curved alluvial channels. *Journal of Hydraulic Research*, 23(1), 57-79. DOI:10.1080/00221688509499377.
- Styles, R., & Hartman, M.A. (2019). Effect of Tidal Stage on Sediment Concentrations and Turbulence by Vessel Wake in a Coastal Plain Saltmarsh. *Journal of Marine Science and Engineering*, 7(6), 192. DOI:10.3390/jmse7060192.
- Svendsen, I.A. (1984). Wave heights and set-up in a surf zone. Coastal engineering, 8(4), 303-329.
- Svendsen, I.A., Madsen, P.Å., & Hansen, J.B. (1978). Wave characteristics in the surf zone. In Coastal Engineering 1978 (pp. 520-539).
- Swart, D.H. (1974). Offshore sediment transport and equilibrium beach profiles. Delft Hydraulics laboratory, publication No. 131. Available at http://resolver.tudelft.nl/uuid:057cb136-5f5b-484a-878d-5616fbaeda4e, last access 24/07/2020.
- Talmon, A.M., Struiksma, N., & Van Mierlo, M.C.L.M. (1995). Laboratory measurements of the direction of sediment transport on transverse alluvial-bed slopes. *Journal of hydraulic research, 33*(4), 495-517. DOI:10.1080/00221689509498657.
- Tamminga, A.D., Brett C.E., & Hugenholtz C.H. (2015). UAS-based remote sensing of fluvial change following an extreme flood event. *Earth Surface Processes and Landforms 40*(11), 1464-1476. DOI: 10.1002/esp.3728.
- Tarolli, P., Sofia, G., Dalla Fontana, G. (2012). Geomorphic features extraction from high-resolution topography: landslide crowns and bank erosion. *Natural Hazards*, *61*(1), 65-83. DOI:10.1007/s11069-010-9695-2.
- Tebbens, L.A., Veldkamp, A., Westerhoff, W. & Kroonenberg, S.B. (1999). Fluvial incision and channel downcutting as a response to Late-glacial and Early Holocene climate change: the lower reach of the River Meuse (Maas), The Netherlands. *Journal of Quaternary Science*, 14, 59-75. DOI:10.1002/(SICI)1099-1417(199902)14:1<59::AID-JQS408>3.0.CO;2-Z.
- Telling, J., Lyda, A., Hartzell, P., & Glennie, C. (2017). Review of earth science research using terrestrial laser scanning. *Earth-Science Reviews*, 169, 35-68. DOI:10.1016/j.earscirev.2017.04.007.
- Tengbeh, G.T. (1989). The effect of grass cover on bank erosion. PhD thesis, Cranfield University, UK. Available at http://hdl.handle.net/1826/3620, last access 19/06/2020.
- Terzaghi, K., Peck, R.B., & Mesri, G. (1996). *Soil mechanics in engineering practice*. John Wiley & Sons. ISBN: 978-0-471-08658-1.
- Theiling, C.H., Janvrin, J.A., & Hendrickson, J. (2015). Upper Mississippi River restoration: implementation, monitoring, and learning since 1986. *Restoration Ecology*, 23(2), 157-166. DOI:10.1111/rec.12170.

- Thom, M., Schmidt, H., Gerbersdorf, S.U., & Wieprecht, S. (2015). Seasonal biostabilization and erosion behavior of fluvial biofilms under different hydrodynamic and light conditions. *International Journal of Sediment Research*, 30(4), 273-284. DOI:10.1016/j.ijsrc.2015.03.015.
- Thoma, D.P., Gupta, S.C., Bauer, M.E., & Kirchoff, C.E. (2005). Airborne laser scanning for riverbank erosion assessment. *Remote sensing of Environment*, *95*(4), 493-501. DOI:10.1016/j.rse.2005.01.012.
- Thoman, R.W., & Niezgoda, S.L. (2008). Determining erodibility, critical shear stress, and allowable discharge estimates for cohesive channels: Case study in the Powder River basin of Wyoming. Journal of hydraulic engineering, 134(12), 1677-1687. DOI:10.1061/(ASCE)0733-9429(2008)134:12(1677).
- Thorne, C.R. (1978). Processes and mechanics of bank erosion. PhD Thesis, University of East Anglia, 450pp.
- Thorne, C.R. (1982). Processes and mechanisms of river bank erosion. In Gravel-bed rivers, 227-259.
- Thorne, C.R. (1990). Effects of vegetation on riverbank erosion and stability. In *Vegetation and erosion:* processes and environments. Thornes, J. B. (ed.). John Wiley and Sons Ltd. ISBN: 0471926302.
- Thorne, C.R. & Hey, R.D. (1979). Direct measurements of secondary currents at a river inflexion point. Nature, 280(5719), 226. DOI:10.1038/280226a0.
- Thorne, C.R. & Tovey, N.K. (1981). Stability of composite river banks. *Earth Surface Processes and Landforms*, 6(5), 469-484. DOI:10.1002/esp.3290060507.
- Thorne, C.R. & Osman, A.M. (1988). The influence of bank stability on regime geometry of natural channels. In *International Conference on River Regime*, 18-20. Wiley: Chichester.
- Thorne, C.R., Russell, A.P., & Alam, M.K. (1993). Planform pattern and channel evolution of the Brahmaputra River, Bangladesh. Geological Society, London, *Special Publications*, 75(1), 257-276. DOI:10.1144/GSL. SP.1993.075.01.16.
- Thorne, S.D., & Furbish, D.J. (1995). Influences of coarse bank roughness on flow within a sharply curved river bend. *Geomorphology*, 12(3), 241-257. DOI:10.1016/0169-555X(95)00007-R.
- Tinoco, R.O., San Juan, J.E., and Mullarney, J.C. (2020). Simplification bias: lessons from laboratory and field experiments on flow through aquatic vegetation. *Earth Surf. Process. Landforms, 45*: 121-143. DOI:10.1002/esp.4743.
- Tolhurst, T.J., Black, K.S., Shayler, S.A., Mather, S., Black, I., Baker, K., & Paterson, D.M. (1999). Measuring the in situ erosion shear stress of intertidal sediments with the Cohesive Strength Meter (CSM). *Estuarine, Coastal and Shelf Science*, 49(2), 281-294. DOI:10.1006/ecss.1999.0512.
- Tonkin, T.N., Midgley, N.G., Graham, D.J., & Labadz, J.C. (2014). The potential of small unmanned aircraft systems and structure-frommotion for topographic surveys: A test of emerging integrated approaches at Cwm Idwal, North Wales. *Geomorphology*, 226, 35-43. DOI:10.1016/j.geomorph.2014.07.021.
- Torsvik, T., Dysthe, K., & Pedersen, G. (2006). Influence of variable Froude number on waves generated by ships in shallow water. *Physics of Fluids*, *18*(6), 062102. Doi:10.1063/1.2212988.
- Trimble, S. W. (1994). Erosional effects of cattle on streambanks in Tennessee, USA. Earth surface processes and landforms, 19(5), 451-464. DOI:10.1002/esp.3290190506.
- Tron, S., Perona, P., Gorla, L., Schwarz, M., Laio, F., & Ridolfi, L. (2015). The signature of randomness in riparian plant root distributions. *Geophysical Research Letters*, 42(17), 7098-7106. DOI:10.1002/2015GL064857.
- Turner, D., Lucieer, A., & de Jong, S. (2015). Time Series Analysis of Landslide Dynamics Using an Unmanned Aerial Vehicle (UAV). *Remote Sensing*, 7, 1736-1757. DOI:10.3390/rs70201736.
- Uijttewaal, W.S.J. (2014). Hydrodynamics of shallow flows: application to rivers. *Journal of Hydraulic Research*, 52(2), 157-172. DOI:10.1080/00221686.2014.905505.

- van Balen, R.T., Kasse, C., & De Moor, J. (2008). Impact of groundwater flow on meandering; example from the Geul River, The Netherlands. *Earth Surface Processes and Landforms*, 33(13), 2010-2028. DOI:10.1002/esp.1651.
- van Ballaer, B., van Liefferinge, C., Backx, H., van Pelt, D. en Meire, P. (2010). Evaluatie van vooroevers langs het Zeekanaal in Grimbergen. Rapport Universiteit Antwerpen, Onderzoeksgroep Ecosysteembeheer, ECOBE 11-R146. Available at https://archief-algemeen.omgeving.vlaanderen.be/xmlui/handle/acd/230094, last access 26/06/2020.
- van Batenburg, K.(2020). Modelling of hydrodynamic and erosion processes at vegetated lake shores. MSc thesis, Delft University of Technology. Available at http://resolver.tudelft.nl/uuid:e9f987c9-e2f7-4e1e-8af9-adffcb8747b2, last access 02/08/2020.
- van Bemmelen, C.W.T., de Schipper, M.A., Darnall, J., & Aarninkhof, S.G.J. (2020). Beach scarp dynamics at nourished beaches. *Coastal Engineering*, *160*, 103725. DOI:10.1016/j.coastaleng.2020.103725.
- van de Lageweg, W.I., van Dijk, W.M., Baar, A.W., Rutten J. & Kleinhans, M.G. (2014). Bank pull or bar push: what drives scroll-bar formation in meandering rivers? *Geology 42*, 319-322. DOI:10.1130/G35192.1.
- van de Lageweg, W.I., McLelland, S.J., & Parsons, D.R. (2018). Quantifying biostabilisation effects of biofilm-secreted and extracted extracellular polymeric substances (EPSs) on sandy substrate. *Earth Surface Dynamics*, *6*(1), 203-215. DOI:10.5194/esurf-6-203-2018.
- van Denderen, R.P. (2019). Side channel dynamics. Enschede: University of Twente. DOI:10.3990/1.9789036547437.
- van Denderen, R.P., Schielen, R.M., Westerhof, S.G., Quartel, S., & Hulscher, S.J. (2019). Explaining artificial side channel dynamics using data analysis and model calculations. *Geomorphology*, *327*, 93-110. DOI:10.1016/j.geomorph.2018.10.016.
- van der Wegen, M., Roelvink, J.A., & Jaffe, B.E. (2019). Morphodynamic resilience of intertidal mudflats on a seasonal time scale. *Journal of Geophysical Research: Oceans, 124,* 8290-8308. DOI:10.1029/2019JC015492.
- van Prooijen, B.C. & Winterwerp, J.C. (2010). A stochastic formulation for erosion of cohesive sediments. *Journal of Geophysical Research: Oceans*, 115(C1). DOI:10.1029/2008JC005189.
- van Prooijen, B.C., Battjes, J.A., & Uijttewaal, W.S. (2005). Momentum exchange in straight uniform compound channel flow. *Journal of hydraulic engineering*, 131(3), 175-183. DOI:10.1061/(ASCE)0733-9429(2005)131:3(175).
- Vannoppen, W., De Baets, S., Keeble, J., Dong, Y., & Poesen, J. (2017). How do root and soil characteristics affect the erosion-reducing potential of plant species? Ecological Engineering, 109, 186-195. DOI:10.1016/j.ecoleng.2017.08.001.
- Vardy, S., Saunders, J.E., Tolhurst, T.J., Davies, P.A., & Paterson, D.M. (2007). Calibration of the high-pressure cohesive strength meter (CSM). *Continental Shelf Research*, 27(8), 1190-1199. DOI: 10.1016/j. csr.2006.01.022.
- Vargas-Luna, A., Crosato, A., Anders, N., Hoitink, A.J., Keesstra, S.D., & Uijttewaal, W.S. (2018). Morphodynamic effects of riparian vegetation growth after stream restoration. *Earth Surface Processes and Landforms*, 43(8), 1591-1607. DOI:10.1002/esp.4338.
- Vargas-Luna, A., Duró, G., Crosato, A., & Uijttewaal, W.S.J. (2019). Morphological adaptation of river channels to vegetation establishment: a laboratory study. *Journal of Geophysical Research: Earth Surface*, 124(7), 1981-1995. DOI:10.1029/2018JF004878.

- Verdonschot, P.F.M., & Nijboer, R.C. (2002). Towards a decision support system for stream restoration in the Netherlands: an overview of restoration projects and future needs. In *Ecological Restoration of Aquatic and Semi-Aquatic Ecosystems in the Netherlands (NW Europe)*, 131-148. Springer, Dordrecht. DOI:10.1023/a:1021026630384.
- Vergani, C., Giadrossich, F., Buckley, P., Conedera, M., Pividori, M., Salbitano, F., Rauchg, H.S., Lovregliob, R. & Schwarz, M. (2017). Root reinforcement dynamics of European coppice woodlands and their effect on shallow landslides: A review. *Earth-science reviews*, 167, 88-102. DOI:10.1016/j.earscirev.2017.02.002.
- Verheij, H.J. (2000). Samenwerkingsproject modellering afslagoevers: Voortgangsrapportage 1999. Rapport nr. Q2529, WL Delft Hydraulics, Delft. Available at https://repository.tudelft.nl/islandora/object/uuid:b51f0de8-4689-4cef-b009-21b458ab459a, last access 06/07/2020.
- Verheij, H.J., Knaap, F.C.M. van der, Sessink, J.T.M (2007). Verder ontwikkelen van oeverafslagmodel BEM. Rapport nr. Q4264.02, WL Delft Hydraulics, Delft. Available at http://resolver.tudelft.nl/uuid:fc63f431-93e7-49c9-a4a5-d538fd4cd732, last access 06/06/2020.
- Vermeulen, B., Hoitink, A.J.F., Berkum, S.W., & Hidayat, H. (2014). Sharp bends associated with deep scours in a tropical river: The river Mahakam (East Kalimantan, Indonesia). Journal of Geophysical Research: Earth Surface, 119(7), 1441-1454. DOI:10.1002/2013JF002923.
- Vignaga, E., Sloan, D.M., Luo, X., Haynes, H., Phoenix, V.R., & Sloan, W.T. (2013). Erosion of biofilm-bound fluvial sediments. *Nature Geoscience*, *6*(9), 770. DOI:10.1038/ngeo1891.
- Westoby, M.J., Brasington, J., Glasser, N.F., Hambrey, M.J., & Reynolds, J.M. (2012). 'Structure-from-Motion' photogrammetry: A low-cost, effective tool for geoscience applications. *Geomorphology, 179*, 300-314. DOI:10.1016/j.geomorph.2012.08.021.
- WFD (2000). EU Water Framework Directive 2000/60/EC. http://data.europa.eu/eli/dir/2000/60/oj, last access 24/07/2020.
- Wiel, M.J.V.D., & Darby, S.E. (2007). A new model to analyse the impact of woody riparian vegetation on the geotechnical stability of riverbanks. *Earth Surface Processes and Landforms*, 32(14), 2185-2198. DOI:10.1002/esp.1522.
- Wilkerson, G.V., & Parker, G. (2011). Physical basis for quasi-universal relationships describing bankfull hydraulic geometry of sand-bed rivers. *Journal of Hydraulic Engineering*, 137(7), 739-753. DOI:10.1061/ (ASCE)HY.1943-7900.0000352.
- Willemsen, P.W.J.M., Borsje, B.W., Hulscher, S.J.M.H., Van der Wal, D., Zhu, Z., Oteman, B., et al. (2018). Quantifying bed level change at the transition of tidal flat and salt marsh: can we understand the lateral location of the marsh edge?. *Journal of Geophysical Research: Earth Surface, 123*(10), 2509-2524. DOI:10.1029/2018JF004742.
- Wilson, G.V., Wells, R., Kuhnle, R., Fox, G., & Nieber, J. (2018). Sediment detachment and transport processes associated with internal erosion of soil pipes. *Earth Surf. Process. Landforms*, 43(1), 45-63. DOI:10.1002/esp.4147.
- Wintenberger, C.L., Rodrigues, S., Bréhéret, J.G., & Villar, M. (2015). Fluvial islands: First stage of development from nonmigrating (forced) bars and woody-vegetation interactions. Geomorphology, 246, 305-320.
- Winterwerp, J.C. & van Kesteren, W.G. (2004). *Introduction to the physics of cohesive sediment dynamics in the marine environment*. Elsevier.
- Winterwerp, J.C., Van Kesteren, W.G.M., Van Prooijen, B., & Jacobs, W. (2012). A conceptual framework for shear flow–induced erosion of soft cohesive sediment beds. *Journal of Geophysical Research: Oceans,* 117(C10). DOI: 10.1029/2012JC008072.
- Wohl, E. (2014). A legacy of absence: wood removal in US rivers. *Progress in Physical Geography, 38*(5), 637-663. DOI:10.1177/0309133314548091.

- Wohl, E., Lane, S.N., & Wilcox, A. C. (2015). The science and practice of river restoration. *Water Resources Research*, *51*(8), 5974-5997. DOI:10.1002/2014WR016874.
- Wollny, J.T., Otte, A., & Harvolk-Schöning, S. (2019). Dominance of competitors in riparian plant species composition along constructed banks of the German rivers Main and Danube. *Ecological engineering*, 127, 324-337. DOI:10.1016/j.ecoleng.2018.11.013.
- Wood, A.L. (2001). A geomorphological analysis of bank toe processes: the fate of failed blocks stored in the basal zone of incised channels (Doctoral dissertation, University of Nottingham). ISNI: 0000-0001-3571-7675.
- Wood, A.L., Simon, A., Downs, P.W., & Thorne, C.R. (2001). Bank-toe processes in incised channels: the role of apparent cohesion in the entrainment of failed bank materials. *Hydrol. Process.*, 15: 39-61. DOI:10.1002/hyp.151.
- Woodget, A.S., Carbonneau, P.E., Visser, F., and Maddock, I.P. (2015). Quantifying submerged fluvial topography using hyperspatial resolution UAS imagery and structure from motion photogrammetry. *Earth Surface Processes and Landforms*, 40, 47-64. DOI:10.1002/esp.3613.
- Woolderink, H.A.G., Kasse, C., Cohen, K.M., Hoek, W.Z., & Van Balen, R.T. (2019). Spatial and temporal variations in river terrace formation, preservation, and morphology in the Lower Meuse Valley, The Netherlands. *Quaternary Research*, *91*(2), 548-569. DOI:10.1017/qua.2018.49.
- Wu, C., Ullah, M.S., Lu, J., & Bhattacharya, J.P. (2016). Formation of point bars through rising and falling flood stages: Evidence from bar morphology, sediment transport and bed shear stress. *Sedimentology*, 63(6), 1458-1473. DOI:10.1111/sed.12269.
- Wu, T.H., McKinnell, W.P. III, & Swanston D. N. (1979). Strength of tree roots and landslides on Prince of Wales Island, Alaska. *Canadian Geotechnical Journal*, *16*(1): 19-33. DOI:10.1139/t79-003.
- Wynn, T.M., Henderson, M.B., & Vaughan, D.H. (2008). Changes in streambank erodibility and critical shear stress due to subaerial processes along a headwater stream, southwestern Virginia, USA. *Geomorphology*, 97(3-4), 260-273. DOI:10.1016/j.geomorph.2007.08.010.
- Zaggia, L., Lorenzetti, G., Manfé, G., Scarpa, G.M., Molinaroli, E., Parnell, K.E., et al. (2017). Fast shoreline erosion induced by ship wakes in a coastal lagoon: Field evidence and remote sensing analysis. *PloS one*, 12(10), e0187210. DOI:10.1371/journal.pone.0187210.
- Zahibo, N., Didenkulova, I., Kurkin, A., & Pelinovsky, E. (2008). Steepness and spectrum of nonlinear deformed shallow water wave. Ocean Engineering, 35(1), 47-52. DOI:10.1016/j.oceaneng.2007.07.001.
- Zen, S. & Perona, P. (2020). Biomorphodynamics of river banks in vegetated channels with self-formed width. *Advances in Water Resources*, *135*, 103488. DOI:10.1016/j.advwatres.2019.103488.
- Zong, Q., Xia, J., Zhou, M., Deng, S., & Zhang, Y. (2017). Modelling of the retreat process of composite riverbank in the Jingjiang Reach using the improved BSTEM. *Hydrological Processes*, 31(26), 4669-4681. DOI:10.1002/hyp.11387.
- Zuo, L., Roelvink, D., Lu, Y., & Li, S. (2017). On incipient motion of silt-sand under combined action of waves and currents. *Applied Ocean Research, 69*, 116-125. DOI:10.1016/j.apor.2017.10.005.

ACKNOWLEDGEMENTS

This research was funded by Nederlandse Organisatie voor Wetenschappelijk Onderzoek (NWO, project number 13516) and the partners of RiverCare programme. It was conducted in the Department of Hydraulic Engineering of Delft University of Technology from 2015 to 2019. I would like to thank the people that made this dissertation possible or contributed to its development and improvement.

Wim, thank you for the dedicated exchanges during our regular meetings in the WaterLab. It was important to have your continuous support and advice, which you made available almost every time. The quality of this thesis was nourished with your critical comments and four years of reasoning together.

Alessandra, thank you for your trust and the support throughout these years. Your empathetic criticism, commitment and passion for research have made this work flourish. I enjoyed our time together along this meandering path, through which I learnt not only analytical and research skills from you. Thank you for reminding me what a big difference a positive attitude can make.

Maarten, thank you for your feedback, ideas, and enthusiasm. Your contribution to this research was a perfect fit within the supervisory team, from large to small scales and back. I learnt a lot and especially enjoyed our discussions.

I would like to acknowledge the help and support of the Hydraulic Engineering Laboratory staff which were essential for the progress of this research. Many thanks to Jaap van Duin for the trips to Oeffelt and many other sites, Arno Doorn for building the plaques for the UAV, Ruben Kunz for helping with fieldwork, Sander de Vree for all kinds of help in the Laboratory and fieldwork preparations, Pieter van der Graag for the assistance, initiative and creative solutions in the field and related arrangements, and Matthieu de Schipper for the support with the RTK GPS and for always picking up the phone to help. Beyond the hard work, it was a pleasure to work together in the field.

I am grateful to Irene Colossimo and Bram van Prooijen for their assistance in the preparations for the ADV-OBS measurements and for sharing their vast experience with field campaigns (and amazing energy too).

I want to especially thank Erik Mosselman for translating the summary of this book into Dutch, and for sharing literature, thoughts, interesting conversations, and above all, for being a source of inspiration.

I appreciate and acknowledge the data or scripts generously shared by Clara Chrzanowski, Frans Hoefsloot, Marion Tissier, Hans Bakker, and Pepijn van Aubel with the ZN-RWS team, which were used in this work or contributed to the analyses and conclusions presented herein.

Thanks to Petra Fleischer for sharing information on Steinmauern bank of the Rhine River, Mario Klosch for the comments on Thurnhaufen bank in the Danube River, and Bernhard Söhngen for hosting the 5th meeting of PIANC Working Group 128 in Worms, including the visit to test sections of alternative technical-biological bank protections. Thanks to Margriet Schoor and Pieter van Vessem for the field visit to Fortmond bank in the Ussel River.

This thesis benefited from the discussions held during the biannual PhD User Committee meetings, with the participation of Ralph Schielen (Rijkswaterstaat), Astrid Blom (TU Delft), Marcela Busnelli (Royal HaskoningDHV), Vincent Vuik (HKV), Frans Hoefsloot (Lievense), Pepijn van Aubel (Rijskwaterstaat), Wouter Rozier (Rijkswaterstaat), and Pepijn van Denderen (UTwente).

I appreciate the discussions on waves with Dano Roelvink, Lodewijk de Vet, and Yorick Broekema, as those with Hessel Woolderink on the Meuse River geology and past dynamics.

Thanks to Merel Verbeek, María Barciela, Zeinab Safar and Erik Hendriks for making a pleasant working place and for the nice shared moments.

It was great to be part of the WaterLab and having had fun together, especially in the music events (Bram I will never forget the sound of that trumpet). Thanks to my former colleagues Alejandra, Ana, Andrés, Antonis, Clara, Claudia, Cynthia, Jakob, Jill, Le, Liselot, Marco, Matt, Meles, Nici, Patricia, Sienna, Stuart, Víctor, and Xin.

Thanks to all the colleagues and coordinators of the RiverCare programme for the discussions, exchanges, and social events.

Sincere thanks to Wim Ridderinkhof and to Ruud Bouw from Witteveen+Bos for the support and encouragement to finish this dissertation during the past year.

Warm thanks to my family and friends, both in the Netherlands and Argentina, who supported me throughout these years. You have been in my heart all this time.

Deep sincere thanks to my beloved partner Adriana, who joined and supported me through this path. It is wonderful to have grown together, and have brought Lara to join this adventure. My great gratitude is also to you little one.

CURRICULUM VITAE

Gonzalo Duró was born on 21 May 1984 in La Plata, Argentina. After graduating in Rafael Hernández National College, he studied hydraulic and civil engineering at the National University of La Plata (UNLP). Since 2005, during his studies, he performed teaching assistance in the subjects Design of Hydromechanical Facilities and Water Resources Management. In 2006 and 2007, he held part-time internships in the Laboratory of Hydromechanics of the UNLP, assisting in studies of hydraulic turbine performance. After receiving degrees in Civil and Hydraulic Engineering in 2008, Gonzalo worked until 2012 in the same Laboratory as consultant and researcher, while keeping his duties in university teaching. He worked on several projects involving hydrodynamic studies, with reduced-scale models and computational fluid dynamics (CFD). He gained extensive experience to optimize efficiency in facilities for pumps, turbines, and water conveyance through hydraulic design.

Gonzalo then followed a Master of Science programme in hydraulic engineering and river basin development at IHE-Delft, graduating cum laude in 2014. He specialized in river engineering, investigating bar dynamics in trained rivers with numerical models, Delft3D and TELEMAC-MASCARET, whose results were published in a peer-review journal. He carried out part of this research at Saint-Venant Hydraulics Laboratory of EDF in Chatou, France. He later applied the gained knowledge on a lowland hydropower project back in the UNLP Laboratory of Hydromechanics, combining hydraulic design with principles of river morphodynamics.

In 2015, Gonzalo started a PhD at Delft University of Technology. Among the duties he carried out, stand out the collaboration in reduced-scale experiments of river morphodynamcis with artificial vegetation in the Hydraulic Engineering Laboratory (WaterLab) and numerous field campaigns in small and midsized rivers. The latter involved topographic surveys with drones, wave measurements with ADV, use and calibration of OBS to measure suspended sediment concentrations, soil coring and geotechnical tests, and RTK GPS profiling. Complementary to these activities, he

developed algorithms to process and analyse large datasets, including the quantification of wave characteristics and systematizing particle tracking velocimetry for experiments. During the last stage of his research, and after conceptualizing observed bank erosion processes, Gonzalo developed a numerical model to represent the non-linear evolution of riverbank erosion induced by ship waves.

In 2019, Gonzalo started working at Witteveen+Bos as project engineer in the group Hydrodynamics and Morphology, where he currently analyses river and coastal systems.

Gonzalo is married to Adriana, with whom he parents their daughter Lara.

PUBLICATIONS

JOURNAL ARTICLES

- Duró, G., Crosato, A., Kleinhans, M. G., Roelvink, D., & Uijttewaal, W. S. J. (2020b). Bank erosion processes in regulated navigable rivers. *Journal of Geophysical Research: Earth Surface, 125*, e2019JF005441. DOI:10.1029/2019JF005441.
- Duró, G., Crosato, A., Kleinhans, M. G., Winkels, T. G., Woolderink, H. A. G., & Uijttewaal, W. S. J. (2020). Distinct patterns of bank erosion in a navigable regulated river. *Earth Surf. Process. Landforms*, 45(2), 361-374. DOI:10.1002/esp.4736.
- Vargas-Luna, A., Duró, G., Crosato, A., & Uijttewaal, W. (2019). Morphological adaptation of river channels to vegetation establishment: A laboratory study. *Journal of Geophysical Research: Earth Surface, 124*, 1981–1995. DOI:10.1029/2018JF004878.
- Duró, G., Crosato, A., Kleinhans, M. G., and Uijttewaal, W. S. J. (2018). Bank erosion processes measured with UAV-SfM along complex banklines of a straight mid-sized river reach, Earth Surface Dynamics, 6, 933-953. DOI:10.5194/esurf-6-933-2018.
- Duró G., Crosato A., Tassi P. (2015). Numerical study on river bar response to spatial variations of channel width. *Advances in Water Resources*, *93*, 21-38. DOI:10.1016/j. advwatres.2015.10.003.

CONFERENCE ARTICLES

Duró, G., Crosato, & Uijttewaal, W. S. J. (2020). Bank erosion in regulated navigable rivers: towards a process-based model of bank retreat. River Flow 2020: Proceedings of the 10th Conference on Fluvial Hydraulics, Delft, the Netherlands. DOI:10.1201/b22619.

- Duró, G., Crosato, A., Kleinhans, M., Uijttewaal W.S.J. (2020). Erosion processes and retreat prediction of re-naturalized banks in regulated navigable rivers. *Managing changing rivers, Proceedings of NCR days 2020*, 122-123.
- Duró, G., Wieggers, J., Uijttewaal, W. S. (2019). Natural riverbanks in a regulated waterway A full restoration approach in the Meuse River. *Smart Rivers conference* 2019, Lyon, France.
- Duró, G., Crosato, A., Kleinhans, M., Uijttewaal W.S.J. (2018). On the morphological evolution of restored banks: case study of the Meuse river. In *E3S Web of Conferences* 40, 02021, River Flow 2018 Ninth International Conference on Fluvial Hydraulics, Lyon, France. DOI:10.1051/e3sconf/20184002021.
- Duró, G., Crosato, A., Kleinhans, M., Uijttewaal W.S.J. (2017). Cohesive bank erosion processes identified from UAV imagery during an exceptional low water level event. 10th Symposium on River coastal and estuarine morphodynamics, 170-170, Trento - Padova, Italy.
- Duró, G., Crosato, A., Kleinhans, M., Uijttewaal W.S.J. (2017). Bank erosion processes in waterways. *Proceedings of NCR days 2017*, 82-83, Wageningen University & Research.
- Duró, G., Crosato, A., Uijttewaal W.S.J. (2015). Research on Natural Bank Erosion Processes. *Proceedings of NCR days 2015*, 113-114. Lenders H.J.R., Collas F.P.L., Geerling G.W. & Leuven R.S.E.W. (eds.).
- Duró G., Crosato A., Tassi P. (2015). Numerical experiments to explore bar management by channel width variations. *36th IAHR World Congress*, The Hague, the Netherlands.
- Duró G., Crosato A., Tassi P. (2014). Morphodynamics structures induced by variations of the channel width. *European Geosciences Union General Assembly*. Vienna, Austria.
- Duró G., de Dios M., López A. (2012). Physical modelling and CFD comparison: case study of a hydro-combined power station in spillway mode. *4th International Junior Researcher and Engineer Workshop on Hydraulic Structures*, Utah State University, Logan, Utah, USA. DOI:10.15142/T3RP4K.
- Duró G. de Dios M. D., López A., Liscia S. O., Angulo M. A. (2012). Comparación de simulaciones en CFD y modelación física de una central hidrocombinada. *Proceedings of XXV Congreso Latinoamericano de Hidráulica, IAHR*. San José de Costa Rica, Costa Rica. DOI:10.13140/RG.2.1.3880.8406 (in Spanish).

Lucino C., Liscia S., Duró G. (2010). Detección de vórtices en dársenas de bombeo mediante modelación matemática. *Proceedings of XXIV Congreso Latinoamericano de Hidráulica, IAHR*. Punta del Este, Uruguay. https://www.academia.edu/7553386/ (in Spanish). English version can be found at www.flow3d.com as 'Vortex detection in pump sumps by means of CFD' (last access: 28 January 2020).



